Dispersive $\pi K \rightarrow \pi K$ and $\pi\pi \rightarrow K\bar{K}$ amplitudes from scattering data, threshold parameters, and the lightest strange resonance κ or $K_0^*(700)$

José R. Peláez [a,*], Arkaitz Rodas [b,c]

[a] Departamento de Física Teórica, Universidad Complutense and IPARCOS, 28040 Madrid, Spain
[b] Department of Physics, College of William and Mary, Williamsburg, VA 23187, USA
[c] Thomas Jefferson National Accelerator Facility, 12000 Jefferson Avenue, Newport News, VA 23606, USA

ARTICLE INFO

ABSTRACT

We discuss the simultaneous dispersive analyses of $\pi K \rightarrow \pi K$ and $\pi\pi \rightarrow K\bar{K}$ scattering data and the $\kappa/K_0^*(700)$ resonance. The unprecedented statistics of present and future hadron experiments, modern lattice QCD calculations, and the wealth of new states and decays require such precise and model-independent analyses to describe final state interactions. We review the existing and often conflicting data and explain in detail the derivation of the relevant dispersion relations, maximizing their applicability range. Next, we review and extend the caveats on some data, showing their inconsistency with dispersion relations. Our main result is the derivation and compilation of precise amplitude parameterizations constrained by several $\pi K \rightarrow \pi K$ and $\pi\pi \rightarrow K\bar{K}$ dispersion relations. These constrained parameterizations are easily implementable and provide the rigor and accuracy needed for modern experimental and phenomenological hadron physics. As applications, after reviewing their status and interest, we will provide new precise threshold and subthreshold parameters and review our dispersive determination of the controversial $\kappa/K_0^*(700)$ resonance and other light-strange resonances.

Contents

* Corresponding author.
   E-mail address: jrpelaez@fis.ucm.es (J.R. Peláez).

1. Introduction

1.1. Motivation

"There is no excellent beauty that hath not some strangeness in the proportion".

Francis Bacon. "Of Beauty", in Essays (1625)

Even though the existing data on $\pi K \rightarrow \pi K$ and $\pi\pi \rightarrow K\bar{K}$ scattering below 2 GeV were obtained between 30 and 50 years ago, there is a longstanding interest in them, which has been renewed over the last years motivated by the following reasons: First, they are relevant by themselves because they test hadron physics and particularly the low-energy realm. Second, because pions and kaons are the lightest hadrons and then they appear in the final state of most hadronic processes, which thus require a description of their interactions. Third, they are of interest for Hadron Spectroscopy, due to the resonances that can be identified in these processes. Finally, on the theoretical side, since the low-energy regime lies out of reach for standard QCD perturbation theory, they test the most recent developments on non-perturbative QCD techniques, like lattice QCD calculations and the low-energy QCD effective theory, known as Chiral Perturbation Theory (ChPT).

Given their relevance and the many years passed since these interactions were measured, readers outside the field may assume that a rigorous and accurate description should have been found many years ago. However, this is not the case and, in brief, this is due to what we could call the "data problem" and the "model-dependence problem". The data problem is that the $\pi K \rightarrow \pi K$ [1–6] and $\pi\pi \rightarrow K\bar{K}$ [7–9] scattering data, obtained in the '70s and '80s, were extracted indirectly from meson–nucleon scattering experiments. Unfortunately, this technique is plagued with systematic uncertainties, leading to conflict within or between data sets, particularly for the controversial S-wave, as we will review here in Section 2. The model-dependence problem arises because, since we cannot use a systematic approach like QCD, for many years simple models and fits were considered good enough to describe such data. Moreover, given that conflicting data exist, any model providing a mere qualitative description was also considered acceptable, even good if the description was semiquantitative. This situation with data and models is illustrated in Fig. 1. Needless to say that this state of affairs has led, for instance, to different resonance contents in different models, or different parameters for the same resonance, to scarce robust and precise determinations of low-energy parameters, etc... Of course, the use of models may have been justified at first, but modern hadron physics demands a more precise, rigorous, and model-independent description.

Dispersion relations, which, as we will also review in Section 3, are a consequence of fundamental properties like relativistic causality and crossing symmetry, provide a solution to these two problems. First, concerning the data problem, they provide stringent constraints on amplitudes, which allow us to neglect or identify inconsistent data and restrict the fits that can be acceptable. We will review in Section 4 how simple and very nice-looking data fits fail to satisfy the dispersive representation. Sometimes, dispersion relations can be solved in a given regime and provide information without using data there. However, in this report, we want to analyze the data and our main result will be to provide in Section 5 a Constrained Fit to Data (CFD) that satisfies all the dispersive constraints. Second, since the dispersive constraints are written in terms of integral relations, they wash out any dependence on the details of input parameterizations. Moreover, dispersion relations provide the correct and model-independent analytic continuation to the complex plane that allows for a rigorous determination of the existence and parameters of resonances, to which Section 6 is dedicated. In particular, after reviewing the general state of the art in 6.1, we will dedicate Section 6.2 to the use of analytic methods to minimize model dependencies when extracting parameters of strange resonances and Section 6.3 to the dispersive determinations of the still debated $\kappa/K_0^*(700)$ meson. In addition, a dispersive determination of the non-ordinary Regge trajectory of the $\kappa/K_0^*(700)$, using as input its pole parameters, is presented in Section 6.4.
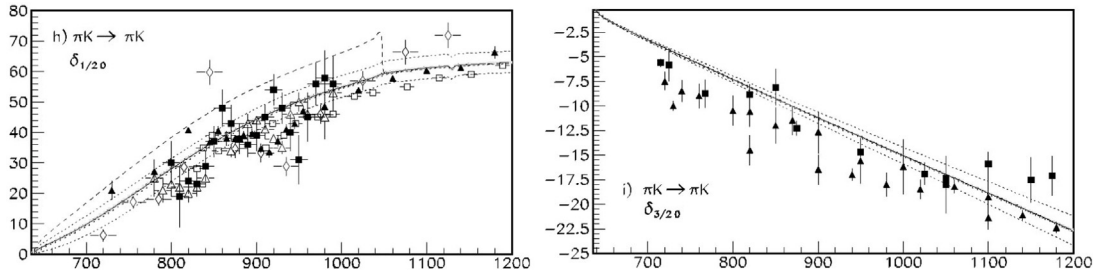
Fig. 1. Plots are taken from [10] to illustrate the conflicting data sets and a rather popular model (unitarized Chiral Perturbation Theory). They represent the phase shifts of the isospin 1/2 (Left) and 3/2 (Right) scalar partial waves. As we will discuss in the main text, the 1/2 phase shifts are not measured directly. See [10] for experimental references.

Finally, apart from their model independence, the use of integrals increases the precision when calculating certain observables, like the threshold or subthreshold parameters. In Section 7.1 we will thus review these so-called sum rule determinations, also providing new results or updating old ones. Further applications related to the πK sigma term and a brief review of the $\pi\pi \to K\bar{K}$ contribution to the calculation of the anomalous magnetic moment of the muon are also presented in Sections 7.2 and 7.3, respectively.

All the advantages of dispersion theory listed above are common to many other processes where they have provided successful descriptions highly demanded by modern developments. The relatively recent and comprehensive reports on their application to $\pi\pi \to \pi\pi$ [11–13] and $\pi N \to \pi N$ [14] are illustrative of this demand. Our aim here is to provide such a comprehensive report for $\pi K \to \pi K$ and $\pi\pi \to K\bar{K}$.

1.2. State of the art and goals

Let us then describe in detail the present situation of the pieces of motivation we have enumerated above and the objectives we want to address in this report.

1.2.1. The interest in $\pi K \to \pi K$ and $\pi\pi \to K\bar{K}$ interactions by themselves

First of all, these processes are interesting by themselves, since, together with $\pi\pi \to \pi\pi$ scattering, they are the simplest two-body interactions of hadrons. Moreover, these are the lightest mesons available, and, being pseudoscalar particles, they do not have the complications associated with their spin. Thus, one would expect that any basic understanding of hadronic interactions should be able to describe these processes.

Indeed, over almost five decades, a lot of work has been devoted to building phenomenological models to describe $\pi K \to \pi K$ and/or $\pi\pi \to K\bar{K}$ scattering. Until the late '70s, we refer the reader to the excellent review in [15] and after that a wide variety of these models can be found in [10,16–40]. Many of them will be discussed below. However, in this report, we will focus on the data analysis within the model-independent dispersive approach, which yields mathematical robust constraints and results, although it may also be limited in its applicability conditions.

Of course, to understand these interactions the first need is to have a reliable data analysis, consistent with fundamental constraints. Unfortunately, we have recently shown in [41,42] that, respectively, the $\pi K \to \pi K$ and $\pi\pi \to K\bar{K}$ data are inconsistent with dispersion relations, sometimes by a large amount. It should be pointed out that in a remarkable work [43], numerical solutions of partial-wave projections of fixed-t dispersion relations, i.e. the so-called Roy–Steiner equations [44–46], were obtained for πK below 1 GeV. As seen in Fig. 2 these solutions were consistent with the scalar-wave data from [5], but not quite so with the prominent $K^*(892)$ in the vector wave. We emphasize that these are solutions to the dispersion relations, which do not use data in the elastic regions of these waves so that the curves are predictions and the results impressive. In the present work, however, we will follow a different approach, not solving Roy–Steiner dispersion relations, but using many types of them as constraints on data in an energy region as large as possible.

Thus, in this report we will explain and review the dispersive formalism for $\pi K \to \pi K$ and $\pi\pi \to K\bar{K}$, paying particular attention to our series of works [41,42,47]. Besides reviewing those results, we will complete the Roy–Steiner analysis applying it simultaneously to $\pi K \to \pi K$ and $\pi\pi \to K\bar{K}$, which so far had been analyzed considering the other one as a fixed input. Moreover, we will derive and use Roy–Steiner relations with various numbers of subtractions, which weight differently different energy regions, and we will use them to determine several threshold parameters. Finally, forward dispersion relations will be used to constrain πK amplitudes up to 1.7 GeV. This defines our main goal, which is to present here simple parameterizations of both $\pi K \to \pi K$ up to 1.8 GeV and $\pi\pi \to K\bar{K}$ up to 2 GeV that describe the data, *and their uncertainties*, while simultaneously satisfying an ample set of dispersion relations covering different regions. This result will be called Constrained Fit to Data (CFD) in contrast to other Unconstrained Fits to Data (UFD) that we will also analyze here. Similarly constrained parameterizations were obtained for $\pi\pi \to \pi\pi$ in a series of works [48–51] by one of the authors together with the Madrid–Krakow group and they have become widely used both in theoretical and experimental studies. To provide the hadron community with similar results for $\pi K \to \pi K$ and $\pi\pi \to K\bar{K}$, this review
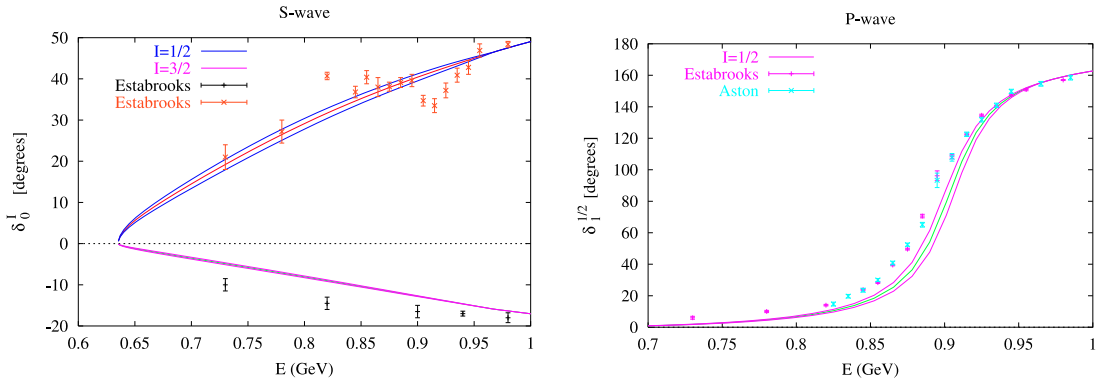
Fig. 2. Solutions of Roy–Steiner equations obtained in [43] for the phase shifts of $\pi K \to \pi K$ scattering partial waves. Left: *S*-waves with isospin 1/2 (positive curves) and 3/2 (negative curves). Right: *P*-wave of isospin 1/2. The data come from [5,6].
Source: The figure is taken from [43].

will therefore deliver the most constrained set of $\pi K \to \pi K$ and $\pi\pi \to K\bar{K}$ partial-wave parameterizations, together with accurate values of threshold and subthreshold parameters as well as a review of the rigorous determination of the $\kappa/K_0^*(700)$ parameters and other heavier strange resonances.

The simplicity of our parameterizations and their uncertainties is a goal we imposed on ourselves so that they are easy to implement in future works, either of phenomenological or experimental character, whose interest on $\pi K \to \pi K$ and $\pi\pi \to K\bar{K}$ we detail in the next subsections.

1.2.2. $\pi K \to \pi K$ and $\pi\pi \to K\bar{K}$ scattering for final state interactions

On the experimental and phenomenological side, we remark once again that a piece of motivation to look for such a CFD parameterization of $\pi K \to \pi K$ and $\pi\pi \to K\bar{K}$ interactions is because, being much lighter than similar hadrons, pions and kaons are ubiquitous in final states of hadron processes. Once they appear in a final state they re-scatter strongly again. These are known as final state interactions (FSI) and are a very relevant contribution to the description of many hadronic processes. Moreover, the interest for a precise and rigorous $\pi K \to \pi K$ and $\pi\pi \to K\bar{K}$ description has increased due to the high statistics at B-meson factories (BaBar, Belle, LHCb), the wealth of new hadron states, their many decay channels and the CP violation studies, which need reliable input from intermediate $\pi\pi, \pi K, K\bar{K}$ states and their FSI. As illustrative examples of these processes, let us mention: multi-body heavy-meson decays like $D \to K\pi\pi$ [52–54], $B^{\pm} \to DK^{\pm}$ with $D \to K\pi\pi$ or $D \to KK\pi$ [55–58], or $B \to 3M$, with $M = \pi, K$ [59], CP violation in $D, B \to K^+\pi^-K^-\pi^+$ [60–62], and the enhancement of CP violation by meson–meson FSI in three-body charmless B decays [63,64], particularly through $\pi\pi \to K\bar{K}$ rescattering [65,66] (see the recent review in [67]). Very often, these FSI are described with simple models fitted to data, which, as we will show here, fail to satisfy the fundamental constraints encoded in dispersion relations. The precision achieved by the already existing data thus asks for model-independent parameterizations and a realistic assessment of their uncertainties. Let us note that such model-independent dispersively constrained parameterizations for $\pi\pi \to \pi\pi$ coauthored by one of us [48] are widely used both by phenomenological and experimental studies. Moreover several of these experimental groups have asked us for our constrained $\pi K \to \pi K$ and $\pi\pi \to K\bar{K}$ parameterizations [41,42] too. This includes the recently accepted KLF proposal [68,69] to use a neutral K_L beam at Jefferson Lab with the Gluex experimental setup, to study strange spectroscopy and the πK final state system up to 2 GeV. Further developments on existing experiments and future Hadron-Physics facilities will be even more demanding for precise and model-independent meson–meson amplitudes like those reviewed in this manuscript.

1.2.3. Lattice QCD and Chiral Perturbation Theory

On the theoretical side, unfortunately, the energy region below 1.5 or 2 GeV lies beyond the applicability realm of perturbative QCD. Nevertheless, unquenched lattice QCD calculations on $\pi K \to \pi K$ [70–72] phase shifts and $\pi\pi \to K\bar{K}$ [73,74], still at unphysical masses, provide scattering information at several different energies. This is illustrated in Fig. 3, where we can see that the main features of the scalar and vector partial waves in the elastic regime are clearly visible, even if for unphysical masses. For a review on scattering processes and resonances from lattice QCD see [75]. We consider it very likely that precise lattice QCD calculations with close to physical pion masses may be available soon. These will also require consistent and precise data analyses, like the one we pursued here, to compare with.

In addition, since the advent of QCD, we know that pions and kaons (together with the eta meson) can be identified with the Nambu–Goldstone-Bosons (NGB) [76–79] associated with the spontaneously broken SU(3) chiral symmetry generators of QCD. In the massless quark limit, these NGB would be massless and separated from all other hadrons by a mass gap of $O(1\text{GeV})$. Note, however, that quarks have a small non-zero mass so that pions and kaons are indeed massive, but they are still much lighter than hadrons with similar quantum numbers. This is why, in purity, they should be called
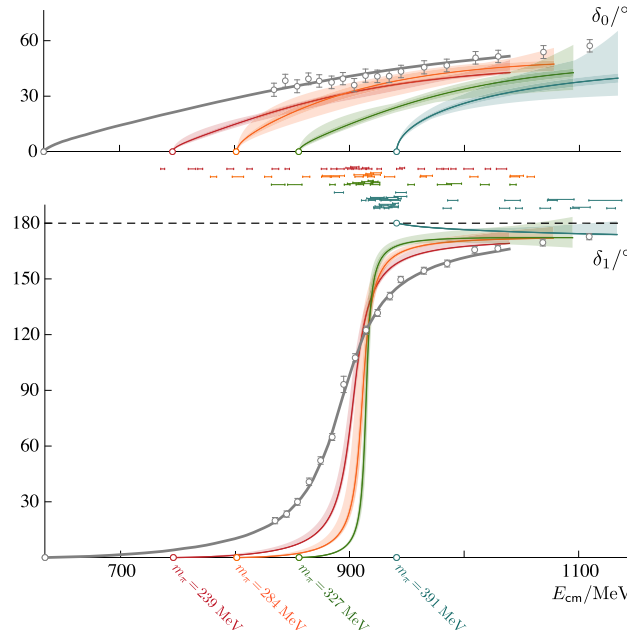
Fig. 3. Comparison between the fitted low energy phase shifts δ_ℓ obtained from lattice QCD calculations for the scalar $f_0^{1/2}(s)$ (top) and vector $f_1^{1/2}(s)$ (bottom) $\pi K \to \pi K$ scattering partial waves, at four different quark masses. Notice how, as the lattice pion mass tends to the physical pion mass, both partial waves approach the gray curves, which represent our UFD fit [41] to real data. Note also that the vector channel at $m_\pi = 391$ MeV has been plotted starting at 180 degrees as the $K^*(892)$ becomes a bound state.
Source: The figure is taken from [72].

"pseudo-NGB". In any case, the mass gap exists even if QCD is not massless. This means that pions, kaons, and etas are the only degrees of freedom of the strong interaction at low energies and the main decay products at all energies.

Perturbative QCD may not be applicable at low energies, but, together with the observed chirally-broken spectrum, it still dictates that the spontaneous chiral symmetry pattern is that of an SU(3)$_L \times$ SU(3)$_R$ group, broken down to an SU(3)$_{L+R}$ group (for introductory texts see [80–82]). Here R, L refer to right and left quark chiralities. It is then possible to formulate the low-energy effective field theory of QCD reproducing this symmetry breaking pattern in terms of pions, kaons, and the eta. This is called Chiral Perturbation Theory (ChPT) [83,84] and provides a rigorous and systematic perturbative treatment of hadron physics in the low-energy regime. This alternative perturbative expansion is organized in even powers of masses or momenta and can be tested against experiments by studying meson–meson interactions at very low energies. Consequently, the so-called threshold or sub-threshold parameters become a central object of study. In particular, the ChPT program has been carried out to NNLO for $\pi K \to \pi K$ scattering in [85], providing rather accurate predictions. Let us note that the pion-only version of ChPT is known to work very well since the pion mass is very small $\sim$0.14 GeV. However, the SU(3) ChPT convergence is not so nice [86] when dealing with kaons, whose mass is $\sim$0.5 GeV.

Interestingly, at present, there is some tension between the scalar πK scattering lengths from QCD [87–93] and the rigorous dispersive determination we mentioned above [43] and our previous dispersively constrained fits to data [41]. This situation is summarized in Fig. 4. Only with NNLO ChPT [86] it is possible to come close to these dispersive values, but then the NNLO lies more than two standard deviations off the bulk of lattice values. Moreover, in such case the scalar πK scattering lengths show "the worst convergence of all" [86].

Thus, another goal in this report is to provide accurate and rigorous determinations of πK threshold and subthreshold parameters, with particular attention to the scalar ones. These will be obtained in Sections 7.1.2 and 7.1.3, respectively, from sum rules derived from dispersion theory, and, once again, we will pay special attention to uncertainties, including those from $\pi\pi \to K\bar{K}$.

1.2.4. Strange meson spectroscopy and the $\kappa/K_0^*(700)$

Finally, the fourth feature of $\pi K \to \pi K$ and $\pi\pi \to K\bar{K}$ interactions motivating this work is that they provide important information on light meson spectroscopy. One aim of spectroscopy is to identify as mesons the bound states of quarks and antiquarks—or, more often, as resonances since we deal with strong interactions that make most of these states rather unstable. For a compilation of our present knowledge about these bound and resonant states, we refer the reader to the Review of Particle Physics (RPP) [95]. Once these states are established, another aim of spectroscopy is to classify them in multiplets related by some symmetry transformation: in our case, isospin, flavor SU(3), and spin multiplets, as well as to identify their parity, etc... Let us remark that SU(3) flavor multiplets require the presence of strange resonances, and it can be checked that the information on many of these strange resonances is dominated by $\pi K \to \pi K$ scattering data.
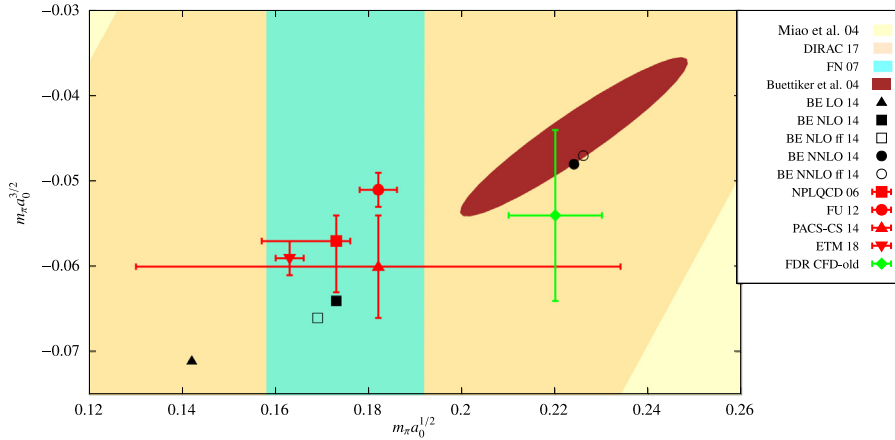
Fig. 4. Comparison between various existing determinations of the $\pi K \to \pi K$ scalar scattering lengths $a_0^{1/2}$ and $a_0^{3/2}$. The only experimental value shown is the beige band of the a_0^- DIRAC measurement [94]. The first lattice result (Miao et al. [87]) yields the rather large yellow band, whereas higher precision is claimed in more recent lattice calculations (In red: NPLQCD [88], Fu [91], PACS-CS [92], ETM [93]) as well as when lattice was combined within an Omnès dispersion relation (Flynn–Nieves [89]). Note that dispersive determinations yield somewhat larger values for both scattering lengths, as in Büttiker et al. [43], or Peláez-Rodas [41] (FDR CFD-old). ChPT calculations to LO, NLO and NNLO come from the Bijnens–Ecker review [86], but note the NNLO parameters are obtained by including in the fit the value of [43].

One area of very active research in Hadron Spectroscopy is the search for non-ordinary mesons, namely, those that are not made of just a valence quark and an antiquark. Probably the most interesting non-ordinary configuration is the glueball. This is a meson made of bound gluons, which contrary to photons can interact with themselves due to QCD being a non-abelian gauge theory. Having no quarks in its composition, a glueball should have zero charge and no flavor, so that it forms a flavor singlet. The lightest one is also expected to be a scalar. This is one of the reasons why understanding light scalar mesons is very important. However, mesons made of quarks should form nonets, i.e. an octet and a singlet. Thus, naively, any singlet not associated with an octet is a glueball candidate. Unfortunately, in practice, this simple picture is complicated by the mixing of resonances with the same quantum numbers. However, the simplest way to identify how many octets should be and where their masses are is by looking at their strange members, which makes the identification of strange resonances even more relevant. As we commented above, a great deal of the information used to determine the existence and properties of strange resonances below 2 GeV comes from $\pi K \to \pi K$ scattering, with all the caveats about data inconsistencies and model dependencies that we have already emphasized. Hence, another goal of this report is to review the recent application of analytic techniques, using our CFD as input, to obtain model-independent determinations of strange resonances below 2 GeV.

Furthermore, the other reason why light scalar mesons are interesting is that the exchange of the lightest one, known as the σ or $f_0(500)$ resonance, is responsible for most of the attractive part of the nucleon–nucleon potential, without which nuclei would not be formed and we would not even exist. The $\sigma/f_0(500)$ is very difficult to observe clearly in experiments, since it is very wide and short-lived, with no charge, isospin zero, and no strangeness, i.e. the vacuum quantum numbers. It has very many properties that make it a robust candidate for a non-ordinary meson. Over the last years there is growing agreement that this state is dominated by some kind of four-quark or two-meson configuration (see [13] for a recent review). Nevertheless, since the $\sigma/f_0(500)$ has the same quantum numbers of the lightest glueball, some works have postulated that it is actually the lightest one of them [28,96]. However, if it were made of quarks it would necessarily have a strange partner, known as the $\kappa/K_0^*(700)$, which once again is a wide and very controversial state. There has been a longstanding debate about the existence and properties of this light strange resonance and, as of today, it still "Needs Confirmation" in the RPP [95]. Once again, the determination of this state is hindered by the data and model-dependence problems commented above. In this case, the model-dependence problem is aggravated because the analytic extension to the complex plane is a very unstable procedure when models are used to extrapolate to the complex plane. Once more, the solution comes from dispersion theory, this time in the form of dispersion relations projected into partial waves. However, we will show here that the problem is so unstable that even using naively the same partial-wave data as input, different dispersion relations can yield different poles. A unique pole is obtained only if the data description in the real axis satisfies dispersion theory. It should be remarked that a rigorous dispersive determination of the $\kappa/K_0^*(700)$, although without using data on the nominal $\kappa/K_0^*(700)$ region, was obtained in [97]. Interestingly, the authors were able to prove that the $\kappa/K_0^*(700)$ pole lies within the applicability domain of partial-wave projected hyperbolic dispersion relations. Then, by using inside the latter the solution predicted from partial-wave projected fixed-t dispersion relations obtained in [43], they obtained their very sound prediction for the $\kappa/K_0^*(700)$ pole. Since this work does not use $\pi K \to \pi K$ data in the $\kappa/K_0^*(700)$ region, in a sense, their resonance is a prediction. Nevertheless, even after that work, the $\kappa/K_0^*(700)$ still "Needs Confirmation" according to the RPP [95].

Within our approach, we are looking for a complementary determination based on data instead. Actually, our recent determination in [98] using analytic techniques based on truncated series of Padé approximants obtained from the derivatives of our dispersively constrained fit to data [99], triggered the 2018 change of the $\kappa/K_0^*(700)$ name and parameters in the Review of Particle Physics (it was $K^*(800)$ until then). It is only recently that we have completed a precise and rigorous dispersive determination of the $\kappa/K_0^*(700)$ pole using partial wave hyperbolic dispersion relations [47]. The final result for our pole and a sketch of the constrained fit to data was given in [47], but one of our goals here is to provide the details of the full calculations.

Let us remark that a recent lattice study [100,101] at unphysical masses already finds a virtual pole that can be associated with the $\kappa/K_0^*(700)$. This behavior was already predicted within unitarized ChPT [102]. Unfortunately, when using more realistic masses, even using the phase shifts shown in Fig. 3, the extraction of the $\kappa/K_0^*(700)$ pole is not so straightforward. When employing models to obtain the analytic continuation, the poles are, once again, rather unstable [72,101]. It seems that a rigorous determination of the $\kappa/K_0^*(700)$ from lattice will also require the analysis of lattice data using analytic and dispersive techniques like the ones we will describe in this report. Note that in this case dispersion relations will not be "solved" but instead used to "constrain" the lattice data, which is the main approach we will follow here.

1.2.5. Other applications

Finally, we will also review other applications of dispersion relations to $\pi K \to \pi K$ or $\pi\pi \to K\bar{K}$ scattering, as well as further applications where, as a part of a larger calculation, a precise knowledge of these interactions may be of interest.

Thus, in Section 6.4, we will illustrate an additional use of dispersion theory for $\pi K \to \pi K$ scattering. The relevant observation is that the analytic properties of Regge trajectories are determined by the analytic properties of the partial wave where they appear (for a textbook introduction to Regge theory see [103]). In the case of an "elastic resonance", i.e. with just one decay channel, these analytic constraints can be combined with elastic unitarity into a dispersion relation for its trajectory, which in turn determines, up to a few subtraction constants, the partial-wave in the energy region dominated by that resonance. Adjusting these constants so that the partial-wave has a pole with the given resonance parameters, one then determines its Regge trajectory. It is here that the poles obtained from dispersive approaches can also be used as input. When this method is applied to relatively narrow resonances like the $\rho(770)$ or $f_2(1270)$ [104,105], their trajectories come almost real and in the form of straight lines in the (M^2, J) plane, with a slope of ~ 1 GeV^{-2}. These are the ordinary resonances associated with quark–antiquark states bound by QCD dynamics. In Section 6.4 we will review how, when this method has been applied to resonance poles in $\pi K \to \pi K$ scattering [106], we have found the expected ordinary trajectories for the $K^*(892)$ and $K_0^*(1430)$. In contrast, the trajectory of the $\kappa/K_0^*(700)$ comes out different, providing strong evidence for the non-ordinary nature of this controversial state. Moreover, we will review how this trajectory is very similar to that of the $\sigma/f_0(500)$ meson, showing once more the striking similarities of these two non-ordinary states.

In the final Section 7 we supply examples of applications where our CFD can be used as input. We have already commented that in this section we provide precise and model-independent values of threshold and subthreshold parameters obtained using our CFD as input. For these we review and also derive a large collection of sum rules from dispersion relations, providing many of their explicit expressions. We hope these are of relevance to test ChPT and low-energy lattice calculations.

In addition, we discuss two more applications where a precise and model-independent description of $\pi K \to \pi K$ or $\pi\pi \to K\bar{K}$ data is of relevance. Regarding the former case, we aim at providing a value of the so-called πK σ-term—a quantity of relevance to understand the inner structure of the kaon. The calculation of one of its contributions requires the value of the πK amplitude at the unphysical Cheng–Dashen point $t = 2m_\pi^2$, $\nu = 0$. For this, we have to use a dispersive sum rule evaluated with our CFD as input, as explained in Section 7.2.

And finally, regarding the need for $\pi\pi \to K\bar{K}$, we review its contribution for the calculation of $(g-2)_\mu$. We comment on how our updated CFD parameterization could be of use since some of our previous parameterizations were used in the past for this purpose. Nevertheless, although it constitutes a nice possible application, the overall effect of $K\bar{K}$ states in intermediate states is always found to be very small, and will not change the status of the present conflict between theoretical calculations and experiment.

1.3. Notation

Throughout this work we will be working in the isospin limit of equal mass for all pions, $m_\pi \equiv m_{\pi^+} = 139.57$ MeV, kaons, $m_K = 496$ MeV, and etas, $m_\eta = 547$ MeV, $m_{\eta'} = 957$ MeV. It is also convenient to define $m_\pm = m_K \pm m_\pi$, $\Sigma_{12} = m_1^2 + m_2^2$ and $\Delta_{12} = m_1^2 - m_2^2$, as well as $t_\pi = 4m_\pi^2$, $t_K = 4m_K^2$. In the rest of this work, and unless stated otherwise, $m_1 = m_K$, $m_2 = m_\pi$, $\Delta = \Delta_{K\pi}$, $\Sigma = \Sigma_{K\pi}$. It is also customary to use the standard Mandelstam variables s, t, u for πK scattering, satisfying $s + t + u = 2\Sigma$. The center-of-mass (CM) momentum of the s-channel πK system will be called $q = q_{\pi K}(s)$, whereas $q_\pi = q_{\pi\pi}(t) = \sqrt{t - t_\pi}/2$, $q_K = q_{KK}(t) = \sqrt{t - t_K}/2$ will be the CM momenta of the respective $\pi\pi$ and $K\bar{K}$ states in the t-channel, i.e. for $\pi\pi \to K\bar{K}$ scattering. Here

$$q_{12}(s) = \frac{1}{2\sqrt{s}}\sqrt{(s - (m_1 + m_2)^2)(s - (m_1 - m_2)^2)} = \frac{1}{2\sqrt{s}}\sqrt{s^2 - 2s\Sigma_{12} + \Delta_{12}^2} \tag{1}$$

Sometimes it will also be convenient to use the so-called phase-space:

$$\sigma_{\pi K}(s) = \frac{2q}{\sqrt{s}}, \quad \sigma_\pi(t) = \frac{2q_\pi}{\sqrt{t}}, \quad \sigma_K(t) = \frac{2q_K}{\sqrt{t}}. \tag{2}$$

Since we will be working in the isospin limit, we will make extensive use of the isospin-defined πK scattering amplitudes, denoted by $F^I(s, t, u)$, where $I = 1/2, 3/2$ is the total isospin of the process. They are related by $s \leftrightarrow u$ crossing as follows:

$$F^{1/2}(s, t, u) = \frac{3}{2}F^{3/2}(u, t, s) - \frac{1}{2}F^{3/2}(s, t, u). \tag{3}$$

For convenience we will frequently use the $s \leftrightarrow u$ symmetric and antisymmetric πK amplitudes, denoted $F^\pm$ respectively. These can be recast as

$$F^+(s, t, u) = \frac{1}{3}F^{1/2}(s, t, u) + \frac{2}{3}F^{3/2}(s, t, u), \tag{4}$$

$$F^-(s, t, u) = \frac{1}{3}F^{1/2}(s, t, u) - \frac{1}{3}F^{3/2}(s, t, u). \tag{5}$$

In addition, using $s \leftrightarrow t$ crossing symmetry, the $\pi\pi \to K\bar{K}$ amplitudes, denoted G^I for isospin $I = 0, 1$, are related to those of πK scattering as follows:

$$G^0(t, s, u) = \sqrt{6}F^+(s, t, u),$$
$$G^1(t, s, u) = 2F^-(s, t, u). \tag{6}$$

In this work we will also use the partial-wave decomposition of both the πK and $\pi\pi \to K\bar{K}$ scattering amplitudes, defined[1] as:

$$F^I(s, t, u) = 16\pi \sum_\ell (2\ell + 1)P_\ell(z_s)f_\ell^I(s), \tag{7}$$

$$G^I(t, s, u) = 16\pi\sqrt{2} \sum_\ell (2\ell + 1)(q_\pi q_K)^\ell P_\ell(z_t)g_\ell^I(t).$$

Let us not forget that, since in the isospin limit pions are identical particles from the point of view of hadronic interactions, irrespective of their charge, then, being bosons, the $\pi\pi$ state must be fully symmetric. Thus, for even (odd) isospin, only even (odd) angular momenta should be considered in the above partial-wave expansion of $G^I(t, s, u)$. Let us remark that it is customary to extract explicitly the $(q_\pi q_K)^\ell$ factors in the partial waves of the t-channel, to ensure good analytic properties for $g_\ell(t)$ (see [107] in the $\pi\pi \to N\bar{N}$ context). The scattering angles in the s and t channels are given by:

$$z_s = \cos\theta_s = 1 + \frac{2st}{\lambda_s}, \qquad z_t = \cos\theta_t = \frac{s - u}{4q_\pi q_K} = \frac{\nu}{4q_\pi q_K} = \frac{\nu}{\sqrt{(t - t_\pi)(t - t_K)}}, \tag{8}$$

where

$$\lambda_s = \lambda(s, m_\pi^2, m_K^2) = (s - m_+^2)(s - m_-^2) = s^2 - 2s\Sigma + \Delta^2 = 4s\,q_{K\pi}^2(s), \tag{9}$$

and $\nu \equiv s - u$ is the antisymmetric variable under $s \leftrightarrow u$ crossing. For convenience, we have also defined the Källén function

$$\lambda(x, y, z) = x^2 + y^2 + z^2 - 2xy - 2xz - 2yz. \tag{10}$$

Let us now recall that in the s-channel partial waves are projected using

$$f_\ell^I(s) = \frac{1}{32\pi} \int_{-1}^1 dz_s P_\ell(z_s) F^I(s, t(z_s)), \tag{11}$$

whereas for the t-channel partial waves are obtained from

$$g_\ell^I(t) = \frac{\sqrt{2}}{32\pi(q_\pi q_K)^\ell} \int_0^1 dz_t P_\ell(z_t) G^I(t, s(z_t)), \tag{12}$$

since now we have two identical particles in the initial state, i.e. the two pions in the isospin conserving formalism. It is worth noticing that very often experimentalists in their partial-wave definitions included an $\sqrt{2\ell + 1}$ factor, which we will have to take into account when comparing with data.

---

[1] Please note that in our Ref. [99] we used the notation $t_\ell^I(s)$ instead of $f_\ell^I(s)$. In addition, we used $F(s, t, u)$ which corresponds to what we would call $F(s, t, u)/4\pi^2$ here. The present notation is the one we used in [42].

For later use we define the scalar πK scattering lengths as follows:

$$a_0^I = \frac{2}{m_+} f_0^I(m_+^2),$$ (13)

and similarly for $a_0^- = (a_0^{1/2} - a_0^{3/2})/3$ and $a_0^+ = (a_0^{1/2} + 2a_0^{3/2})/3$. These parameters come from the low-energy effective range expansion for partial waves

$$\frac{2}{\sqrt{s}} \text{Re} f_\ell^I(s) \simeq q^{2\ell} \left(a_\ell^I + b_\ell^I q^2 + c_\ell^I q^4 + \cdots \right),$$ (14)

whose coefficients are called scattering lengths (a_ℓ^I), effective ranges (b_ℓ^I), shape parameters (c_ℓ^I), etc... and are generically referred to as threshold parameters. All them are similarly defined for the expansion of the $f_\ell^\pm$ combinations.

The relation with the S-matrix partial waves, which allows for a direct comparison with some experiments, is:

$$S_\ell^I(s)_{\pi K \to \pi K} = 1 + i \frac{4q}{\sqrt{s}} f_\ell^I(s) \theta(s - m_+^2),$$ (15)

$$S_\ell^I(t)_{\pi\pi \to K\bar{K}} = i \frac{4(q_\pi q_K)^{\ell+1/2}}{\sqrt{t}} g_\ell^I(t) \theta(t - t_K).$$

When it is clear from the context that the energy under consideration is above the corresponding physical threshold it is also usual to write these equations omitting the step function.

Let us now remind that the S-matrix should be unitary, which means that if, for a given energy, the initial state i can evolve not only into a given final state f but also to many other states n, then $\sum_n S_\ell^I(s)_{in} S_\ell^I(s)_{nf}^\dagger = \delta_{if}$.

In case only one state is available, as for πK at sufficiently low energies, we say the reaction is elastic. The elastic unitarity condition translates into the following algebraic relation for πK partial waves

$$\text{Im} f_\ell^I(s) = \sigma_{\pi K}(s) |f_\ell^I(s)|^2,$$ (16)

which implies that the elastic $\pi K \to \pi K$ partial wave can be recast in terms of a real phase shift, called $\delta_\ell^I(s)$, as follows:

$$f_\ell^I(s) = \frac{\hat{f}_\ell^I(s)}{\sigma_{\pi K}(s)} = \frac{e^{i\delta_\ell^I(s)} \sin \delta_\ell^I(s)}{\sigma_{\pi K}(s)} = \frac{1}{\sigma_{\pi K}(s)} \frac{1}{\cot \delta_\ell^I(s) - i},$$ (17)

where we have introduced the "Argand" partial wave $\hat{f}(s)$ for later convenience. In practice, πK scattering is elastic below approximately 1 GeV for all waves, and so are the maximal isospin waves within the whole region of interest in this review. In such cases, the knowledge of $\delta_\ell^I(s)$ is enough to characterize the full complex amplitude. We detail in Appendix A the explicit functional form used in this work when describing this elastic region.

In contrast, in the inelastic regime, and like any other complex function, the description of a partial wave requires the knowledge of two real functions, i.e., the phase and the modulus. We will often use those quantities, but sometimes it is also convenient to define an elasticity function $0 \leq \eta_\ell^I \leq 1$ to write:

$$f_\ell^I(s) = \frac{\hat{f}_\ell^I(s)}{\sigma_{\pi K}(s)} = \frac{\eta_\ell^I(s) e^{2i\delta_\ell^I(s)} - 1}{2i\sigma_{\pi K}(s)}.$$ (18)

Note that when the elasticity is one, we recover the elastic formalism.

When partial waves are considered as analytic functions of the s variable, they have a complicated cut structure in the complex plane that will be explained in detail in Section 3. However, the so-called "physical" or "unitarity" cut can already be observed in Eq. (16) from the $\sigma_{\pi K}(s)$ factor. It starts at threshold and extends to infinity, and produces two Riemann sheets, each for a different sign of the imaginary part of the momentum. So far we have been dealing with the expressions in the first or "physical" Riemann sheet, so that our $f(s)$ should have been called $f^{(I)}(s)$. The partial wave in the second Riemann sheet. i.e., $f^{(II)}(s)$, is accessible by crossing continuously the unitarity cut.

Let us now recall that, for elastic scattering, the S-matrix in the second Riemann sheet is the inverse of the S-matrix on the first. But then, since the f-matrix partial waves are related to the S-matrix partial waves by $S(s) = 1 - 2i\sigma_{\pi K}(s)f(s)$, where we have suppressed the isospin and angular momentum indices for simplicity, we can write the amplitude in the second Riemann sheet $f^{(II)}(s)$ in terms of the one in the first Riemann sheet $f^{(I)}(s)$, as follows:

$$f^{(II)}(s) = \frac{f^{(I)}(s)}{1 + 2i\sigma_{\pi K}(s)f^{(I)}(s)}.$$ (19)

Note that in the equation above the determination of $\sigma_{\pi K}(s)$ is chosen such that $\sigma_{\pi K}(s^*) = -\sigma_{\pi K}(s)^*$ to ensure the Schwarz reflection symmetry of the amplitude. In other words, on the upper half s plane we can take $\sigma_{\pi K} = +2q_{\pi K}/\sqrt{s}$ as usual, whereas on the lower half s plane we must then take $\sigma_{\pi K}(s) = -\sigma_{\pi K}(s^*)^*$.
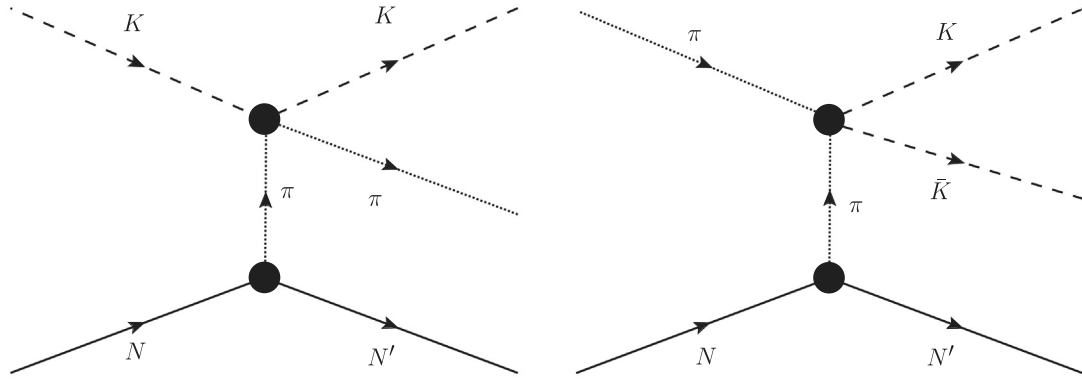
Fig. 5. One-pion exchange diagrams for the processes used to extract meson–meson scattering data. It is then assumed that, when the exchanged pion is nearly on-shell, the meson–meson interaction factorizes out in the whole process description. Left panel: $\pi K \rightarrow \pi K$ case. Right panel $\pi\pi \rightarrow K\bar{K}$ case.

The above equation is useful to look for poles associated with elastic resonances, which are found in the second sheet. In particular, a pole at $\sqrt{s_R} = M_R - i\,\Gamma_R/2$ in the second sheet, corresponds exactly with the position of a *zero* of the S-matrix partial wave in the first Riemann sheet. Restoring the isospin and angular momentum indices back, this reads:

$$S_\ell^I(s) = 1 + 2i\hat{f}_\ell^I(s) = e^{2i\delta_\ell^I} = 0. \tag{20}$$

This zero condition may be recast as

$$\cot\delta_\ell^I(s_R) = -i\,, \tag{21}$$

where, of course, $\cot\delta_\ell^I(s)$ now corresponds to a function in the complex plane that has all the singularities of the amplitude, except for the cut along the real axis above threshold, where it coincides with the physical $\cot\delta_\ell^I(s)$. We will use this method to find elastic resonances from a given parameterization of data in Section 6. The inelastic case is not so simple and specific analytic methods to find resonances will be discussed in Section 6.2.

Finally, once the pole position s_p of a resonance is found, another parameter of relevance is its coupling to the partial wave, defined as

$$g^2 = -16\pi(2\ell+1)\lim_{s\to s_p}\left(s - s_p\right)\frac{f_\ell^{RS}(s)}{(2q_{\pi K}(s))^{2\ell}}\,, \tag{22}$$

where $f_\ell^{RS}(s)$ represents the partial wave in the contiguous Riemann sheet.

2. The data

2.1. $\pi K \rightarrow \pi K$ scattering data

2.1.1. Introduction

Most of the data on πK scattering were obtained during the '70s and the '80s. Due to the practical impossibility of making pion or kaon beams sufficiently luminous to measure these collisions directly, data are measured indirectly in fixed-target $KN \rightarrow K\pi N'$ experiments assuming they are dominated by the exchange of a single pion. This generic mechanism is illustrated in the left panel of Fig. 5. Here N is a nucleon and N' can either be a nucleon or a Δ resonance (although some experiments used deuterium in the initial state and pp in the final one). Experimentally, events whose momentum transfer is as close as possible to the pion pole are selected and then approximated by considering that the exchanged pion is on-shell. This technique was first proposed for $\pi\pi$ scattering [108,109] and later extended to $\pi K \rightarrow \pi K$ in [110–114], see [115] for a textbook introduction. Unfortunately this one-pion-exchange formalism needed to extract πK scattering amplitudes from $KN \rightarrow K\pi N'$ is just an approximation and has several sources of large systematic uncertainties. Namely: corrections to the on-shell extrapolation of the exchanged pion, rescattering effects, absorption, exchange of other resonances, etc... (see [116]). However, most experimental works only quote statistical uncertainties for each solution and it is therefore rather usual that different experiments disagree within their quoted experimental errors, which do not include these sources of systematic uncertainties. This will be clearly seen in the figures below. One of our main tasks in later sections will be to estimate the systematic uncertainty for different sets, or data points within the same set, in conflict within a specific energy region.

Before presenting the data on each partial-wave, let us recall that isospin is conserved to a very good approximation and we will thus work in the isospin limit. Then, there are two possible isospins for a πK state, i.e. $I = 1/2$ and $I = 3/2$.

In particular, cross-section measurements for the $I = 3/2$ isospin channel were obtained in the early '70s using different reactions. These include $K^-d \to K^-\pi^-pp$ in Y. Cho et al. [1], $K^-n \to K^-\pi^-p$ in A.M. Bakker et al. [2] as well as $K^\pm p \to K^\pm\pi^-\Delta^{++}$ in B. Jongejans et al. [4]. In practice, this isospin channel is elastic up to at least 1.8 GeV and then it is straightforward to obtain its phase shift from the cross-section. This was done by D. Linglin et al. in [3] using their $K^-p \to K^-\pi^-\Delta^{++}$ data. Generically, experiments in the earlier '70s have low statistics. An excellent review on the experimental and phenomenological situation until 1978, which also comments on dispersive approaches, can be found in [15]. Fortunately, such a situation was improved by the end of the decade. Indeed, in 1978 P. Estabrooks et al. [5] presented an analysis of $K^\pm p \to K^\pm\pi^+n$ and $K^\pm p \to K^\pm\pi^-\Delta^{++}$ at 13 GeV with relatively high statistics and obtained the $I = 3/2$ πK scattering contribution, without any evidence of inelasticity up to 1.8 GeV.

Concerning isospin $I = 1/2$ scattering, let us first of all note that, when extracted from $KN \to K\pi N'$, it always appears mixed with $I = 3/2$ in the following isospin combination: $f_l = f_l^{1/2} + f_l^{3/2}/2$. This was the case, for example, of the first experiments by R. Mercer et al. in [117] using $K^+p \to K^+\pi^-\Delta^{++}$ and $K^+p \to K^0\pi^0\Delta^{++}$ reactions. In practice, they separated different isospins by combining their results with a heterogeneous and not very precise data collection that existed at the time, which was called the "World Data Summary Tape". Together with their low statistics, this means that their results for both the $I = 1/2$ and $3/2$ waves have huge uncertainties. For this reason these data are usually neglected against later and more precise experiments.

The first study of $\pi K \to \pi K$ scattering with relatively high statistics for the $f_l \equiv f_l^{1/2} + f_l^{3/2}/2$ isospin combination, up to 1.85 GeV, was published in 1978 by Estabrooks et al. [5], using the SLAC 13 GeV spectrometer. However, the experiment with the highest statistics so far was performed about a decade later by Aston et al. [6], using the Large Acceptance Superconducting Solenoid (LASS) Spectrometer at SLAC. This LASS experiment studied the $K^-p \to K^-\pi^+n$ reaction at 11 GeV and obtained the same πK partial-wave combination up to 2.6 GeV. These two experiments are the most widely used in the literature, particularly the latter.

Apart from the large, but frequently omitted, systematic uncertainties, an additional problem affects $\pi K \to \pi K$ scattering data phases. Namely, ambiguities appear in the determination of the phase leading to different solutions even when extracted from the same $KN \to K\pi N$ experiment. In the case of Aston et al. [6], they appear above the region of interest for this review. However, Estabrooks et al. [5] presented four solutions above 1.5 GeV. We will only consider Solution B since it is the one qualitatively closer to the LASS results.

So far we have discussed fixed-target experiments, from which data on both the modulus and the phase of the amplitude can be obtained. However, it is also possible to gather experimental information on the meson–meson scattering phase by measuring processes where two mesons appear in the final state, as long as the other particles interact very weakly with the two mesons and among themselves. Then, Watson's theorem [118] implies that the phase of the whole process is the same as the phase of its two-meson rescattering. This technique has been applied using D or η_c meson decays. Unfortunately, the uncertainties are much bigger than those from fixed-target experiments. Nevertheless, they are useful because they provide direct access to $I = 1/2$. We will review them here too.

Finally, let us recall that the $I = 3/2$ data ends at 1.74 GeV. That is the reason why all our plots in this subsection end at 1.74 or 1.8 GeV at most. Nevertheless, above that energy, we will not use the partial-wave expansion but Regge parameterizations obtained from the factorization of nucleon–nucleon and meson–nucleon cross-sections. Since these are not $\pi K \to \pi K$ data but phenomenological parameterizations, they will be described in Section 4.3.

Let us then discuss the data on each partial wave in detail.

2.1.2. S-wave data
$I = 3/2$ S-wave data

We will first describe the $I = 3/2$ data since it is rather large and needed to extract the $I = 1/2$. As commented above, several experiments measured first this wave in the early '70s: Y. Cho et al. [1], A.M. Bakker et al. [2], D. Linglin et al. [3] and B. Jongejans et al. in [4] . None of them found any evidence of inelasticity up to 1.8 GeV so that the amplitude is fully determined in terms of the phase shift, which is shown in Fig. 6 as a function of the CM energy. The first observation is that these phase shifts are negative, which means that the interaction in this channel is repulsive, and no resonances occur. Second, it can be seen that most of these experiments have relatively large uncertainties and provide data between 800 and 1100 MeV, except for [1], which reaches up to 1.7 GeV. In contrast, the data from Estabrooks et al. [5], obtained in 1977 and also reaching 1.75 GeV, quotes much smaller uncertainties. It will therefore dominate any fit, particularly at high energies. Although there is a crude agreement at low-energies, the conflict between different experimental sets when taking the uncertainties at face value is evident from the plot, particularly between Estabrooks et al. and Bakker et al. at low energies or Cho et al. at higher energies. It is also important to remark that the lowest data points sit around 700 MeV, and therefore somewhat far from threshold at 636 MeV. Hence, the direct extraction of threshold parameters, like scattering lengths, from a fit to data requires an extrapolation that produces large uncertainties. For example, although in [5] a value of $a_0^{3/2} = -0.14 \pm 0.07$ is quoted (in m_π^{-1} units), the compilation of low-energy parameters in 1983 [119] provided five values for this scattering length ranging from -0.14 to -0.05. We already commented that this observable is relevant for chiral perturbation theory and is the subject of a renewed interest from lattice QCD. It will be discussed in Section 7.1, where we will provide more precise and robust determinations from sum rules using our constrained parameterizations.
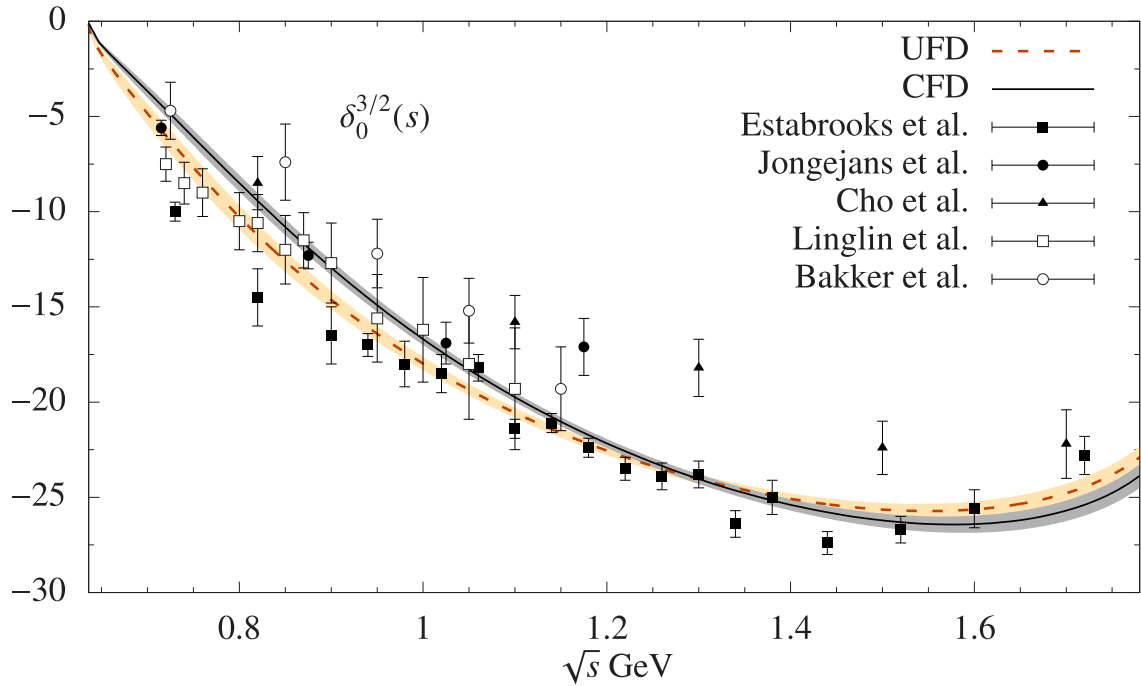
Fig. 6. Phase-shift data on the $S^{3/2}(s)$ $\pi K \to \pi K$ from [5] (solid squares), [4] (solid circles), [1] (solid triangles), [3] (empty squares) and [2] (empty circles). We also show the results of our Unconstrained and Constrained Fits to Data (UFD and CFD respectively).

I = 1/2 S-wave data

This is the wave with the most structure and the most interesting for spectroscopy. Unfortunately, as already discussed, in fixed-target experiments the data on this isospin always appears mixed with $I = 3/2$ in the following combination: $f_S \equiv f_0^{1/2} + f_0^{3/2}/2$. Its modulus and phase are defined as follows:

$$f_S(s) = |f_S(s)| e^{i\Phi_S(s)}, \tag{23}$$

which, in principle, were measured independently and therefore will be fitted separately. For comparison with data, the following normalization is used:

$$\hat{f}_S(s) = f_S(s)\sigma_{\pi K}(s), \tag{24}$$

where the phase space $\sigma_{\pi K}(s)$ was defined in Eq. (2). With this notation, we show in Fig. 7 the high-statistics data from the fixed-target experiments [5,6]. Taking into account that the $I = 3/2$ has a negative phase decreasing smoothly from zero to about -25 degrees, then the structure that is observed in f_S is mostly due to $I = 1/2$. In particular, there is a peak in the modulus and a simultaneous rapid increase of the phase around 1430 MeV. This is a scalar strange resonance, nowadays called $K^*(1430)$, whose existence was supported by both experiments. In addition, there is a considerable increase in the modulus and the phase from threshold to 1.2 GeV, but not clearly resonant, which is the origin of the long-standing controversy about the existence of the $\kappa/K_0^*(700)$ meson, which still "Needs confirmation" according to the present edition of the Review of Particle Physics [95]. We will dedicate Section 6 to review the dispersive determination of this resonance.

Let us note the discrepancies between both sets of data in the whole energy region. Since the quoted errors are purely statistical, it is evident that there are systematic effects that we will have to estimate and consider when fitting the data. In addition, it is important to remark that there are only two points below 800 MeV, coming from [5], and thus the extraction of the $I = 1/2$ scattering length from fits to data requires a large extrapolation, which yields large uncertainties. For illustration, the compilation of low-energy parameters from data in 1983 [119] provided five values for this scattering length ranging from 0.13 ± 0.09 to 0.33 ± 0.01 (in m_π units). The latter is from [5]. The LASS data [6] starts even higher, at 825 MeV. Once again, we recall that this scattering length is relevant for chiral perturbation theory and has been the subject of a renewed interest from lattice QCD. We will provide robust results from sum rules using our constrained parameterizations in Section 7.1.

Up to here, we have discussed scattering data from fixed-target experiments on nucleons. However, it is also possible to extract $I = 1/2$ data from heavy meson decays. In particular, when πK are the only strongly interacting products in the decay, Watson's theorem implies [118] that, in the πK elastic region, the phase of the whole process should be the same as the $\pi K \to \pi K$ scattering phase shift.
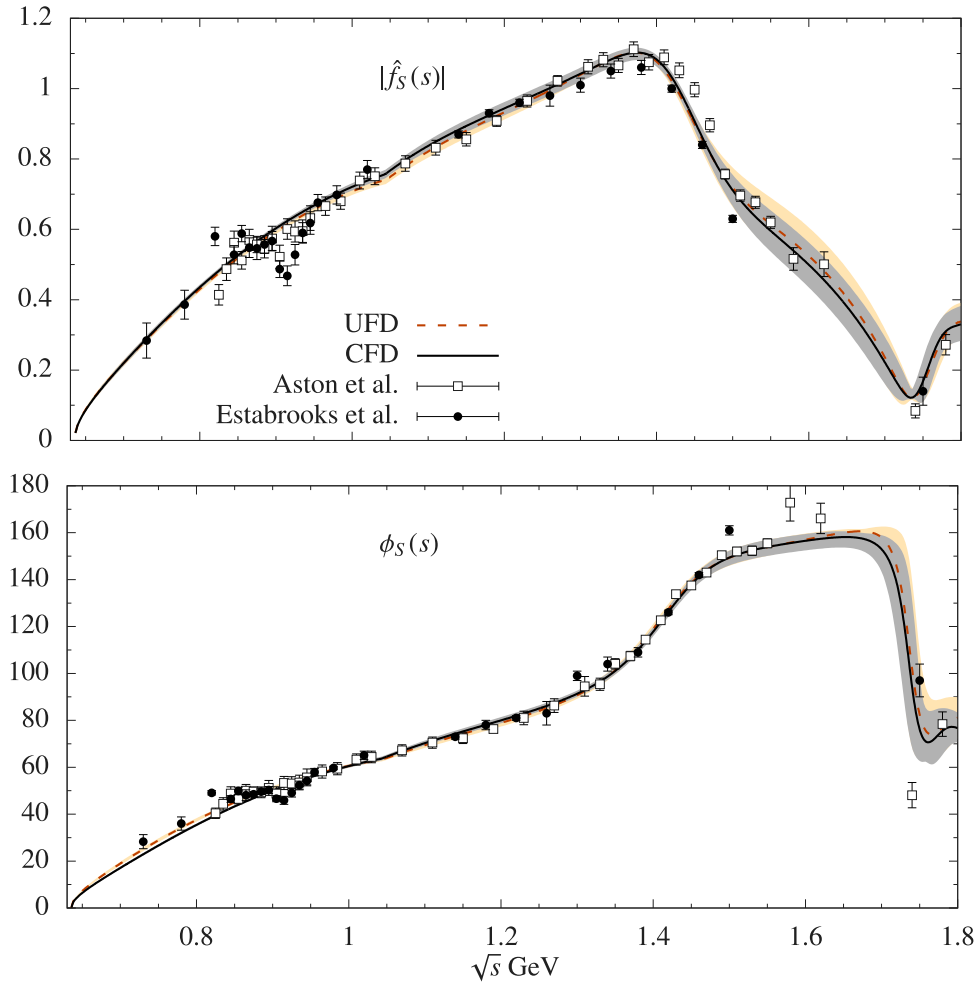
Fig. 7. Data on the *S*-wave, measured by Estabrooks et al. [5] and Aston et al. [6]. The upper panel shows the modulus and the lower panel the phase. We also show the results of our Unconstrained and Constrained Fits to Data (UFD and CFD respectively).

The ideal situation is when the other particles in the decay are weakly interacting, as in so-called semileptonic decays. For example, the $I = 1/2$ phase-shift difference between S and P waves has been measured from $D^+ \to K^-\pi^+ e^+ \nu_e$ decays by the BaBar and BESIII Collaborations [120,121]. In the left panel of Fig. 8 we illustrate how $\pi K \to \pi K$ rescattering (represented as a black disk) appears in this process. Note that the lepton and neutrino come from a weakly interacting W boson, represented by a gray disk. Thus, in the left panel of Fig. 9 we show the *S*-wave phase, extracted from the measured $S - P$ phase difference with a simple model for the *P*-wave, whose uncertainties are much smaller than those of the *S*-wave and therefore can be neglected. In that plot, it can be seen that both the BaBar and BESIII results are quite consistent with those of the LASS experiment (separated from the $I = 3/2$ component using their parameterization). However, they will not be included in our fits because their uncertainties are much larger than those from fixed-target experiments and they should only be the same in the elastic region. Nevertheless, they provide a nice check of consistency.

Furthermore, the $I = 1/2$ phase of the πK *S*-wave amplitude has also been obtained from Dalitz plot analyses of $D^+ \to K^-\pi^+\pi^+$ by the E791 [53], FOCUS [54,122] and CLEO-c [123] collaborations, as well as a recent similar analysis of $\eta_c \to K\bar{K}\pi$ by the BaBar Collaboration [124]. The illustration of how $\pi K \to \pi K$ rescattering appears in these processes is shown in the center and right panels of Fig. 8, respectively. In principle, these phases (and amplitudes) are not necessarily those of πK scattering due to the presence of a third meson that could also interact strongly. However, a comparison with the scattering data has shown that, within the large uncertainties and at least in the elastic region, the resulting phase (but not the amplitude) still bears some similarity to that of LASS. It seems that, to a good approximation, the third meson acts as a spectator and its effect on the phase can be recast as a global constant shift. Thus, we show in the right panel of Fig. 9 that, up to 1.5 GeV and mostly due to their large uncertainties, the phases obtained from E791 and BaBar [53,124] are fairly compatible with those of LASS (extracting once again their $I = 1/2$ with their own $I = 3/2$ parameterization). Note, however, that the data from BaBar are displaced by 34° while those from E791 are displaced

14
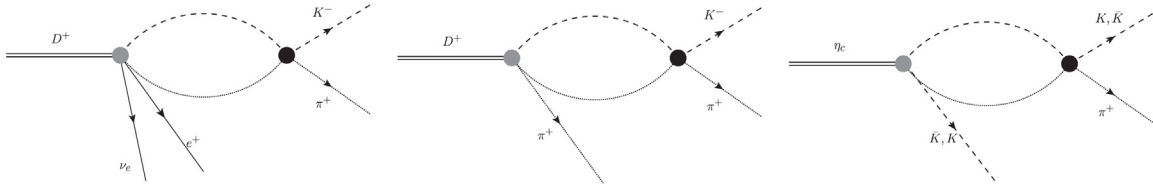
Fig. 8. Other mechanisms that are sensitive to πK scattering through its appearance as part of the final state. Assuming the other particles in the final state are spectators, Watson's theorem implies that the phase of the whole process is that of πK scattering. Left: The cleanest case is when the other particles do not interact strongly as the lepton and neutrino produced in $D^+ \to K^- \pi^+ e^+ \nu_e$ decays observed by the BaBar and BESIII Collaborations [120,121]. Center: $D^+ \to K^- \pi^+ \pi^+$ measured by the E791 [53], FOCUS [54,122] and CLEO-c [123] collaborations. Right: $\eta_c \to K\bar{K}\pi$ measured by the BaBar Collaboration [124]. In the last two processes, the πK scattering phase is obtained assuming the effect of the spectator particle plays a minor role in the energy dependence of the phase-shift, which is then observed displaced by a constant phase.
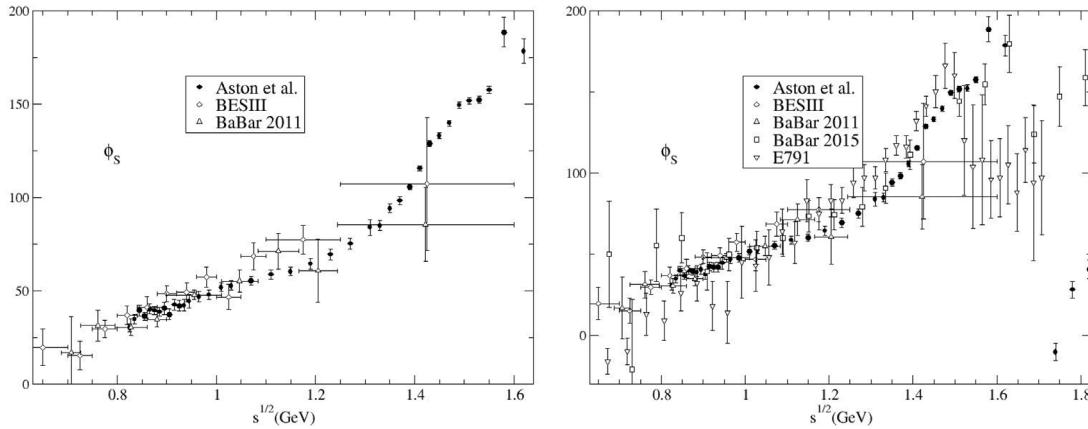
Fig. 9. $I = 1/2$ S-wave phases obtained from the decay of heavy mesons versus the LASS data (using their own $I = 3/2$ model to separate the $I = 3/2$ component). Left: From the semileptonic $D^+ \to K^- \pi^+ e^+ \nu_e$ decay measured by BaBar and BESIII Collaborations [120,121], which used a simple P-wave model to separate the P wave component. Right: From Dalitz plot analyses of $D^+ \to K^- \pi^+ \pi^+$ by the E791 Collaboration [53] and of $\eta_c \to K\bar{K}\pi$ by the BaBar Collaboration [124]. Statistical plus systematic uncertainties are plotted for [53]. As explained in the main text, the data from BaBar are displaced by 34° while those from E791 are displaced by 86°, to ease the comparison with πK data.

by 86°. We do not show FOCUS and CLEO-c data, because they only provide some curves coming from their model for the phase, which, once displaced by a similar constant phase are relatively similar to that of LASS. The additional phase is originated in the production process, represented by the gray disk in Fig. 8, as well as in the interaction with the additional pion. Within the range of interest, these two energy dependencies are expected to be very mild compared to that of πK scattering itself and therefore crudely approximated by a constant. Nevertheless, apart from their huge uncertainty, which makes them of little use, these data cannot be interpreted as a scattering phase beyond this simplistic approximation. As a matter of fact, the effect of the interaction with the second pion has been investigated [125–130] within several theoretical frameworks implementing rescattering beyond what is typically called the isobar model and, to a varying degree, they explain why the $I = 1/2$ S-wave phase shift extracted from D-decays should not be expected to agree with the scattering data. Therefore, D-meson decay data are not included in our fits, although they still provide a qualitative check of consistency, at least in the elastic region.

2.1.3. P-wave data
$I = 3/2$ P-wave data

Only Estabrooks et al. [5] provide data for the $I = 3/2$ P-wave phase-shift up to 1.74 GeV, which we show in Fig. 10. No inelasticity is observed. As it happened in the scalar case, this isospin wave is negative and therefore also repulsive. However, the phase is an order of magnitude smaller. Actually, below 1.1 GeV the modulus of the phase shift is less than 1°, below 1.4 GeV is less than 2°, and below 1.74 GeV it is less than 3°. For this reason, is very frequently neglected in many analyses. However, it should be considered for precision studies, and in particular to separate its contribution from that of $I = 1/2$ in fixed-target experiments. Finally, it should be noted that data starts at 1 GeV and has huge oscillations. Therefore there is no information on its behavior near threshold, although NLO and NNLO ChPT [85,131] and sum rules [43] predict that the scattering length should be positive. This suggests that the phase might be positive close to threshold and below 1 GeV, which will be confirmed by our dispersive analysis.

$I = 1/2$ P-wave data
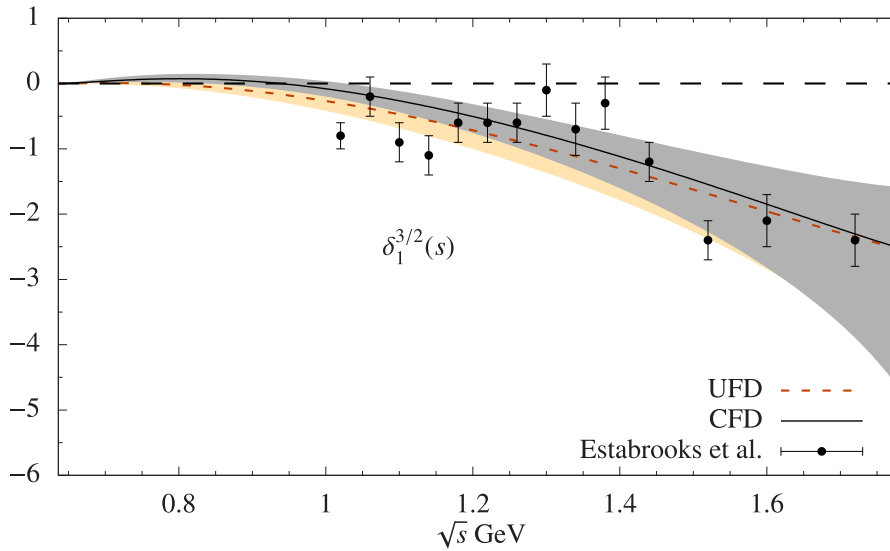
Fig. 10. Data on the $I = 3/2$ P-wave from Estabrooks et al. [5]. We also show our CFD result as a solid line with a gray uncertainty band, which is obtained by fitting these data together with the data on the $f_P = f_1^{1/2} + f_1^{3/2}/2$ combination. For comparison, we show with a dashed line the unconstrained fit to the data in this figure, whose uncertainty is delimited by the orange band.

Once again this wave is measured mixed with the $I = 3/2$ component in the combination $f_P \equiv f_1^{1/2} + f_1^{3/2}/2$, whose modulus and phase we define as follows:

$$f_P(s) = |f_P(s)| e^{i\Phi_P(s)}, \tag{25}$$

although for comparison with data, the following normalization is used:

$$\hat{f}_P(s) = f_P(s) \sigma_{\pi K}(s), \tag{26}$$

where the phase space $\sigma_{\pi K}(s)$ was defined in Eq. (2). With this notation, we show in Fig. 11 the data measured by Estabrooks et al. [5] and the LASS Collaboration [6]. There is a previous production experiment that was able to extract the P-wave [117]. However, its statistics are low compared to LASS experiments, yielding remarkably larger uncertainties, for which we consider it superseded by later experiments.

Then, taking into account that the $I = 3/2$ contribution is tiny, one can see the general features of this $I = 1/2$ P-wave. The low-energy part below 1.2 GeV is completely dominated by the presence of the $K^*(892)$ resonance peak and its very rapid associated increase of 180° in the phase. This is a very well-established resonance, measured in many other processes. For the neutral case, which is the one measured in [5,6], the Review of Particle Physics quotes a mass of 895.55 ± 0.20 MeV and a width of 47.3 ± 0.5 MeV. These features are usually described by means of some sort of Breit–Wigner parameterization, which may be justified when high precision is not required. Above 1.2 GeV, there are two other strange resonances: First, the $K^*(1410)$ whose mass and width averages in the RPP are 1403 ± 7 MeV and 174 ± 13 MeV, respectively. This resonance couples very little to the πK channel and, accordingly, its associated peak is very small in the modulus. In contrast, the $K^*(1680)$, whose mass and width averages at the RPP are 1718 ± 18 MeV and 322 ± 110 MeV, has a $\simeq 40\%$ branching fraction to πK and its peak is more visible. The LASS experiment, using different decays channels, plays a very relevant role in the determination of the parameters of these resonances. Note that, being so close and wide, they largely overlap and interfere, giving rise to the complicated behavior observed in the phase. Obviously, since these resonances decay predominantly to other channels, the $\pi K \to \pi K$ inelasticity becomes large in some parts of this region. Concerning the threshold parameters, note once more that there are only two points below 800 MeV so that simple extrapolations of data down to threshold are rather unstable. Moreover, these two points are at odds with the rest of the data and the dispersion relations, so we do not include them in our fits. We will provide sum-rule determinations of these threshold parameters in Section 7.1.

Besides scattering experiments on nuclei, other ways of extracting information on πK scattering in the P-wave are possible as shown in Fig. 12. In particular, according to [134], data measured on $D^+ \to K^+\pi^-\mu^+\nu$ by the FOCUS collaboration [133] could provide stringent constraints on the P-wave phase shifts. In addition, there are two measurements of $\tau \to K\pi\nu_\tau$ decays [132,135]. These observations, together with information on other decays, have been recently used to improve our knowledge of the πK form factors [136–140]. Furthermore, the first extraction of the $f_+(0)|V_{us}|$ term coming from these combined analyses was performed in [141]. Due to the fact that the πK vector partial wave is the dominant contribution in all these processes, the $K^*(892)$ plays a very relevant role in all these
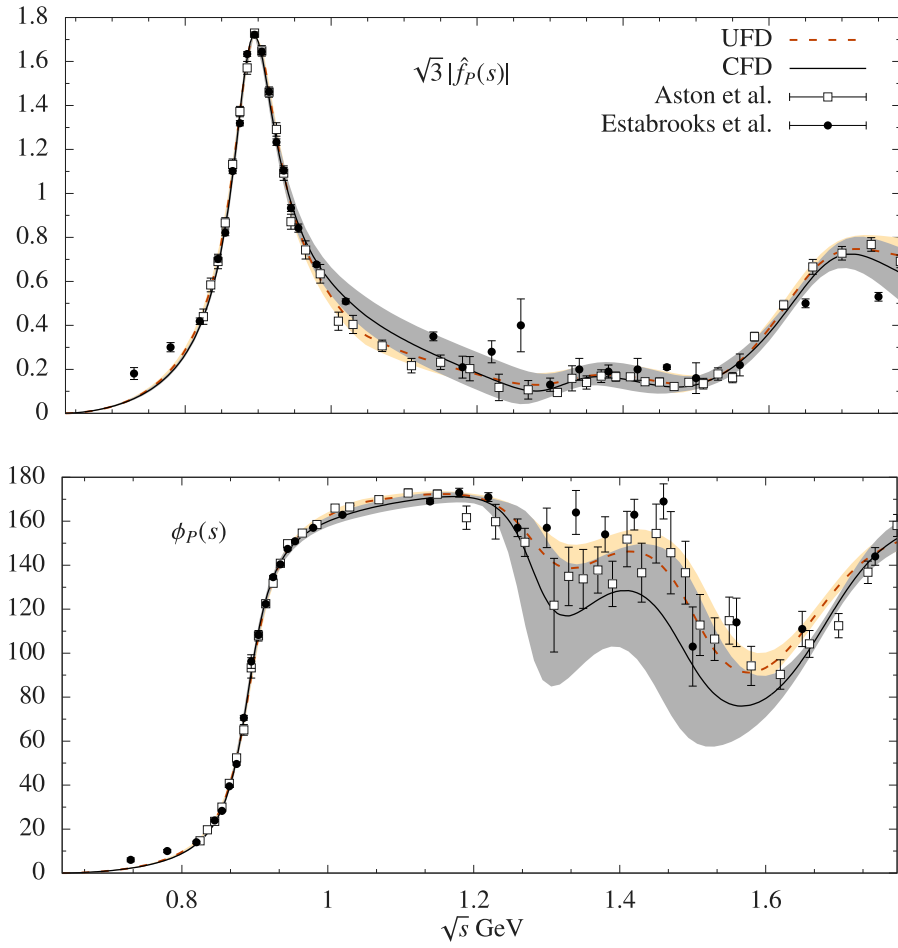
Fig. 11. Experimental results on P-wave $\pi K \to \pi K$ scattering from Estabrooks et al. [5] and Aston et al. [6]. Top: Data on $|\hat{f}_P(s)|$. Bottom: Data on $\phi_P(s)$. The continuous line is our constrained fit (CFD), whose uncertainties are covered by the gray band, whereas the dashed line is the Unconstrained Fit to Data (UFD), whose corresponding uncertainties are delimited by the orange band.
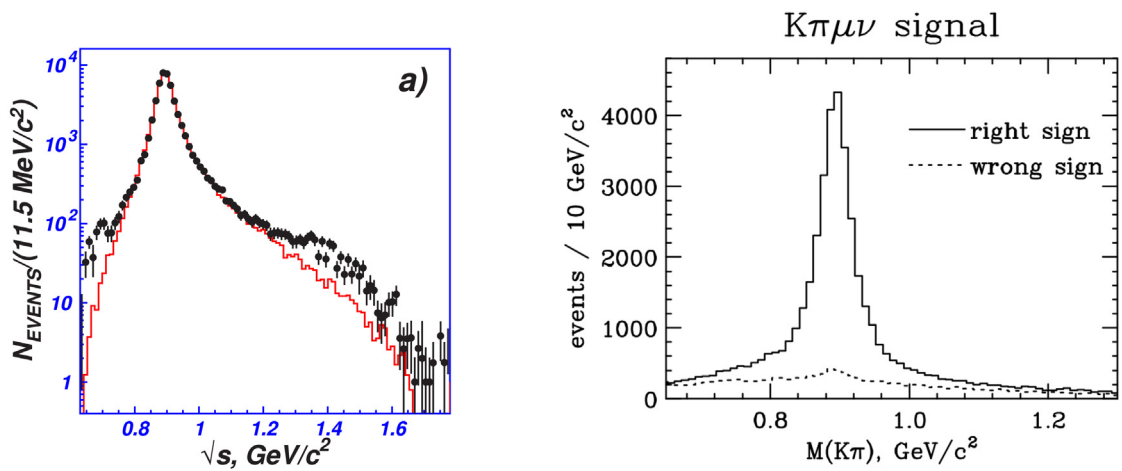
Fig. 12. $\tau \to K\pi\nu_\tau$ data measured by the BELLE collaboration (left panel) [132] and $D^+ \to K^+\pi^-\mu^+\nu$ data measured by the FOCUS collaboration (right panel) [133].
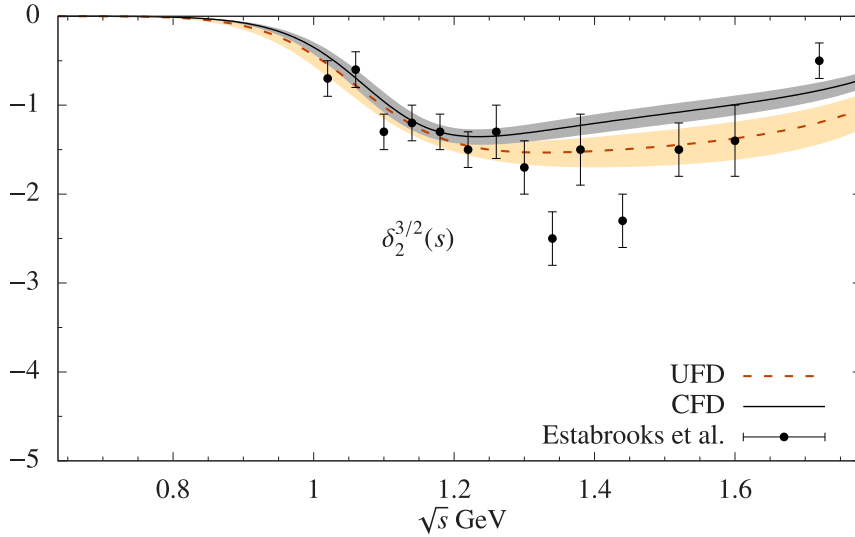
Fig. 13. Data on the $I = 3/2$ D-wave from Estabrooks et al. [5]. We also show our UFD and CFD parameterizations (dotted and continuous lines, respectively).

works. Therefore, in Appendix B we describe a new alternative elastic P-wave obtained by using the fits of the FOCUS collaboration [133], and we also perform there its dispersive study. Fortunately, although starting from different data, the dispersively constrained final result of the alternative description and the one we will discuss in the main text, using scattering data only, turn out to be very similar and compatible, which is why we have relegated the alternative one to the appendix.

2.1.4. D-waves data
    I = 3/2 D-wave data

As with the $I = 3/2$ P-wave, only Estabrooks et al. [5] provide data for the $I = 3/2$ D-wave phase shift up to 1.74 GeV. Since no inelasticity has been measured, the phase shift determines completely the amplitude. The data for the phase shift are shown in Fig. 13 and are very small in the whole energy region, not even reaching 3°. Note there are no data below 1 GeV so that there is no information on threshold, however, in this case, both NNLO ChPT [85] and sum rules [43] yield a negative scattering length, and then it is natural to assume that the phase shift is also negative from threshold up to the first data point. We will confirm this with our dispersive analysis.

    I = 1/2 D-wave data

As it happened with the S and P-waves, the $I = 1/2$ D-wave is only measured together with the $I = 3/2$-wave in the $f_D \equiv f_2^{1/2} + f_2^{3/2}/2$ combination, for which, once again, we define the modulus and the phase

$$f_D(s) = |f_D(s)| \, e^{i\Phi_D(s)}, \tag{27}$$

as well as the usual normalization to compare with data:

$$\hat{f}_D(s) = f_D(s) \, \sigma_{\pi K}(s). \tag{28}$$

With this notation we show in Fig. 14 the experimental results of [5,6]. Since the $I = 3/2$ component is so small and featureless, all the features seen in that figure correspond to the $I = 1/2$ channel. In particular, below 1.8 GeV there is just a clear peak and phase motion corresponding to the well-established $K_2^*(1430)$ strange resonance. This resonance is seen in many other processes, but note that the averaged mass of the neutral case is dominated in the RPP by the results of [5] and LASS. Its decay branching ratio to πK is approximately 50% and an inelastic formalism will be needed. Let us remark that the data starts above 1.1 GeV so that there is no real experimental information on threshold and extrapolations are unstable. Actually, although NNLO ChPT [85] and sum rules [43] predict a positive scattering length, they are not very consistent with each other. We will review this situation and provide sum rule determinations from our constrained dispersive fits in Section 7.1.

2.1.5. I = 1/2 F-wave data
    As usual with other waves we define

$$f_F(s) \equiv |f_F(s)| \, e^{i\phi_F(s)}, \quad \hat{f}_F(s) = f_F(s) \, \sigma_{\pi K}(s). \tag{29}$$
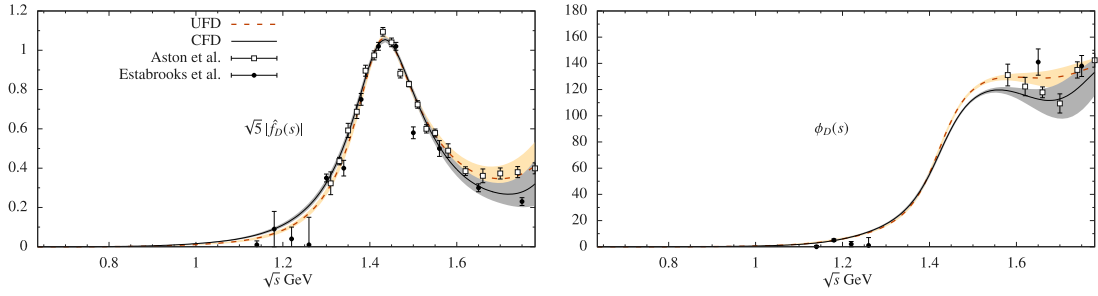
Fig. 14. Data on the D-wave isospin combination f_D measured by Estabrooks et al. [5] and Aston et al. [6]. Left: Modulus of $|\hat{f}_D|$. Right: Phase Φ_D. We also show our UFD and CFD parameterizations (dotted and continuous lines, respectively).
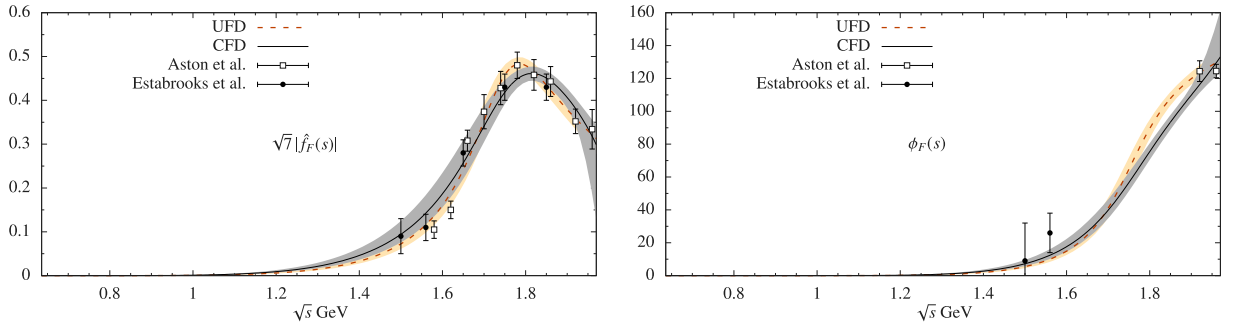
Fig. 15. Scattering data on the $\pi K \to \pi K$ F-wave measured by Estabrooks et al. [5] and Aston et al. [6]. Left: Modulus of $|\hat{f}_F|$. Right: Phase Φ_F. We also show our UFD and CFD parameterizations as dashed and continuous lines, respectively, with their corresponding uncertainty bands (gray and orange respectively).

However, for this wave, there are no observations of $I = 3/2$ scattering, which is therefore neglected in the literature. We can thus consider that the whole f_F is just $I = 1/2$. We show in Fig. 15 the data obtained in [5,6]. Note that the threshold suppression is so large that there are no data below 1.5 GeV. We will provide sum-rule results for the scattering length.

The most salient feature of this wave is the peak of the $K_3^*(1780)$ resonance, whose branching ratio to πK is slightly less than 20%. We will thus need an inelastic formalism. In the RPP, the parameters of this wave are completely dominated by the LASS Collaboration results [6].

2.2. $\pi\pi \to K\bar{K}$ scattering data

Let us recall that, in the isospin limit, all pions are identical particles, and, being bosons, the $\pi\pi$ state must be fully symmetric. Thus, the two possible isospin states that couple to $K\bar{K}$, which are $I = 0$ and $I = 1$, are expanded in terms of only-even or only-odd partial waves, respectively. For all of them, we define a modulus and a phase $g_\ell^I = |g_\ell^I|e^{i\phi_\ell^I}$.

The experimental results on $\pi\pi \to K\bar{K}$ partial waves that will be reviewed next were obtained in the early eighties [7,8], indirectly from fixed-target experiments on $\pi N \to K\bar{K}N'$. In order to extract the meson–meson amplitude, it is then assumed that the one-pion-exchange mechanism illustrated in the right panel of Fig. 5 dominates the whole process and that the meson–meson sub-process is factorizable. This is a fairly good approximation if the events are selected with the exchanged pion momenta close to the pion mass shell, but as commented in the $\pi K \to \pi K$ case, and as illustrated below, the final result is plagued with systematic uncertainties. It is therefore usual to find that different experiments do not agree within their statistical uncertainties, and a systematic uncertainty will have to be considered. For our purposes, the data can be grouped in four different types. First, we will use data on phases and modulus for the g_0^0, g_1^1 partial waves extracted from $\pi^- p \to K^- K^+ n$ and $\pi^+ n \to K^- K^+ p$ at the Argonne National Laboratory [7] and from $\pi^- p \to K_S^0 K_S^0 n$ at the Brookhaven National Laboratory in a series of three works [8,9,142]. The latter will be called Brookhaven-I, Brookhaven-II, and Brookhaven-III, respectively. Second, although data for the modulus of the tensor g_2^0 wave was obtained in Brookhaven-II and Brookhaven-III, we will see that the old experimental parameterizations are not quite compatible with the resonance parameters presently compiled in the RPP. Third, for higher partial waves, which play a very minor role in the dispersive analysis of the lower waves and have no scattering data, we use simple resonance parameterizations adjusting their parameters to those in the RPP.

Finally, let us remark that in the high-energy region above 2 GeV there are no data on all the partial waves we need for our dispersive integrals. It is for this reason that our plots in this subsection will end at that energy. Nevertheless, we
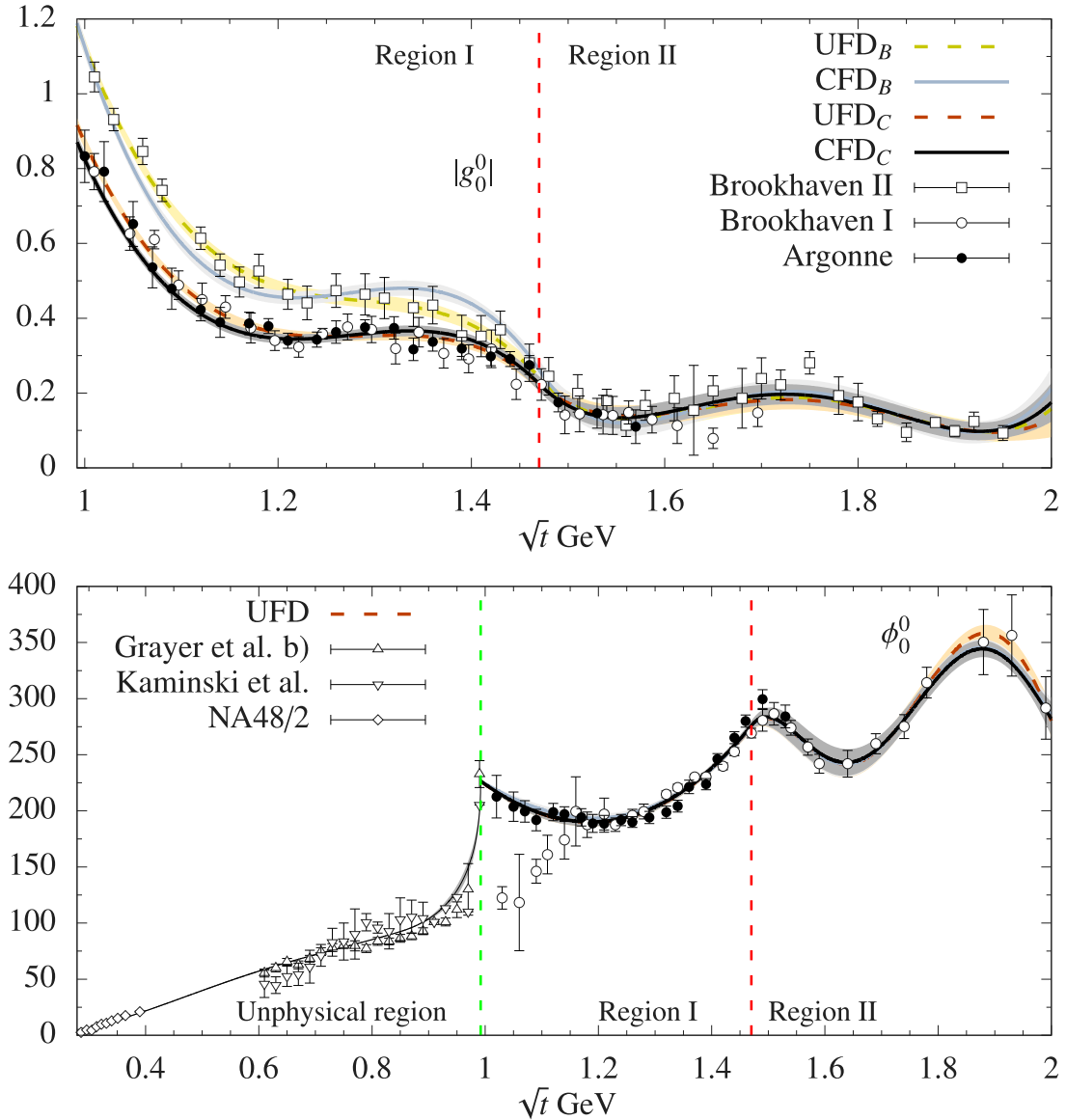
Fig. 16. $\pi\pi \to K\bar{K}$ scattering data on the scalar–isoscalar partial wave g_0^0, coming from [7] (Argonne), [8] (Brookhaven-I) and [9] (Brookhaven-II). As explained in the main text, in the "unphysical region" below $K\bar{K}$ threshold, due to Watson's theorem and the fact that no multi-pion states are observed, the $\pi\pi \to K\bar{K}$ phase shift is precisely that of $\pi\pi \to \pi\pi$ scattering. Thus in that region, we provide a representative sample of such $\pi\pi$ scattering data [145] (Grayer et al. solution b), [146,147] (Kaminski et al.), or the very precise $K_{\ell4}$ decays from [148] (NA48/2). We have also separated Region I, where we will be able to apply dispersion relations as tests or constraints, from Region II, where these relations are not applicable.

will follow closely our approach in [42] and rely on recent updates [41,48,97] of Regge parameterizations [143] obtained from factorization from nucleon–nucleon and meson–nucleon processes and the phenomenological observations of Regge trajectories or the Veneziano model [144]. All this will be discussed in Section 4.3.

Let us then describe the $\pi\pi \to K\bar{K}$ data for each partial wave in detail.

2.2.1. $I = 0$ S-wave

This $g_0^0(t)$ wave is quite complicated but also a very interesting one for hadron spectroscopy, since it couples to the much-debated scalar–isoscalar resonances. Data for both the modulus $|g_0^0|$ and the phase ϕ_0^0 exist in the physical region and are shown in Fig. 16. Although data for both observables extend up to 2.4 GeV, we only show them up to 2 GeV, since above that energy we will use Regge parameterizations.

Note that in the lower panel of Fig. 16 we also show data on the phase below $K\bar{K}$ threshold, coming from $\pi\pi$ elastic scattering in the scalar–isoscalar channel. Watson's theorem [118] tells us that in the $\pi\pi$ scattering elastic regime this is also the $\pi\pi \to K\bar{K}$ phase. Since multi-pion states have not been observed in $\pi\pi$ scattering below the $K\bar{K}$ threshold, this phase shift is in practice the same as that of $\pi\pi \to K\bar{K}$ below threshold.

There are several incompatible data sets in different parts of the inelastic regime and some of them will be discarded based on physical shortcomings, like Watson's theorem. However, for the modulus two distinct sets can be seen: on the one hand the Argonne and Brookhaven I data, which are roughly compatible, and, on the other hand, the Brookhaven II set. In [41] we studied them both and we were able to find constrained fits describing either one of them while satisfying simultaneously the dispersive representation, although the combined solution of Argonne and Brookhaven I seemed slightly favored. Of course, that was done with a fixed $\pi K \to \pi K$ input, and here we will complete that analysis constraining simultaneously $\pi K \to \pi K$ and $\pi\pi \to K\bar{K}$. Thus we will analyze dispersively again the two different g_0^0 incompatible sets, referring by default to the combined solution in the main text, and explaining the alternative one in Appendix C. To this end it is more convenient to separate the whole inelastic fit range into two regions, as follows:

(I) Region I, extending from $\sqrt{t_{min,I}} = 2m_K$ up to $\sqrt{t_{max,I}} = 1.47$ GeV. As shown in Appendix D, this region lies within the applicability domain of Roy–Steiner equations and will be constrained to satisfy dispersion relations in Section 5.3 below.

It is clearly seen in the lower panel of Fig. 16 that from $2m_K$ up to 1.2 GeV, the phase ϕ_0^0 from the Argonne [7] and Brookhaven-I [8] collaborations are incompatible. However, by Watson's theorem, ϕ_0^0 at $K\bar{K}$ threshold should be the same as that of the scalar–isoscalar $\pi\pi \to \pi\pi$ phase shift $\delta_0^{(0)}$. Here one should notice that, as seen in the figure in the unphysical region, both the $\pi\pi \to \pi\pi$ data and their dispersive analyses with Roy and GKPY equations [48,149], which extend up to or beyond $K\bar{K}$ threshold, find $\delta_0^{(0)} > 200°$. The huge rise of the phase right below $K\bar{K}$ threshold is due to the presence of the well-known $f_0(980)$ resonance. Thus, it seems that the phase of Brookhaven-I [8] right above $K\bar{K}$ threshold is inconsistent with Watson's theorem. Moreover, this phase was extracted using a g_2^0 wave that also violates Watson's theorem, as we will see soon below. Hence, for our fits, we will discard the Brookhaven-I phase data [8] below $\sim$1.15 GeV, i.e. until it agrees again with that of Argonne [7]. Concerning the data on $|g_0^0|$, shown in the upper panel of Fig. 16, we can see that, up to roughly 1.4 GeV, the sets of Argonne and Brookhaven-I are consistent among themselves but not with Brookhaven-II. For later purposes, it is relevant to remark that the latter is consistent up to 1.2 GeV with the so-called "dip solution" of the elasticity favored from dispersive $\pi\pi \to \pi\pi$ analyses [48,149], assuming that only $\pi\pi$ and $K\bar{K}$ states are relevant. In contrast, Brookhaven-II would require the presence of some non-negligible coupling to another state, possibly four pions. As we did in [42] we will consider both alternative possibilities in our fits. Finally, in the 1.2 GeV to 1.47 region the "dip" solution from $\pi\pi$ scattering has such large uncertainties that it is roughly consistent with the three data sets.

(II) Region II, extending from $\sqrt{t_{min,II}} = 1.47$ GeV up to $\sqrt{t_{max,II}} = 2$ GeV. We only use this region as input for our dispersive calculations for lower energies, since Roy–Steiner equations are not applicable here (see Appendix D). Above 1.4 GeV all sets seem compatible again although the data from Argonne finishes around 1.5 GeV, whereas the Brookhaven-I set reaches up to $\sim$1.7 GeV and only Brookhaven-II reaches up to 2 GeV. It should be noticed that above 1.5 GeV this wave is rather small and possible resonance shapes are not evident. Nevertheless, several scalar–isoscalar resonances are claimed to exist above $K\bar{K}$ threshold: the $f_0(1370)$, $f_0(1500)$ and $f_0(1710)$. They enjoy different statuses: from still some debate about the existence and parameters of the first, to well established for the $f_0(1500)$. In general, their parameters are not determined very precisely. However, for all three, both their couplings to $\pi\pi$ and $K\bar{K}$ are small and they do not appear as clear peaks in the plot of $|g_0^0|$. Also, they seem to be fairly wide and there should be a significant overlap between them.

2.2.2. $I = 1$ P-wave data

In the physical $\pi\pi \to K\bar{K}$ region, only the Argonne Collaboration (Cohen et al. [7]), has provided $\pi\pi \to K\bar{K}$ scattering data on the g_1^1 partial wave. They reach up to $\sim$1.55 GeV for both the modulus $|g_1^1|$ and its phase ϕ_1^1 and are shown in Fig. 17. It can be noticed that, for the phase, the error bars are very large in the 1 to 1.2 GeV region as well as in the last two data points above 1.45 GeV.

In addition, in Fig. 17 we also show below $K\bar{K}$ threshold, the data on the phase coming from $\pi\pi$ elastic scattering with these quantum numbers. Note that the very rapid increase of the $\rho(770)$ meson is clearly seen. Since multiple pion states have not been observed in $\pi\pi$ scattering below the two-kaon threshold, Watson's theorem tells us that this is also the $\pi\pi \to K\bar{K}$ phase in this pseudo-physical region. We will need this phase later on for our dispersive representation. Let us remark that the uncertainties here are much smaller than in the physical region.

Finally, the fact that there are no scattering data above 1.6 GeV and very poor information above 1.4 GeV, forces us to consider the information on resonances measured in other processes. Apart from the $\rho(770)$ that dominates completely the region below 1 GeV, there are three other resonances below 2 GeV listed in the RPP with $J^{PC} = 1^{--}$ quantum numbers. However, only two of them are relevant for us. Namely, the $\rho' = \rho(1450)$ and $\rho'' = \rho(1700)$, which have sizable couplings to both the $\pi\pi$ and $K\bar{K}$ channels. The values of these parameters will be reviewed and used in Section 4.2 for our fits. In contrast, the couplings of these two channels to the $\rho(1570)$, whose existence is less certain (according to the RPP it " may be an OZI-violating decay mode of the $\rho(1700)$"), have not been seen. We will therefore neglect it in our analysis.
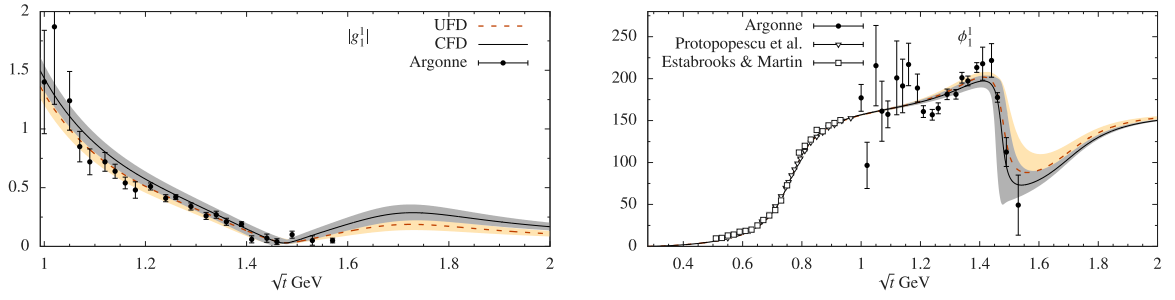
Fig. 17. Modulus (Left) and phase (Right) of the $g_1^1(t)$ $\pi\pi \to K\bar{K}$ partial wave. The continuous line and the gray uncertainty band correspond to the CFD parameterization described in the text, whereas the dashed line and orange band correspond to the UFD. Note that due to Watson's theorem, the phase below $K\bar{K}$ follows that of $I = 1, \ell = 1$ elastic $\pi\pi$ scattering [48]. The white circles and squares come from the $\pi\pi$ scattering experiments of Protopopescu et al. [150] and Estabrooks and Martin [151], respectively. Let us remark that this is the only case for $\ell \geq 1$ when the data on the modulus was provided with the same normalization as ours, i.e. without a $\sqrt{2\ell + 1}$ factor.
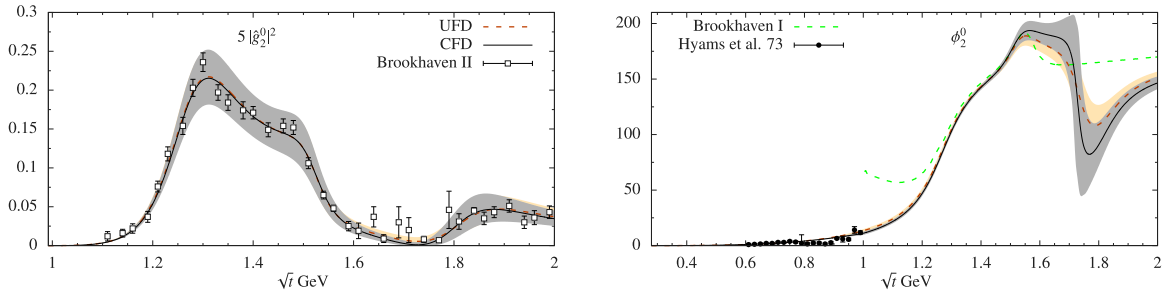
Fig. 18. Left: Data on the modulus of $\hat{g}_2^0(t)$ from the Brookhaven-II analysis [9] together with our UFD and CFD parameterizations, described in the text. Right: Phase of the $g_2^0(t)$ partial wave. Watson's theorem implies that in the "unphysical" region below $K\bar{K}$ scattering this phase should be the same as for elastic $\pi\pi$ scattering with the same quantum numbers because an inelasticity to other states has not been observed. Note that both our UFD and CFD satisfy this theorem since they match the $\pi\pi$ scattering data below 1 GeV [152] and the dispersive analysis in [48], whereas the Brookhaven-I model [8], does not.

2.2.3. $I = 0$ D-wave data

We show in Fig. 18 the data for this wave in the physical region. These data were obtained in the Brookhaven-II analysis [9], which was published 6 years after Brookhaven-I. Brookhaven-II was a study of $\pi\pi \to K\bar{K}$ scattering in the $I = 0, J^{PC} = 2^{++}$ channel employing a coupled-channel formalism, which included data from other reactions. Later on, some members of that collaboration published in [142] a re-analysis, that we call Brookhaven-III, including even further information on other processes. Note that our normalization differs from that used by the experimental collaborations and this is why we are plotting $|\hat{g}_2^0|$, defined as:

$$\hat{g}_2^0(t) \equiv \frac{2(q_\pi q_K)^{5/2}}{\sqrt{t}} g_2^0(t) \equiv |\hat{g}_2^0(t)| e^{i\phi_2^0(t)}. \tag{30}$$

Concerning the phase, below the $K\bar{K}$ threshold we will use Watson's theorem and the elastic data on $\pi\pi$ scattering. However, the relevant observation here is that for this partial wave there are no data on the $\pi\pi \to K\bar{K}$ phase in the physical region. Thus, we need to look at the information on resonances with these quantum numbers observed in other processes. According to the RPP, there are eight possible $J^{PC} = 2^{++}$ resonances below 2 GeV. These are the $f_2(1270)$, $f_2(1430)$ $f_2'(1525)$, $f_2(1565)$, $f_2(1640)$, $f_2(1810)$, $f_2(1910)$ and $f_2(1950)$. The only really well-established and clearly seen in many different processes are the $f_2(1270)$, $f_2'(1525)$ and $f_2(1950)$. Although the first couples predominantly to $\pi\pi$ and the second to $K\bar{K}$, their decays to both states have been measured and therefore they do couple significantly to $\pi\pi \to K\bar{K}$. Actually, the peak of the $f_2(1270)$ is the most prominent feature in Fig. 18 and there is a hint of a second structure around 1.5 GeV. However, the existence of the other five resonances is much into question, and either they "Need confirmation" or they are omitted from the summary RPP tables. Still, in Fig. 18 there is some hint of a raise in the modulus above 1.8 GeV, and the $f_2(1810)$ resonance was considered both by Brookhaven-II and Brookhaven-III [9,142] in their phenomenological fits.

2.2.4. Data on higher $\pi\pi \to K\bar{K}$ partial waves

There are no data on $\pi\pi \to K\bar{K}$ scattering for partial-waves with an angular momentum higher than $\ell > 2$. We thus have to resort to the information on resonances below 2 GeV from the RPP. For $J^{PC} = 3^{--}$ there is one well-established

resonance, the $\rho_3(1690)$ with a ~ 160 MeV width, whose decays to $\pi\pi$ and $K\bar{K}$ are both measured and should therefore couple significantly to $\pi\pi \to K\bar{K}$. A not-so-well-established $\rho_3(1990)$ candidate is too high for our purposes and no decays to $K\bar{K}$ have been reported. Concerning $J^{PC} = 4^{++}$, an $f_4(2050)$ resonance is listed in the RPP, with sizable decays to $\pi\pi$ and $K\bar{K}$. Its width is ~ 240 MeV so that its tail should affect somewhat $\pi\pi \to K\bar{K}$ below 2 GeV, but we have checked that its effect is negligible in our calculations.

3. Dispersion relations for $\pi K \to \pi K$ and $\pi\pi \to K\bar{K}$

Dispersion relations are the mathematical consequence of causality once we consider that pions and kaons have a sufficiently long life that they can propagate to infinity, which is a remarkably good approximation compared to the size of typical hadronic interactions. Causality implies that the amplitude has to be analytic in the first Riemann sheet of the complex plane except for cuts due to the presence of thresholds (see [13,153] for introductory texts) in the direct or crossed channels. Poles associated with bound states can only appear in the real axis below threshold, but this does not occur in $\pi K \to \pi K$ nor $\pi\pi \to K\bar{K}$ scattering and we can thus ignore them. Rigorous proof of this connection between causality and analyticity only exists within non-relativistic scattering [153], but for relativistic scattering there is no general proof beyond axiomatic field theory or perturbation theory [154]. For the general non-perturbative case we resort to the so-called Mandelstam hypothesis [155,156] or "maximal analyticity", which we will assume throughout this review.

Dispersion relations take the form of integral equations in which the amplitude is represented as an integral over its imaginary part. In Section 4, we will review and update tests showing that the data on both $\pi K \to \pi K$ and $\pi\pi \to K\bar{K}$ do not satisfy different dispersive representations. One of the aims of this review, attained in Section 5, is to provide an update of data parameterizations that satisfy the different kinds of dispersion relation that we will present below, by imposing them as constraints on the fits to data.

The derivation of dispersion relations requires the use of Cauchy's theorem for a single complex variable. Since two-body scattering depends on two variables, different kinds of dispersion relations are obtained depending on whether we fix one variable, we relate one variable to the other, or whether we integrate one variable leaving just the explicit dependence on the other one. Respectively, these cases correspond in this review to fixed-t, hyperbolic, and partial-wave dispersion relations that we describe in detail next.

In Fig. 19 we illustrate how a fixed-t dispersion relation is obtained by applying Cauchy's theorem to the integral over the contour C (in blue) that encloses the complex plane except for the cuts (shown in black). The right cut corresponds to the opening of the s channel threshold at $s = m_+^2$, which then extends to $+\infty$, whereas the left cut corresponds to the opening of the $\pi K \to \pi K$ u-channel, starting at $s = m_-^2 - t$ and extending to $-\infty$. Then, the value of the amplitude at any point s inside this contour is given by:

$$F(s, t, u) = \frac{1}{2\pi i} \oint_C \frac{F(s', t, u')}{s' - s} ds'. \tag{31}$$

If the contribution of the amplitude in the curved part vanishes as its radius R is taken to infinity, we are left only with the straight contours, separated by an infinitesimal distance ϵ from the real axis. Since amplitudes satisfy the reflection symmetry $F(s' + i\epsilon, t, u' - i\epsilon) = F^*(s' - i\epsilon, t, u' + i\epsilon)$, in the $\epsilon \to 0$ limit, and given that the straight contours above and below the real axis run in opposite sense, we are left with

$$F(s, t, u) = \frac{1}{\pi} \int_{m_+^2}^{\infty} ds' \frac{\mathrm{Im}F(s', t, u')}{s' - s} + \frac{1}{\pi} \int_{-\infty}^{m_-^2 - t} ds' \frac{\mathrm{Im}F(s', t, u')}{s' - s}. \tag{32}$$

This is a fixed-t dispersion relation valid everywhere in the s-complex plane except on the singularities. If we want the amplitude from the dispersion relation in the real axis over the cut singularities, we must then consider the amplitude at $s + i\epsilon$ with s real, and use the relation:

$$\frac{1}{s' - s - i\epsilon} = PV \frac{1}{s' - s} + i\pi\delta(s' - s), \tag{33}$$

where PV denotes the principal value. Note that the effect of $i\pi\delta(s' - s)$ on Eq. (32) is to extract $i\,\mathrm{Im}\,T(s, t, u)$ out of the first integral, which cancels out the imaginary part on the left side. Hence on the real axis, we find:

$$\mathrm{Re}F(s, t, u) = \frac{1}{\pi}PV \int_{m_+^2}^{\infty} ds' \frac{\mathrm{Im}F(s', t, u')}{s' - s} + \frac{1}{\pi} \int_{-\infty}^{m_-^2 - t} ds' \frac{\mathrm{Im}F(s', t, u')}{s' - s}. \tag{34}$$

Therefore, for real values of s dispersion relations provide the real part of the amplitude from its imaginary part.

When the amplitude $F(s, t, u)$ does not tend to zero fast enough at ∞, the circular contribution of the contour will not vanish. In such cases, we can try applying the theorem to the "subtracted" function $\left(F(s, t, u) - F(s_0, t, u)\right)/(s - s_0)$, to write

$$F(s, t, u) - F(s_0, t, u) = \frac{1}{2\pi i}(s - s_0) \oint ds' \frac{F(s', t, u')}{(s' - s)(s' - s_0)}, \tag{35}$$
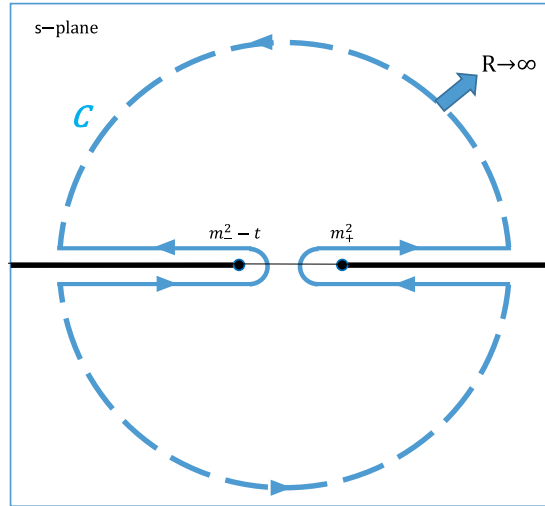
Fig. 19. Analytic structure of the fixed-t $\pi K \to \pi K$ amplitude in the complex s-plane. We show as continuous thick black lines the "right" or "physical" cut, extending from m_+^2 to $+\infty$, as well as the "left" cut, from $m_-^2 - t$ to $-\infty$. In blue we show the typical contour C used to obtain a dispersion relation from Cauchy's theorem, enclosing the complex plane but avoiding the two cuts and sending the radius of its curved part (dashed) to infinity. Its straight sections are infinitesimally close to the cuts on the real axis.

and for the circular part of C to vanish it is enough to demand $F(s, t, u)/s$ to tend to zero at ∞ faster than $1/s$. This yields a so-called "once subtracted" dispersion relation, which now reads:

$$F(s, t, u) = F(s_0, t, u) + \frac{s - s_0}{\pi} \int_{m_+^2}^{\infty} ds' \frac{F(s', t, u')}{(s' - s)(s' - s_0)} + \frac{s - s_0}{\pi} \int_{-\infty}^{m_-^2 - t} ds' \frac{F(s', t, u')}{(s' - s)(s' - s_0)}. \tag{36}$$

The price to pay is that the amplitude at the subtraction point s_0 is now required as input. If that is still not enough to ensure the vanishing of the circular part of C, one can make another subtraction, typically at the same point, finding

$$F(s, t, u) = F(s_0, t, u) + (s - s_0)\left(\frac{\partial}{\partial s} F(s, t, u)\right)_{s = s_0} + \frac{1}{2\pi i}(s - s_0)^2 \oint ds' \frac{F(s', t, u')}{(s' - s)(s' - s_0)^2}.$$

This is now called a "twice subtracted" dispersion relation, which requires the knowledge of two subtraction constants. In principle, one can calculate dispersion relations with an arbitrary number of subtractions. However, due to the Froissart bound [157], i.e. $\sigma_{tot}(s) < c(\log s)^2$, two subtractions are enough to ensure convergence. Nevertheless, more subtractions than strictly needed can be made in order to weigh some regions of the integrand more than others. Actually, in this review, we will use the same dispersion relation with different numbers of subtractions with that purpose.

The previous discussion was made in terms of a fixed-t dispersion relation, but for partial waves one can proceed similarly once the analytic structure is known. Thus we show in Fig. 20 the analytic structure in the complex plane for the $\pi K \to \pi K$ scattering $f_\ell^I(s)$ partial waves (top panel) and the $g_\ell^I(t)$ $\pi\pi \to K\bar{K}$ partial waves (bottom panel). Due to the partial-wave integration and the two different masses involved in the process, the $\pi K \to \pi K$ partial waves have an additional circular cut. It is also important to notice that, in the $\pi\pi \to K\bar{K}$ case, the right cut extends below the physical $K\bar{K}$ threshold down to the two-pion threshold, which is the so-called "pseudo-physical" or "unphysical" region.

The main problem with dispersion relations is to recast all the integrals in terms of the amplitudes in physical regions. For this, crossing symmetry is essential. It is particularly easy to implement for fixed-t amplitude dispersion relations, giving rise to closed and simple expressions. In contrast, it is more cumbersome for partial-wave relations, since for each partial wave in a given channel they might involve the infinite tower of partial waves in the crossed channel. We will derive expressions for all the dispersion relations of interest in the next subsections.

However, let us remark that the previous derivation of a dispersion relation and the derivations in the next subsections are purely formal. For the sake of brevity, we will proceed as if our manipulations on integrals, series, etc... are always well justified. For instance, we will assume that Im $F(s, t, u)$ is a real function, or that the partial-wave expansions converge. However, these conditions are only met in certain regions of the (s, t) Mandelstam plane. The applicability domain of all dispersion relations described next is studied in rigor and detail in Appendix D.

3.1. State of the art

As explained above, a dispersion relation can always be written for a given amplitude in a certain region of the Mandelstam plane. These integral equations enforce not only analyticity, but also crossing, and thus, when constrained
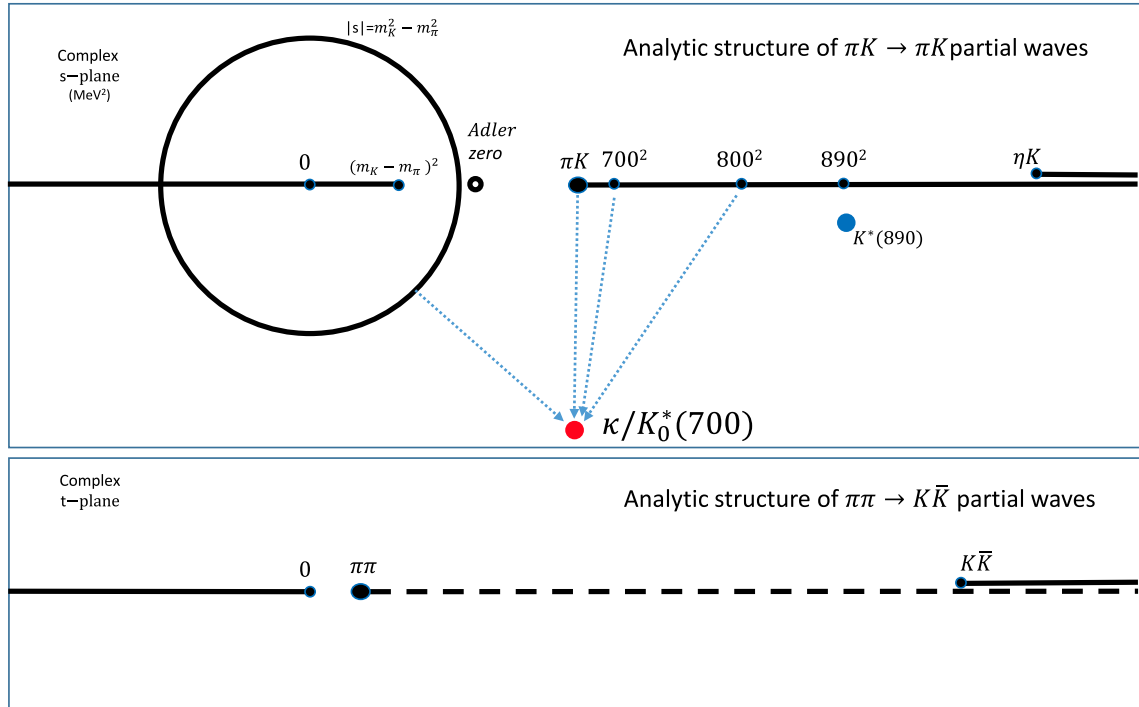
Fig. 20. Analytic structure of partial-wave amplitudes in the complex plane for $\pi K \to \pi K$ scattering ($f_\ell^I(s)$, top) and $\pi\pi \to K\bar{K}$ scattering ($g_\ell^I(t)$, bottom). Note that both present "right cuts" from each threshold to infinity. We only show two-particle thresholds. In the $\pi\pi \to K\bar{K}$ case, the real axis segment from the two-pion threshold to the $K\bar{K}$ threshold is below the physical region, but the imaginary part of the amplitudes is non-zero. This is called the pseudo-physical region. In addition, both types of partial waves have "left cuts" for negative values of their center-of-mass Mandelstam variable. However, $\pi K \to \pi K$ partial waves also have a circular cut, centered at $s = 0$ with radius $m_K^2 - m_\pi^2$, and an additional piece of left cut on the real axis from $s = 0$ to $(m_K - m_\pi)^2$. We also show the position of several dynamical features of $\pi K \to \pi K$ scattering, like the Adler zero required by spontaneous chiral symmetry breaking (we show that of the $f_0^{1/2}$ wave), and the position of the $\kappa/K_0^*(700)$ and $K^*(892)$ poles in the second Riemann sheet of the $f_0^{1/2}$ and $f_1^{1/2}$, respectively. Note that while the latter is much closer to its nominal mass in the real axis, the $\kappa/K_0^*(700)$ is as close to its nominal mass region in the real axis as it is to the $\pi K \to \pi K$ threshold, or the left and circular cuts. Adler zeros [158] appear in scalar partial waves only as a consequence of spontaneous chiral symmetry breaking. To leading order in ChPT, they are located in the real axis slightly above the circular cut, roughly as depicted in the upper panel.

with unitary partial waves, produce as a result a system of scattering amplitudes that fulfill all three first principles. On top of that, it has been proven for two-hadron elastic scattering that dispersive solutions are unique under certain conditions [159]. Considering, as explained in Section 2, that experimental data are usually plagued with systematic uncertainties, dispersion relations offer the possibility to constrain the desired amplitudes and their data description, without including any model dependencies. As a result, such dispersive analyses are considered very robust results within the hadron physics community and, in practice, "model-independent" studies, up to minor simplifying assumptions like isospin conservation, or that hadronic states are truly asymptotic, etc. For studies of isospin violation in πK scattering, we refer the reader to [160–163].

Furthermore, one of the most relevant topics in Hadron Physics is the extraction of resonances. The most interesting resonances nowadays are not those easily identified by nice peaks in cross-sections, but those which are very wide and/or masked by thresholds or other nearby resonances and dynamical features. An example is the much-debated lowest-lying scalar-nonet $\sigma/f_0(500)$, $f_0(980)$, $a_0(980)$ and $\kappa/K_0^*(700)$. We will dedicate the whole Section 6 to the latter. When these complications occur, one has to resort to the rigorous resonance definition in terms of its associated pole in the complex plane, which is a feature that cannot be removed by any other nearby effect. The pole position of these resonances is usually far from the real axis, or surrounded by nearby thresholds, which produce a very unstable analytic extrapolation. Actually, different models providing similar-quality descriptions of data may yield rather different poles. Dispersion relations can also overcome this problem, since they are derived from Cauchy's theorem, thus supplying the correct analytic continuation to the complex plane, which is also very stable. Last but not least, apart from resonance poles, several interesting parameters or quantities can only be determined far from the physical region, like the renowned πN σ term, Adler zeros, etc... which can only be extracted with high precision if a stable analytic extrapolation is performed.

The formulation of dispersion relations using crossing constraints and coupling partial waves from crossed channels appeared in the '70s. These lead to the so-called Roy equations [44] for $\pi\pi$ scattering and Steiner-equations [46,164]

for πN scattering. Other phenomenological works along these lines where developed during that decade on $\pi\pi$ scattering [165–170] together with the developments of sum-rules for the determination of low-energy $\pi\pi$ parameters, also using analyticity and crossing [171]. These techniques were soon applied to $\pi K \to \pi K$ and $\pi\pi \to K\bar{K}$ scattering in [172–177] and, although these works were mostly focused on the determination of low-energy parameters, they laid the ground for the formalism we will use here. For a nice description of dispersive $\pi K \to \pi K$ and $\pi\pi \to K\bar{K}$ analyses at the end of that decade, we refer the reader once again to the excellent review in [15].

With the advent of QCD, the interest in these techniques faded partially, but a renewed interest arose around the '90s, which continues to our days, due, first, to the appearance of ChPT and its need for very precise and rigorous low-energy observables to which it could be compared, and, second, to the efforts to determine the existence and properties of the much-debated lightest scalar resonances. This has given rise to extensive studies of $\pi\pi$ scattering with Roy or similar equations [11,12,48,178–185], so that very high-precision amplitude parameterizations have been built over the years, with various dispersive solutions converging to very similar final results. Furthermore, these techniques also produced a very precise extraction of the $\sigma/f_0(500)$ and $f_0(980)$ resonances [149,186,187], which lead to a major revision of their status in the 2012 Review of Particle Physics, reducing the quoted uncertainty for the former by a factor of 5 and even changing its name to the present one, i.e., $f_0(500)$. On the πN front, similar dispersive analyses [14,188] exist, that will be of relevance for our $\pi K \to \pi K$ system. Moreover, besides determining the amplitudes on the real axis, all these dispersive techniques allow to extract information on different observables like the πN σ-term [189–194], the matching to ChPT [195,196] or several other relevant quantities associated with the nucleon [197,198]. We will also follow this path here for πK when discussing applications in Section 7. Finally, we would like to point out that, given the success of these techniques, they have also been applied recently to other processes like: $e^+e^- \to \pi^+\pi^-$ [199] and $\gamma^{(*)}\gamma^{(*)} \to \pi\pi$ [200–204].

Concerning $\pi K \to \pi K$ and $\pi\pi \to K\bar{K}$ scattering, several previous dispersive studies must be recalled before addressing the details of our calculations. Seminal works using fixed-t [205] or hyperbolic dispersion relations can be found in [172,173,175–177], although they mostly focused on the determination of scattering lengths and very low-energy or even sub-threshold regions. A contemporary study on $\pi\pi \to K\bar{K}$ scattering lengths[2] using an alternative dispersive technique is also found in [174]. Unfortunately the data at that time was not so good and the precision attained by all those works is comparatively poorer than more recent developments. In particular, more modern works used dispersion theory to obtain sum rules for threshold parameters to compare with SU(3) ChPT [206,207]. Finally, the most rigorous and robust dispersive analysis of $\pi K \to \pi K$ scattering was carried out in a series of works by the Paris group [43,97]. In the first work [43] they *solved* the partial-wave projected fixed-t dispersion relations, to obtain a prediction of low-energy S and P partial waves, below ~ 1 GeV, using as input higher partial waves, data above 1 GeV and phenomenological fits to $\pi\pi \to K\bar{K}$ scattering. The results describe well the data on the S-wave and just qualitatively the data on the P-wave, particularly around the $K_0^*(892)$ resonance, see Fig. 2. Later on, they used their solutions inside partial-wave projected hyperbolic dispersion relations to determine with high accuracy the pole position of the light scalar $\kappa/K_0^*(700)$ resonance [97]. We definitely consider this work very robust. However, note that the dispersion relations used for this pole extraction were not the same ones solved in the first work. Moreover, the $\pi\pi \to K\bar{K}$ input was kept fixed from simple fits to data, and not all the possible sources of uncertainty were considered. Despite the existence of this rigorous determination of the $\kappa/K_0^*(700)$ pole, it still "Needs Confirmation" in the Review of Particle Physics.

Thus, even more recently, we have pursued an alternative "data-driven" dispersive program, whose completion we finally present in this report. We have aimed at using several different dispersion relations, including hyperbolic ones, to constrain data parameterizations up to as high as possible energies, simultaneously for $\pi K \to \pi K$ and $\pi\pi \to K\bar{K}$ and to use the resulting amplitudes also to determine the $\kappa/K_0^*(700)$ pole. In particular, we first obtained [41] a precise description of $\pi K \to \pi K$ scattering consistent with forward dispersion relations (FDRs) up to ~ 1.6 GeV. Next, keeping those πK amplitudes fixed, we obtained [42] a precise description of $\pi\pi \to K\bar{K}$ scattering up to 1.47 GeV, consistent with hyperbolic dispersion relations. In all these cases we paid particular attention to uncertainties, both statistical and systematic. Our final result, that we will present below in full detail, is to use all dispersion relations together to constrain simultaneously the data description of both $\pi K \to \pi K$ and $\pi\pi \to K\bar{K}$. In [47], we already advanced the result of this analysis for the $\kappa/K_0^*(700)$ resonance, quite consistent with the result in [97].

We would not like to finish this state-of-the-art section without mentioning that there are several other applications of dispersion relations related to $\pi K \to \pi K$ interactions [203,208–213], in which some simplifying approximations are made, or cutoffs are used, etc..., which lie outside the scope of this manuscript. These include "unitarized" ChPT for $\pi K \to \pi K$ or $\pi\pi \to K\bar{K}$ [10,13,23–26,34,214–218] and in general chiral unitary approaches. In the elastic case they can be justified from a dispersion relation for the inverse of the partial wave (since its imaginary part is known exactly from elastic unitarity), or in the coupled-channel case can be derived from Bethe–Salpeter equations [219] or the so-called N/D method [220] (see also [221] for a recent review). The latter assumes that, similarly to the elastic case, the right cuts, which are common to all coupled partial waves, can be obtained from unitarity in coupled channels together with a dispersion relation for the denominator. Such a dispersion relation is coupled to another one for the numerator that carries the other cuts (left cut, circular, etc...). In both the elastic and inelastic cases, subtractions are needed, whose values can be obtained from Chiral Perturbation Theory (ChPT) up to a specific order. These methods are very successful

---

[2] For this inelastic process, scattering lengths are defined as $\tilde{a}_\ell^I = \lim_{q_K \to 0^+} g_\ell^I(s)$.

phenomenologically, although, due to the approximations they use, not so suited for the kind of precision we are after in this report. For this reason, their success and details lie beyond the scope of this work. For a thorough discussion of the advantages and disadvantages of these unitarization methods versus fully dispersive approaches, we refer the reader to the recent extensive review in [222].

Thus, in the next sections we will summarize the dispersion relations we will implement for our full dispersive analysis here. These are a total of *sixteen* dispersion relations that comprise:

- *Two* forward dispersion relations (FDRs), useful to constrain the $\pi K \to \pi K$ scattering amplitudes up to roughly 1.7 GeV. Contrary to partial-wave dispersion relations (PWDR), FDRs constrain the full partial-wave series instead of individual partial waves. These dispersion relations are the ones reaching the highest in applicability and, in addition, they help to obtain an improved description of the high-energy asymptotic region described in Section 4.3. One obvious advantage is that they do not need $\pi\pi \to K\bar{K}$ input. We already made use of them in [41]. Unfortunately, they alone cannot reach the second Riemann sheet, in search of resonances.

- *Four* Hyperbolic partial-wave projected dispersion relations (HPWDR) for the crossed channel $\pi\pi \to K\bar{K}$. For our purposes, it is enough to study dispersively the lowest three partial waves in this channel, for which data exist. Note we will make use of an extra dispersion relation for g_1^1. The reason is that we found inconsistencies for the continuation to the pseudo-physical region between subtracted and unsubtracted dispersion relations when using unconstrained fits as input. This region of the *P*-wave is relevant for the determination of the $\kappa/K_0^*(700)$ resonance and we want to make sure both solutions are consistent in the end. We already enlarged their applicability region to 1.47 GeV and made use of them in [42], but keeping fixed the πK input.

- *Four* Fixed-*t* partial-wave projected dispersion relations (FTPWDR) for the four $\pi K \to \pi K$ partial waves $f_{0,1}^{\pm}$. These are mostly dominated by their own inputs, and thus offer a simpler dispersive constraint than the HPWDR. Unfortunately, as explained in detail in Appendix D, their applicability region ends slightly above 1 GeV in the real axis and in the complex plane does not reach the $\kappa/K_0^*(700)$ pole. These were solved in the [43] analysis, keeping the $\pi\pi \to K\bar{K}$ input fixed, whose influence is small.

- *Six* Hyperbolic partial-wave projected dispersion relations (HPWDR) for the four $\pi K \to \pi K$ partial waves $f_{0,1}^{\pm}$. Again as in the case of the crossed channel, extra dispersion relations will be used to obtain consistency between the unsubtracted and once-subtracted anti-symmetric dispersion relations. These produce a more intricate realization of the crossing between the two channels and this time the $\pi\pi \to K\bar{K}$ crossed channel provides a quite significant contribution, which therefore really links together the two channels. Although, as the FTPWDR, they reach only up to ~1 GeV in the real axis, we need these HPWDR because the $\kappa/K_0^*(700)$ pole lies inside their applicability region.

As detailed in Section 5 these constraints are enough to obtain a very consistent result not only concerning dispersion relations, but also with the existing $\pi K \to \pi K$ and $\pi\pi \to K\bar{K}$ data within uncertainties.

Let us now describe in detail the derivation and subtleties of each one of these dispersion relations we have just enumerated.

3.2. Fixed-t dispersion relations

In this review, we will show three relevant uses of fixed-*t* dispersion relations for $F^{\pm}(s)$: First, they will be an intermediate step for the derivation of more elaborated dispersion relations for partial waves [43,46,223]. Second, they will provide sum rules for low-energy parameters [171,174,207]. Third, FDRs, which correspond to the fixed $t = 0$ case, will be used as checks and constraints on amplitudes [41]. FDRs have the advantage that they converge for any value of s (see Appendix D). In contrast, partial-wave dispersion relations obtained from fixed-*t* dispersion relations have a limited applicability range, for $\pi K \to \pi K$ scattering amplitudes, up to roughly 1.05 GeV. Finally, one might wonder why we consider fixed-*t* for $\pi K \to \pi K$ amplitudes but not fixed-*u* or fixed-*s* dispersion relations for $\pi\pi \to K\bar{K}$ amplitudes. The reason is that, as shown in Appendix D, their applicability region does not reach the physical region where data exist.

According to Eqs. (6), F^+ and F^- correspond, by crossing, to the exchange of isospin 0 or 1 in the *t*-channel, respectively. This means that, at high energies, F^+ is dominated by the *t*-channel exchanges of the Pomeron and P' trajectories, with no ρ trajectory contribution, whereas the opposite occurs for F^-. If one looks only at either the right or the left-hand-side integral, one would then need two subtractions to ensure the convergence of the Pomeron contribution and one for that of the ρ trajectory. Thus, when used as intermediate steps for the derivation of other dispersion relations, fixed-*t* dispersion relations for F^+ are customarily written with two subtractions and those for F^- at least with one. However, the $s \leftrightarrow u$ behavior of the $F^{\pm}$ amplitudes implies that the leading Regge contributions in the right-hand and left-hand cuts cancel against each other. As a consequence, it is enough to have one or no subtraction to ensure the convergence of the F^+ and F^- fixed-*t* dispersion relations, respectively. These minimally subtracted fixed-*t* dispersion relations have been recently used for $\pi\pi$ scattering FDR in [48–51] and for πK in [41]. Generically, fewer subtractions are convenient to avoid the propagation of the uncertainties in the subtraction constants becoming too large in the resonance region, whereas more subtractions are useful when concentrating on the threshold region.

Thus, using crossing symmetry to write the left-hand cut contribution as an integral over the right one, the unsubtracted fixed-*t* dispersion relation for F^- reads:

$$F^-(s,t) = \frac{1}{\pi} \int_{m_+^2}^{\infty} ds' \text{Im}\, F^-(s',t) \left[\frac{1}{s'-s} - \frac{1}{s'-u} \right]. \tag{37}$$

One of the main advantages of using this non-subtracted relation is that it provides a sum rule for the scattering length a_0^-, which therefore is not input. Another relevant advantage is that it does not depend on the crossed channel $\pi\pi \to K\bar{K}$, thus avoiding an additional source of uncertainty.

In contrast, for the fixed-t dispersion relation of F^+, we need two subtractions. For the moment and later convenience, we choose the subtraction point at $s = 0$. Once again we can use crossing symmetry to rewrite the left cut in terms of an integral over the right one. It can be shown [44,176] that it can always be recast into the following simple form:

$$F^+(s, t) = c^+(t) + \frac{1}{\pi} \int_{m_+^2}^{\infty} ds' \frac{\text{Im } F^+(s', t)}{s'^2} \left[\frac{s^2}{s' - s} + \frac{u^2}{s' - u} \right], \tag{38}$$

where $c^+(t)$ is a subtraction constant once each value of t is fixed. In Section 3.4 below, we will show how this subtraction constant can be determined using a hyperbolic dispersion relation for F^+ and the resulting fixed-t dispersion relation, Eq. (46), will therefore have some dependence on $\pi\pi \to K\bar{K}$.

Fixed-t dispersion relations will be used as intermediate steps for partial wave dispersion relations in later sections where this subtraction constant will be rewritten using a hyperbolic dispersion relation. At that point, we will introduce a mild dependence on the crossed channel.

Furthermore, we will also use the particular case when we fix $t = 0$, i.e., FDRs, that we describe in detail next.

3.3. Forward dispersion relations for $\pi K \to \pi K$

The $t = 0$ case is useful because forward scattering is related by the optical theorem to the total cross-section, for which there is experimental information at high energies for many hadron scattering processes. Moreover, this is the only fixed value of t for which the integrands in the dispersion relation are given directly in terms of the imaginary part of a physical amplitude. FDRs are applicable at any energy, in contrast to Roy-like equations which, in practice, have a limited applicability energy range of $O(1\text{GeV})$ due to the projection in partial waves (see Appendix D). Actually, we recently used FDR to check different sets of πK data and to obtain a set of constrained data parameterizations of πK that satisfy well these FDRs up to 1.6 GeV [41]. In this report, we go one step forward and we will impose them together with Roy–Steiner-like equations, the latter both for πK and $\pi\pi \to K\bar{K}$ channels.

The unsubtracted FDR for F^- can be obtained from Eq. (37) just by setting $t = 0$. The only subtlety is that, since we will use the FDRs as checks or constraints on the amplitudes for physical values of s, we need the s variable to lie on the real positive axis above threshold. Therefore, we have to use the principal value as in Eqs. (33) and (34)

$$\text{Re } F^-(s) = \frac{2(s - \Sigma)}{\pi} PV \int_{m_+^2}^{\infty} ds' \frac{\text{Im } F^-(s')}{(s' - s)(s' + s - 2\Sigma)}. \tag{39}$$

For the F^+ FDR, however, it is convenient to make the subtraction at threshold, instead of $s = 0$, so that the subtraction constant can be recast later in terms of πK scattering lengths. For this reason the FDR is not obtained directly by setting $t = 0$ in Eq. (38), but can be recast as:

$$\text{Re } F^+(s) = F^+(m_+^2) + \frac{(s - m_+^2)}{\pi} PV \int_{m_+^2}^{\infty} ds' \left[\frac{\text{Im } F^+(s')}{(s' - s)(s' - m_+^2)} - \frac{\text{Im } F^+(s')}{(s' + s - 2\Sigma)(s' + m_+^2 - 2\Sigma)} \right]. \tag{40}$$

Their main drawback is that when looking for resonances, their associated poles appear in the second sheet of partial waves with the same quantum numbers of each resonance. FDRs do not deal with partial waves, and even worse, just by themselves, they do not provide access to the second Riemann sheet. These two drawbacks can be overcome by the use of partial-wave dispersion relations, although then the advantages of the FDRs are lost.

3.4. Hyperbolic dispersion relations

In this kind of dispersion relations, abbreviated as HDR, the t variable is not fixed to the same value for all s, but by imposing that u and s should lie in a hyperbola $(s - a)(u - a) = b$. In the literature, it has been usual to set $a = 0$, but we have recently obtained in [42] HDRs for arbitrary a. As shown in Appendix D, the advantage of such generalization is that the a value can then be chosen to modify the HDR applicability domain, as well as the weight of different parts of the integral. In particular, in [42] we chose a to maximize the applicability of HDR for either πK or $\pi\pi \to K\bar{K}$ in their respective physical regions. Since in this report we are also interested in the precise determination of the $\kappa/K_0^*(700)$ resonance, in Appendix D we have determined the a value that maximizes the partial-wave HDR applicability reach in the πK physical region while enclosing the $\kappa/K_0^*(700)$ pole region in the complex plane.

In this section we will briefly review our results in [42]. In addition, we will also provide the expression for the subtraction constant of the fixed-t F^+ dispersion relation in Eq. (38) and the once-subtracted expression for the F^- HDR.

Thus, in what follows s_b and u_b will be the values of s and u that lie in the hyperbola $(s - a)(u - a) = b$ for a given value of t. Together with the condition $s + t + u = 2\Sigma$, these values can be recast as:

$$s_b \equiv s_b(t) = \frac{1}{2} \left(2\Sigma - t + \sqrt{(t + 2a - 2\Sigma)^2 - 4b} \right),$$

$$u_b \equiv u_b(t) = \frac{1}{2}\left(2\Sigma - t - \sqrt{(t + 2a - 2\Sigma)^2 - 4b}\right). \tag{41}$$

Then we can write the following once-subtracted hyperbolic dispersion relation for F^+

$$F^+(t, b, a) = h^+(b, a) + \frac{t}{\pi}\int_{4m_\pi^2}^{\infty}\frac{\operatorname{Im} G^0(t', s_b')}{\sqrt{6}\,t'(t' - t)}dt' + \frac{1}{\pi}\int_{m_+^2}^{\infty}ds'\frac{\operatorname{Im} F^+(s', t_b')}{s'}\left(\frac{s}{s' - s} + \frac{u}{s' - u}\right), \tag{42}$$

where

$$s_b' \equiv s_b(t'), \quad u_b' \equiv u_b(t'), \quad t_b' = 2\Sigma - s' - \frac{b}{s' - a} - a. \tag{43}$$

Note that one subtraction is enough in Eq. (42) since the first term converges because at high energies its leading Regge exchange is the K^*-trajectory, whereas the second term is backward scattering.

Then, similarly to what was done in [207] for $a = 0$, by combining the fixed-t dispersion relation in Eq. (38) with Eq. (42) right above at $t = 0$ and $b_0 = a^2 - 2\Sigma a + \Delta^2$, we can determine both subtraction terms $c^+(t)$ and $h^+(b, a)$. Thus we can rewrite the HDR for F^+ as follows:

$$\begin{aligned}
F^+(s_b, t) = &8\pi m_+ a_0^+ + \frac{t}{\pi}\int_{4m_\pi^2}^{\infty}\frac{\operatorname{Im} G^0(t', s_b')}{\sqrt{6}\,t'(t' - t)}dt' \\
&+ \frac{1}{\pi}\int_{m_+^2}^{\infty}ds'\frac{\operatorname{Im} F^+(s', t_b')}{s'}\left[h(s', t, b, a) - h(s', 0, b, a)\right] \\
&+ \frac{1}{\pi}\int_{m_+^2}^{\infty}ds'\frac{\operatorname{Im} F^+(s', 0)}{s'^2}\left[g(s', b, a) - g(s', \Delta^2, 0)\right],
\end{aligned} \tag{44}$$

where we have defined

$$\begin{aligned}
h(s', t, b, a) &= \frac{s'(2\Sigma - t) - 2[b - a^2 + (2\Sigma - t)a]}{s'^2 - s'(2\Sigma - t) + [b - a^2 + (2\Sigma - t)a]}, \\
g(s', b, a) &= \frac{s'(2\Sigma)^2 - 2[b - a^2 + 2\Sigma a](s' + \Sigma)}{s'^2 - s'2\Sigma + [b - a^2 + 2\Sigma a]}.
\end{aligned} \tag{45}$$

Moreover, since we have also determined $c^+(t)$, we can now rewrite, as promised in the previous section, the fixed-t dispersion relation in Eq. (38) as:

$$\begin{aligned}
F^+(s, t) = &8\pi m_+ a_0^+ + \frac{1}{\pi}\int_{m_+^2}^{\infty}ds'\frac{\operatorname{Im} F^+(s', t)}{s'^2}\left[\left(\frac{s^2}{s' - s} + \frac{u^2}{s' - u}\right) - k(s', t)\right] \\
&+ \frac{t}{\pi}\int_{4m_\pi^2}^{\infty}\frac{\operatorname{Im} G^0(t', s_{b_0}')}{\sqrt{6}\,t'(t' - t)}dt' + \frac{1}{\pi}\int_{m_+^2}^{\infty}ds'\frac{\operatorname{Im} F^+(s', t_{\Delta^2})}{s'}\left[h(s', t, \Delta^2, 0) - h(s', 0, \Delta^2, 0)\right],
\end{aligned} \tag{46}$$

where we have now defined

$$k(s', t) = \frac{1}{s'^2}\frac{s'(2\Sigma - t)^2 - 2\Delta^2 s' - \Delta^2(2\Sigma - t)}{s'^2 - s'(2\Sigma - t) + \Delta^2}. \tag{47}$$

For the F^- case, in this report we will use both the unsubtracted and once-subtracted hyperbolic dispersion relations. This is just because, as we will show later, we have found that the unconstrained data fits do not satisfy well these two dispersion relations simultaneously. For convenience one has to write the HDR for the $s \leftrightarrow u$ symmetric combination $F^-/(s - u)$. Thus, the unsubtracted relation reads:

$$\frac{F^-(s_b, t)}{s_b - u_b} = \frac{1}{2\pi}\int_{4m_\pi^2}^{\infty}dt'\frac{\operatorname{Im} G^1(t', s_b')}{(t' - t)(s_b' - u_b')} + \frac{1}{\pi}\int_{m_+^2}^{\infty}ds'\frac{\operatorname{Im} F^-(s', t_b')}{(s' - s_b)(s' - u_b)}, \tag{48}$$

whereas the once-subtracted reads:

$$\frac{F^-(s_b, t)}{s_b - u_b} = h^-(b, a) + \frac{t}{2\pi}\int_{4m_\pi^2}^{\infty}dt'\frac{\operatorname{Im} G^1(t', s_b')}{t'(t' - t)(s_b' - u_b')} + \frac{1}{\pi}\int_{m_+^2}^{\infty}\frac{ds'}{s'}\frac{\operatorname{Im} F^-(s', t_b')}{(s_b' - u_b')}\left[\frac{s}{s' - s} + \frac{u}{s' - u}\right]. \tag{49}$$

For the latter, the subtraction constant can be determined, as done in [207] for the $a = 0$ case and for F^+ above. Namely, by using the once-subtracted fixed-t dispersion relation

$$F^-(s, t) = c^-(t)(s - u) + \frac{1}{\pi}\int_{m_+^2}^{\infty}\frac{ds'}{s'^2}\operatorname{Im} F^-(s', t)\left[\frac{s^2}{s' - s} - \frac{u^2}{s' - u}\right]. \tag{50}$$

Thus, we can rewrite Eq. (49) as

$$
\frac{F^-(s_b, t)}{s_b - u_b} = \frac{8\pi m_+ a_0^-}{m_+^2 - m_-^2} + \frac{t}{2\pi} \int_{4m_\pi^2}^\infty dt' \frac{\mathrm{Im}\, G^1(t', s_b')}{t'(t'-t)(s_b' - u_b')}
$$
$$
+ \frac{1}{\pi} \int_{m_+^2}^\infty ds' \mathrm{Im}\, F^-(s', t_b') \big[d(s', t, b, a) - d(s', 0, b, a) \big]
$$
$$
+ \frac{1}{\pi} \int_{m_+^2}^\infty ds' \mathrm{Im}\, F^-(s', 0) \big[f(s', b, a) - f(s', \Delta^2, 0) \big], \tag{51}
$$

with

$$
d(s', t, b, a) = \frac{1}{s'^2 - s'(2\Sigma - t) + [b - a^2 + (2\Sigma - t)a]},
$$
$$
f(s', b, a) = \frac{1}{s'^2 - s'2\Sigma + [b - a^2 + 2\Sigma a]}. \tag{52}
$$

We have explicitly checked that setting $a = 0$ we recover the same expressions as in [173,176,207] for the once-subtracted HDR. However, as already commented and explained in Appendix D, with our $a \neq 0$ HDR above we will be able to choose the a parameter to maximize the applicability region for the s or t channels of the HDR once projected into partial waves, while still reaching the $\kappa/K_0^*(700)$ region.

3.5. Partial-wave dispersion relations. Roy-Steiner equations

Once the $F(s, t, u)$ and $G(t, s, u)$ amplitudes are calculated dispersively, one can just project Eqs. (37), (44),(46), (48) and (49) to write partial-wave dispersion relations. Of course the partial-wave projection is different for the s and t channels and we will examine them separately in what follows.

3.5.1. s-channel partial-wave dispersion relations

We now use Eq. (11) to obtain πK scattering partial waves. First, we project the fixed-t dispersion relations Eqs. (37) and (46), obtaining:

$$
f_l^+(s) = \frac{m_+ a_0^+}{2} + \frac{1}{\pi} \sum_\ell \int_{m_+^2}^\infty ds' L_{l,\ell}^+(s, s') \mathrm{Im}\, f_\ell^+(s') + \frac{1}{\pi} \sum_{\ell \geq 0} \int_{4m_\pi^2}^\infty dt' L_{l,2\ell}^0(s, t') \mathrm{Im}\, g_{2\ell}^0(t'),
$$
$$
f_l^-(s) = \frac{1}{\pi} \sum_\ell \int_{m_+^2}^\infty ds' L_{l,\ell}^-(s, s') \mathrm{Im}\, f_\ell^-(s'), \tag{53}
$$

where the kernels $L_{l,\ell}^\pm(s, s')$, $L_{l,2\ell}^I(s, t')$ were given in [176] and can be found here in Appendix E. Beware that when fixing t, the z_s variable changes within the range $[-\lambda(s)/s, 0]$. This makes the L kernels relatively simple. Note also that there are no subtractions for $F^-(s, t)$.

In Appendix D we show that the applicability of these partial-wave relations obtained from fixed-t dispersion relations reaches $\sqrt{s_{max}} \simeq 1.05$ GeV in the real axis. Unfortunately, they do not reach the $\kappa/K_0^*(700)$ region in the complex plane, which is one of the reasons why we have to resort to HDR.

In contrast, the projection over an HDR is more complicated, since now $t_b = 2\Sigma - s - b/(s-a) - a$, and b is determined implicitly by $b = (s-a)(2\Sigma - s - t - a)$. In addition, we will now find inside the integrands the crossed-channel partial waves $g_\ell^I(t)$, defined in Eq. (12).

Then, projecting into s-wave partial waves the HDR for F^+ in Eq. (44), which has one subtraction, we find:

$$
f_l^+(s) = \frac{m_+ a_0^+}{2} + \frac{1}{\pi} \sum_{\ell \geq 0} \int_{4m_\pi^2}^\infty dt' K_{l,2\ell}^0(s, t') \mathrm{Im}\, g_{2\ell}^0(t') + \frac{1}{\pi} \sum_\ell \int_{m_+^2}^\infty ds' K_{l,\ell}^+(s, s') \mathrm{Im}\, f_\ell^+(s'), \tag{54}
$$

where the kernels $K_{l,2\ell}^0(s, t')$ and $K_{l,\ell}^+(s, s')$ were already obtained in [42] and are collected here in Appendix E for completeness.

Let us recall that for the antisymmetric amplitude F^- we are considering here both the unsubtracted HDR, Eq. (48), and the once-subtracted HDR, Eq. (49). When projected into s-channel partial waves, they read, respectively:

$$
f_l^-(s) = \frac{1}{\pi} \sum_\ell \int_{m_+^2}^\infty ds' K_{l,\ell}^-(s, s') \mathrm{Im}\, f_\ell^-(s') + \frac{1}{\pi} \sum_{\ell \geq 1} \int_{4m_\pi^2}^\infty dt' K_{l,2\ell-1}^1(s, t') \mathrm{Im}\, g_{2\ell-1}^1(t'),
$$
$$
f_l^-(s) = \delta_{l,0} \frac{m_+ a_0^-}{2} \frac{3s^2 - 2s\Sigma - \Delta^2}{8sm_\pi m_K} + \delta_{l,1} \frac{m_+ a_0^-}{2} \frac{m_\pi^4 + (m_K^2 - s)^2 - 2m_\pi^2(m_K^2 + s)}{24sm_\pi m_K}
$$
$$
+ \frac{1}{\pi} \sum_\ell \int_{m_+^2}^\infty ds' \hat{K}_{l,\ell}^-(s, s') \mathrm{Im}\, f_\ell^-(s') + \frac{1}{\pi} \sum_{\ell \geq 1} \int_{4m_\pi^2}^\infty dt' \hat{K}_{l,2\ell-1}^1(s, t') \mathrm{Im}\, g_{2\ell-1}^1(t'), \tag{55}
$$

where we have used a hat to denote the once-subtracted $\hat{K}^-_{l,\ell}(s,s')$, $\hat{K}^1_{l,2\ell-1}(s,t')$ kernels, which are provided in Appendix E for the $a \neq 0$ case. For completeness, we also provide there the $K^-_{l,\ell}(s,s')$, $K^1_{l,2\ell-1}(s,t')$ unsubtracted kernels that were obtained in [42] for the $a \neq 0$ case.

In Appendix D we show how we can now choose the a parameter to maximize the applicability reach of partial-wave HDR. For instance, the applicability range in the real axis is maximized with the choice $a = -13.9 m_\pi^2$, reaching $\sqrt{s_{max}} \simeq 0.989$ GeV. However, this choice leads to an applicability domain that does not cover the $\kappa/K_0^*(700)$ region in the complex plane, which was shown in [97] to be reachable with the $a = 0$ choice. The latter, however, was only applicable up to $\sqrt{s_{max}} \simeq 0.934$ GeV int the real axis. We have thus adopted an intermediate round value $a = -10 m_\pi^2$, which yields an applicability domain that encloses the $\kappa/K_0^*(700)$ region and extends up to $\sqrt{s_{max}} \simeq 0.976$ GeV in the real axis. This is only a small improvement in the applicability in the real axis for $\pi K \to \pi K$ scattering, but the choice of a is much more relevant for the t-channel case that we study next.

3.5.2. t-channel partial-wave dispersion relations

For $\pi\pi \to \bar{K}K$, we are only considering HDR. Now, recalling the $s \leftrightarrow t$ crossing relation in Eq. (6) we see that these HDR are once again those in Eqs. (44), (48) and (49) we have just used for the s-channel, but this time we will project them into t-channel partial waves g_ℓ^I, using Eq. (12). Of course, since the HDRs also need the crossed channel, we will find the πK partial waves $f_\ell^I(s)$ inside the integrals. Specifically, we get the following once-subtracted partial-wave dispersion relations for $I = 0$ and $\ell = 0, 2$:

$$
\begin{aligned}
g_0^0(t) = &\frac{\sqrt{3}}{2} m_+ a_0^+ + \frac{t}{\pi} \int_{4m_\pi^2}^\infty \frac{\mathrm{Im}\, g_0^0(t')}{t'(t'-t)} dt' + \frac{t}{\pi} \sum_{\ell \geq 2} \int_{4m_\pi^2}^\infty \frac{dt'}{t'} G^0_{0,2\ell-2}(t,t') \mathrm{Im}\, g_{2\ell-2}^0(t') \\
&+ \frac{1}{\pi} \sum_\ell \int_{m_+^2}^\infty ds' G^+_{0,\ell}(t,s') \mathrm{Im}\, f_\ell^+(s'),
\end{aligned}
$$

$$
\begin{aligned}
g_2^0(t) = &\frac{t}{\pi} \int_{4m_\pi^2}^\infty \frac{\mathrm{Im}\, g_2^0(t')}{t'(t'-t)} dt' + \frac{t}{\pi} \sum_{\ell \geq 3} \int_{4m_\pi^2}^\infty \frac{dt'}{t'} G'^0_{2,2\ell-2}(t,t') \mathrm{Im}\, g_{2\ell-2}^0(t') \\
&+ \frac{1}{\pi} \sum_\ell \int_{m_+^2}^\infty ds' G'^+_{2,\ell}(t,s') \mathrm{Im}\, f_\ell^+(s').
\end{aligned}
\tag{56}
$$

The explicit expressions of the $G^0_{\ell\ell'}(t,t')$, $G^+_{\ell\ell'}(t,s')$ integration kernels are given in Appendix E for completeness, although they were already derived in [42].

We also write two dispersion relations for $I = 1$, $\ell = 1$, unsubtracted or once-subtracted. These read, respectively:

$$
\begin{aligned}
g_1^1(t) = &\frac{1}{\pi} \int_{4m_\pi^2}^\infty \frac{\mathrm{Im}\, g_1^1(t')}{t'-t} dt' + \frac{1}{\pi} \sum_{\ell \geq 2} \int_{4m_\pi^2}^\infty dt' G^1_{1,2\ell-1}(t,t') \mathrm{Im}\, g_{2\ell-1}^1(t') \\
&+ \frac{1}{\pi} \sum_\ell \int_{m_+^2}^\infty ds' G^-_{1,\ell}(t,s') \mathrm{Im}\, f_\ell^-(s'),
\end{aligned}
$$

$$
\begin{aligned}
g_1^1(t) = &\frac{2\sqrt{2} m_+ a_0^-}{3(m_+^2 - m_-^2)} + \frac{t}{\pi} \int_{4m_\pi^2}^\infty \frac{\mathrm{Im}\, g_1^1(t')}{t'(t'-t)} dt' + \frac{t}{\pi} \sum_{\ell \geq 2} \int_{4m_\pi^2}^\infty \frac{dt'}{t'} \hat{G}^1_{1,2\ell-1}(t,t') \mathrm{Im}\, g_{2\ell-1}^1(t') \\
&+ \frac{1}{\pi} \sum_\ell \int_{m_+^2}^\infty ds' \hat{G}^-_{1,\ell}(t,s') \mathrm{Im}\, f_\ell^-(s').
\end{aligned}
\tag{57}
$$

The expressions for the once-subtracted $\hat{G}^1_{\ell\ell'}(t,t')$, $\hat{G}^-_{\ell\ell'}(t,s')$ kernels have been obtained in this review and are given in Appendix E, together with the unsubtracted $G^1_{\ell\ell'}(t,t')$, $G^-_{\ell\ell'}(t,s')$ that were already derived in [42] but are also provided for completeness.

Since we have left the a parameter-free, it can be used to maximize the applicability of the equations right above. Let us remark that constraints are coming from the applicability of the HDR in Eqs. (44), (48) and (49) as well as from the convergence of the partial-wave expansions. As shown in Appendix D, by setting $a = -10.9 m_\pi^2$ the applicability range of these equations is $-0.286\,\mathrm{GeV}^2 \leq t \leq 2.19\,\mathrm{GeV}^2$. In other words, we can study the physical region from the $K\bar{K}$ threshold $\simeq 0.992$ GeV up to $\sqrt{t} \simeq 1.47$ GeV. In contrast, the HDR projected into partial waves in the $a = 0$ case are only valid up to $\simeq 1.3$, GeV. Thus, with our choice of a, the applicability of the dispersive approach in the physical region, where we can test or use data as input, can be extended by 55% in terms of the $\sqrt{t}$ variable, or 67% in terms of t.

3.6. Muskhelishvili–Omnès Method for the unphysical $\pi\pi \to K\bar{K}$ region.

A very important complication when dealing with dispersive integrals for the $\pi\pi \to K\bar{K}$ channel is that the integration region starts at $\pi\pi$ threshold. This implies that they should be calculated over an "unphysical" region where actual

$\pi\pi \to K\bar{K}$ scattering data cannot occur. Fortunately, below $K\bar{K}$ threshold the inelasticity to more than two-pion states is negligible in practice. Consequently, $\pi\pi$ is the only available state and then Watson's theorem [118] implies that the g_ℓ^I phase in that region is nothing but that of $\pi\pi$ scattering, i.e. $\phi_\ell^I(t) = \delta_{\ell,\pi\pi\to\pi\pi}^I(t)$. However, Watson's theorem does not provide any direct information on the modulus of g_ℓ^I. Nevertheless, as already illustrated in [42,43,176,188,201,207], once the phase is known, $|g_\ell^I|$ in the unphysical region can be described using the rather standard Muskhelishvili–Omnès method [224,225], which we describe next.

Let us first separate the left- and right-hand contributions in Eqs. (56) as follows:

$$g_\ell^0(t) = \Delta_\ell^0(t) + \frac{t}{\pi}\int_{4m_\pi^2}^\infty \frac{dt'}{t'}\frac{\mathrm{Im}\,g_\ell^0(t)}{t'-t}, \quad \ell = 0, 2,$$

$$g_1^1(t) = \Delta_1^1(t) + \frac{1}{\pi}\int_{4m_\pi^2}^\infty dt'\frac{\mathrm{Im}\,g_1^1(t)}{t'-t}, \tag{58}$$

where $\Delta_\ell^I(t)$ contains both the left-hand cut contributions and subtraction terms. It is important to realize that $\Delta_\ell^I(t)$ does not depend on g_ℓ^I itself, but on the other $g_{\ell'}^I$ with $\ell' \geq \ell + 2$. Fortunately, these last are much more suppressed than g_ℓ^I in the unphysical region, due to the centrifugal barrier.

In principle, the Muskhelishvili–Omnès method is only needed in the region between the two-pion and two-kaon thresholds. However, its solution would then depend very strongly on the value of the amplitude at $t_K = 4m_K^2$. This is inconvenient in practice, because, first, the experimental data starts above that energy and, second, this threshold is very sensitive to isospin breaking. In particular for the scalar I=0 wave. The reason is that, in reality, there are two different thresholds for K^+K^- and $K^0\bar{K}^0$ separated by 8 MeV, which are felt by experiment but not accommodated by our isospin-conserving formalism. For these reasons, following [207] and our previous analysis in [42], we apply the method up to a "matching energy point" $t_m > t_K$. The best choice for t_m is dictated by phenomenology and will be discussed in detail below.

It is now that we introduce the Omnès function

$$\Omega_\ell^I(t) = \exp\left(\frac{t}{\pi}\int_{4m_\pi^2}^{t_m}\frac{\phi_\ell^I(t')dt'}{t'(t'-t)}\right), \tag{59}$$

satisfying

$$\Omega_\ell^I(t) \equiv \Omega_{\ell,R}^I(t)e^{i\phi_\ell^I(t)\theta(t-4m_\pi^2)\theta(t_m-t)}, \tag{60}$$

where, in the real axis, $\Omega_{l,R}^I(t)$ is now defined as:

$$\Omega_{\ell,R}^I(t) = \left|\frac{t_m}{t_\pi}(t-t_\pi)^{-\phi_\ell^I(t)/\pi}(t_m-t)^{\phi_\ell^I(t)/\pi}\right|\exp\left(\frac{t}{\pi}\int_{4m_\pi^2}^{t_m}dt'\frac{\phi_\ell^I(t')-\phi_\ell^I(t)}{t'(t'-t)}\right). \tag{61}$$

Note that, for real values of s, $\Omega_{\ell,R}^I$ is nothing but the modulus of Ω_ℓ^I, and hence a real function.

Since the Omnès function has the same cut from $4m_\pi^2$ to t_m as $g_\ell^I(t)$, we can now define an auxiliary function

$$F_\ell^I(t) = \frac{g_\ell^I(t) - \Delta_\ell^I(t)}{\Omega_\ell^I(t)}, \tag{62}$$

which is analytic except for a right-hand cut starting at t_m. Therefore, it is possible to write dispersion relations for $F_\ell^I(t)$ along that cut, which, recast back in terms of $g_\ell^I(t)$, read:

$$g_0^0(t) = \Delta_0^0(t) + \frac{t\,\Omega_0^0(t)}{t_m-t}\left[\alpha + \frac{t}{\pi}\int_{4m_\pi^2}^{t_m}dt'\frac{(t_m-t')\Delta_0^0(t')\sin\phi_0^0(t')}{\Omega_{0,R}^0(t')t'^2(t'-t)} + \frac{t}{\pi}\int_{t_m}^\infty dt'\frac{(t_m-t')|g_0^0(t')|\sin\phi_0^0(t')}{\Omega_{0,R}^0(t')t'^2(t'-t)}\right],$$

$$g_1^1(t) = \Delta_1^1(t) + \Omega_1^1(t)\left[\frac{1}{\pi}\int_{4m_\pi^2}^{t_m}dt'\frac{\Delta_1^1(t')\sin\phi_1^1(t')}{\Omega_{1,R}^1(t')(t'-t)} + \frac{1}{\pi}\int_{t_m}^\infty dt'\frac{|g_1^1(t')|\sin\phi_1^1(t')}{\Omega_{1,R}^1(t')(t'-t)}\right],$$

$$g_1^1(t) = \hat{\Delta}_1^1(t) + t\,\Omega_1^1(t)\left[\frac{1}{\pi}\int_{4m_\pi^2}^{t_m}dt'\frac{\hat{\Delta}_1^1(t')\sin\phi_1^1(t')}{\Omega_{1,R}^1(t')t'(t'-t)} + \frac{1}{\pi}\int_{t_m}^\infty dt'\frac{|g_1^1(t')|\sin\phi_1^1(t')}{\Omega_{1,R}^1(t')t'(t'-t)}\right],$$

$$g_2^0(t) = \Delta_2^0(t) + t\,\Omega_2^0(t)\left[\frac{1}{\pi}\int_{4m_\pi^2}^{t_m}dt'\frac{\Delta_2^0(t')\sin\phi_2^0(t')}{\Omega_{2,R}^0(t')t'(t'-t)} + \frac{1}{\pi}\int_{t_m}^\infty dt'\frac{|g_2^0(t')|\sin\phi_2^0(t')}{\Omega_{2,R}^0(t')t'(t'-t)}\right]. \tag{63}$$

Note that, as explained above, for the g_1^1 wave we are interested in both the unsubtracted and once-subtracted relations, whose expressions are provided in the equations above in that respective order. Of course, when t is real and larger than the $\pi\pi$ threshold, a principal value must be taken on each integral, as illustrated with Eqs. (33) and (34) in the introduction of this section. Beware that, since by construction the Omnès function removes the phase, on the left-hand

sides of these equations the partial wave is reduced to its modulus between $\pi\pi$ threshold and t_m. In contrast, it is reduced to its real part above t_m.

Note also that we have considered a once-subtracted relation for the $g_0^0(t)$ Omnès solution. This is because, in what follows, we will choose t_m with $\phi_0^0(t_m) \geq \pi$ and then a subtraction is needed to ensure the convergence when $t \to t_m$. The corresponding subtraction constant α will be determined by imposing numerically a non-cusp condition for $g_0^0(t)$ at t_m.

Let us now explain the use of these equations. On the one hand, we need input from πK scattering, which in [41] we took as fixed input from the data analysis constrained with dispersion relations in [41]. However, in this report, we will use these partial-wave HDR to analyze first and constrain later both the $\pi K \to \pi K$ and $\pi\pi \to K\bar{K}$ data parameterizations simultaneously. Thus, instead of fixing one set of partial waves when studying the other, we will allow both sets to vary when considering their coupled HDR.

On the other hand, let us recall we need the Muskhelishvili–Omnès method because *in the unphysical region* there is no $\pi\pi \to K\bar{K}$ data and it may seem that we will not know what input to provide. Nevertheless, the equations above do not need the full knowledge of $g_\ell^I(t)$ in the unphysical region, but only their phases and the Δ_ℓ^I. As already explained, Watson's theorem tells us that these phases are known from $\pi\pi$ scattering, since in that regime other possible states made of more pions are negligible. For this purpose we will take these $\phi_\ell^I(t) = \delta_{\ell,\pi\pi\to\pi\pi}^I(t)$ phase shifts from the dispersive analysis of [48]. In addition, each Δ_ℓ^I does not involve $g_\ell^I(t)$ itself, but only other partial waves with $\ell' - \ell \geq 2$. However, in the unphysical region, such higher partial waves are suppressed compared to that with ℓ. We have explicitly checked that the $\ell = 3$ contribution to the $g_1^1(t)$ is rather small indeed, and even higher waves are negligible. Thus, with our simple phenomenological description of $g_3^1(t)$ we can get a good dispersive representation of $g_1^1(t)$. In addition, the $\ell = 4$ contribution to $g_2^0(t)$, which we have also considered, is almost negligible. Once we have $g_2^0(t)$ it can be used as input for Eq. (63) to obtain the dispersive representation of $g_0^0(t)$. (Note that the $\ell = 4$ contributions for $g_0^0(t)$ were neglected in [41] but are considered here.)

There is one technicality worth mentioning here. Since we will parameterize the high-energy region in terms of Regge amplitudes, which in principle contain all partial waves, we must subtract, from the Regge contribution to $\Delta_\ell^I(t)$, the projection of the Regge amplitude itself into the I, ℓ partial wave under consideration. Fortunately, this projection is negligible, and we have explicitly checked that the integrals barely change whether we use the full Regge amplitude or the one with its own projection into I, ℓ subtracted.

Finally, we have to choose a value for the matching energy t_m, which should always be above the $K\bar{K}$ threshold. It is relevant to keep in mind that the derivation of the dispersion relations above implies $g_{output}(t_m) = g_{input}(t_m)$. This condition will always occur for the integral output irrespective of whether the data at that energy has a statistical or systematic deviation or if it is in good or bad agreement with dispersion relations. As a consequence, if the data in that energy region were not close to the dispersive solution, the output will nevertheless be compelled to describe it, forcing the dispersive calculation to be distorted in other regions. In practice, we have found that, given the existing data, the g_0^0 wave is the most sensitive to this instability, the effect is more moderate on g_2^0 and almost negligible for g_1^1 because it is already very consistent for any t_m choice. For that reason, we studied in [42] what energy region is most consistent for g_0^0 when changing t_m. We concluded that two regions yield systematically rather consistent results between input and output: one around $\sqrt{t_m} = 1.2\,\text{GeV}$, which is also valid for g_2^0, and another one around $\sqrt{t_m} = 1.45\,\text{GeV}$. For the latter choice, however, we found that the resulting uncertainty in the dispersive calculation between $K\bar{K}$ threshold and 1.2 GeV is so large that there is no dispersive constraint at all. Actually, with such large uncertainties, we could even find that the dispersive output using any of the two $g_0^0(t)$ solutions as input (see Section 2), comes out compatible with itself as well as with the other one. Furthermore, note that t_m in Eq. (63) is the energy above which $|g_\ell^I|$ is used as input for its own equation. Since within our approach we are either testing or constraining the data parameterizations, we are then interested in maximizing that region by choosing the smallest possible t_m. Taking into account the previous considerations we have finally chosen $\sqrt{t_m} = 1.2\,\text{GeV}$ for g_0^0 and g_2^0, and $t_m = 1\,\text{GeV}$ for g_1^1. This energy is above $K\bar{K}$ threshold where the two most important inelasticities, i.e. $K\bar{K}$ and $\eta\eta$, show no cusps. Moreover, the g_2^0 data are well understood and under control at this energy, since its largest contribution comes from the well-established $f_2(1270)$ resonance, which lies very near t_m. As a final consistency check, we have shown in Appendix F that, once a constrained solution is obtained, the different choices of t_m produce negligible variations in the dispersive output, as expected.

4. Data parameterizations and unconstrained fits to data

In this section, we will present simple but rather flexible parameterizations that can describe the data and, very importantly, a realistic estimation of the experimental uncertainties. Our aim for simplicity is to allow for easy implementation for later use in experimental or theoretical analyses. Our parameterizations will thus follow the spirit of what was traditionally known as "energy-dependent" data analyses, just simple functions that describe data and we will avoid any particular model dependence. Of course, some approximations will be performed, like imposing isospin conservation or elastic unitarity on partial waves, not only in the strictly elastic regime but also where experiments have not found evidence of inelasticity or imposing fundamental constraints as the correct dependence on the powers of momenta near threshold. In the region where the existence of resonances is well established, we will introduce rather flexible resonant shapes, but not necessarily pure Breit–Wigner formulae.

Note that, with these parameterizations, we will first obtain a set of Unconstrained Fits to Data, that we will refer to as the UFD set. This is what this section is about. The flexibility of the parameterizations is required so that later on we can impose on them the dispersive constraints we have discussed in previous sections, while still describing the data. In this way, the parameterizations will stay the same but their parameters will change to define a Constrained Fit to Data (CFD) discussed in Section 5.

Concerning uncertainties, we will not only consider the statistical error provided by experiments but we will include estimates of systematic uncertainties needed to reconcile the observed incompatibilities within the same data set and/or between different experiments.

A word of caution is in order. As seen in Section 2, data are not precise nor numerous enough to exclude large fluctuations between successive data points. And this is particularly evident in some relatively large energy regions where just a few data points may exist. In principle, we cannot exclude complicated parameterizations that would adjust perfectly every single piece of data but produce large fluctuations or structures between points. Thus, from the outset, we make it clear that we assume such fluctuations not to occur and that the data can be fitted with simple and relatively smooth parameterizations. Obviously, the size of our uncertainties depends on this assumption. We have chosen the parameterizations we provide below because they satisfy the above assumption and yield uncertainty bands that do not show wild fluctuations or become too large in the regions where data do not exist or do not require so. In addition, we have explored many alternatives: different conformal expansions (with different centers and more terms in the expansion, see Appendix A), simpler or more complicated polynomials in different variables, adding or removing resonant shapes, etc. Of course, we can make them fit the data, but in so doing their central result is always very similar to our final choice. Therefore, apart from a few exceptions of interest, we spare the reader the list of pros and cons of the many other parameterizations we tried and we just present our final choice. Moreover, for a given parameterization, and once the systematic uncertainty that affects the data has been estimated, we have decided to stop adding parameters when the χ^2/dof has roughly "converged" to 1, or normalize it in case it is needed.

The existing data for the $\pi K \to \pi K$ and $\pi\pi \to K\bar{K}$ scattering have been reviewed in detail in Section 2. However, for our purposes, we will also need parameterizations of the amplitudes up to, in principle, arbitrarily high energies, where no data for strange trajectories exists. This region provides small, but non-negligible contributions to our integrals, and here we will also provide high-energy parameterizations of $\pi K \to \pi K$ and $\pi\pi \to K\bar{K}$ amplitudes in terms of Regge theory. Thus, in Section 4.3, we will present the required Regge parameterizations that complete what we call the UFD set since no dispersion relations will be imposed upon them in this first stage.

One might wonder why the dispersive constraints are not imposed from the very beginning. There are several reasons for this. First, in the future more or better data may appear in a particular wave and then one may refit that wave without altering the other ones. This will not be so easy once we impose the constraints, since dispersion relations will correlate all waves among themselves. Second, we want to check if there are data points or sets of data that fare particularly bad against the dispersive representation and then prune the experimental data before imposing any constraint. As long as experimental analyses do not incorporate these relations, it seems natural to check the consistency of the data with respect to causality and crossing symmetry, at least within experimental uncertainties. Since we have already seen that meson–meson scattering data are affected by large systematic errors, which are not usually included in the experimental uncertainties, it should not be surprising that unconstrained fits to $\pi\pi$ [48,50,51], $\pi K \to \pi K$ [41,97] or $\pi\pi \to K\bar{K}$ [42] data do not satisfy well these dispersive constraints.

Later on, we will construct a "Constrained Fit to Data" (CFD) set by imposing the fulfillment of dispersion relations in the fits. But note that, although differing in the values of the parameters, the functional form of the UFD and CFD parameterizations are the same. Therefore, the parameterizations will be presented in what follows, discussing for the moment just the UFD values of the fit parameters and leaving the CFD for Section 5.

4.1. $\pi K \to \pi K$ Parameterizations and unconstrained fits to data

In principle, since the quantities of interest like resonance poles or threshold parameters, etc... will be obtained from the output of dispersion relations, any parameterization that describes data could do as input, i.e. a model, polynomials, or even splines. However, the whole approach becomes easier if some relevant physical features like cuts, unitarity, Adler zeros, or some poles associated with resonances are already implemented in our parameterizations from the very start. In addition, for many later applications, the full rigor of dispersion relations may not be needed, but it could be more interesting to use a relatively simple parameterization that is consistent with the dispersive representation, the data and that is also able to describe the most salient analytic features. Hence, in this section we will provide parameterizations that we will use as input for our dispersion relations but that satisfy unitarity, display the required analytic structures like thresholds, or possible poles to accommodate resonant structures. In addition, we will make a particular effort in doing this while keeping them relatively simple for later applications while describing not just the data but also their uncertainties. Moreover, we want them flexible enough to be able to satisfy the dispersive constraints when we will impose them in a later section.

Thus, following the usual conventions, when the partial-wave decomposition is possible, we will provide the phase shift (or its cotangent) and, in the inelastic regime, also the elasticity function for each partial wave. At high energies, where no partial-wave data exist or the partial-wave expansion does not converge, we will use Regge theory.

The $\pi K \to \pi K$ partial-wave parameterizations we will present here follow closely those we first introduced in [41], although we have made some slight modifications in the $S^{1/2}$, $S^{3/2}$, $P^{1/2}$ and $P^{3/2}$ waves. Our main goal with these modifications is to improve the description of the uncertainties associated with the data, especially when estimating systematic errors.

In particular, we fit the data discussed in Section 2, but only up to $\sim$1.7 GeV, and thus we will only fit S, P, D and F waves, since there are no data for G, H, and higher waves below 1.8 GeV. The reason to choose a common maximum energy for all partial-wave fits is that above some energy we have to stop relying on partial waves for the input within our integrals, and we have to use total amplitudes, which are the only ones for which data exist at high energies. We choose to parameterize them with Regge theory, which in principle includes all partial waves, so, once we start using high-energy parameterizations we cannot separate partial waves any longer. In addition, the convergence of the partial-wave expansion becomes less reliable as the energy increases.

4.1.1. General form of our $\pi K \to \pi K$ partial-wave parameterizations

Some generic features will be shared by most of our partial-wave parameterizations. In waves with little structure, as those that are elastic in the whole energy region, a single functional form will be used throughout the whole energy range. However, more complicated waves will require different functional forms in different regions. Typically these piece-wise functions will be matched at thresholds demanding continuity. Otherwise, a continuous matching will be imposed and if possible even a continuous derivative at least for the central value of the fit. Let us then describe separately the elastic and inelastic generic forms:

Partial waves in elastic regions

Following Eq. (17) in the Notation Section 1.3, πK elastic partial waves can be recast as

$$f_\ell(s) = \frac{1}{\sigma(s)} \frac{1}{\cot \delta_\ell(s) - i}, \tag{64}$$

where for simplicity we have suppressed the isospin index with respect to Section 1.3. Thus, we will just provide a parameterization of $\cot \delta_\ell(s)$.

Although in principle any parameterization would do if we just want to calculate the dispersive integrals, from Section 3 we know that in the complex s-plane, partial waves for the scattering of two particles with different masses have a distinct analytic structure in the first Riemann sheet, shown for the $\pi K \to \pi K$ case in the upper panel of Fig. 20. First of all, there is a right-hand cut, also called "physical cut", extending from πK threshold to infinity. In addition, due to the thresholds in the crossed channels, there is a left-hand cut extending from $(m_K - m_\pi)^2$ to $-\infty$, as well as a circular-cut at $|s|^2 = (m_K^2 - m_\pi^2)^2$. For πK scattering no other singularities appear in the complex plane since this system has no bound states that could give rise to poles in the real axis below threshold. The cut singularities are reproduced in the second Riemann sheet, where poles associated with resonances can appear.

Then, to describe the amplitude in the complex s-plane, it is customary to use the elastic unitarity condition in Eq. (17) and, defining an *effective range function* $\Phi_\ell(s)$, recast the partial wave as

$$f_\ell(s) = \frac{q^{2\ell}}{\Phi_\ell(s) - iq^{2\ell}\sigma(s)}. \tag{65}$$

Of course, *in the elastic region of the real axis*,

$$\Phi_\ell(s) = \frac{2q^{2\ell+1}}{\sqrt{s}} \cot \delta_\ell(s). \tag{66}$$

Abusing this notation it is usual to write:

$$\cot \delta_\ell(s) = \frac{\sqrt{s}}{2q^{2\ell+1}} \Phi_\ell(s) \tag{67}$$

as a complex function on the whole complex-s plane, although, of course, it is only the cotangent of a real angle when s lies in the real axis between the elastic and any inelastic threshold.

At this point we will use a conformal expansion in order to incorporate the analyticity properties of the partial wave, taking advantage of the fact that it is analytic in the whole plane except for the cuts shown in the upper panel of Fig. 20. The conformal expansions we are interested in for πK scattering are explained in detail in Appendix A, and they are of the type

$$\cot \delta_\ell(s) = \frac{\sqrt{s}}{2q^{2\ell+1}} F(s) \sum_n B_n \omega(s)^n. \tag{68}$$

Generically, we set $F(s) = 1$. For scalar waves, which have an Adler zero at s_{Adler}, we take $F(s) = 1/(s - s_{Adler})$, as well as $F(s) = (s - m_r^2)$ for waves that exhibit a clear narrow resonance and whose phase shift crosses $\pi/2$ at m_r. The conformal variable is defined as:

$$\omega(y) \equiv \omega(y(s)) = \frac{\sqrt{y(s)} - \alpha\sqrt{y_0 - y(s)}}{\sqrt{y(s)} + \alpha\sqrt{y_0 - y(s)}}, \quad y(s) = \left(\frac{s - \Delta_{K\pi}}{s + \Delta_{K\pi}}\right)^2, \quad y_0 = y(s_0). \tag{69}$$

This change of variables, which maps the complex s-plane into the unit circle, is relatively similar to those used for $\pi\pi$ scattering in [51,226] or πK scattering in [227], and is explained in detail in Appendix A. Suffices here to say that such a conformal expansion ensures a rapid convergence of the series. Thus, in practice, we will find that no more than three B_i coefficients are needed for the fits to each wave in the elastic region. Note that, for each partial wave, the s_0 and α constants are fixed, not fitted. The intuitive meaning of these two parameters is that s_0 sets the maximum energy at which this mapping is applicable on the real axis, whereas α fixes the energy around which the expansion is centered. As explained in Appendix A, they are chosen so that the region where data exist lies well inside the convergence region $|\omega| < 1$ and with a fairly symmetric distribution of the data on the left and the right sides of the center of the expansion.

Partial waves in inelastic regions

First of all, an important remark is in order. Recall that the $\pi K \to \pi K$ partial wave is inelastic when $|S_\ell^I(s)_{\pi K \to \pi K}| < 1$ or, using Eq. (18), $\eta_\ell^I(s) < 1$. Let us drop the I, ℓ indices for a moment. With our parameterizations, we will fit the data on the phase and the modulus of each $\pi K \to \pi K$ partial wave. Therefore we will have information about the inelasticity as a whole and we will not be able to discern what channels and by how much they contribute to $\eta(s)$ being smaller than one. However, once we use our inelastic formalism all states that contribute physically to the inelasticity are taken into account (within uncertainties). This is in contrast to the familiar "coupled-channel models", for which one chooses just a few coupled states (usually two-body states or approximated as such) that are the only ones to contribute to the whole inelasticity. Within these models, it is possible to separate the sources of inelasticity and include information from other channels if it exists, but the caveat is that you can also miss states if they are not explicitly included in the model from the start.

This said, in practice, we have to choose the energy from which we allow $\eta(s)$ to be less than one. For the S-wave, the inelastic region is dominated by the $K_0^*(1430)$, whose branching fractions are $\simeq 93\%$ to πK and $\simeq 8.5\%$ to $K\eta$. Thus the $K\eta$ threshold at $\simeq 1042$ MeV seems the natural choice to allow for inelasticity. In contrast, when looking at the P, D and F-waves, the main decay channels other than $K\pi$ for the $K^*(1410)$, $K_2^*(1430)$, $K^*(1680)$ and $K_3^*(1780)$ resonances are $K^*(892)\pi$ and $K\rho(770)K$. The thresholds of these two states are nominally placed at $\simeq 1032$ MeV and $\simeq 1266$ MeV. One might also wonder about the $K\pi\pi$ channel but, in practice, this state is observed as one of the previous two. For a description of the P-wave with a coupled channel formalism with the three $K\pi$, $K^*\pi$ and $K\rho(770)$ channels, see [228]. Unfortunately, the $K^*(892)\pi$ and $K\rho(770)$ thresholds are not as sharply defined as the $K\eta$ threshold, due to the widths of the $K^*(892)$ and $\rho(770)$, which are $\simeq 50$ and $\simeq 170$ MeV, respectively.

Driven by our desire for simplicity we have decided to set our inelastic formalism to start at the $K\eta$ threshold, since it is sharply defined, very close to the nominal one for $K^*(892)\pi$ and well below the nominal one for $K\rho(770)$. An additional practical reason is that a well-defined threshold allows for a cusp, i.e. a discontinuity of the derivative, which facilitates the matching between the elastic and inelastic regimes. Actually, we can easily take into account the inelastic parts using a step function $\Theta_{K\eta} = \Theta(s - (m_K + m_\eta)^2)$ and ensure the continuity by using the $q_{\eta K}$ momenta, which vanishes at the $K\eta$ threshold, in the equations. Only for one wave, we will also allow for a similar treatment of the $K\eta'$ threshold. Nevertheless, we insist that, once we allow for the inelasticity to exist, all possible inelastic channels contribute to it. Our use of the $K\eta$ threshold to start our inelastic region by no means implies that we are assuming that the $K\eta$ channel dominates the inelasticity in all channels, it is just that we allow our parametrizations to acquire an inelasticity from that point. The data will then tell us how big that total inelasticity is, irrespective of what channels are producing it.

Once we have decided from where we will allow our amplitudes to become inelastic, following [41], the majority of our partial-wave parameterizations in the inelastic region have been chosen to implement in a relatively simple way several resonances observed experimentally, while providing a continuous match with their corresponding parameterization in the elastic regime. Note, however, that for the $D^{1/2}$ and $F^{1/2}$-waves data only exist in the inelastic region, and thus we will use an inelastic formalism throughout the whole energy region, which reduces to the elastic case below $K\eta$ threshold. In [41] we tried different expressions, including polynomial fits and splines in powers of the πK, $K\eta$ momenta, or the s or $\sqrt{s}$ variables. However, we found that once fitted to data, the error bands of such parameterizations tend to be both rather small near the elastic region and too big at larger energies. This does not reproduce well the uncertainty observed by simple inspection of the data and leads to very large correlations.

As a matter of fact, in [41] we found, as others before us [43], that this region is most efficiently described in terms of products of exponential or rational functions, as follows:

$$f_\ell(s) = \frac{1}{2i\sigma(s)}\left(\prod_n S_n(s) - 1\right). \tag{70}$$

In this way it is far easier to implement resonant structures, usually overlapping, together with other background features, while yielding more uniform uncertainty bands throughout the whole fit region. In particular, complex exponentials will be used to describe a non-resonant background

$$S_n = S_n^b = \exp\left[2iq_{ij}^{2\ell+1}(\phi_0 + \phi_1 q_{ij}^2 + \cdots)\right], \tag{71}$$

with ϕ_k real parameters, whereas rational functions

$$S_n = S_n^r = \frac{s_{rn} - s + i(P_n(s) - Q_n(s))}{s_{rn} - s - i(P_n(s) + Q_n(s))}, \tag{72}$$

will be used to accommodate resonances and their associated poles. Here s_{rn} are real parameters and $P_n(s)$ and $Q_n(s)$ are polynomials that have the same sign over the inelastic region. Let us remark that if these polynomials were constant, S_n^r reduces to the simplest form of the familiar Breit–Wigner parameterization. In the following subsections, we will explain in detail our choice of polynomials for different waves.

Of course, these functional forms are also chosen because they satisfy $|S_n| \leq 1$ and then unitarity is satisfied trivially, even in the inelastic regime.

A continuous matching with each corresponding elastic region is achieved by fixing the $P_n(s)$ polynomial in S_n that has the pole with the smallest s_{rn}. This formalism is a modification of the parameterizations used by [43] in this energy region. In order to recover the elastic case, it is enough to set $Q_n \equiv 0$, which as explained above is of relevance for the $D^{1/2}$ and $F^{1/2}$ waves.

As already commented, near a resonance (or more precisely, its associated pole) each of the S_n^r functions bears some resemblance to the familiar Breit–Wigner functional form, which is just a simple model. Our parameterizations are much more flexible since they can incorporate inelastic resonances even if they overlap with other resonances or analytic structures. In particular, when combining the S_n in our complete functional form in Eq. (70), unitarity is satisfied exactly. This is definitely not the case of a simple sum of Breit–Wigner amplitudes, which violates unitarity and is nevertheless often used in the literature. Let us emphasize that the actual resonance parameters have to be calculated with the full partial-wave expression evaluated at the pole position in the complex plane, and never from just one individual S_n^r piece on the real axis.

Finally, to conclude this introduction to the generic form of our parameterizations, let us recall that we will use partial waves to describe data up to ~ 1.8 GeV for $\pi K \to \pi K$, and ~ 2 GeV for $\pi \pi \to K\bar{K}$ scattering. Beyond that energy, we will use Regge theory to describe the whole amplitudes $F(s, t, u)$. These parameterizations will be described last in Section 4.3.

4.1.2. S-wave

The S-wave $\pi K \to \pi K$ scattering data were discussed in Section 2.1.2. Let us recall that the main data sets, shown in Fig. 7, are measured in the $f_0^{1/2} + f_0^{3/2}/2$ isospin combination. Since the $I = 3/2$ partial wave has been measured independently, see Fig. 6, it can be used to separate the $f_0^{1/2}$ component. In practice, we will fit the two waves simultaneously. In view of the data, it is evident that there are large systematic uncertainties between different data sets and even within the same data sets. In particular, there are a few points that provide most of the χ^2 of the fit and are largely incompatible with the rest of the sample.

In our first analysis of $\pi K \to \pi K$ [99], we chose not to discard any data point and we followed an elaborate procedure to estimate the uncertainties of the resulting fit. In particular, we followed one of the techniques suggested in [229,230], which had been previously applied to NN and $\pi\pi$ scattering. In brief, we checked several Gaussianity tests on the data with respect to the fit and then enlarged the uncertainties of those data points that spoiled the tests (typically those beyond 3-standard deviations). This data purge leads to a new fit upon which the procedure is iterated until the Gaussianity test is satisfied. We also tried other simpler approaches and we found that the uncertainty band was rather similar.

However, the method we used in [99] to estimate systematic uncertainties for this particular wave, is somewhat cumbersome and will be abandoned here. The reason why we can do this is that, as already remarked, in this case, most of the contribution to the χ^2 of any fit is due to just a few data points which are abnormally separated from the rest. Hence, we will simply discard all data points that deviated from the best fit by more than 3.5 standard deviations. As a matter of fact, and in agreement with the expectations derived from [230], given the total number of data points to be fit for the S wave, deviations above 3.5 sigmas should be extremely unlikely, but we find many more than expected. As a consequence, just by removing these dramatically inconsistent values, the χ^2/dof of the fits in all regions of the $f_0^{3/2}$ and $f_0^{1/2} + f_0^{3/2}/2$ combinations gets immediately reduced below 3. Remarkably, the residues of the fit still follow roughly a gaussian distribution, even if we have not imposed such a feature from the onset. Finally, it is enough to re-scale the statistical uncertainties of the remaining points by a given factor to normalize the χ^2/dof. When these systematic errors are taken into account, they translate into larger uncertainties for the fit coefficients. Of course, the data outliers still remain outside the band, although in this way they do not contaminate the fit.

After removing the conflicting points we get $\chi^2_{S3/2}/dof = 2.6$, $\chi^2_{e\,S1/2+S3/2/2}/dof = 1.4$ and $\chi^2_{in\,S1/2+S3/2/2}/dof = 1.7$, where the $\chi^2_{e\,S1/2+S3/2/2}$ combination is the result of the fit in the elastic region, whereas the latter corresponds to the inelastic one, above the $K\eta$ threshold. One could then re-scale the uncertainties of the data by a uniform factor to get a $\chi^2/dof \sim 1$, which is roughly normally distributed.

Let us then provide the specific details of the S-waves parameterizations, whose general features were previously discussed.

$I = 3/2$ S-wave

For this wave, we will keep the very same simple parameterization we already introduced in [99], although the values of the parameters will change due to our new fitting strategy. It is worth noting that so far there is no evidence of inelasticity up to ~ 1.8 GeV and this wave can be considered elastic. Hence, we will make use of a truncated conformal parameterization to fit the phase shift. We have checked that just three conformal parameters are enough since the addition of a fourth one does not improve the fit. Therefore, we use

$$\cot \delta_0^{3/2}(s) = \frac{\sqrt{s}}{2q(s_A - s)} \left(B_0 + B_1\omega(s) + B_2\omega(s)^2 \right). \tag{73}$$

Table 1
Parameters of the $S^{3/2}$-wave. In GeV^2 units.

Parameter	UFD	CFD
B_0	2.15 ± 0.03	2.21 ± 0.03
B_1	3.96 ± 0.13	3.46 ± 0.13
B_2	3.15 ± 0.32	3.13 ± 0.32

Note the Adler zero is factorized explicitly and fixed to its leading order within Chiral Perturbation Theory (LO ChPT): $s_A = \Sigma_{K\pi} \simeq (516\,\text{GeV})^2$. For this particular wave, we choose the conformal variable in Eq. (69) with the following fixed parameters:

$$\alpha = 1.4, \quad s_0 = (1.84\,\text{GeV})^2. \tag{74}$$

The parameters of the unconstrained fit to data (UFD) are shown in Table 1. Compared to the results using our parameters in [41], this UFD will produce a much better agreement with dispersion relations to start with, even though its uncertainties have been reduced. It is worth noticing that a simple fit to the whole data collection, without removing the conflicting data points as explained above, would lead to way greater deviations between the fit and the dispersive results. Moreover, its scattering length would lie further away from the sum-rule result than our new UFD.

Our resulting UFD phase is plotted as a dashed line with a light orange band in Fig. 6. Note that at low-energies the curve follows closely the data of [2,3] whereas at high energies it is dominated by data from [5].

Finally, let us remark that we also considered leaving the Adler Zero as a free parameter, instead of fixing it to the ChPT leading order value. The motivation was that, in Section 7.1.3, we will provide the best value for this Adler zero, $\sim 0.550\,\text{GeV}$, obtained from dispersion relations using a constrained fit, whereas the LO ChPT value that we have used here is located at $\sim 0.516\,\text{GeV}$. However, since S-wave data starts at energies around 0.75 GeV, roughly 200 MeV above the Adler Zero, the best fit with a free Adler zero does not improve the overall χ^2 at all, whereas both the scattering lengths and the resulting Adler Zero are at odds with the dispersive values that we will obtain later. In other words, the pure unconstrained fit to data does not provide sufficient information to determine accurately the threshold and subthreshold regions, which is not unexpected considering that there are no data at threshold, and the lowest-lying data points are incompatible between themselves. Since, at this point, we are interested in a phenomenological parameterization of the data, and the subthreshold region is less relevant, we consider that setting the Adler zero to the LO ChPT position, i.e., within 10% of its actual value, is good enough for our purposes. We reiterate that the position of this Adler zero will be obtained in Section 7.1.3 from dispersion relations with a $\sim 2\%$ accuracy.

$S^{1/2}$ partial wave

For the $I = 1/2$ S-wave we will keep the very same functional form we already used in [41], although the values of the parameters will change slightly due to our new fitting strategy. Let us recall that inelasticity in this wave has been measured above 1.3 GeV and that, as we saw in Fig. 7, this part of the inelastic region is dominated by the $K_0^*(1430)$ resonance, whose width is estimated in the RPP to be $\Gamma = 270 \pm 80$ MeV.

Let us start then with the elastic region, for which we use the general form discussed above in terms of a truncated conformal expansion to fit the phase shift. For this particular wave we have found that just two conformal parameters are enough and therefore we use:

$$\cot \delta_0^{1/2}(s) = \frac{\sqrt{s}}{2q(s - s_A)}\left(B_0 + B_1\omega(s)\right). \tag{75}$$

Once again, we have factorized explicitly an Adler zero at s_A, whose position we take from leading order ChPT:

$$s_A = \left(\Sigma_{K\pi} + 2\sqrt{4\Delta_{K\pi}^2 + m_K^2 m_\pi^2}\,\right)/5 \simeq (0.486\,\text{GeV})^2 \simeq 0.236\,\text{GeV}^2. \tag{76}$$

Actually, there are two such zeros, but here we are considering the one closer to threshold since it has the largest influence on the shape of the wave in the physical region. The other one is obtained by replacing the first plus sign with a minus [217]. Hence, it lies inside the circular-cut and thus outside the applicability region of the conformal mapping. As it happened with the $I = 3/2$ S-wave, we fix the Adler zero instead of considering it a free parameter, because for our fits we are interested in the physical region, where data exist, and not so much in the subthreshold region. Since the data lie quite far from threshold and thus even further away from the Adler zero, simple fits are not enough to determine it with accuracy. Later on, in Section 7.1.3, we will obtain the value of this Adler zero from the dispersive representation at $\simeq 0.470\,\text{GeV}$. Thus, the LO ChPT calculation we use here, which only deviates by 4% from our final value, is enough for our purposes of fitting the data well, while keeping or approximating some basic features of the amplitude even outside the physical region.

In order to keep the data region reasonably centered within the conformal circle without distorting the uncertainty bands, we have found convenient to fix the constants that define the center of the conformal variable ω to the following values (see Appendix A)

$$\alpha = 1.15, \quad s_0 = (1.1\,\text{GeV})^2. \tag{77}$$

Table 2
Parameters of the elastic $S^{1/2}$-wave. In GeV^2 units.

Parameter	UFD	CFD
B_0	0.402 ± 0.006	0.403 ± 0.006
B_1	0.222 ± 0.031	0.173 ± 0.031
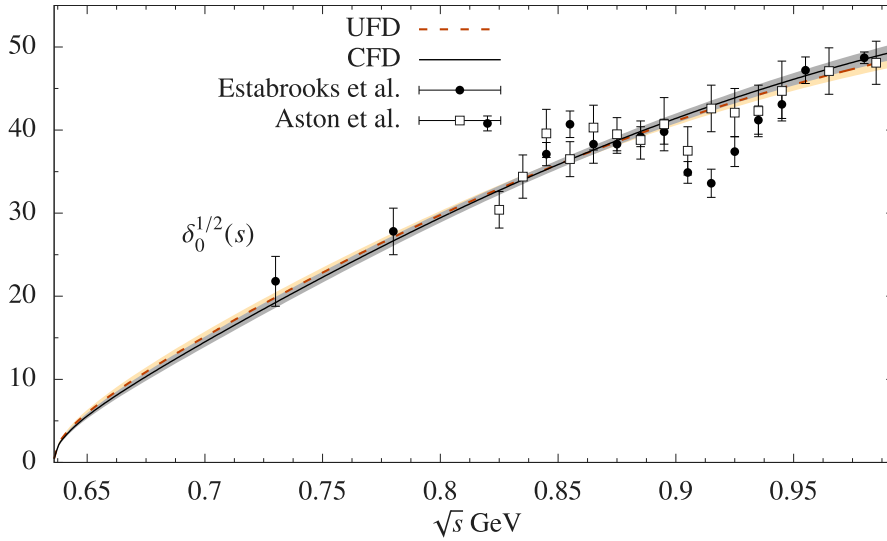
Fig. 21. $S^{1/2}(s)$ $\pi K \to \pi K$ partial wave. We show the UFD fit as a dashed line, compared to the final CFD result as a continuous line. The data shown comes from [6] (empty squares) and [5] (solid circles).

The Unconstrained Fits to Data (UFD) parameters are given in Table 2, and they are pretty similar to our original fit in [41].

The resulting phase and modulus of the $f_0^{1/2} + f_0^{3/2}/2$ combination can be seen as a dashed curve and a light-orange uncertainty band in Fig. 7. These are the data that we fit together with those of the $I = 3/2$ S-wave. Nevertheless, in this subsection we also provide in Fig. 21 the $\delta_0^{1/2}$ phase-shift in the elastic region. The "data" in this figure are not measured directly but are extracted from the previous isospin combinations using [5,6]. Note that, even if there is a considerable rise in the phase, it does not reach 90° below 1 GeV, and there is no clear sign of a resonance peak. This is the reason for the longstanding debate about the existence of a $\kappa/K_0^*(700)$ resonance. We will see in later sections that this shape together with dispersion relations requires the existence of a pole very deep in the complex plane that is identified with the very wide $\kappa/K_0^*(700)$ resonance.

Actually, our very simple UFD parameterization does have a $\kappa/K_0^*(700)$ pole in the second Riemann sheet, which can be obtained using Eqs. (75) above with Eqs. (21). It is located at: $\sqrt{s_p} = (651 \pm 14) - i(336 \pm 5)$ MeV, which is in the ballpark of the precise value obtained from dispersion relations in [47,97], as will be explained in Section 6.3. Thus, as it happened with the Adler zero, our simple UFD parameterization provides an approximation to another analytic feature of the amplitude in the non-physical region. Nevertheless, this is still a model-dependent extraction from a fit of the elastic region only which has not been constrained with dispersion relations. The rigorous and accurate model-independent extraction will be provided in Section 6.3.

Let us now turn to the parameterization of the $S^{1/2}$-wave in the inelastic region, i.e. for $s \geq (m_K + m_\eta)^2$. Once more we use the very same functional form we considered in [41], but with updated parameters due to our new fitting strategy. This parameterization follows the generic inelastic form of Eq. (70) discussed above, but for this particular case, it consists of two resonant forms S_1^r and S_2^r and a background S_0^b. The first one will accommodate the $K_0^*(1430)$ that was already discussed when we presented the S-wave data in Section 2.1.2. The second one is purely phenomenological, since $\sqrt{s_{r2}}$ will come out around 1.8 GeV, well above the maximum energy where we are going to check and/or impose dispersion relations. Therefore we will only see its low-energy tail and for us, it is more like a background contribution. However, it will give more flexibility to mimic the low tail of resonances heavier than 1.7 GeV in this channel, like the $K_0^*(1950)$, although not their precise position or parameters. Remember that above 1.84 GeV we will be using Regge theory, not partial waves. Thus, our $S^{1/2}$-wave parameterization reads:

$$f_0^{1/2}(s) = \frac{S_0^b S_1^r S_2^r - 1}{2i\sigma(s)},$$

(78)

Table 3
Parameters of the $S^{1/2}$ inelastic fit.

Parameters	UFD	CFD
ϕ_0	-0.08 ± 0.031 GeV^{-1}	-0.002 ± 0.031 GeV^{-1}
ϕ_1	4.64 ± 0.16 GeV^{-3}	4.65 ± 0.16 GeV^{-3}
a	-5.46 ± 0.03 GeV^{-2}	-5.53 ± 0.03 GeV^{-2}
b	8.1 ± 0.1 GeV^{-4}	8.2 ± 0.1 GeV^{-4}
c	-1.65 ± 0.04 GeV^{-2}	-1.62 ± 0.04 GeV^{-2}
$\sqrt{s_{r1}}$	1.401 ± 0.004 GeV	1.412 ± 0.004 GeV
$\sqrt{s_{r2}}$	1.813 ± 0.013 GeV	1.800 ± 0.013 GeV
e_1	1	1
e_2	0.179 ± 0.026	0.138 ± 0.026
G_1	0.443 ± 0.024 GeV	0.439 ± 0.024 GeV
G_2	0.32 ± 0.10 GeV	0.25 ± 0.10 GeV
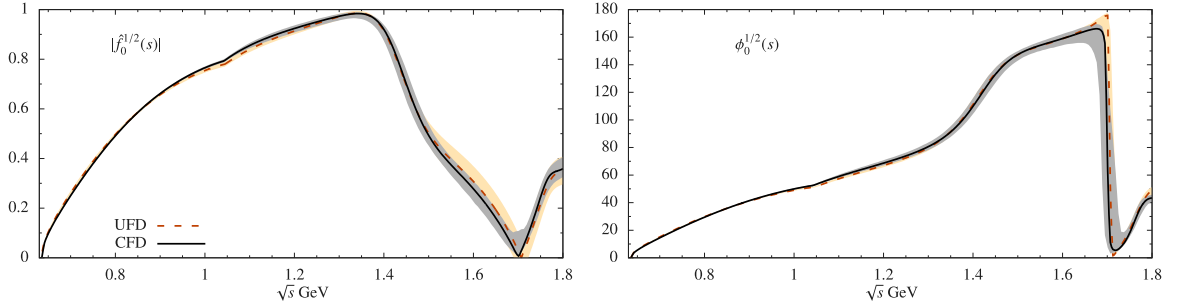
Fig. 22. $S^{1/2}$ partial wave UFD vs CFD parameterizations for the modulus (left panel) and the phase (right panel). Notice that both fits are fairly in the whole energy region.

where

$$S_0^b = \exp\left[2iq_{\eta K}(\phi_0 + \phi_1 q_{\eta K}^2)\right]. \tag{79}$$

For S_1^r we use Eq. (72) with

$$P_1(s) = (s_{r1} - s)\beta + e_1 G_1 \frac{p_1(q_{\pi K})}{p_1(q_{\pi K}^r)} \frac{q_{\pi K} - \hat{q}_{\pi K}}{q_{\pi K}^r - \hat{q}_{\pi K}}, \tag{80}$$

$$Q_1(s) = (1 - e_1)G_1 \frac{p_1(q_{\pi K})}{p_1(q_{\pi K}^r)} \frac{q_{\eta K}}{q_{\eta K}^r} \Theta_{\eta K}(s), \tag{81}$$

where $p_1(x) = 1 + ax^2 + bx^4$, $q_{ij}^r = q_{ij}(s_r)$, $\hat{q}_{ij} = q_{ij}((m_\eta + m_K)^2)$ and $\Theta_{\eta K}(s) = \Theta(s - (m_K + m_\eta)^2)$ is the step function at $K\eta$ threshold. In addition, for S_2^r we use Eq. (72) with

$$P_2(s) = e_2 G_2 \frac{p_2(q_{\pi K})}{p_2(q_{\pi K}^r)} \frac{q_{\pi K} - \hat{q}_{\pi K}}{q_{\pi K}^r - \hat{q}_{\pi K}}, \tag{82}$$

$$Q_2(s) = (1 - e_2)G_2 \frac{p_2(q_{\pi K})}{p_2(q_{\pi K}^r)} \frac{q_{\eta K}}{q_{\eta K}^r} \Theta_{\eta K}(s), \tag{83}$$

with $p_2(x) = 1 + cx^2$.

Since we have chosen to match the elastic and inelastic parameterizations at $K\eta$ threshold, we only need to demand continuity. This is ensured by defining $\beta \equiv 1/\cot\delta_0^{1/2}((m_K + m_\eta)^2)$, where the cotangent is now calculated from the elastic part, using Eq. (75).

All in all, the resulting fit parameters for the inelastic region parameterization are listed in Table 3.

In Fig. 22 we show both the modulus and phase of the $\hat{f}_0^{1/2} = |\hat{f}_0^{1/2}| \exp(i\phi_0^{1/2})$ partial wave from threshold up to 1.7 GeV. The UFD parameterization of this wave is represented by a dashed line and the corresponding orange band for its uncertainty. There we can see the wide structure attributed to the $\kappa/K_0^*(700)$ below 1 GeV, as well as the dominant feature around 1.4 GeV due to the $K_0^*(1430)$ resonance, whose fast increase in the phase is clearly seen between 1300 and 1500 MeV. By comparing with the measured combination $f_S \equiv f_0^{1/2} + f_0^{3/2}/2$ shown in Fig. 7, we see the appearance of a zero around 1.7 GeV, which is not seen in Fig. 7 due to the presence of the $f_0^{3/2}$ component.

Table 4
Parameters of the $P^{3/2}$-wave. In GeV^2 units.

Parameter	UFD	CFD
B_0	-9.19 ± 2.4	-8.39 ± 2.4
B_1	-3.2 ± 6.6	-2.4 ± 6.6
$\hat{s}$	0.57 ± 0.17	0.88 ± 0.17

4.1.3. P-waves

The data for these waves were discussed in Section 2.1.3. Let us describe here the specific details of our $I = 3/2$ and $I = 1/2$ parameterizations, which follow the generic form described in Section 4.1.1.

$P^{3/2}$ partial wave

Since no inelasticity has been observed for this wave, we use a purely elastic formalism. In this case, we have slightly modified our two-parameter conformal map in [41]. The reason is that as seen in Fig. 10, there are no scattering data below 1 GeV. When we did the two-parameter fit, the data were described nicely, but then the scattering length becomes negative. However, this is in disagreement with the sum rule obtained from fixed-t dispersion relations in [43], where it was found $m_\pi^3 a_1^{3/2} = (0.65 \pm 0.44) \, 10^{-3}$. Moreover, as we will see in Section 7.1.2, when calculating our own sum rules for this report we also find positive values for $a_1^{3/2}$, which is also the case of NLO and NNLO ChPT [85,131,231]. Moreover, we have found that a negative scattering length could not be accommodated by the very accurate P-wave HDR near threshold. Therefore, we have included a purely phenomenological additional factor, only relevant at low energies, to facilitate the phase-shift change of sign between threshold and the data region, i.e. the appearance of a zero of the amplitude so that we can also fit the sum rule in [43].

Of course, we still fix the α and s_0 parameters to the values we used in [41] and in the $S^{3/2}$ partial wave right above since they make the data to be centered within the conformal disk without producing unrealistic uncertainty bands. We take

$$\alpha = 1.4, \quad s_0 = (1.84 \, \text{GeV})^2. \tag{84}$$

All in all, our new parameterization reads

$$\cot \delta_1^{3/2}(s) = \frac{\sqrt{s}}{2q^3} \frac{s}{s - \hat{s}} \Big(B_0 + B_1 \omega(s) \Big). \tag{85}$$

The $\hat{s}$ parameter will be the energy where this amplitude becomes zero and the phase shift changes sign.

The fit parameters are given in Table 4 and the resulting phase shift is shown in Fig. 10 against the data as a dashed curve whose uncertainties are covered by the orange band. Note that the phase shift is tiny and positive near threshold, ensuring a very small but positive scattering length, it then crosses zero around 0.75 GeV and becomes negative, describing the existing scattering data, which lies above 1 GeV. The fitted $\chi^2/dof = 1.2$.

$P^{1/2}$ partial wave

In this case, we use the very same parameterization we introduced in [41], which follows the generic forms discussed in Section 4.1.1 above. However, we will slightly modify the choice of data to be fit in the elastic region, whereas we will keep the same choice in the inelastic region.

Let us start describing the fit to the elastic region, i.e. $s \leq (m_\eta + m_K)^2$, which, as seen in Fig. 11, is dominated by the $K^*(892)$. We use again the conformal parameterization of [41], with just three conformal parameters, namely:

$$\cot \delta_1^{1/2}(s) = \frac{\sqrt{s}}{2q^3} (m_r^2 - s) \Big(B_0 + B_1 \omega(s) + B_2 \omega(s)^2 \Big). \tag{86}$$

Note we have explicitly factorized $(m_r^2 - s)$ so that the phase crosses $\pi/2$ at the energy of the peak associated with the $K^*(892)$ resonance. At $s = m_r^2$ the phase shift reaches 90°. As explained in Appendix A, the constants α and s_0, which define the conformal variable, are fixed from the choice of the center of the expansion and the highest energy of the fit to be

$$\alpha = 1.15, \quad s_0 = (1.1 \, \text{GeV})^2. \tag{87}$$

There are several reasons to revisit our fitting strategy in the elastic regime. First, although the Estabrooks et al. [5] and Aston et al. [6] data in Fig. 11 may seem compatible, they are actually not, given their tiny statistical uncertainties. In order to estimate them, we have first followed what we did in [41]. Namely, whenever two points of these data sets are incompatible, we fit their average, taking as the uncertainty the combination of their statistical and systematic errors, the latter defined as half of their difference. This procedure cannot be followed for isolated points and, initially, we do not attach them any systematic uncertainty. We nevertheless fit the data. However, when we find some datum severely deviated from this first fit – typically by more than 3 σ – we add a systematic uncertainty which is half of its deviation from the fit. Then the procedure is iterated until a reasonable $\chi^2 \simeq 1$ is found. In practice, this is only
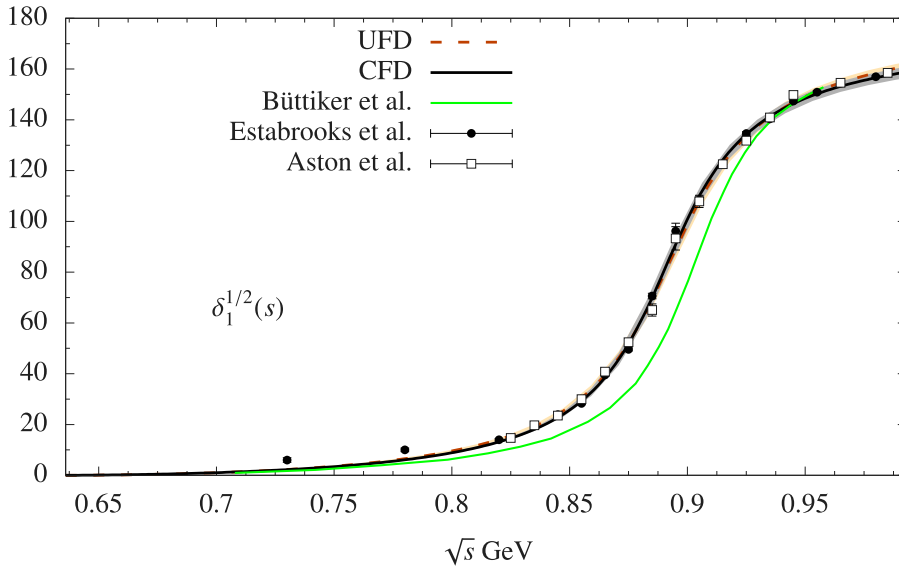
Fig. 23. $\pi K \to \pi K$ scattering phase shift for the $P^{1/2}$ partial wave, we show the UFD fit as a dashed line, compared to the final CFD result as a continuous line. The data shown comes from [6] (empty squares) and [5] (solid circles).

Table 5
Parameters of the $P^{1/2}$-wave. Note that in this case the B_i are dimensionless.

Parameter	UFD	CFD
B_0	0.970 ± 0.025	1.054 ± 0.025
B_1	0.56 ± 0.34	0.36 ± 0.28
B_2	2.66 ± 0.83	0.89 ± 0.83
m_r	0.8955 ± 0.0018 GeV	0.8946 ± 0.0018 GeV

needed for the two lowest-energy data from [5] seen as clear outliers in Fig. 11. Systematic uncertainties coming from this procedure were the only ones considered in [41]. However, isospin-violating effects are at least of the same order of statistical uncertainties. Measurements are done in the neutral channel but, due to our isospin-conserving formalism, we are considering the same mass for the neutral and charged $K^*(892)$. Hence, we will now include an explicit systematic uncertainty of $\simeq 1.8$ MeV in the m_r error bar. The rest of the data will be fitted as in [41]. Of course, we have checked that fitting the whole data set without including these systematic uncertainties worsens considerably the dispersive description, yielding large deviations for the scattering lengths compared to their sum-rule values.

The parameters of the unconstrained fit are listed in Table 5, and the resulting phase shift for the elastic region of the $P^{1/2}$ is shown in Fig. 23 as a dashed line with its corresponding orange uncertainty band. Note that, as seen in Fig. 10 the $P^{3/2}$ wave is almost compatible with zero in the elastic region, and therefore the $P^{1/2}$ phase shift shown in Fig. 23 is, for all means and purposes, the same as those for $f_P \equiv f_1^{1/2} + f_1^{3/2}/2$.

In Fig. 23 we also show, as a continuous green line, the solution of [43], obtained *solving* Roy–Steiner equations, which clearly deviates from all data. Furthermore, the mass and width associated to the $K^*(892)$ coming from this solution is at odds with all determinations listed in the RPP, by several standard deviations. It should be noticed that the [43] result for the P-wave is still remarkable because they do not use data in that region and it is a prediction obtained by solving Roy–Steiner equations with input from higher energies and other waves. Recall that in this report we are following the "data-driven" approach, i.e. using dispersion relations as constraints on data fits, instead of "solving" the equations. Thus, our parameterizations describe very well the existing scattering data. Moreover, they actually contain a pole in the second Riemann sheet at: $\sqrt{s_p} = (892 \pm 2) - i(28.6 \pm 1.1)$ MeV. From this, we see that the $K^*(892)$ width that we obtain is $\Gamma \sim 57$ MeV.

At this point, it is worth noting that in some experiments other than scattering [120,121,123,133,232,233], the $K^*(892)$ comes out somewhat narrower, between 45 and 50 MeV. For this reason, we have also studied an "alternative P-wave" in Appendix B, implementing a narrower $K^*(892)$, compatible with those other experiments. The relevant observation is that, when we impose the dispersive representation on our UFD, the width becomes narrower, whereas when we impose it on the "alternative" P-wave, the width becomes wider. Thus, at the very end, the constrained fits turn out to be very similar. That is why we only comment on one solution in the main text and leave the alternative in the appendix. Finally, note that the dispersive solution in [43] (green line in Fig. 23) does not resolve this issue with the width, because it has the wrong mass.

Table 6
$P^{1/2}$-wave parameters in the inelastic region.

Parameters	UFD	CFD
a_1	-2.07 ± 0.14 GeV^{-2}	-1.60 ± 0.14 GeV^{-2}
a_2	-2.11 ± 0.27 GeV^{-2}	-1.79 ± 0.27 GeV^{-2}
a_3	-1.34 ± 0.09 GeV^{-4}	-1.37 ± 0.09 GeV^{-4}
$\sqrt{s_{r1}}$	0.896 GeV (fixed)	0.896 GeV (fixed)
$\sqrt{s_{r2}}$	1.344 ± 0.013 GeV	1.347 ± 0.013 GeV
$\sqrt{s_{r3}}$	1.647 ± 0.005 GeV	1.657 ± 0.005 GeV
e_1	1 (fixed)	1 (fixed)
e_2	0.049 ± 0.008	0.067 ± 0.008
e_3	0.304 ± 0.016	0.324 ± 0.016
G_1	0.034 ± 0.005 GeV	0.049 ± 0.005 GeV
G_2	0.218 ± 0.043 GeV	0.212 ± 0.043 GeV
G_3	0.301 ± 0.018 GeV	0.292 ± 0.018 GeV

Let us then turn to the inelastic region. Once more, our parameterization will be exactly the one we obtained in [41], which is of the generic form discussed in Section 4.1.1. For this wave it has three resonant shapes to accommodate the upper tail of the $K^*(892)$, which is still felt in the inelastic region, the $K^*(1410)$, which couples very little to πK, and the $K^*(1680)$. As discussed in Section 2.1.3 the last two resonances are wide objects, and their pole positions are rather uncertain in the RPP. According to the RPP, the dominant branching ratios of the $K^*(1410)$ are 40% to $K^*(892)\pi$, 6,6% to $K\pi$ and less than 7% to $K\rho(770)$. For the $K^*(1680)$, these are 38.7% $K\pi$, 31.4% $K_\rho(770)$, 30% $K^*(892)\pi$ and only 1% $K\eta$. Remember that, in our formalism, we set the inelastic region to start at the $K\eta$ threshold, but all possible inelastic channels contribute to make $|S_\ell^I| < 1$, and we cannot separate individual contributions from each channel that makes $\eta(s)_\ell^I$ less than one. We only describe the total elasticity $\eta(s)$ as given by the fit to the modulus of the $K\pi$ amplitude. All in all, we write:

$$f_1^{1/2}(s) = \frac{S_1^r S_2^r S_3^r - 1}{2i\sigma(s)}, \tag{88}$$

where all the S_k^r are of the form in Eq. (72), with

$$P_1 = (s_{r1} - s)\beta + e_1 G_1 \frac{p_1(q_{\pi K})}{p_1(q_{\pi K}^r)} \frac{q_{\pi K}^2 - \hat{q}_{\pi K}^2}{(q_{\pi K}^r)^2 - \hat{q}_{\pi K}^2} \frac{q_{\pi K}}{q_{\pi K}^r},$$

$$P_{2,3} = e_{2,3} G_{2,3} \frac{p_{2,3}(q_{\pi K})}{p_{2,3}(q_{\pi K}^r)} \frac{q_{\pi K}^2 - \hat{q}_{\pi K}^2}{(q_{\pi K}^r)^2 - \hat{q}_{\pi K}^2} \frac{q_{\pi K}}{q_{\pi K}^r}, \tag{89}$$

$$Q_{1,2,3} = (1 - e_{1,2,3}) G_{1,2,3} \frac{p_{1,2,3}(q_{\pi K})}{p_{1,2,3}(q_{\pi K}^r)} \left(\frac{q_{\eta K}}{q_{\eta K}^r}\right)^3 \Theta_{\eta K}(s).$$

In addition,

$$p_i(q_{\pi K}) = 1 + a_i q_{\pi K}^2, \tag{90}$$

and $\Theta_{\eta K}(s) = \Theta(s - (m_K + m_\eta)^2)$ is the step function at $K\eta$ threshold. Again, in order to impose continuity at $K\eta$ threshold we have defined $\beta \equiv 1/\cot \delta_1^{1/2}((m_K + m_\eta)^2)$, where the cotangent is now calculated using the elastic parameterization in Eq. (86).

As we saw in Fig. 10, the $f_1^{3/2}$ amplitude is small but not entirely negligible in this region, so we always fit together the $f_1^{3/2}$ and $f_1^{1/2} + f_1^{3/2}/2$ combination. In Table 6 we provide the updated parameters of the inelastic parameterization. Note that, in the inelastic region, although we fit the same parameterization and data we used in [41], there is a small change in the parameters since we are matching with the elastic part, for which we changed slightly our fitting strategy.

The result of our UFD for $f_P = f_1^{1/2} + f_1^{3/2}/2$ in both the elastic and inelastic regions can be seen in Fig. 11, as a dashed line with its corresponding orange uncertainty band. Note the small contribution of the resonant shape around 1.4 GeV and a somewhat clearer resonant shape around 1650 MeV. The smallness of the partial-wave modulus in the 1.2 to 1.6 GeV region, translates into a rather large phase uncertainty in that interval. The fit to data in the elastic region has $\chi^2/dof = 1.1$ and $\chi^2/dof = 0.9$ in the inelastic one.

4.1.4. D-waves
For these waves, we keep the same parameterizations and the same fitting strategy and data that we used in [41].

$D^{3/2}$ partial wave
As we discussed in Section 2.1.4, and seen in Fig. 13, only data from [5] are available up to 1.74 GeV, which are shown together with our fits. No inelasticity has been observed and we will thus apply our generic elastic formalism with a

Table 7
Parameters of the $D^{3/2}$-wave. In GeV^4 units.

Parameter	UFD	CFD
B_0	-1.70 ± 0.12	-1.78 ± 0.12
B_1	-6.5 ± 1.7	-7.88 ± 1.7
B_2	-36.1 ± 8.7	-56.4 ± 8.7

Table 8
Parameters of the $D^{1/2}$ fit.

Parameters	UFD	CFD
ϕ_0	2.17 ± 0.26 GeV^{-5}	3.05 ± 0.26 GeV^{-5}
ϕ_1	-12.1 ± 1.7 GeV^{-5}	-16.6 ± 1.7 GeV^{-5}
$\sqrt{s_{r1}}$	1.446 ± 0.002 GeV	1.453 ± 0.002 GeV
e_1	0.466 ± 0.006	0.455 ± 0.006
G_1	0.220 ± 0.010 GeV	0.256 ± 0.010 GeV
a	-0.53 ± 0.16 GeV^{-2}	-0.82 ± 0.16 GeV^{-2}

conformal mapping as in Eq. (65). We found that three terms are enough to get a good χ^2 fit and we write

$$\cot\delta_2^{3/2}(s) = \frac{\sqrt{s}}{2q^5}\left(B_0 + B_1\omega(s) + B_2\omega(s)^2\right), \tag{91}$$

where the parameters α and s_0 are equal to those of the S and P $I = 3/2$ partial waves, namely $\alpha = 1.4$, $s_0 = (1.84\,\text{GeV})^2$. The resulting fit parameters are exactly the same as in [41], but for the sake of completeness we repeat them here in Table 7. The resulting UFD curve can be seen in Fig. 13, as a dashed line with an orange uncertainty band, without any remarkable feature except for its smallness. Actually, most studies neglect this wave.

$D^{1/2}$ partial wave

As for the S and P-waves, the $I=1/2$ D-wave is only measured together with the $I=3/2$-wave in the $f_D \equiv f_2^{1/2} + f_2^{3/2}/2$ combination. However, we have seen that the $D^{3/2}$ is minuscule and overwhelmed by the $D^{1/2}$ contribution. The latter is dominated by the $K_2^*(1430)$ resonance, whose branching ratio to πK is approximately 50%, but also has smaller although significant decay branching ratios to $K^*(892)\pi$ and $K\rho(770)$. The centrifugal barrier suppression makes this wave very small until this resonance is felt. Hence, it is most convenient to use our generic inelastic formalism, discussed in Section 4.1.1 above, in our whole fitting range. As we found in [41], it is enough to consider a non-resonant background and a resonant-like form, to write:

$$f_2^{1/2} = \frac{S_0^b S_1^r - 1}{2i\sigma(s)}, \tag{92}$$

where the background term is

$$S_0^b = e^{2ip(s)}, \tag{93}$$

with

$$p(s) = \phi_0 q_{\eta K}^5 \Theta_{\eta K}(s) + q_{\eta' K}^5(\phi_1 + \phi_2 q_{\eta' K}^2)\Theta_{\eta' K}(s),$$

and $\Theta_{ab} = \Theta(s - (m_a + m_b)^2)$. The resonant term for the $K_2^*(1430)$ shape, is written as

$$S_1^r = \frac{s_{r1} - s + i(P_1 - Q_1)}{s_{r1} - s - i(P_1 + Q_1)}, \tag{94}$$

$$P_1 = e_1 G_1 \frac{p_1(q_{\pi K})}{p_1(q_{\pi K}^r)}\left(\frac{q_{\pi K}}{q_{\pi K,r}}\right)^5,$$

$$Q_1 = (1 - e_1)G_1 \frac{p_1(q_{\pi K})}{p_1(q_{\pi K}^r)}\left(\frac{q_{\eta K}}{q_{\eta K,r}}\right)^5 \Theta_{\eta K}(s),$$

with $p_1(q_{\pi K}) = 1 + aq_{\pi K}^2$. Note that here we parameterize our inelasticity allowing for two possible cusps due to the sharp two-particle thresholds of $K\eta$ and $K\eta'$.

For our unconstrained fit, we get exactly the same parameters we found in [41], listed here in Table 8 for completeness. The resulting curves can be seen as a dashed line in Fig. 14 with its corresponding orange uncertainty band attached. The shape of the $K_2^*(1430)$ is evident and well reproduced. The uncertainties are rather small except beyond 1.6 GeV where the two existing data sets separate significantly.

Table 9
Parameters of the $F^{1/2}$-wave.

Parameters	UFD	CFD
$\sqrt{s_{r1}}$	1.801 ± 0.013 GeV	1.840 ± 0.013 GeV
e_1	0.181 ± 0.006	0.173 ± 0.006
G_1	0.47 ± 0.05 GeV	0.60 ± 0.05 GeV
a	-0.88 ± 0.10 GeV^{-2}	-1.06 ± 0.10 GeV^{-2}

4.1.5. F-waves

As we saw in Section 2.1.5 there are no measurements of the $F^{3/2}$-wave below 2.5 GeV and we will neglect it. For all means and purposes the data in Fig. 15 is just given by the $F^{1/2}$-wave, showing a clear signal for a $K_3^*(1780)$ resonance, whose main branching ratios are roughly 30% to $K\rho(770)$ and around 20% both to πK and $K^*(892)\pi$. Note that scattering data have only been measured above 1.5 GeV due to the large kinematic suppression. We will thus use, as in [41], an inelastic formalism dominated by that resonance. Namely

$$f_3^{1/2} = \frac{S_1^r - 1}{2i\sigma(s)}, \tag{95}$$

with

$$S_1^r = \frac{s_{r1} - s + i(P_1 - Q_1)}{s_{r1} - s - i(P_1 + Q_1)}, \tag{96}$$

$$P_1 = e_1 G_1 \frac{p_1(q_{\pi K})}{p_1(q_{\pi K}^r)} \left(\frac{q_{\pi K}}{q_{\pi K,r}}\right)^7,$$

$$Q_1 = (1 - e_1)G_1 \frac{p_1(q_{\pi K})}{p_1(q_{\pi K}^r)} \left(\frac{q_{\eta K}}{q_{\eta K,r}}\right)^7 \Theta_{\eta K}(s).$$

Here, $p_1(q_{\pi K}) = 1 + a q_{\pi K}^2$ and $\Theta_{\eta K}(s) = \Theta(s - (m_\eta + m_K)^2)$.

Since the data sample and the parameterization are the same, the UFD parameters for this wave are exactly those we obtained in [41], listed again here in Table 9, for completeness. The resulting curves can be seen as dashed lines and their corresponding orange uncertainty bands in Fig. 15. The resonant shape of the $K_3^*(1780)$ is nicely reproduced. The uncertainty band is somewhat larger than for other waves because the data error bars are also somewhat larger.

4.2. $\pi\pi \to K\bar{K}$ Unconstrained Fits to Data

Let us now consider the parameterization of the t-channel $\pi\pi \to K\bar{K}$. Except for the g_1^1 partial wave, all other $\pi\pi \to K\bar{K}$ partial-wave parameterizations we review here are those we introduced recently in our Roy–Steiner dispersive analysis [42]. Our main goal with the modifications in g_1^1 is to improve the description of the uncertainties associated with the data and make it flexible enough to achieve the refined level of accuracy we reach in this review.

Contrary to the $\pi K \to \pi K$ case, which had many resonant and non-resonant waves as well as elastic and inelastic cases, for $\pi\pi \to K\bar{K}$ we only need to fit three partial waves, g_0^0, g_1^1 and g_2^0, in the inelastic regime. In general, we will describe them with phenomenological but elaborated combinations of Breit–Wigner-like forms, whose shape is clearly noticeable in the data. The only one treated differently is the g_0^0 whose difficulty lies in the existence of conflicting data sets that cover different energy regions. Also, the presence and parameters of some resonances there, like the $f_0(1370)$, is still somewhat controversial. Thus we have avoided resonant shapes in favor of a piece-wise but continuous and differentiable parameterization in terms of polynomials. Let us start describing this wave first.

4.2.1. g_0^0 partial wave

We saw in Fig. 16 that there are data in the whole region of interest for both the modulus $|g_0^0|$ and the phase ϕ_0^0. The data sets extend from $K\bar{K}$ threshold up to $t \simeq 2.4$ GeV, but we do not fit that whole region because from 2 GeV we will use Regge parameterizations.

For the ϕ_0^0 phase we have already shown that, due to Watson's theorem, only one set of data makes sense. However, two sets of incompatible data can be studied for the modulus. Thus, we will provide two alternative UFD parameterizations for $|g_0^0|$, both sharing the same UFD parameterization for the ϕ_0^0 phase. Moreover, the applicability of $\pi\pi \to K\bar{K}$ dispersion relations only reaches 1.47 GeV, and this is why in [41] we decided to parameterize our amplitudes by a two-piece function defined differently in the two regions of the inelastic regime explained in Section 2.2.1. In Region I, Roy–Steiner equations will be used to test or constrain our parameterization, whereas in Region II amplitudes are just used as input for dispersion relations.

In order to parameterize the partial wave on each region, we will make use of Chebyshev polynomials, because they are simple and, in practice, yield very low correlations among their parameters. They are defined as:

$$p_0(x) = 1, \quad p_1(x) = x,$$

Table 10
Parameters of ϕ_0^0 in the inelastic region. Note there is just one ϕ_0^0 UFD common to the two UFD$_B$ and UFD$_C$ for $|g_0^0|$. However, once we constrain the fits there are two sets of parameters for the ϕ_0^0 CFD$_B$ and CFD$_C$.

Parameter	UFD	CFD$_B$	CFD$_C$
B_1	23.6 ± 1.3	22.6 ± 1.3	24.0 ± 1.3
B_2	29.4 ± 1.3	28.1 ± 1.3	29.5 ± 1.3
B_3	0.6 ± 1.6	1.9 ± 1.6	0.7 ± 1.6
C_1	34.3932 fixed	29.2374 fixed	27.6328 fixed
C_2	4.4 ± 2.6	4.8 ± 2.6	4.1 ± 2.6
C_3	-32.9 ± 5.2	-29.3 ± 5.2	-29.1 ± 5.2
C_4	-16.0 ± 2.2	-12.4 ± 2.2	-12.6 ± 2.2
C_5	7.4 ± 2.4	8.9 ± 2.4	8.5 ± 2.4

$$p_{n+1}(x) = 2x p_n(x) - p_{n-1}(x). \tag{97}$$

Thus we first map each energy region $i = I, II$ into the $x \in [-1, 1]$ interval through the linear transformation

$$x_i(t) = 2 \frac{\sqrt{t} - \sqrt{t_{min,i}}}{\sqrt{t_{max,i}} - \sqrt{t_{min,i}}} - 1. \tag{98}$$

Note that $p_n(1) = 1$ and $p_n(-1) = (-1)^n$, for all n, which will be used to ensure a smooth matching at $\sqrt{s} = 1.47$ GeV, i.e. between the two pieces describing regions I and II, up to and including the first derivative (although only for the central value of the derivative). Between the elastic and inelastic regions, the matching at t_K only ensures continuity, thus allowing for a proper cusp behavior.

Now, for the ϕ_0^0 phase, our parameterization is just

$$\phi_0^0(t) = \begin{cases} \sum_{n=0}^{3} B_n p_n(x_I(t)), & \text{Region I,} \\ \sum_{n=0}^{5} C_n p_n(x_{II}(t)), & \text{Region II,} \end{cases} \tag{99}$$

where we need to impose

$$B_0 = \delta_0^{(0)}(t_K) + B_1 - B_2 + B_3, \tag{100}$$
$$C_0 = \phi_0^0(t_{max,I}) + C_1 - C_2 + C_3 - C_4 + C_5, \tag{101}$$

to ensure, respectively, continuity at $K\bar{K}$ threshold as well as between Regions I and II. Here, $\delta_0^{(0)}(t)$ is the $\pi\pi \to \pi\pi$ phase shift that we take from [48], leading to $\delta_0^{(0)}(t_K) = (226.5 \pm 1.3)°$. Continuity is enough at t_K since there is a cut due to the opening of a new threshold. However, we will also impose a continuous derivative for the central value of our fit between Regions I and II, and thus the C_1 parameter is also fixed numerically. The parameters of the fit are given in Table 10. The total $\chi^2/dof = 1.5$, which comes slightly larger than one due to the incompatibilities between data sets. Consequently, the uncertainties of the parameters in Table 10 have been re-scaled by a factor $\sqrt{1.5}$.

In contrast to ϕ_0^0, which only had one data set, for the modulus $|g_0^0|$ we want to provide parameterizations for the two incompatible sets of data. Hence, we have obtained two Unconstrained Fits to Data (UFD) in Region I: The one fitting Brookhaven-II data [9] is called UFD$_B$, whereas the one fitting the "Combined" Argonne [7] and Brookhaven-I [8] data is labeled UFD$_C$. Both of them use the same data in Region II and thus they are almost identical there, although with slightly different parameters due to the different matching with Region I. All in all, we use:

$$|g_0^0(t)| = \begin{cases} \sum_{n=0}^{3} D_n p_n(x_I(t)), & \text{Region I,} \\ \sum_{n=0}^{4} F_n p_n(x_{II}(t)), & \text{Region II,} \end{cases} \tag{102}$$

where, in order to ensure continuity between the two regions, we impose:

$$F_0 = |g_0^0(t_{max,I})| + F_1 - F_2 + F_3 - F_4. \tag{103}$$

In addition, F_1 is fixed numerically to secure a continuous derivative for the central value.

The parameters for $|g_0^0|$ of both the UFD$_B$ and UFD$_C$ are listed in Tables 11 and 12, respectively. Let us remark that both have $\chi^2/dof \sim 1$. Their respective curves are shown as dashed lines with orange uncertainty bands in Fig. 16.

4.2.2. g_1^1 partial wave

For this wave, we will keep the very same parameterization we used in [42], which we actually took from [43,234]. However, we will consider some minor changes in the way we implement the fit to the g_1^1 partial wave, although we will not modify the data choice, shown in Fig. 17. These minor changes are due to the way we added systematic uncertainties

Table 11
Parameters of the UFD$_B$ and CFD$_B$ fits to $|g_0^0|$.

Parameter	UFD$_B$	CFD$_B$
D_0	0.588 ± 0.01	0.591 ± 0.01
D_1	-0.380 ± 0.01	-0.339 ± 0.01
D_2	0.12 ± 0.01	0.13 ± 0.01
D_3	-0.09 ± 0.01	-0.12 ± 0.01
F_1	-0.04329 fixed	-0.04312 fixed
F_2	-0.008 ± 0.009	-0.008 ± 0.009
F_3	-0.028 ± 0.007	-0.034 ± 0.007
F_4	0.026 ± 0.007	0.038 ± 0.007

Table 12
Parameters of the UFD$_C$ and CFD$_C$ fits to $|g_0^0|$.

Parameter	UFD$_C$	CFD$_C$
D_0	0.462 ± 0.008	0.446 ± 0.008
D_1	-0.267 ± 0.013	-0.236 ± 0.013
D_2	0.11 ± 0.01	0.10 ± 0.01
D_3	-0.078 ± 0.009	-0.087 ± 0.009
F_1	-0.04153 fixed	-0.03765 fixed
F_2	-0.010 ± 0.008	-0.016 ± 0.008
F_3	-0.023 ± 0.007	-0.023 ± 0.007
F_4	0.021 ± 0.006	0.028 ± 0.006

in the original fit of [42], which we have decided to improve here. In our work, [42] we included these systematic uncertainties multiplying the errors of all data points by an overall factor so that we got a global $\chi^2/dof \sim 1$ as is customary. However, most of the χ^2/dof is coming from the phase in the inelastic region, where, as seen in Fig. 17, the data are clearly of less quality. Thus, when multiplying all data by the same common factor we were producing an overestimated uncertainty in the other regions, which had a decent χ^2/dof from the start. Hence, here we will only multiply the uncertainties of the phase data by a factor of ~ 1.4 in the inelastic region, where a fit without any systematic uncertainties would yield $\chi^2/dof \sim 2$.

Apart from updating our strategy to estimate systematic uncertainties, we use the same functional form as in [42,43, 234,235]

$$g_1^1(t) = \frac{C}{\sqrt{1 + r_1 q_\pi^2(t)}\sqrt{1 + r_1 q_K^2(t)}} \left\{ \overline{BW}(t)_\rho + (\beta + \beta_1 q_K^2(t))\overline{BW}(t)_{\rho'} + (\gamma + \gamma_1 q_K^2(t))\overline{BW}(t)_{\rho''} \right\}.$$

This parameterization is devised to accommodate the three vector resonances $\rho(770)$, $\rho' = \rho(1450)$, $\rho'' = \rho(1700)$, by means of a combination of three Breit–Wigner-like shapes:

$$\overline{BW}(t)_V = \frac{m_V^2}{m_V^2 - t - i\Gamma_V \sqrt{t} \frac{2G_\pi(t) + G_K(t)}{2G_\pi(m_V^2)}},$$

$$G_P(t) = \sqrt{t} \left(\frac{2q_P(t)}{\sqrt{t}} \right)^3. \tag{104}$$

Here m_V and Γ_V stand for the "Breit–Wigner" mass and width of the resonances under consideration, which are not necessarily those obtained from poles within a rigorous dispersive approach. For our purposes they are just phenomenological parameters, whose values, together with those of the other parameters are listed in Table 13.

The resulting curves of our unconstrained fit to data are shown in Fig. 17 as dashed lines with an orange uncertainty band. Note that our fit also describes the phase ϕ_1^1 in the "unphysical" region below the $K\bar{K}$ threshold, which, given that only two-pions are observed there, is nothing but the $\pi\pi \to \pi\pi$ phase shift according to Watson's theorem. This "unphysical" region is completely dominated by the $\rho(770)$ resonance. Observe that the uncertainties of our fit are fairly small except for the phase above 1.4 GeV.

4.2.3. g_2^0 partial wave

For this wave, we keep the same parameterization, data sample, and fit strategy for the unconstrained fit that we followed in [42]. Our UFD is therefore exactly the same, but we provide it here again for completeness. The CFD will of course change because here we will use the dispersive constraints simultaneously on $\pi K \to \pi K$ and $\pi\pi \to K\bar{K}$, instead of just the latter, as we did in [42]. In practice, our [42] parameterization had two pieces. One piece, providing both the modulus and the phase for the "physical region" above t_K, where actual $\pi\pi \to K\bar{K}$ data exist, and another piece, just for the phase below t_K. The latter, due to Watson's theorem, is given by the isoscalar angular momentum-2 phase shift of $\pi\pi \to \pi\pi$ scattering, for which we take the parameterization obtained in the dispersive analysis of [48].

Table 13
Parameters of the g_1^1 wave. Masses and widths are given in GeV whereas, C, β_1, γ_1 and r_1 are given in GeV^{-2}.

Parameter	UFD	CFD
m_ρ	0.7759 ± 0.0010	0.7756 ± 0.0010
Γ_ρ	0.1517 ± 0.0016	0.1509 ± 0.0016
$m_{\rho'}$	1.440 ± 0.031	1.464 ± 0.031
$\Gamma_{\rho'}$	0.310 ± 0.016	0.339 ± 0.016
$m_{\rho''}$	1.72	1.72
$\Gamma_{\rho''}$	0.25	0.25
C	1.29 ± 0.08	1.35 ± 0.08
r_1	4.54 ± 0.64	3.84 ± 0.64
β	-0.163 ± 0.004	-0.167 ± 0.004
β_1	0.36 ± 0.02	0.35 ± 0.02
γ	0.09 ± 0.02	0.08 ± 0.02
γ_1	-0.03 ± 0.03	0.06 ± 0.03

We start describing the physical region and recall that, as discussed in Section 2.1.4, the main resonances in this partial wave are the $f_2(1270)$ and $f_2'(1525)$, which are well established. Actually, there is a clear peak for the former in the Brookhaven II data we showed in Fig. 18 and a hint of the latter, which appears as a hunchback to the right of the main peak. However, the $f_2'(1525)$ mass and width used in the Brookhaven II and III fits are at odds with their present values. This will be amended in our fits. In addition, we have considered an additional $f_2(1810)$, already introduced in the Brookhaven II and III analyses [9,142], contrary to what the Brookhaven collaboration did in [236]. Nevertheless, the reader should keep in mind that our dispersive representations do not reach such high energies. Thus, for us, this 1.8 GeV resonance is just a convenient way of parameterizing the rise in the data on $|g_2^0|$ starting around 1.8 GeV. However, this choice implies a particular shape for the phase at those energies, for which there are no data.

We then use a phenomenological formula, rather similar to the one used for g_1^1, given by

$$\hat{g}_2^0(t) = \frac{C\sqrt{[q_\pi(t)q_K(t)]^5}}{\sqrt{t}\sqrt{1+r_2^2 q_\pi^4(t)}\sqrt{1+r_2^2 q_K^4(t)}}\left\{e^{i\phi_1}BW(t)_1 + \beta e^{i\phi_2}BW(t)_2 + \gamma e^{i\phi_3}BW(t)_3\right\}, \tag{105}$$

with

$$BW(t)_T = \frac{m_T^2}{m_T^2 - t - im_T\Gamma_T(t)}, \tag{106}$$

$$\Gamma_T(t) = \Gamma_T\left(\frac{q_T(t)}{q_T(m_T^2)}\right)^5 \frac{m_T}{\sqrt{t}}\frac{D_2(r\,q_T(m_T^2))}{D_2(r\,q_T(t))},$$

where $D_2(x) = 9 + 3x^2 + x^4$ provides the familiar Blatt–Weisskopf barrier factor for $\ell = 2$, with a typical $r = 5\,\text{GeV}^{-1} \simeq 1\,\text{fm}$. The index $T = 1, 2, 3$ refers to the $f_2(1270)$, $f_2'(1525)$ and $f_2(1810)$ respectively.

Concerning the unphysical region, $t < t_K$, the relevant observation is that, since the contribution of the four pion state is negligible, for all means and purposes $\pi\pi$ scattering is elastic there. Then Watson's theorem allows us to identify $\phi_2^0 = \delta_2^{(0)}$, where $\delta_2^{(0)}$ is the $\pi\pi$-scattering phase shift. At first, one could think about taking directly the result obtained in the $\pi\pi \to \pi\pi$ dispersive analysis in [48]. However, we want a continuous matching with our parameterization. Thus, as we did in [41] we just fit $\delta_2^{(0)}$ to the CFD result from [48], using a truncated conformal expansion similar to that in [48] but with one more parameter B_2 that is then fixed to ensure the continuous matching of g_2^0 at $K\bar{K}$ threshold. Namely:

$$\cot\phi_2^0(t) = \frac{f^{1/2}}{2q_\pi^5}\left(m_{f_2(1270)}^2 - t\right)m_\pi^2\left(B_0 + B_1 w(t) + B_2 w(t)^2\right),$$

$$w(t) = \frac{\sqrt{t} - \sqrt{t_0 - t}}{\sqrt{t} + \sqrt{t_0 - t}}, \quad t_0^{1/2} = 1.05\,\text{GeV}, \tag{107}$$

where

$$B_2\,\omega(t_K)^2 = \frac{q_\pi^5(t_K)\cot(\phi_2^0(t_K))}{m_K\left(m_{f_2(1270)}^2 - t_K\right)m_\pi^2} - B_0 - B_1\,\omega(t_K), \tag{108}$$

has been fixed by continuity with the piece above t_K in Eq. (105).

Let us note that using these parameterizations to fit the data as such, we would reproduce with remarkable accuracy the description of the CFD phase-shift in [48], whereas in the inelastic part we would obtain a $\chi^2/dof = 1.4$. Looking at Fig. 18, this is not really due to the existence of any other physical feature but rather it seems that there is some small systematic uncertainty. Thus, as we did in [42], we have re-scaled the data uncertainties in that region by a factor of

Table 14
Parameters of the g_2^0 wave.

Parameter	UFD	CFD
$m_{f_2(1270)}$	1.271 ± 0.0036 GeV	1.272 ± 0.0036 GeV
$m_{f_2'(1525)}$	1.522 ± 0.005 GeV	1.522 ± 0.005 GeV
$m_{f_2(1810)}$	1.806 ± 0.017 GeV	1.800 ± 0.017 GeV
$\Gamma_{f_2(1270)}$	0.187 ± 0.009 GeV	0.184 ± 0.009 GeV
$\Gamma_{f_2'(1525)}$	0.108 ± 0.016 GeV	0.116 ± 0.016 GeV
$\Gamma_{f_2(1810)}$	0.201 ± 0.028 GeV	0.180 ± 0.028 GeV
$\phi_{f_2(1270)}$	-0.049 ± 0.015	-0.081 ± 0.015
$\phi_{f_2'(1525)}$	2.62 ± 0.16	2.58 ± 0.16
$\phi_{f_2(1810)}$	-0.72 ± 0.16	-0.88 ± 0.16
B_0	12.5 ± 0.4	12.4 ± 0.4
B_1	10.3 ± 1.0	13.2 ± 1.0
C	1.82 ± 0.09 GeV^{-2}	1.80 ± 0.09 GeV^{-2}
r_2^2	6.68 ± 0.72 GeV^{-4}	6.85 ± 0.72 GeV^{-4}
β	0.070 ± 0.016	0.083 ± 0.016
γ	0.093 ± 0.02	0.103 ± 0.02

~1.2 and refitted. In Table 14 we provide the parameters obtained when fitting together the inelastic part and the CFD phase-shift in [48]. Once again, the latter is reproduced very nicely, but, in addition, in [42] we checked that the phase in the elastic regime is also compatible within uncertainties with the dispersive analysis of the $\pi\pi$ D-wave using Roy and GKPY equations in [184]. In the inelastic region, our uncertainty band covers quite conservatively the data collection.

The resulting curves for our UFD D-wave parameterization are shown in Fig. 18 as a dashed line with an orange uncertainty band. Note that for the phase we are also giving a few points obtained from $\pi\pi \to \pi\pi$ scattering by Hyams et al. [152]. Of course, the phase in the inelastic region is a pure prediction based on our assumption that it is dominated by the effect of resonances that are fitted to describe the data on the modulus. We will see that this assumption fares reasonably well against the dispersive checks.

Let us remark once again that, as can be seen in Fig. 18 the original fit to data by the Brookhaven collaboration [236] does not match continuously with the $\pi\pi$ D-wave phase shift at the $K\bar{K}$ threshold, thus violating Watson's theorem. On top of that, they did not include the $f_2(1810)$ resonance in their first analysis, which produces a different phase at higher energies. Our $g_2^0(t)$ does include all these features instead. At this point, it is worth noticing that the Brookhaven collaboration measured $|g_0^0 - g_2^0|$ and extracted their g_0^0 assuming their g_2^0 model. It is therefore pertinent to reconsider the extraction of $g_0^0(t)$ partial wave phase. This is the reason why we give in Appendix C an alternative solution for $\phi_0^0(t)$, including its dispersive constrained results. Fortunately, the effect of this wave on the other wave dispersive constraints is very small, and using our main fit or the alternative one is irrelevant. For the g_0^0 dispersive treatment, the differences between the main UFD fit or the alternative one appear at high energies, beyond the applicability range of our dispersion relations, which barely change their output. This is why the alternative solution is relegated to the appendix.

4.2.4. $\pi\pi \to K\bar{K}$ partial waves with $\ell > 3$

These waves are going to be just input for our dispersion relations and their contributions will be in general small. As commented in Section 2.2.4, there are no scattering data and thus, as we did in [42], we will simply use Breit–Wigner descriptions with the averaged parameters listed in the RPP. In particular, for the $g_3^1(t)$ wave we will consider a single $\rho_3(1690)$ resonance, whereas for the $\ell = 4$ partial wave, we consider the $f_4(2050)$. Nevertheless, the latter will only be input for the $g_2^0(t)$ dispersion relation since its contribution is completely negligible for the $g_0^0(t)$.

4.3. High-energy region. Regge parameterizations

The dispersive integrals we have seen in Section 3 extend to infinite energy, although the integrands will be sufficiently suppressed at large energies to make them converge. However, we need another description, since at high energies the partial-wave expansion is no longer valid. From the theoretical point of view this is because, strictly speaking, it is a low-energy expansion. From the practical point of view, it is also because we only have data on a few partial waves with the lowest angular momentum and not too high energies. In particular, there are no data for $I = 3/2$ $\pi K \to \pi K$ scattering above 1.74 GeV, although these waves present a rather monotonous behavior and it seems fine to extrapolate them a little further. For this reason, we have chosen 1.84 GeV, as done in [41], as the energy beyond which we will not use $\pi K \to \pi K$ partial waves anymore. Concerning $\pi\pi \to K\bar{K}$ scattering, we have chosen to stop using partial waves at 2 GeV. It is true that data for the g_0^0 and g_2^0 waves reaches as high as 2.4 GeV, however, the g_1^1 scattering data ends at 1.6 GeV. Nevertheless, since the $\rho''(1700)$ is well established in the RPP and has a 250 MeV width, we think we have a fairly reasonable description of all waves up to those 2 GeV.

The problem now is that no direct high-energy experimental data on $\pi\pi \to K\bar{K}$ nor on $\pi K \to \pi K$ exist. Notwithstanding, the high energy behavior of both processes can be confidently predicted from the factorization of Regge amplitudes of other hadron-scattering processes. In this regime, hadron–hadron scattering is understood as the

contribution of the so-called Pomeron exchange (a transfer of momentum and no other quantum number, fairly well understood in terms of colorless exchanges of gluons) or families of resonances exchanged in the t-channel, called Reggeons. For pedagogical introductions we recommend [237–239]. This is a well-established approach that we already used in [41,42]. In particular, for $\pi K \to \pi K$, which at high energies and low t is dominated by the exchange of non-strange Reggeons, we will follow our analysis in [41] and use here the Regge-model factorization analysis presented in [143], although later on updated in [41,48]. In contrast, to describe $\pi\pi \to K\bar{K}$ above 2 GeV, which involves the exchange of strange Reggeons, we will follow our analysis in [42] and use the asymptotic forms of the Veneziano model [144,240–242], with the updated parameters in [43], but relaxing the degeneracy with the ρ trajectory assumed for simplicity in [143].

High-energy Regge parameterizations for $\pi K \to \pi K$

For the $\pi K \to \pi K$ symmetric amplitude we have both the Pomeron $P(s,t)$ and the f_2-Reggeon, or $P'(s,t)$, exchanges:

$$\text{Im } F_{\pi K}^+(s,t) = \frac{\text{Im } F_{\pi K}^{(I_t=0)}(s,t)}{\sqrt{6}} = \frac{4\pi^2}{\sqrt{6}} f_{K/\pi} \left[P(s,t) + rP'(s,t) \right]. \tag{109}$$

Since we follow the notation in [143] the Regge P and P' amplitudes refer to $\pi\pi \to \pi\pi$ scattering and for simplicity absorb the $\pi\pi-$Reggeon factor

$$\begin{aligned}
P(s,t) &= \beta_P \psi_P(t) \alpha_P(t) \frac{1+\alpha_P(t)}{2} e^{\hat{b}t} \left(\frac{s}{s'}\right)^{\alpha_P(t)}, \\
P'(s,t) &= \beta_{P'} \psi_{P'}(t) \frac{\alpha_{P'}(t)(1+\alpha_P(t))}{\alpha_{P'}(0)(1+\alpha_P(0))} e^{\hat{b}t} \left(\frac{s}{s'}\right)^{\alpha_{P'}(t)}, \\
\alpha_P(t) &= 1 + t\alpha'_P, \qquad \psi_P = 1 + c_P t, \\
\alpha_{P'}(t) &= \alpha_{P'}(0) + t\alpha'_{P'}, \qquad \psi_{P'} = 1 + c_{P'} t.
\end{aligned} \tag{110}$$

Factorization allows us then to convert one $\pi\pi-$Reggeon vertex into a $KK-$Reggeon vertex by multiplying by the $f_{K/\pi}$ factor, as we have done in Eq. (109). The constant r is related to the branching ratio of the $f_2(1270)$ resonance to $K\bar{K}$ instead of $\pi\pi$.

Just for illustration, the extraction of $f_{K/\pi}$ and r is particularly simple from combinations of data on total cross sections for proton–proton, proton–antiproton, K^+-proton, and K^--proton, which we show in Fig. 24. Then one should recall that the optical theorem tells us that the total cross section is proportional to the imaginary part of the *forward*, i.e. $t=0$, amplitude. Hence, following [143], for large s, it is possible to write:

$$\sigma_{pp} + \sigma_{p\bar{p}} \simeq \frac{4\pi^2}{\lambda^{1/2}(s, m_p^2, m_p^2)} f_{N/\pi}^2 \left[P(s,0) + (1+\epsilon)P'(s,0) \right], \tag{111}$$

$$\sigma_{K^+p} + \sigma_{K^-p} \simeq \frac{4\pi^2}{\lambda^{1/2}(s, m_K^2, m_p^2)} f_{N/\pi} f_{K/\pi} \left[P(s,0) + rP'(s,0) \right], \tag{112}$$

where λ is the Källén function defined in Eq (10). Fits of these two expressions to the data at sufficiently high energies, which are also shown in Fig. 24 to describe the data very well, yield the desired factors [143].

Several considerations about the Pomeron we use are now in order. When it dominates, the predicted cross-section tends to a constant value. For example, the Pomeron πK cross-section tends asymptotically to $\simeq 10.3$ mb, as seen in the top left panel of Fig. 25. This is roughly twice the $\simeq 5 \pm 2.5$ mb value used in [43], inspired by the $\pi\pi$ scattering asymptotic value of 6 ± 5 mb. However, this $\pi\pi$ value was revisited later by members of the same group [182] yielding 12.2 ± 0.1 mb for $\pi\pi$ scattering, thus supporting our larger value $\simeq 10 \pm 3$ mb for πK. The constant asymptotic value is a simplification that works rather well up to 20–30 GeV, good enough for the accuracy we need in our amplitudes. However, it is well known now that the Pomeron cross-section, although it cannot grow asymptotically as a power of s, could still grow if it does not violate the Froissart bound $\sigma_P \leq \log^2 s$. This slow growth of hadron total sections has been observed (see the "Total Hadronic Cross Sections" review at the RPP [95]), and it would require an slightly more complicated Pomeron expression than Eq. (110), which can also be found in [143]. Nevertheless, for our purposes here the simple Pomeron expression in Eq. (110) is accurate enough.

In addition, r is expected to come out very small, and indeed it does, due to the small coupling of the $f_2(1270)$ resonance to $K\bar{K}$, which suppresses the P' contribution. Thus one may wonder whether more Regge subleading contributions should be considered in Eq. (110). However, the next Reggeon, associated with the $f_2'(1525)$ trajectory, which couples strongly to $K\bar{K}$ scattering, couples very little to nucleons or pions. This, together with its small intercept $\alpha_{f_2'} \simeq -0.3$, makes this Reggeon contribution very suppressed. Therefore, the KN and πK isospin zero high-energy exchange is almost only due to the Pomeron, as assumed in Eq. (110).

Let us now consider the antisymmetric amplitude, which is dominated by the exchange of a Reggeized-ρ resonance. Then, following [143] we write:

$$\text{Im } F_{\pi K}^-(s,t) = \frac{\text{Im } F_{\pi K}^{(I_t=1)}(s,t)}{2} = 2\pi^2 g_{K/\pi} \text{Im } F_{\pi\pi}^{(I_t=1)}(s,t), \tag{113}$$
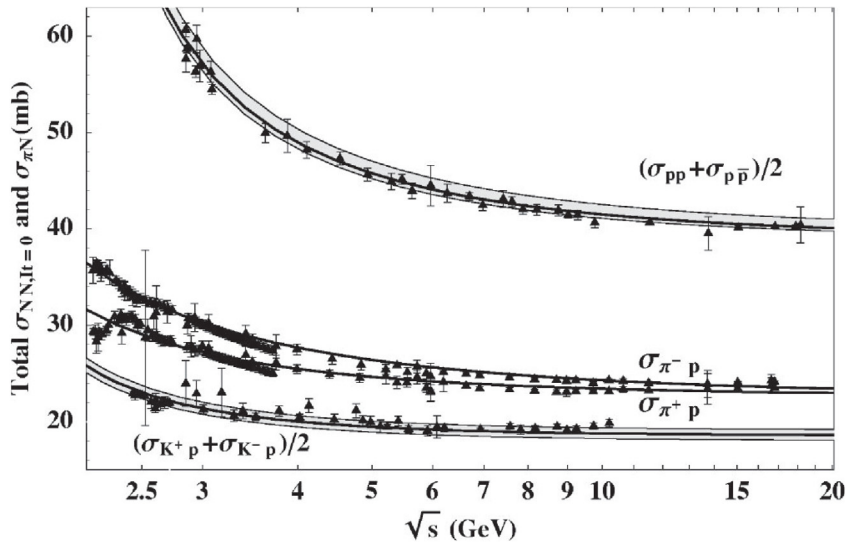
Fig. 24. High-energy hadron–hadron total cross-section data versus the Regge description in [143], that we also use here although updated to the values in [48].
Source: The figure is taken from [143].

where now $g_{K/\pi}$ is the factorization constant that converts the $\pi\pi-$Reggeized-ρ vertex into a $K\bar{K}-$Reggeized-ρ vertex. The Reggeized-ρ contribution is:

$$\mathrm{Im}\, F^{(I_t=1)}_{\pi\pi}(s,t) = \beta_\rho \frac{1+\alpha_\rho(t)}{1+\alpha_\rho(0)} \varphi(t) e^{\hat{b}t} \left(\frac{s}{s'}\right)^{\alpha_\rho(t)},$$

$$\alpha_\rho(t) = \alpha_\rho(0) + t\alpha'_\rho + \frac{1}{2}t^2\alpha''_\rho,$$

$$\varphi(t) = 1 + d_\rho t + e_\rho t^2. \tag{114}$$

There is not much information about the value of $g_{K/\pi}$ although, in practice, it can be obtained from factorization. Its extraction is somewhat more complicated than the simple case for the Pomeron trajectory that we used as an example above, and we refer the reader to [143].

Let us now discuss the parameters obtained from high-energy fits and factorization. For our purposes in this review, we treat them differently depending on whether they depend on observables with strangeness or not.

In particular, all parameters in Eqs. (110) and (114) correspond to non-strange Reggeon exchanges (the Pomeron, P' or f_2 and ρ) and have been determined in [143] and updated in [48], from processes that do not involve kaons. Their updated values from the CFD parameterizations are given in [48] are listed in Table 15. Hence, as we did in [41], we will keep their values fixed both for our unconstrained and constrained fits here.

In contrast, the determination of the $f_{K/\pi}$, r and $g_{K/\pi}$ factors requires input from kaon interactions. In principle, both of them were determined in [143] from KN factorization and we take the $f_{K/\pi}$ and r values from that reference. The values and uncertainties of $f_{K/\pi}$ and r are rather robust. However, for $g_{K/\pi}$ we take our UFD updated value from the forward dispersion relation study of πK scattering in [41], which is further constrained. We provide their values in Table 15. We will also add in quadrature a systematic uncertainty associated with the errors coming from $\pi\pi$ that we keep fixed. Since their determination involves kaon interactions, we will allow them to vary when constraining our fits with dispersion relations, i.e. from the UFD to the CFD sets. However, in the tables it is seen that the change is always within 2 sigmas of the UFD values.

Once the parameters needed for the high energy description of $\pi K \to \pi K$ have been determined, we obtain the curves plotted in the left panels of Fig. 25. Note that, to ease the comparison with the other hadron total cross-sections shown in Fig. 24, we have also plotted cross sections for the symmetric and antisymmetric isospin combinations in Fig. 25.

At this point, some technical remarks about Regge parameterizations are in order. It is often said that Reggeons and resonances are dual representations of hadronic physics (see [103,239] for textbook introductions) and which one is better suited to describe some energy region depends on whether it can be better approximated with just a few Reggeons or a few resonances, instead of the full collection of them. However, this duality is semi-local, which, for our purposes, means that Regge theory at low energies does not necessarily yield the correct value of an amplitude at every value of the energy, but instead it yields the correct value *on the average* over a sufficiently large energy region. Of course, since we use Regge theory only at high energies and only inside integrals, this is good enough. To illustrate this "on the average" description,
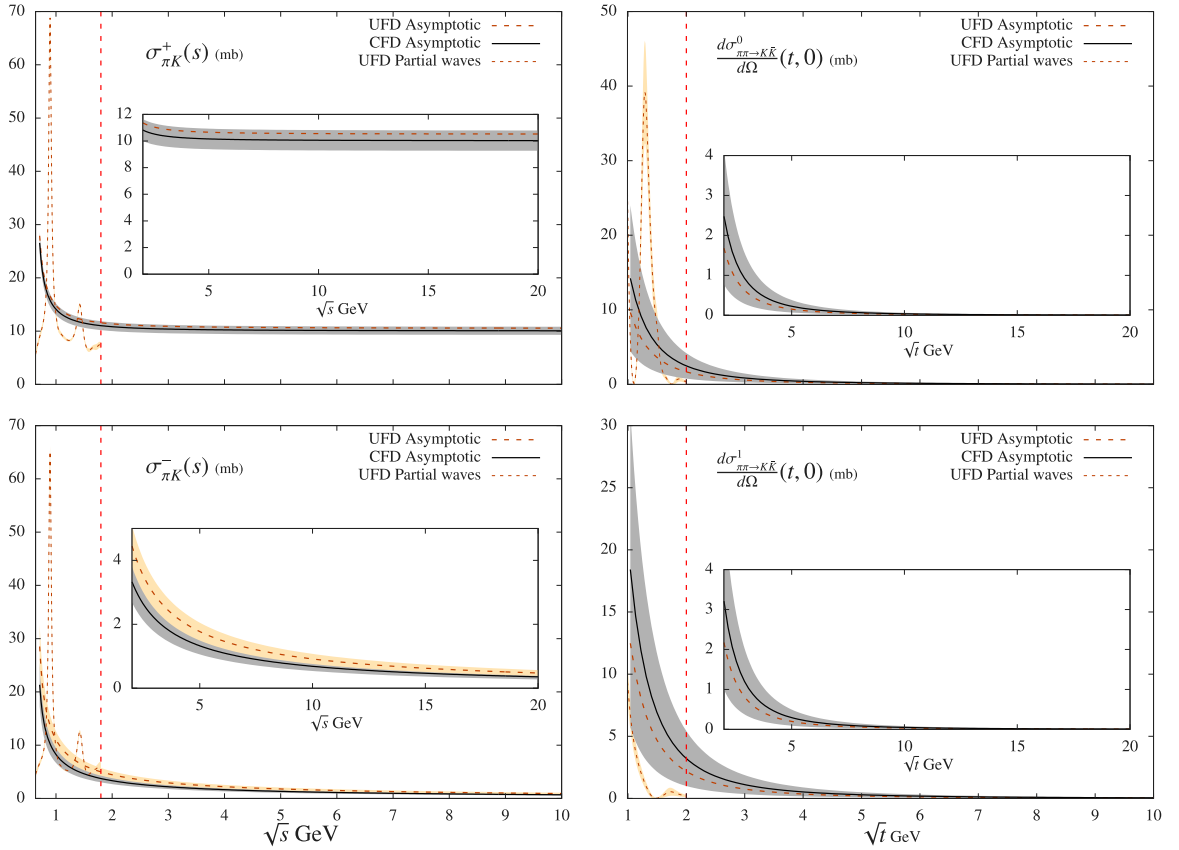
Fig. 25. High-energy total cross sections for πK or differential forward cross-sections $\pi\pi \to K\bar{K}$ scattering (Left and right panels respectively), in millibarns. They are both proportional to their corresponding imaginary part of the forward amplitudes provided in the main text. Note that for the symmetric $\pi K \to \pi K$ scattering $\sigma^+(s)$ tends asymptotically to a constant $\simeq 10.3$ mb. All other cross-sections of interest tend to zero asymptotically. Regge parameterizations are used only above 1.84 GeV for $\pi K \to \pi K$ and 2 GeV for $\pi\pi \to K\bar{K}$ (vertical lines). This is shown in detail in the insets up to 20 GeV. We show curves up to 20 GeV, since the dispersive integrals are suppressed by several factors at high energies, and their contributions from even higher energies are very small. Below 2 GeV, we use the corresponding partial wave expansion, whose central value is also shown as a dashed curve. Nevertheless, it can be noticed that, in that region, Regge theory is a crude average of the result obtained from partial waves. Note however that, plotting cross-sections, we cannot show the $\pi\pi \to K\bar{K}$ case below $K\bar{K}$ threshold, where more resonances appear. The gray and orange bands stand for the uncertainties of the CFD and UFD, respectively, although when they overlap we do not plot the uncertainty of the latter, to simplify the view.

in Fig. 25 we have extrapolated the Regge bands below the region where we use them, i.e. below 1.84 GeV (vertical dashed lines). As expected, they do not describe the resonance peaks, but they seem to average them.

Still, one might wonder how well the detailed partial-wave reconstruction agrees with the Regge description around 1.84 GeV, where we shift from one description to another inside our integrals for $\pi K \to \pi K$ scattering. In Fig. 25 we can check that they are fairly consistent within uncertainties, except for the symmetric amplitude (upper left panel) for which they do not match by several standard deviations. We insist this is not incorrect, because one description is local and the other is an averaged description. Furthermore, this mismatch does not produce any noticeable effects in the Roy–Steiner equations below 1 GeV. However, it does produce a significant effect when studying the forward dispersion relations close to this point. The dispersive output of the FDR, coming from and integral, will change smoothly between the values of the partial-wave reconstruction below 1.84 GeV and the Regge values above. As a result, the partial-wave input and the dispersive output for $F^+(s)$ are not compatible around 1.8 GeV, as will be shown in Fig. 27. Actually, this is one of the main reasons why we cannot claim to have a data description consistent with the F^+ FDR up to 1.84 GeV, but only up to ~1.7 GeV. Of course, we have looked at whether it was possible to start using our Regge description from an energy where it matches the partial-wave reconstruction. Unfortunately, the closest point available below 2 GeV is around 1.4–1.5 GeV, too low to rely on Regge theory for $\pi K \to \pi K$ scattering, whereas the closest point above is at around 2.2 GeV. Even though this last point may seem appealing, there are no data for the $I = 3/2$ partial waves above 1.74 GeV, and as already explained in [41] and in the introduction to this section, the partial-wave truncated series are not reliable much beyond that. In addition, we do not want to use the Regge description at too-low energies. All in all, we thus consider that a value

Table 15
Values of Regge parameters obtained in [48,51]. Since these could be fixed using reactions other than πK or $\pi\pi \to K\bar{K}$ scattering, they will be fixed both in our UFD and CFD parameterizations.

Regge parameters	Used both for UFD and CFD
s'	1 GeV^2
$\hat{b}$	2.4 ± 0.5 GeV^{-2}
α'_P	0.2 ± 0.1 GeV^{-2}
$\alpha'_{P'}$	0.9 GeV^{-2}
c_P	0.6 ± 1 GeV^{-2}
$c_{P'}$	-0.38 ± 0.4 GeV^{-2}
β_P	2.50 ± 0.04
$c_P(0)$	0 ± 0.04
$\beta_{P'}$	0.80 ± 0.05
$c_{P'}(0)$	-0.4 ± 0.4
$\alpha_{P'}(0)$	0.53 ± 0.02
$\alpha_\rho(0)$	0.53 ± 0.02
α'_ρ	0.9 GeV^{-2}
α''_ρ	-0.3 GeV^{-4}
d_ρ	2.4 ± 0.5 GeV^{-2}
e_ρ	2.7 ± 2.5
β_ρ	1.47 ± 0.14

around 1.84 GeV is well suited to shift from the partial-wave to the Regge description, and we then will not constrain the amplitudes above 1.7 GeV.

High-energy Regge parameterizations for $\pi\pi \to K\bar{K}$

To describe the high-energy region of $\pi\pi \to K\bar{K}$, we need to consider the exchange of strange Reggeons, which are much worse known than the Pomeron, P', and ρ trajectories. Following [42] we will consider that the two dominant trajectories, which are those of the $K_1^*(892)$ and $K_2^*(1430)$, are degenerate. Hence we will describe them with a common trajectory $\alpha_{K^*}(s) = \alpha_{K^*} + \alpha'_{K^*}s$, whose parameters are listed in Table 15. They are obtained from their linear Regge trajectories and will thus be kept fixed for both our UFD and CFD sets. In practice, all these features are incorporated in the dual-resonance Veneziano–Lovelace model [115,144,240–242], which was already used before us in the Roy–Steiner context for πK scattering [43,207].

Nevertheless, let us recall that, as explained in Section 3, for the dispersive analysis of $\pi\pi \to K\bar{K}$ we will make use of hyperbolic dispersion relations defined along the curve $(s - a)(u - a) = b$. Then, for a given t, s_b is the value of s that lies in the previous hyperbola, which, in view of Eq. (41), for large t behaves as $s_b \to a$. Therefore, inside the integrals for the high-energy region of t, we need:

$$\frac{\text{Im } G^0(t, s_b)}{\sqrt{6}} = \frac{\text{Im } G^1(t, s_b)}{2} = \frac{\pi \lambda (\alpha'_{K^*}t)^{\alpha_{K^*} + a\alpha'_{K^*}}}{\Gamma(\alpha_{K^*} + a\alpha'_{K^*})} \left[1 + \frac{\alpha'_{K^*}b}{t}\left(\psi(\alpha_{K^*} + a\alpha'_{K^*}) - \log(\alpha'_{K^*}t)\right)\right], \tag{115}$$

where ψ is the polygamma function. Note that, although numerically small, we have kept an $O(b/t)$ term, since it allows us to recover, as a check, the expressions in [43], where $a = 0$.

The last parameter λ was estimated in [42] assuming, for its central value, exact degeneracy between the ρ and K^* trajectories. Therefore, we take the ρ contribution in Eq. (113) at 2 GeV and match it with the expression from the degenerate Veneziano model with its original parameter $\alpha_\rho^V = 0.475$. This leads to

$$\lambda \simeq \frac{2\pi \Gamma(\alpha_\rho^V)}{\alpha_{K^*}'^{\alpha_\rho^V}} 4^{\alpha_\rho - \alpha_\rho^V} \simeq 10.6 \pm 2.5. \tag{116}$$

This value is compatible with the one estimated in [43], $\lambda = 14 \pm 4$. Conservatively we add in quadrature a 30% uncertainty as a crude estimate of the breaking of degeneracy and, rounding up, we write

$$\lambda \simeq 11 \pm 4, \tag{117}$$

also listed in Table 16. Once again, given that this trajectory involves strangeness and also because it is a crude estimate, we will allow this value to vary from exact degeneracy when constraining our fits to obtain the CFD sets. As we will see in Section 5, after imposing the dispersive constraints we will obtain $\lambda = 13.4 \pm 4.0$, which, if we use degeneracy between the ρ and K^* families, suggests $g_{K/\pi} \sim 0.6 \pm 0.2$, in fair agreement with the CFD value used here that comes from the dispersive $\pi K \to \pi K$ study.

Once these Regge parameters have been fixed, our Regge parameterizations of the πK total cross-sections and the imaginary part of the forward $\pi\pi \to K\bar{K}$ amplitudes are shown in Fig. 25.

Table 16
Values of Regge parameters involving strangeness. They are all allowed to vary from our UFD to our CFD sets except for α_{K^*} and α'_{K^*} since they are both determined from linear Regge trajectory fits to strange resonances.

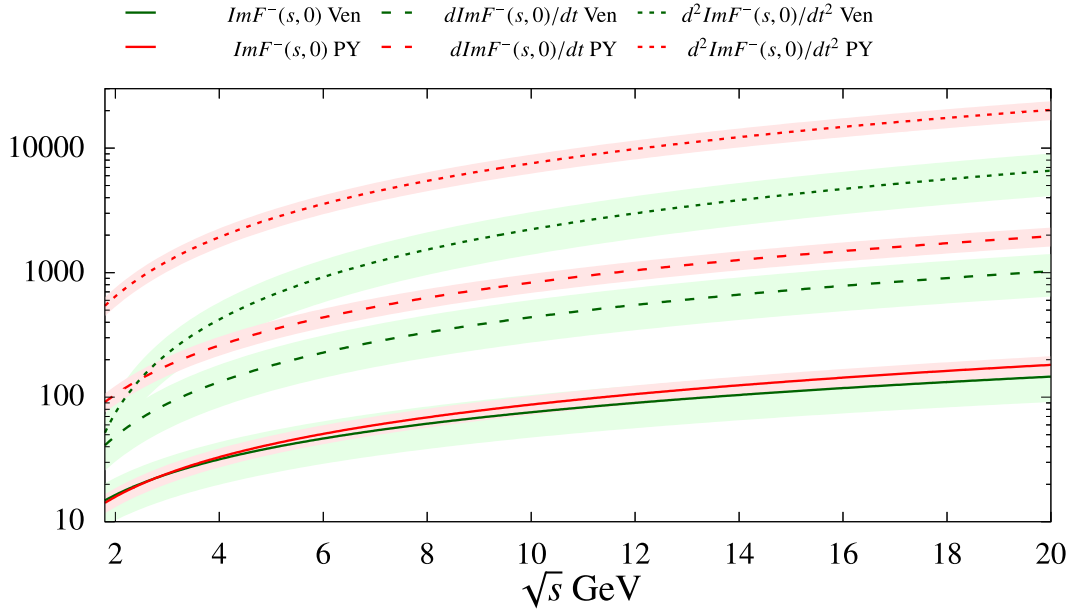| Regge	UFD	CFD
$f_{K/\pi}$	0.67 ± 0.02	0.64 ± 0.02
$g_{K/\pi}$	0.70 ± 0.09	0.52 ± 0.09
r	0.050 ± 0.010	0.056 ± 0.010
α_{K^*}	0.352	0.352
α'_{K^*}	$0.882 \ \text{GeV}^{-2}$	$0.882 \ \text{GeV}^{-2}$
λ	11.0 ± 4.0	13.4 ± 4.0

Fig. 26. Comparison between the Regge model of [143] (red lines) and the Veneziano–Lovelace model [115,144,240–242] (green lines). Note that although their results for $\text{Im}F^-(s, 0)$ (continuous lines) are very similar and overlap within uncertainties, their first and second derivatives (dashed and dotted lines, respectively) can differ substantially from one another to the point of being clearly incompatible. The fixed-t sum rules for higher ℓ partial waves are dominated by such contributions, so that for these dispersion relations we have added a systematic uncertainty for the derivatives to cover both models, as detailed in Section 7.

To end this section, two technical remarks are in order.

First, the Regge models we have shown, either based on [143] or the asymptotic forms of the Veneziano model, are particularly robust for the high-s dependence and small t. As shown in Fig. 26, for Im $F^-(s, t)$ these two models produce consistent descriptions of the close to forward region in the s variable. As a result, it is irrelevant whether we use one or the other inside our FDR and S, P partial-wave projected dispersion relations. However, the $\ell \geq 2$ fixed-t sum rules of Section 7.1 receive substantial contributions from this asymptotic region from terms with derivatives on the t-variable, in particular second and third-order derivatives. Unfortunately, the second or third derivatives with respect to t of these models are no longer compatible. This is illustrated in Fig. 26 for the first and second derivatives. Thus, just for the D-wave sum rules, we have considered the average of the two models with a combined uncertainty coming from the statistical ones and a systematic error estimated as the difference between the two models. Fortunately, this contribution is negligible for the sum rules obtained from hyperbolic dispersion relations, which are therefore much more precise and reliable.

Second, let us recall that for $\pi\pi \to K\bar{K}$ the only dispersive representation we have in the physical region comes from partial-wave HDR relations obtained in Section 3 above. In such case, we take integrals over b for a family of $(s - a)(u - a) = b$ hyperbola, while keeping the *negative* value $a = -10.9M_\pi^2$ fixed (see Appendix D). This means that the exponent $\alpha_{K^*} + a\alpha'_{K^*} < \alpha_{K^*}$ and thus the Regge contribution to the $\pi\pi \to K\bar{K}$ dispersion relations, given the same number of subtractions, is suppressed when compared to its size in [43], where $a = 0$. This allows us to consider fewer subtractions without Regge contributions becoming too large. Of course, this same suppression occurs for the high-energy $\pi\pi \to K\bar{K}$ contributions to the $\pi K \to \pi K$ partial-wave dispersion relations obtained from HDR, where now $a = -10M_\pi^2$.

4.4. Tests of the dispersive representation

Once again, we recall the reader that we aim at providing a simple set of parameterizations that are consistent with basic requirements as analyticity, unitarity, and crossing. In the previous subsections, we have obtained such a relatively simple description of data, paying particular attention to both statistical and systematic uncertainties. Our parameterizations even contain some basic features known to exist in these two-meson amplitudes (cuts, poles, resonance poles, Adler zeros...). However, in this section, we will show that they are still not good enough. Actually, we are going to show now that, by itself, the previous Unconstrained Fit to Data (UFD) description fails to satisfy to different degrees several of the dispersion relations we have derived in Section 3. In passing, we will also show what is in practice the weight of different contributions to each dispersion relation. The present section will then justify the need for a Constrained Fit to Data (CFD) that we will present in Section 5 below.

Let us then list the dispersive equations detailed in Section 3 that we will study here: the forward dispersion relations (FDRs) in Eqs. (39) and (40), the partial-wave relations obtained either from fixed-t dispersion relations (FTPWDR) as in Eq. (53) or from Hyperbolic dispersion relations (HPWDR) as in Eqs. (54),(55), (56) and (57). Let us recall that we use two versions of the HDR for the F^- amplitude, with a different number of subtractions, so that both f_ℓ^- and g_1^1 will have two versions of their HPWDR. The main reason to consider a different number of subtractions is that while the unsubtracted F^- relation is adequate to obtain a sum rule at threshold, thus constraining efficiently the low-energy region, its Regge contribution is not negligible. Moreover, its crossed channel contribution, in particular, that from g_1^1, plays an important role at low energies, which entails the correlated fulfillment of dispersion relations for both $\pi K \to \pi K$ and $\pi\pi \to K\bar{K}$. Hence, in order to get a different constraint, keeping the Regge asymptotic region almost negligible, so that the partial waves that build F^- are dominated by their own input, we will consider also partial-wave relations from the once-subtracted F^- HDR. Note, however, that this is not needed for the FTPWDR, since in this case both the high-energy region and the crossed channel contributions are largely suppressed.

How do we test then these integral relations? We follow a similar approach to what we did in [41,42]. Namely, we first introduce a χ^2/dof-like function measuring the deviation between the input coming from the data fits and the output of a given dispersion relation

$$\hat{d}^2 = \frac{1}{N} \sum_{i=1}^{N} \left(\frac{d_i}{\Delta d_i} \right)^2 . \tag{118}$$

By "output" we mean the integral part of the dispersion relation and by "input" the non-integral part that is calculated directly from the data fit. The d_i above, with $i = 1, \ldots, N$, are the differences between input and output at a set of discrete energies, and Δd_i are the uncertainties of the difference, obtained from the errors of the initial parameters. Each dispersion relation will then have an associated distance which provides a fair estimate of its fulfillment. In particular, we will use $N = 50$ points equally spaced in $\sqrt{s_i}$ between the πK threshold and 1.7 GeV for the two FDRs. We will then use $N = 30$ points, again equally spaced in $\sqrt{s_i}$, between the πK threshold and 0.98 GeV for both the $\pi K \to \pi K$ FTPWDR and HPWDR. Finally, we define the $\pi\pi \to K\bar{K}$ HPWDR distances by using again 30 points but now spaced between the $K\bar{K}$ threshold and 1.47 GeV. Furthermore, we will use as input our fitted partial waves below $s' \leq 1.84$ GeV^2 for $\pi K \to \pi K$ scattering, and below $t' \leq 2$ GeV^2 for $\pi\pi \to K\bar{K}$, using above those energies the Regge asymptotic contributions described in Section 4.3 above.

We consider that a given dispersive equation is satisfied within uncertainties if this χ^2/dof-like function is 1 or less. Of course, it is not enough that this $\hat{d}^2$ should be one in the whole energy region, we have to make sure that this happens uniformly and there are no regions where the fulfillment is bad but they are compensated by other regions where the agreement is very good. For this reason, we will present both global numbers, but also plots of the difference between input and output and their corresponding uncertainty.

4.4.1. Dispersive tests for $\pi K \to \pi K$

Tests of forward dispersion relations

Starting then with the FDRs for $\pi K \to \pi K$, our results here are very similar to those we obtained in [41], but updated with the new parameterizations and uncertainties. Thus, we show in the central panels of Fig. 27 the input and output of the two FDRs for F^+, i.e. Eq. (40), and F^-, Eq. (39) (upper and lower panels respectively) as a function of $\sqrt{s}$. We show one error band, which is the uncertainty in the difference between the two, attached to the "output" central value. If a dispersion relation is to be satisfied, both "input" and "output" curves should overlap within this uncertainty band. The inconsistency of both FDRs when using the UFD as input is obvious. On average, the input and output lie more than 3 standard deviations away from each other when considering most of the energy region from πK threshold up to 1.74 GeV, although the deviation is larger above 1 GeV.

In addition, in the left panels, we provide the decomposition of the integral "output" for each relation. It is worth noticing that up to 1.2 GeV both amplitudes are dominated by the $P^{1/2}$-wave, i.e. the $K^*(892)$ resonance. The shape around 1.4 GeV is dominated by the $D^{1/2}$, which corresponds to the $K_2^*(1430)$, and from that point there is no clear dominance. Above 1.6 GeV Regge contributions become dominant, although they do not produce any distinct shape but
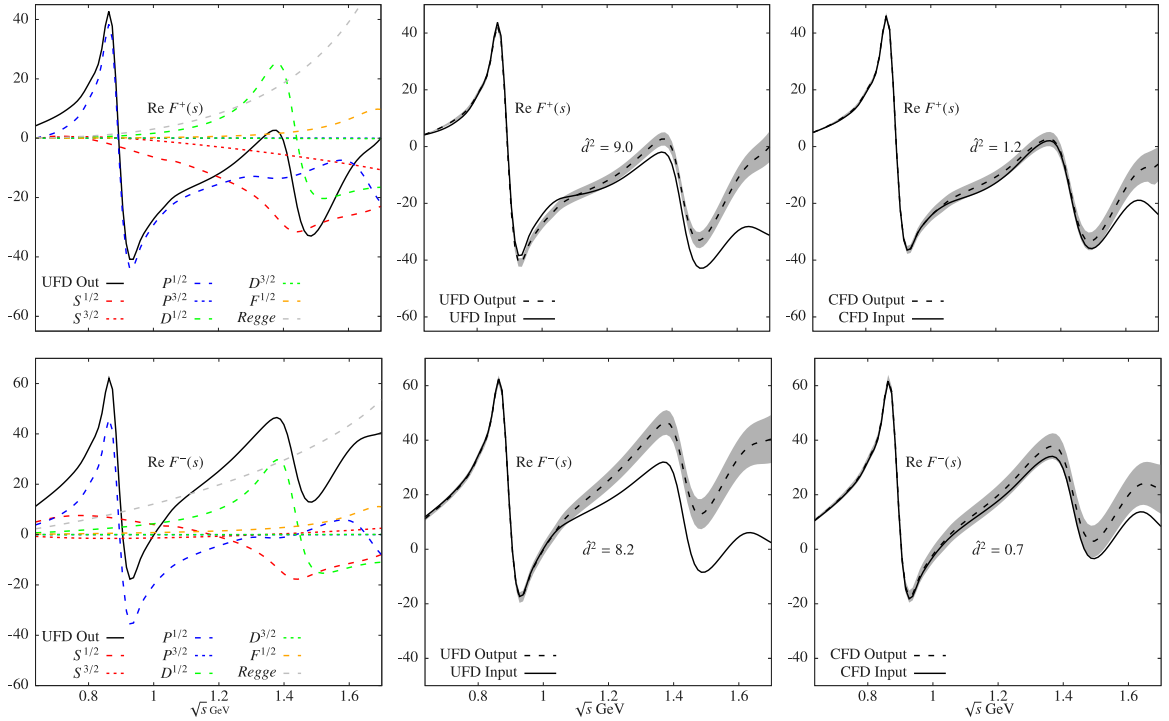
Fig. 27. Checks of the $F^+(s)$ and $F^-(s)$ forward dispersion relations. The gray bands are the uncertainties in the difference between input and output, although we attach them to the output to ease the comparison. Note the large inconsistencies between input and output for the UFD and the nice consistency of the CFD, except in the region above 1.6 GeV for F^+, which we cannot fix while keeping a decent description of data there. In the first column, we show the size of different contributions for each dispersion relation.

just a monotonous rise. Beyond 1.8 GeV, the UFD violates dispersion relations by more than 5 sigmas and we do not plot it anymore.

Compared to the previous analysis we carried out in [41], the low-energy region is better described by the updated S and P fits. However, at higher energies, the observed inconsistencies are similar, if not worse as now our uncertainties have shrunk slightly with the update. Actually, we already saw in [41], and have found again with the updated parameterizations, that, even imposing the FDRs as constraints, it is not possible to have a simultaneous fair description of data and FDRs beyond 1.7 GeV for F^- or 1.6 GeV for F^+. This is partially due to the non-smooth match shown in Fig. 25, but also caused by the fact that there is no centrifugal suppression anymore so that many partial waves contribute to the full amplitudes with similar strength.

Hence, as we concluded in [41] and we have checked again here with updated fits, the UFD fails to satisfy the FDRs, particularly at high energies, and asks for improvement. This will be achieved in Section 5 by constraining the data fits with dispersion relations, including these FDRs.

Tests for partial waves from fixed-t dispersion relations

The previous FDR test the whole amplitudes $F^\pm(s, 0)$, which in the region of applicability are built as sums of partial waves. However, in Section 3 we also derived dispersion relations for individual partial waves. For $\pi K \to \pi K$ scattering, we will test the S and P partial waves, i.e. $\ell = 0, 1$, both in the symmetric and antisymmetric isospin combinations. Higher partial waves are input for these. Remember that these partial-wave dispersion relations can be obtained either from fixed-t, i.e. FTPWDR, or HDR dispersion relations.

Thus, in the central panels of Fig. 28 we show the output versus input for the four FTPWDR, obtained from Eq. (53), for the $f_\ell^\pm$ partial waves, with $\ell = 0, 1$. As a technical remark, note that in Fig. 28 we only show our curves up to 0.98 GeV, although these FTPWDR are applicable up to $s \sim 1.1 \text{GeV}^2$. However, for simplicity and the sake of comparison, we will only impose all partial-wave dispersion relations up to $\sqrt{s} = 0.98$ GeV, which is the highest allowed value for the HPWDR.

Now, as can be seen in Fig. 28, the deviations between input and output are not as large as for FDRs. However, there is a clear deviation in the f_0^+ case (Top center), not only because the overall $\hat{d}^2 = 6.2$ but because the shapes of input and output do not look very similar. The best one is f_0^- which, on the average, deviates by less than 1.3 standard deviations. The input and output for both vector waves f_1^+ and f_1^- seem to lie very close, but the uncertainties are very small and on average they deviate by more than 1.8 and 2.2 sigmas, respectively.
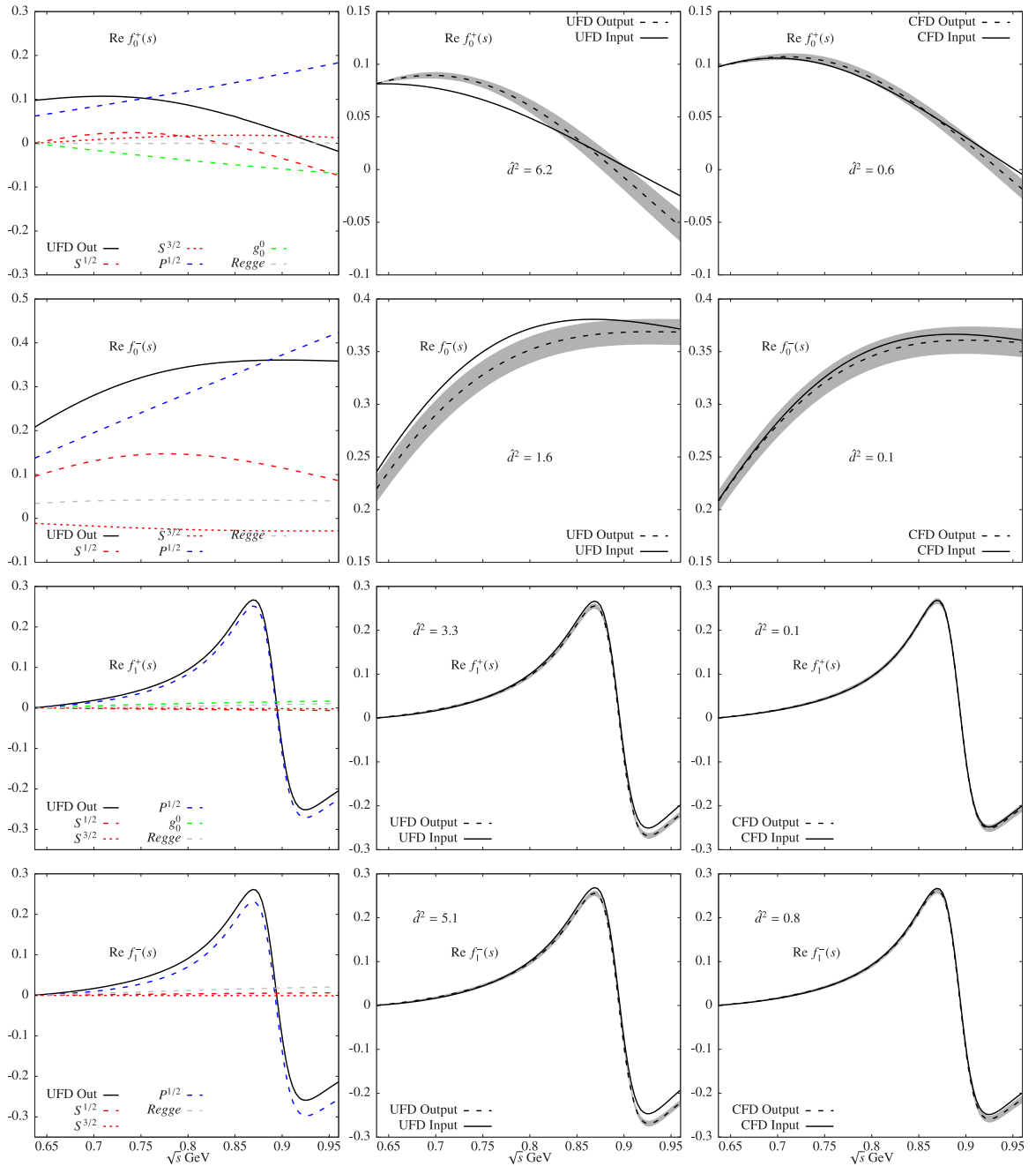
Fig. 28. Tests of the $f_\ell^+(s), f_\ell^-(s)$ fixed-t partial-wave dispersion relations. The gray bands are the uncertainties in the difference between input and output, although we attach them to the output to ease the comparison. Note the large deviations between input and output in the UFD and the remarkable agreement within uncertainties of the CFD partial waves. We show in the first column the size of different contributions to each dispersion relation.

On the left panels of Fig. 28 we show the size of different contributions to these FTPWDR. It is worth mentioning that the $P^{1/2}$-wave dominates completely the vector dispersion relations, the other contributions being practically zero. Thus, the inconsistency of these relations will require some honing of the $P^{1/2}$ and in particular our $K^*(892)$ description. For scalar waves, the most salient feature is that the Regge contribution is completely negligible and the observed shape is a cancellation between the dominant $P^{1/2}$ contribution and the subdominant S-waves and, for the f_0^+, even the g_0^0 wave of the crossed channel. It is also worth mentioning that the contribution from the $\pi\pi \to K\bar{K}$ crossed channel is small.
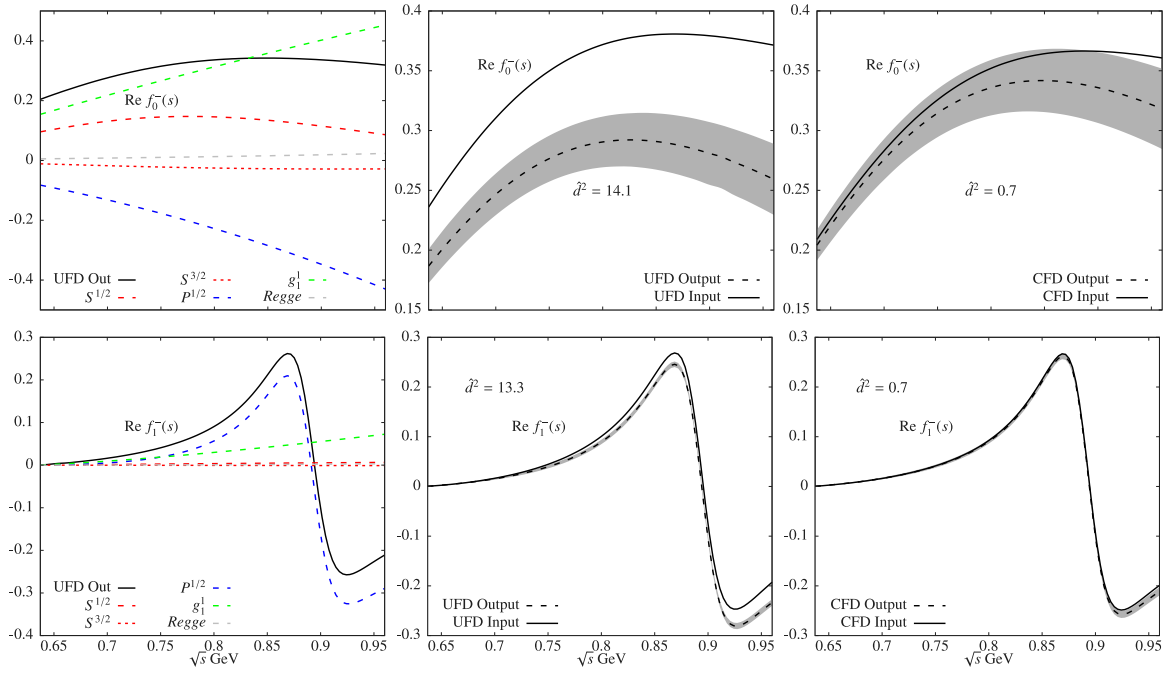
Fig. 29. Checks of the $f_\ell^-(s)$ non-subtracted hyperbolic partial-wave dispersion relations. The gray bands are the uncertainties in the difference between input and output, although we attach them to the output to ease the comparison. Note the large deviations between input and output in the UFD and the remarkable agreement of the three CFD partial waves. In the first column, we show the size of different contributions to each dispersion relation.

The largest one comes from g_0^0 and we can see that is much smaller than the dominant ones. For this reason, it does not make any difference to use as input our UFD_B or UFD_C (which we actually used for these plots).

Let us remark that this check would be much worse in case we had used the original fits of [41] instead of the new ones. The main effect comes from the UFD $S^{3/2}$ partial wave, which is now much closer to the final constrained result. Therefore this comparison supports our updated parameterization and disfavors substantially the lowest lying data points of [5].

In any case, although somewhat better satisfied than the FDRs, the partial-wave tests obtained from fixed-t dispersion relations also suggest revisiting the data fits using them as constraints, as we will do in Section 5.

Tests for partial-waves from hyperbolic dispersion relations

First of all, recall that there are HPWDR for both the $\pi K \to \pi K$ channel, i.e. Eqs. (54) and (55), as well as for the $\pi\pi \to K\bar{K}$ channel, i.e. Eqs. (56) and (57). For the former, we only test the S and P-waves in the isospin symmetric or antisymmetric combinations, whereas for the latter we test g_0^0, g_1^1 and g_2^0. Also, recall that we have two versions, depending on whether we subtract the F^- dispersion relation or not. In addition, we have two alternative fits for g_0^0, i.e. UFD_B and UFD_C, but we will see that their contribution to dispersion relations other than their own are very small, if any, and taking one or the other yields the same result. Unless otherwise stated, we use UFD_C when g_0^0 is needed.

Thus, in the central column of Fig. 29 we show the tests for the f_ℓ^- $\pi K \to \pi K$ partial waves, with the F^- HDR unsubtracted. The large inconsistency of the scalar wave in the top central panel is striking: the output lies uniformly well below the input, by more than 3.7 standard deviations on the average. Moreover, the inconsistency for the vector channel in the bottom central panel is as large as for the scalar one, i.e. an average of more than 3.6 standard deviations, although since the uncertainty band is much smaller, the central values of the curves look very close in the plot. These are the largest inconsistencies we will find when using the UFD.

On the left panels of Fig. 29 we show the size of the different contributions. In both cases, the dominant ones are the $P^{1/2}$-wave and the crossed-channel g_1^1 contributions. In the scalar case they suffer a large cancellation among themselves, and the curve shape is given by the scalar $S^{1/2}$-wave. The Regge part is negligible in both cases. The strong violations we report are also related to the deviation from the dispersive F^- sum rule we found in [41]. Actually, note that, for the scalar case, the low-energy region is dominated by the g_1^1 partial wave. Even more specifically, the part that dominates the g_1^1 wave is the pseudo-physical region, included as input between $4m_\pi^2$ and $4m_K^2$. This may seem surprising, since the phase in that region comes from the $\pi\pi \to \pi\pi$ P-wave, taken from the dispersive study of [48], but it is worth remembering this is produced by the peak of the ρ resonance, as it appears in $\pi\pi \to K\bar{K}$, which cannot be measured. Actually, the UFD modulus (Fig. 33), obtained employing an unsubtracted Muskhelishvili–Omnès dispersion relation as explained in

Section 3 is small around the ρ resonance. This adds to the fact that the phase-shift crosses 90° there, producing a large imaginary part contributing to the dispersion relations. We will see that this modulus will suffer a remarkable change when imposing the dispersive constraints on g_1^1.

When looking at the f_ℓ^+ and f_ℓ^- once-subtracted HPWDR tests in Fig. 30, we find again a rather large disagreement. Somewhat larger indeed for the scalar waves than the vector ones. The deviations between input and output are slightly worse but relatively similar in size to those we already observed in Fig. 28 in the partial-wave tests coming from FTPWDR. Comparing the panels in the left column of Fig. 30 versus their counterparts in Fig. 28, we see that, for vector waves, the $K^*(892)$ dominates both kinds of dispersion relations, as should be expected. However, for all waves, the respective sizes of the other contributions for the two kinds of dispersion relations are rather different. As a consequence, FTPWDR and HPWDR provide independent tests, and both show a clear inconsistency of the UFD parameterization. Let us also remark that the g_0^0 contribution is very small and therefore it is irrelevant whether we use our CFD$_B$ or CFD$_C$ parameterization as input (we used the latter for these plots).

Compared to the HPWDR unsubtracted case in Fig. 29, we find a smaller disagreement for f_0^- but note that this time the output comes *above* the input. Thus, the disagreement between the unsubtracted and subtracted f_0^- outputs, which in principle should be equal, is dramatic. These tests would have been worse if the original fits of [41] had been used instead of the ones presented here. The g_1^1 partial wave is now less dominant, albeit big, and several cancellations produce a way more stable result, almost dominated by its own input. In particular, the Regge contributions have been suppressed. However, the a_0^- scattering length is much more relevant now.

In summary, we find that the UFD no matter how nicely it describes the data, fails to satisfy well almost all the dispersion relations under consideration: FDRs and partial-wave dispersion relations either coming from fixed-t or HDR. We will dedicate the whole Section 5 to find a constrained fit that will describe fairly well and simultaneously all dispersion relations and the data within uncertainties, not only for $\pi K \to \pi K$ but also for $\pi\pi \to K\bar{K}$, whose UFD we will see next that also fails to pass the dispersive tests.

4.4.2. Dispersive tests for $\pi\pi \to K\bar{K}$ and prediction for the unphysical region

Let us now recall that only partial-wave dispersion relations from HDR can be used to test or constrain this process, and only up to 1.47 GeV (see Appendix D). These tests were already studied by us in [42], but here we have updated them to the new parameterizations, finding relatively similar results. In addition, the dispersive representation yields a prediction for the modulus of the partial waves in the unphysical region, where data on the modulus do not exist, but the phase can be obtained from $\pi\pi \to \pi\pi$ scattering. This region is relevant because it is input for other dispersion relations in this and the crossed channel.

As a technical remark, we have slightly changed the value of the matching point of the $g_1^1(t)$ Muskhelishvili–Omnès from $\sqrt{t_m} = 1.2$ GeV used in [42] to $\sqrt{t_m} = 1$ GeV. The reason is that this new point makes the pseudo-physical region more sensitive to changes occurring in the low-energy physical one, thus allowing us to have more room for improvement when using the dispersion relations as constraints. At the same time, it reduces our uncertainties and uses the fit to the data on a larger input region, as explained in Section 3.6.

Thus, in Fig. 31, we show the results for both the unsubtracted and subtracted g_1^1 dispersion relations (top and bottom panels, respectively). Note that we can only compare input and output for the modulus in the physical region since the unphysical one is just output. Both waves show some inconsistency with the dispersive output, milder for the unsubtracted case. By comparing the upper and lower left panels, we can see how the weight of different contributions changes considerably by subtracting or not the dispersion relation. While the unsubtracted output is largely dominated by the g_1^1 wave itself, the largest contribution to the subtracted one comes from S-waves, particularly in the region below the ρ mass.

Concerning g_0^0, the dispersive test is shown in the top central panel of Fig. 32 for the UFD$_C$. Once again, we find an overall disagreement between input and dispersive output, although it is concentrated below 1.2 GeV and more intensely in the ~20 MeV region right above $K\bar{K}$ threshold. Beyond this near-threshold region the agreement is much better. We already found this behavior in [42]. Actually, this was the most likely place for our isospin-conserving approximation to fail, since there are indeed two thresholds, one for $K^0\bar{K}^0$ and another for K^+K^-, separated by $\simeq 8$ MeV, but our isospin-symmetric formalism only has one. In other waves this effect is less relevant, but in the S-wave it is enhanced by the isospin-violating mixing of the nearby $f_0(980)$ and $a_0(980)$ resonances [243,244].

In the corresponding left panel, we also see that the dispersive output for the g_0^0 wave is dominated below threshold by the $\pi K \to \pi K$ P-wave, whereas g_0^0 itself dominates above $K\bar{K}$ threshold. However, right at threshold there is a cancellation between three significant contributions, i.e. those from the g_0^0, P, and S-waves. The Regge contribution is rather small and well under control. Note that we $\pi\pi$ phase contribution is always subsumed inside other terms through the Omnès function and that is why we do not consider it separately.

In addition, in the lower panels of Fig. 32, we show the dispersive tests for the tensor wave g_2^0. In this case, the agreement is quite acceptable, save the very near threshold. Once again the isospin-violating splitting of the $K\bar{K}$ threshold commented above may play a role in this mismatch, although it is milder than for the g_0^0 wave since for g_2^0 no resonances are sitting right at t_K. Well above $K\bar{K}$ threshold, the wave is largely dominated by the $f_2(1270)$ resonance and by the $\pi K \to \pi K$ P-wave in the unphysical region.
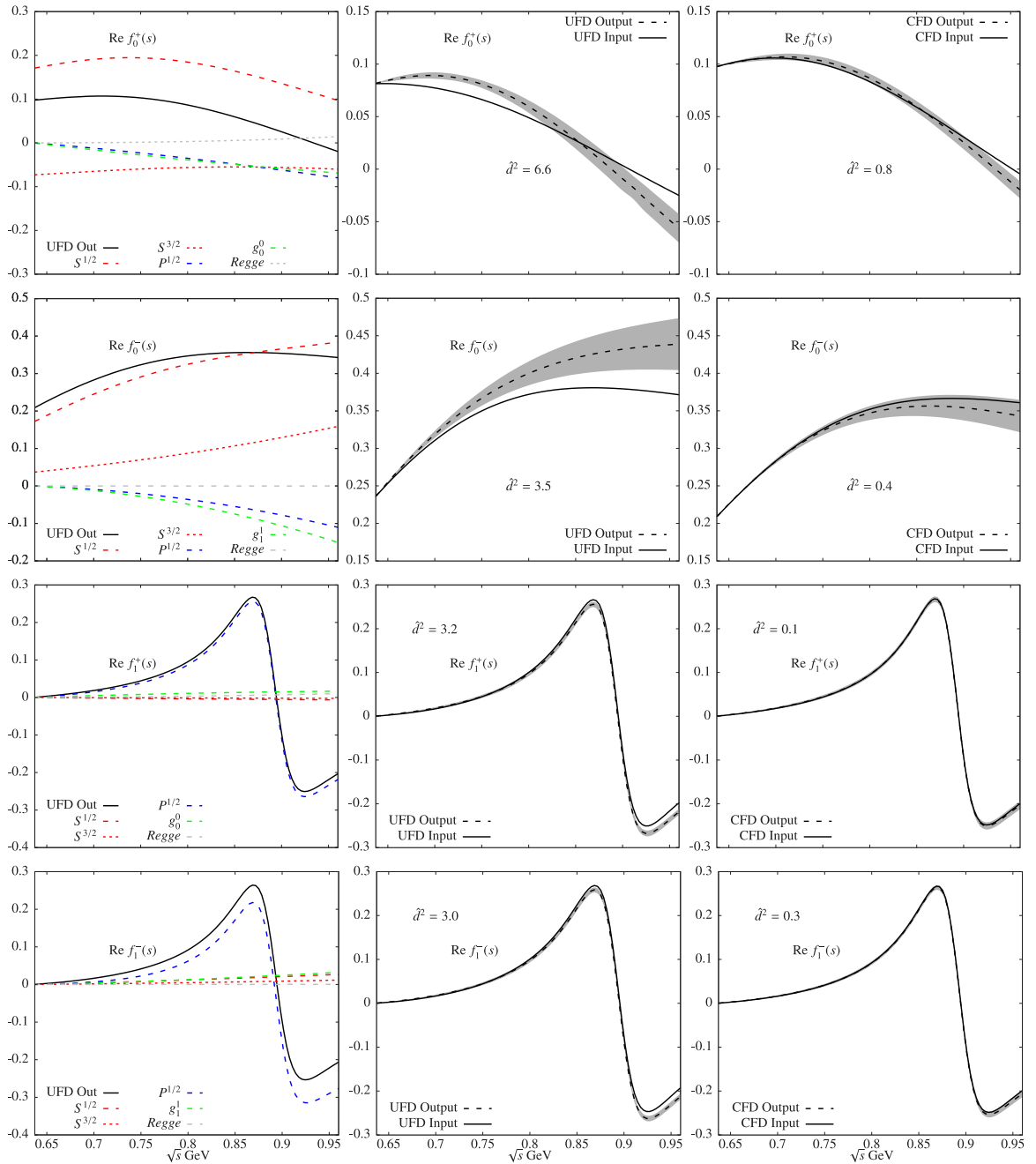
Fig. 30. Checks of the $f_\ell^+(s)$ and $f_\ell^-(s)$ once-subtracted hyperbolic partial-wave dispersion relations. The gray bands are the uncertainties in the difference between input and output, although we attach them to the output to ease the comparison. Note the large deviations between input and output in the UFD and the remarkable agreement of the four CFD partial waves. In the first column, we show the size of different contributions to each dispersion relation.

Finally, in Fig. 33 we show the dispersive predictions for the modulus of the g_0^0, both for UFD$_B$ and UFD$_C$, as well as the modulus of g_1^1, but this time down to the unphysical region and versus data in the physical region. Recall there are no data for these moduli in the unphysical region. Our only input there is the $\pi\pi \to \pi\pi$ phase shift with the corresponding quantum numbers. These moduli are calculated using the Muskhelishvili–Omnès formalism explained in Section 3. Obviously, the predictions for the unphysical region of g_0^0 differ when using the UFD$_B$ or UFD$_C$, since they provide different inputs. In both cases we clearly see a peak corresponding to the $f_0(980)$ resonances and a lower energy "bump" that is associated with the $\sigma/f_0(500)$ resonance, which is well-known to be very wide and not a Breit–Wigner-like
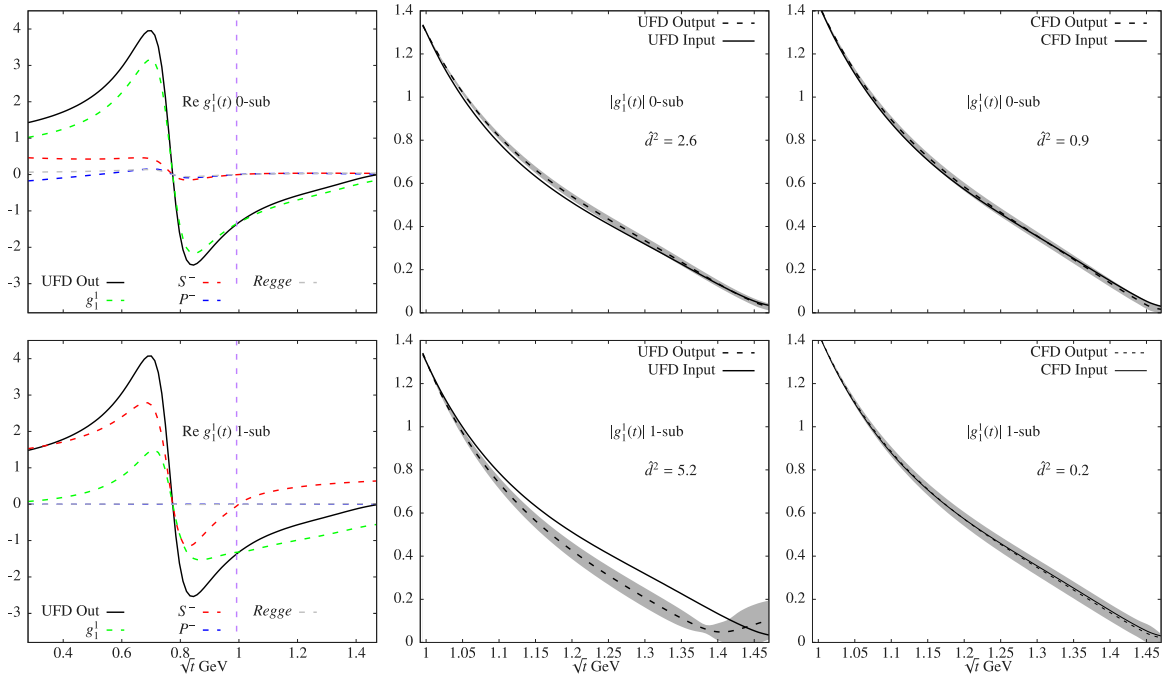
Fig. 31. Checks of the $g_1^1(t)$ partial waves with none (Top) and one subtraction (Bottom) for the F^- amplitude. The gray bands are the uncertainties in the difference between input and output, although we attach them to the output to ease the comparison. Note the inconsistency for the UFD case (central column), particularly for the once-subtracted case, which disappears for the CFD (right column). On the left column we show the size of different contributions to the dispersive output. The vertical dashed line on the left panels signals the $K\bar{K}$ threshold.
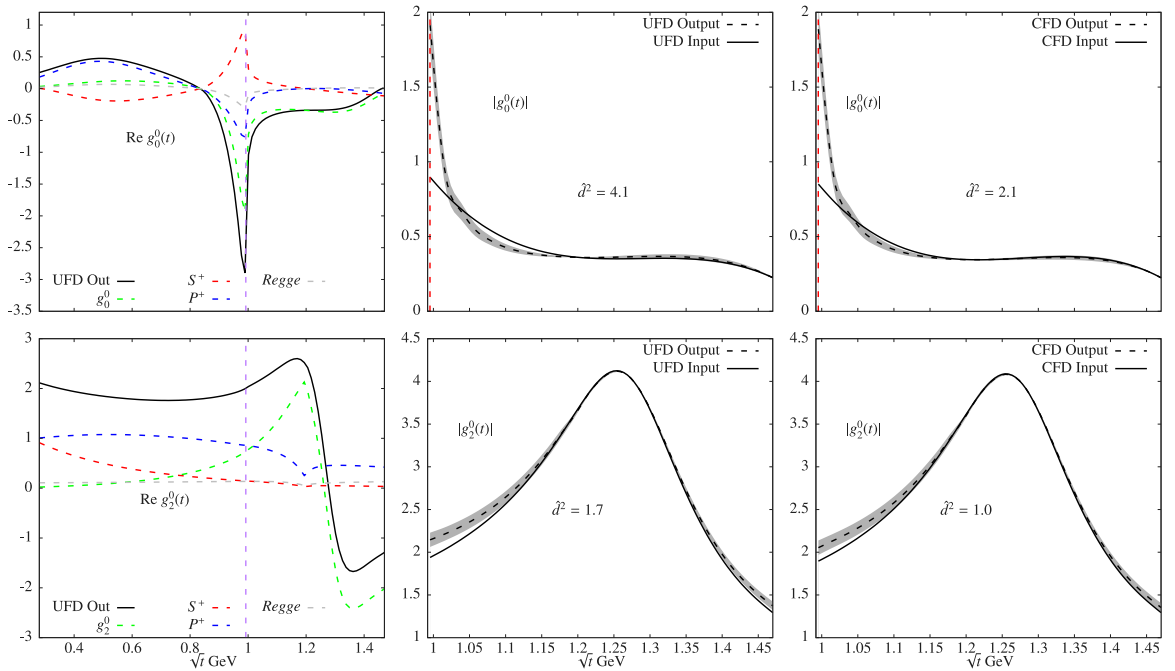

Fig. 32. Checks of the $g_0^0(t)$ and $g_2^0(t)$ partial waves with one subtraction for the F^+ amplitude. The gray bands are the uncertainties in the difference between input and output, although we attach them to the output to ease the comparison. Note the consistency improvement from the UFD to the CFD results (central and right columns, respectively). For the g_0^0 we show as UFD and CFD the UFD_C and CFD_C, since the UFD_B and CFD_B are of similar qualitative behavior. Nevertheless, even for the CFD, the region close to the $K\bar{K}$ threshold (vertical dashed line) cannot be well described with our isospin-symmetric formalism at this level of precision. This is particularly evident for the g_0^0 since that region is enhanced by the presence of the $f_0(980)$ resonance and its isospin violating mixing with the $a_0(980)$. On the left column, we show the size of different contributions to the dispersive output.
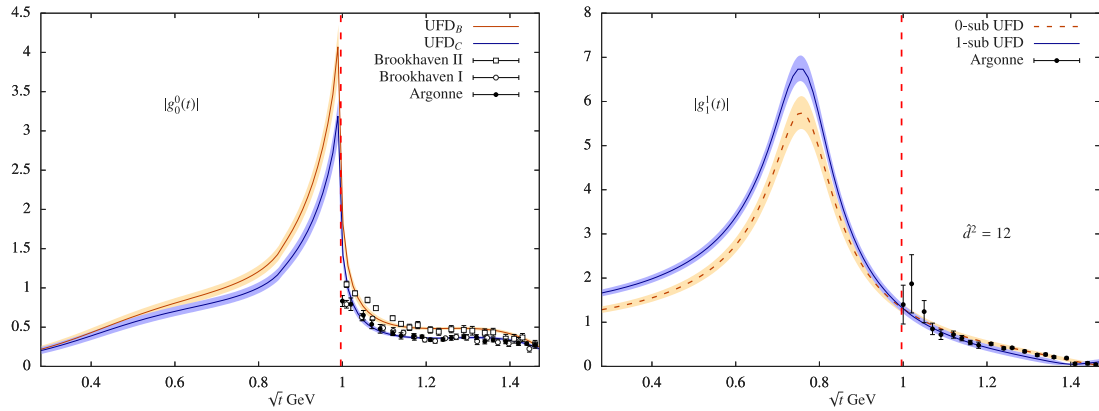
Fig. 33. Dispersive result for the modulus of the UFD $g_0^0(t)$ and $g_1^1(t)$ partial waves. Left: We show the two alternative g_0^0 fits UFD$_B$ and UFD$_C$. Since they differ in the physical region, they also differ below. Right: Notice the discrepancy between the unsubtracted and once-subtracted dispersion relations for $g_1^1(t)$, even if using the same UFD input in the physical region. We have calculated as an illustration the average $\hat{d}$ distance between the two g_1^1 dispersion relations in the pseudo-physical region between $2m_\pi$ and $2m_K$, divided by the relative uncertainty between them. They are clearly incompatible by more than 3 standard deviations.

shape [13]. In general, since the modulus of the UFD$_B$ is larger than that of the UFD$_C$ in the physical region, it is also larger in the unphysical one. Fortunately, we have already seen that the contributions of this wave to other dispersion relations are not significant, and thus they barely change when using one input or the other.

In contrast, we have seen that g_1^1 plays a relevant role, if not dominant, for several dispersion relations, even for the crossed channel and in particular for the $\pi K \to \pi K$ scalar waves (where the controversial scalar resonance $\kappa/K_0^*(700)$ lies). Remarkably, as seen in the right panel of Fig. 33, *for the same UFD input*, we get two incompatible predictions for the unphysical region, depending on whether they come from the unsubtracted or once-subtracted dispersion relation. In principle, they should be the same. As we have seen, this is in part responsible for the dramatic difference in the dispersive output for the $\pi K \to \pi K$ S-wave. This will severely affect the extraction of the $\kappa/K_0^*(700)$ pole that we will discuss in Section 6.

Thus, the conclusion we reach from this first test is that fairly good-looking fits to the data do not fulfill the dispersive representation. And this happens in different energy regions and affects different contributions in both the s and t channel processes. Fortunately, it will be possible to amend this in the next section.

5. Constrained fits to data

5.1. Fulfillment of the dispersive representation

In the previous sections, we have first obtained, within the isospin-symmetric approximation, a set of 16 dispersion relations, which are a consequence of first principles like causality and crossing symmetry, that the scattering amplitudes should satisfy. Next, we have obtained a relatively simple description of the existing scattering data on both $\pi K \to \pi K$ and $\pi\pi \to K\bar{K}$ scattering, which also gives a fair representation of the existing statistical and systematic uncertainties. These are our Unconstrained Fits to Data (UFD). However, as we already found in [41,42], we have just seen that using our UFD as input for the dispersion relations, the output is inconsistent with the input, in some cases not by much, but in others by a rather large difference.

To address these inconsistencies, in [41] we constrained the $\pi K \to \pi K$ amplitudes to satisfy forward dispersion relations (FDR), whereas in [42] we constrained the $\pi\pi \to K\bar{K}$ amplitudes with partial-wave hyperbolic dispersion relations (HPWDR), i.e. hyperbolic Roy–Steiner equations, but keeping the $\pi K \to \pi K$ input from [41] fixed. We should also recall that there is also a $\pi K \to \pi K$ scattering dispersive analysis [43] *solving*, in the elastic region, partial-wave dispersion relations coming from fixed-t dispersion relations and keeping the $\pi\pi \to K\bar{K}$ input fixed from phenomenological models not constrained dispersively. This "solving" approach was also followed for other processes in [11,12,14,43,188].

However, no matter whether one solves the dispersion relations or uses them as constraints, one might wonder about correlations between the crossed $\pi K \to \pi K$ and $\pi\pi \to K\bar{K}$ channels. Namely, whether solving or constraining one channel would require the modification of the other to ensure consistency. This kind of coupled analysis between the s and t channels, including both physical regions, has never been performed for the $\pi K \to \pi K$ system and is the main original result of this review, from which all other original results derive.

How we impose the dispersion relations in our fit is similar to what we have done in our previous works. We will allow the parameters of our fits to vary to improve the consistency with dispersion relations, but keeping their uncertainties fixed, whose corrections we consider second-order effects. Then we make use of the averaged $\hat{\chi}^2$-like distances $\hat{d}_i^2$, already defined in Eq. (118), as penalty functions, by minimizing them together with the χ^2 of the data fits. In this work, each

Table 17
List of weights used to determine our final penalty functions that constrain the data fits.

Weight/DR	F^+	F^-
FDR	8	8

Weight/DR	f_0^+	f_1^+
Fixed-t	3	3
HDR	3	3

Weight/DR	f_0^-	f_1^-
Fixed-t	3	3
HDR 0-sub	3	3
HDR 1-sub	3	3

Weight/DR	g_0^0	g_1^1	g_2^0
HDR 0-sub		3	
HDR 1-sub	5	3	4

Table 18
List of weights used to determine our final χ^2_{data} for $\pi K \to \pi K$ and $\pi\pi \to K\bar{K}$ scattering.

	$S^{1/2}$	$S^{3/2}$	$P^{1/2}$	$P^{3/2}$	$D^{1/2}$	$D^{3/2}$	$F^{1/2}$	$G^{1/2}$
$W_{pw\,i}$	12	3	12	3	5	2	3	2

	g_0^0	g_1^1	g_2^0
$W_{pw\,i}$	10	10	8

penalty function $\hat{d}_i^2$ is assigned the weight W_i given in Table 17. In order to arrive at those values of W_i, we first considered each W_i to be roughly the apparent number of degrees of freedom of the respective curve, and then we tune it until, after minimization, we get a d_i^2 reasonably close to one in the whole range of energies where the dispersion relation is applied. The dependence of the minimization procedure on these weights is smooth and we have tried different choices, leading to very similar final results consistent within uncertainties. The one we provide in the tables ensures a quite uniform consistency of the dispersion relations throughout their applicability region. We will see that some dispersion relations yield a very small $\hat{d}_i^2$ once the other ones are satisfied.

In addition, we define another distance, Δ_p, between the initial and final parameters of the high-energy asymptotic formulas described in Section 4.3, divided by their uncertainties. The weight of these parameters will be simply their total number. Finally, we will add these distances to the χ^2 of the data, although the data χ^2 for each partial wave has also been weighted by its apparent degrees of freedom $W_{pw\,i}$, that we list in Table 18. All in all, the final formula to be minimized reads

$$\sum_i \left(W_{pw\,i}\chi_i^2 + W_i\hat{d}_i^2 \right) + \Delta_p^2 + W_{FDR}\,\hat{d}_{FDR}^2 + W_{p'}\Delta_{p'}^2. \tag{119}$$

The result of minimizing this quantity is our Constrained Fit to Data (CFD), which satisfies all our dispersion relations within uncertainties, while still providing a fairly good description of data. The parameters of this CFD have already been provided in the tables of Section 4 together with the UFD ones, but here we will comment on its features. A technical remark is in order first, though. After minimization, most of the parameters vary by 1 and 2 σ from their UFD to their CFD values. However, in practice, there are a few highly correlated parameters, for which their CFD result could lie far from the UFD one. Nevertheless, there is always another solution, with a negligibly larger χ^2, where these few parameters remain closer to their UFD counterparts. Since we have decided to keep the CFD uncertainties fixed to their UDF values, those latter values are preferred. For this reason, we have also added once again the $\Delta_{p_i}^2$ of every parameter that deviates by more than 3σ from its UFD value. We denoted by $\Delta_{p'}^2$ the sum of all these contributions, which is summed at the end of Eq. (119) above. Given that any contribution to this sum starts at 9, and the other contributions to the total function to be minimized are expected to be of order one, we have found that $W_{p'} \sim 0.1$ is enough to ensure that only a handful of our parameters are deviated by a bit more than 3 σ from their UFD values, and very rarely beyond that. We have also checked that the dispersive results and the data description do not vary substantially when adding this penalty, it just helps produce a CFD set of parameters without problematic outliers.

Let us then show the improvement in the fulfillment of dispersion relations by comparing the UFD versus CFD $\hat{d}_i^2$ for all our dispersion relations.

Thus, in Table 19 we have collected all the UFD $\hat{d}_i^2$ that we obtained for $\pi K \to \pi K$ dispersion relations in Section 4.4 and we have displayed them together with the $\hat{d}_i^2$ resulting from the CFD. The improvement is dramatic: except for the F^+ FDR, all the CFD averaged distances between input and output are one or less, showing a remarkable fulfillment of dispersion relations. The $\hat{d}^2$ for F^+ is 1.2, but in the top right panel of Fig. 27 we see that almost all the deviation comes from the region around and above 1.6 GeV. We already found this problem in [41] and it simply means that we are not able to obtain a consistent description of this FDR above 1.6 GeV if we still want to describe the data there. As discussed in Section 4.3, the deviation is due to the non-continuous matching between the data and the Regge asymptotic formulas, which are an "average" description, which occurs at 1.84 GeV, as shown in Fig. 25 (top left panel). Nevertheless, below 1.6 GeV the consistency is remarkable. The agreement is particularly impressive for the FDRs and the $\pi K \to \pi K$ unsubtracted HPWDR, taking into account the huge deviations they had in the UFD case.

A substantial improvement is also reached when using the CFD in the HPWDR for the $\pi\pi \to K\bar{K}$ channel, as shown in Table 20. We show results for the CFD$_C$ set, but the CFD$_B$ set is very similar. All these dispersion relations are well satisfied, with a $\hat{d}^2$ smaller than one, except for the g_0^0, whose $\hat{d}^2 = 2.1$, which is nevertheless half of what was found with the UFD. Notwithstanding, as shown in the top right panel of Fig. 32, almost the whole contribution to $\hat{d}^2$ for this dispersion

Table 19
Average $\hat{d}^2$ distances for the various $\pi K \to \pi K$ dispersion relations using the UFD or the CFD parameterizations. The improvement in the CFD case is remarkable.

FDR	UFD	CFD		HPWDR 0-sub	UFD	CFD
$F^+(s)$	9.0	1.2		$f_0^-(s)$	14.1	0.7
$F^-(s)$	8.2	0.7		$f_1^-(s)$	13.3	0.7
FTPWDR	**UFD**	**CFD**		**HPWDR 1-sub**	**UFD**	**CFD**
$f_0^+(s)$	6.2	0.6		$f_0^+(s)$	6.6	0.8
$f_0^-(s)$	1.6	0.1		$f_0^-(s)$	3.5	0.4
$f_1^+(s)$	3.3	0.1		$f_1^+(s)$	3.2	0.1
$f_1^-(s)$	5.1	0.8		$f_1^-(s)$	3.0	0.3

Table 20
Average $\hat{d}^2$ distances for the various $\pi\pi \to K\bar{K}$ dispersion relations. The improvement in the consistency of the CFD with respect to the UFD is remarkable. For the CFD, the only $\hat{d}^2 > 1$ is that of $g_0^0(t)$, but the largest contribution comes from the 10–20 MeV region right above the $K\bar{K}$ threshold and is mostly due to isospin breaking effects that cannot be accommodated within our isospin symmetric formalism. Otherwise, its CFD $\hat{d}^2$ is less than one.

HPWDR	UFD	CFD
$g_0^0(t)$	4.1	2.1
$g_2^0(t)$	1.7	1.0
$g_1^1(t)$ 0-sub	2.6	0.9
$g_1^1(t)$ 1-sub	5.2	0.2

relation comes from the region very near the $K\bar{K}$ threshold, which we are afraid cannot be described consistently within the isospin symmetric formalism. Beyond that threshold region, the agreement is once again remarkable and the averaged $\hat{d}^2$ would be roughly one.

This said it is not enough to check that the averaged distances $\hat{d}_i^2$ are close to one or less. It is also important that this global fulfillment of dispersion relations is uniform in their applicability domain. This is indeed the general case with the only two exceptions already noted. We illustrate this rather uniform consistency throughout the energy regions of interest in the right panels of Figs. 27 to 32.

In particular, in the right column of Fig. 27 we show the output of the two FDRs versus the input when using the CFD. The remarkable improvement in the whole energy region can be seen by comparing these figures to their UFD counterpart in the central column of the same figure. For both $F^\pm$ FDRs, the CFD input and output now overlap within errors, except in the region around 1.6 GeV. However, for the F^- FDR (lower right panel), the deviation in that region is only very slightly outside the uncertainty band, whereas for the F^+ (upper right panel) the deviation between input and output is rather large and we must conclude, as we already commented above and already found in [41] that, whereas the F^- FDR consistency is very good even up to 1.7 GeV, we cannot find a consistent description of the F^+ beyond $\sim$1.6 GeV unless we force a large deviation from data.

Let us now discuss the improvement in the consistency of the FTPWDR. Thus, in the right panels of Fig. 28 we show their input versus output when using the CFD, which has to be compared with their UFD counterparts in the central column of the same figure. Only for f_0^+ and f_1^- we can see that the input lies very slightly outside the uncertainty band in the region around 0.95 GeV. Thus, the consistency between CFD input and output for all partial-wave dispersion relations from fixed-t is rather uniform.

Something similar happens with the πK HPWDR. We show first the CFD case for the f_ℓ^- obtained with the unsubtracted F^- in the right panels of Fig. 29. The improvement with respect to the UFD case, shown in the central panel, is the most striking of them all. The huge inconsistencies of the UFD case have disappeared, and only beyond 0.9 GeV we can observe a very slight deviation outside the uncertainty band. Next, we show the once-subtracted CFD case in the right column of Fig. 30. Once again we find a very nice and quite uniform consistency within uncertainties in the whole energy region, correcting all the rather large discrepancies found in the UFD case (central panels).

The situation with the $\pi\pi \to K\bar{K}$ HPWDR is illustrated in the right columns of Figs. 31 and 32. Once again, the inconsistencies we found for the UFD set (central panels) disappear when using the CFD as input. The only exception, as already commented, is the region close to $K\bar{K}$ threshold, particularly for the g_0^0 wave, which is enhanced by the presence of the $f_0(980)$ resonance. We attribute this discrepancy to using an isospin-symmetric formalism, which is not well suited, at this level of precision, to the actual existence of two different thresholds for $K^0\bar{K}^0$ and K^+K^-. As a matter of fact, it is well known that isospin violation is enhanced around these thresholds due to the simultaneous presence of the $f_0(980)$

and $a_0(980)$ and their mixing [243,244]. But beyond, say, 10 or 20 MeV above t_K the agreement between input and output is very nice again.

One might wonder if our dispersion relations become strongly correlated among themselves and then we overweight their combined constraint. Of course, some correlation is unavoidable, because they share the same input. Also, having one more subtraction we introduce a dependence on a combination of threshold parameters through the additional subtraction constant, which is not really an independent parameter from the parameterizations. However, we have seen in the previous section that, by using different subtractions or fixed-t instead of hyperbolic dispersion relations, the input is weighted very differently, to the point that different dispersion relations have different dominant contributions, yielding different central values and uncertainties. In an ideal world with perfect data without uncertainties, they should be the same, but when we have data and uncertainties weighted differently on each dispersion relation, it is not trivial that they are all satisfied for all values of s. In particular, the W_i are chosen so that the final $\hat{d}^2$ is uniformly close or smaller than one in the whole applicability region. This said, the existence of correlations is seen because forcing the dispersion relations with worse unconstrained $\hat{d}^2$ (larger than 5 or 10) to be satisfied uniformly, produces a general improvement in the others, which, starting from not so large $\hat{d}^2$ end up with values much smaller than 1. This can be due to their correlations or to the different sizes of the uncertainties. Nevertheless, in practice, the penalty function of the dispersion relations that start with the smaller distances has little real weight, and its contribution to the constrain is minimal.

Of course, now that we have shown the remarkable consistency of the CFD, one might wonder if the constraints in the fits have spoiled badly the data description. We have already advanced that the CFD is still a fairly good description of data, although some deviations from the UFD to the CFD are worth noticing and we will comment on them next in detail.

When discussing the quality of the fits we should first recall that we have included systematic uncertainties in the data and that this makes the UFD have $\chi^2/dof \sim 1$ on the average. After imposing the whole set of 16 dispersion relations on the fits, and using the same procedures to calculate systematic uncertainties, we find that the CFD set has $\chi^2/dof \sim 1.6$. Thus, the price to pay to satisfy the dispersion relations is that our fits central values lie on the average about 1.25 standard deviation from data. This means that we will not find large deviations from CFD to UFD, except maybe in some particular waves and regions. However, the $\hat{d}^2$ per dispersion relations decreases from 5.5 for the UFD to 0.6 for the CFD.

5.2. $\pi K \to \pi K$ CFD

Let us start discussing how each $\pi K \to \pi K$ partial wave is modified in detail. Remember these are used only up to 1.84 GeV. Beyond that, we use Regge parameterizations.

5.2.1. CFD S-waves

As it can be seen in Fig. 7, the whole CFD S-wave barely changes with respect to its UFD in the whole energy region from $\pi K \to \pi K$ threshold up to 1.8 GeV. The very small deviations between the CFD and UFD central values are well within their uncertainties. However, that is for the $f_0^{1/2} + f_0^{3/2}/2$ combination and we will see next that whereas the $S^{1/2}$ barely changes, the $S^{3/2}$ suffers a somewhat larger variation.

$S^{3/2}$ partial wave

The CFD is shown in Fig. 6 and it mostly changes with respect to the UFD curve below 1 GeV, becoming less negative and moving away from the Estabrooks et al. data [5], which is clearly disfavored by the dispersive constraint. This is the main cause why the χ^2/dof goes from 2.6 to a bit above 3. As a consequence, we will see in Section 7.1.2 below that the CFD scattering length is also less negative and then remarkably consistent with its sum-rule value, contrary to the UFD case. In general this CFD variation makes the direct calculation of most threshold parameters and their combinations to agree much better with the more robust results from sum rules, as we will see in Section 7.1.2.

The CFD parameters have already been provided in Table 1. There we can see that they are rather similar to their UFD counterparts, except for B_2, which lies above 3 standard deviations away.

Up to here, we have been discussing our parameterization of the $S^{3/2}$-wave. However, one of the goals of this report is to provide robust and model-independent descriptions of $\pi K \to \pi K$ partial waves, by using the dispersive representation. We may wonder if we have achieved our goal, but so far we have shown the consistency of the dispersive representation for symmetric and antisymmetric $f_\ell^\pm$ waves. Consistency is then also expected for the f_ℓ^I in the isospin basis. Thus in Fig. 34 we show the three dispersive calculations of the real part of f_ℓ^I, namely, those coming from FTPWDR (orange) as well as unsubtracted or subtracted HPWDR (blue and red, respectively). The input from the CFD parameterization is represented by a continuous black line and the error bands represent the uncertainty on the difference between this input and the corresponding dispersive representation.

In particular, in the second row of Fig. 34 we see the dispersive results for $f_0^{3/2}$ in the elastic region. The UFD results (left) are largely inconsistent since the different dispersion relations for this partial wave do not agree with each other. However, we can see that this inconsistency disappears for the CFD (right), and all the dispersive representations overlap and agree with our direct use of the CFD parameterizations, which is therefore very robust.
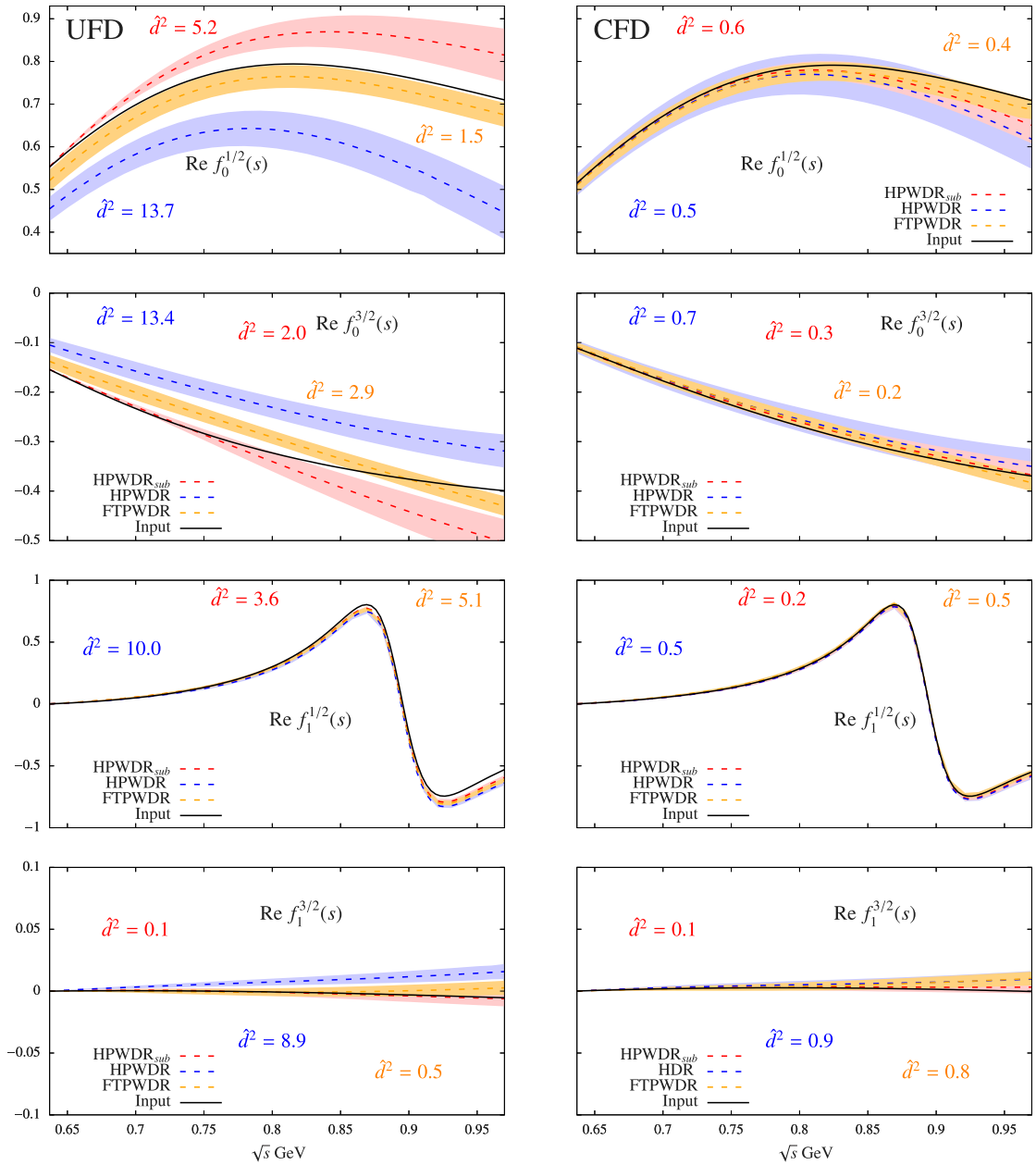
$S^{1/2}$ partial wave

Fig. 34. Dispersive and direct results for UFD (left) versus CFD (right) real parts of the $f_0^{1/2}(s), f_0^{3/2}(s), f_1^{1/2}(s)$ and $f_1^{3/2}(s)$ partial waves, in respective order from top to bottom. The uncertainty bands correspond to the uncertainty in the difference between the input and the respective dispersive representation, although we have attached them to their dispersive central value for simplicity. In the HPWDR and HPWDR$_{sub}$ cases the F^- HDR has been used unsubtracted and once-subtracted, respectively.

In the elastic region, shown in Fig. 21, the change from UFD to CFD is almost imperceptible. Actually, the χ^2/dof goes from 1.4 to around 1.8, and the UFD and CFD scattering lengths are compatible. In addition, we already commented that our simple parameterization of the elastic region does have a $\kappa/K_0^*(700)$ pole in the second Riemann sheet, which for the CFD now lies at $\sqrt{s_p} = (673 \pm 13) - i(331 \pm 5)$ MeV. It is relatively close to the UFD pole we gave in Section 4.1.2. However, it is interesting to note that, despite the CFD and UFD curves being almost indistinguishable in the real axis, their naive continuation to the complex plane displaces the real part of this pole position by almost two-standard deviations. This is an illustration of the instability of naive extrapolations of models to the complex plane, which cannot be trusted for precision studies, particularly for wide resonances. This is why a dispersive approach is needed to determine rigorously the $\kappa/K_0^*(700)$ pole position and residue, as we will review in Section 6 below.

The CFD versus UFD curves are shown in Fig. 22 in the complete energy range of the study. There we also see that in the inelastic regime they are also consistent within uncertainties. Once more we find almost the same χ^2.

The fact that we find fewer deviations between UFD and CFD than in our previous analysis in [41], is due to the improvement in the $S^{3/2}$-wave, needed to separate the $S^{1/2}$ component, and to our new fitting strategy, since when we constrain the fit now we also fit the data and not the parameters of the UFD fit as done in the past.

The CFD parameters of this wave were already given in Tables 2 and 3. Many of them barely move. However, there are several that change by around two standard deviations. Nevertheless, correlations among them leave the curves within one standard deviation.

So far, we have been discussing our parameterization of the $S^{1/2}$-wave. Concerning the dispersive outputs, in the first line of Fig. 34 we have gathered all the dispersive results for $f_0^{1/2}$ and compared them with the direct use of the CFD. On the left, we see that, although the results coming from FTPWDR are roughly consistent with the input, the two hyperbolic determinations are at odds with the UFD input and even more inconsistent among themselves. This is very important, for instance, for the determination of the $\kappa/K_0^*(700)$ pole, since, strictly speaking, that pole is only within the reach of HPWDRs, not the projected fixed-t. Therefore, the same UFD input would yield incompatible $\kappa/K_0^*(700)$ poles depending on what HPWDR is used. We will see this in detail in Section 6.

Nevertheless, all these problems disappear for the CFD parameterization (top right), since the three dispersive representations are consistent among themselves and with the CFD parameterization. We thus consider that the latter is a very robust and consistent description of this controversial wave.

5.2.2. CFD P-waves

The CFD result for the P-wave, obtained in the $f_P \equiv f_1^{1/2} + f_1^{3/2}/2$ combination was already shown in Fig. 11, versus data and the UFD. There, it can be noticed that the CFD and UFD are pretty similar in the elastic region but there is some visible deviation in the inelastic regime. Of course, since in the inelastic region the uncertainties are rather large, the deviation between CFD and UFD is within or only slightly off the uncertainty, except maybe beyond 1.6 GeV, where our dispersive representation does not reach. We, therefore, conclude that the CFD still provides a fairly reasonable description of data. In terms of the separated isospin contributions the situation is as follows:

$P^{3/2}$ partial wave

As it can be seen in Fig. 10, the $P^{3/2}$ phase barely changes from the UFD (orange) to the CFD (black continuous curve with the gray band). Recall that, for all means and purposes, this wave is elastic up to 1.8 GeV, and thus is completely determined by its phase. The χ^2/dof of the data, with the same systematic uncertainty estimations used for the UFD fit, changes from 1.2 for the UFD to around 2 for the CFD.

However, it can be noticed that the central value of the CFD phase stays positive from threshold up to $\sqrt{s} \simeq 1$ GeV. As we will see in Section 7.1, this makes the scattering length larger and somewhat closer to the sum rule and ChPT results. Actually, all our dispersive sum rules in Table 29 in Section 7.1, the predictions coming from the ones of Büttiker et al. [245] and the ChPT determinations [85,231] point to a slightly positive scattering length, even though the partial wave far from threshold has to be negative according to the existing data, which lie above 1 GeV.

The CFD parameters of this wave are listed in Table 4. They lie within less than one-third of the uncertainties of their UFD counterpart, except for $\hat{s}$, which signals the energy where the phase changes sign, which has moved by two standard deviations up to (0.88 ± 0.17) GeV^2.

The consistency of this CFD parameterization with its dispersive representations can be seen in the bottom right panel of in Fig. 34, whereas for the UFD case (bottom left) there was a considerable disagreement with the HPWDR when the F^- is used unsubtracted.

$P^{1/2}$ partial wave

Given that the $P^{3/2}$-wave is so small, the plot in Fig. 11 already tells us that the change from UFD to CFD for the $S^{1/2}$ is very mild.

In particular, using the same systematic uncertainty estimates, the χ^2/dof changes from 1.1 to around 2.1 in the elastic region, which is plotted in Fig. 23. Nevertheless, the data error bars are so small that the CFD and UFD difference is almost imperceptible to the eye, except in the region above the $K^*(892)$ nominal mass, which is mostly responsible for the increase in χ^2. This produces a non-negligible shift in the value of the phase at the matching point used by the Paris group [43]. As already explained in [41], we think this might contribute to the deviation from the data of the dispersive solution in [43], which is shown as a green line in Fig. 23.

The CFD parameters of the elastic part were given in Table 5 and although B_1 and the peak mass of the resonance m_r are consistent with their UFD counterparts, B_0 and B_2 lie more than two standard deviations apart. As we will see in Section 7.1, this has important consequences for the slope threshold parameter, which for the CFD becomes consistent with the sum rule and the ChPT estimate, whereas the UFD result was not.

The elastic parameterization of this wave also has a pole in the second Riemann sheet associated with the $K^*(892)$ resonance. For the CFD case this is found at $\sqrt{s_p} = (891 \pm 2) - i(27 \pm 1)$ MeV, which overlaps within uncertainties with the UFD pole we gave in Section 4.1.3. Although this is a narrow resonance and its pole parameters are relatively stable when extracted from simple parameterizations of the data around its peak, we will also provide a rigorous dispersive value in Section 6.

Once again we use Fig. 34 to illustrate the consistency and robustness of the CFD parameterization of this wave, displayed in the third row of panels. Despite the small uncertainty bands, it can be noticed that using the UFD (left), the input did not agree with the three dispersive representations. However, they all agree well within uncertainties for the CFD. We, therefore, consider that the description of the scattering data in the elastic region is very robust.

As already commented in Section 2 the elastic phase shift could also be obtained from other sources. In Appendix B we have studied this possibility, but the resulting CFD is almost indistinguishable from the CFD presented here.

In the inelastic region, the phase changes by a fair margin, better visible in Fig. 11, since the uncertainties are larger and the χ^2 increases from 0.9 up to somewhat more than 2. It seems that the $K^*(1410)$ interference with the other two resonances should be slightly different than that obtained from unconstrained fits.

The parameters of the inelastic CFD for this wave were already given in Table 6. There we can see that they are very similar to their UFD counterparts, but given the size of the uncertainties, the variations reach three standard deviations in a few instances.

5.2.3. CFD D-waves

Contrary to the previous cases, we have not used their partial-wave dispersion relations as constraints. Nevertheless, they are still modified because they are input for the forward dispersion relations and for the other partial-wave dispersion relations.

$D^{3/2}$ partial wave

Let us recall that this wave is tiny up to 1.8 GeV, barely reaching $-2°$ at most. The CFD result can be found in Fig. 13. It can be seen that it is fairly consistent with the UFD up to $\simeq 1.2$ GeV, but beyond that energy, the CFD prefers an even less negative phase, closer to $-1°$. As a result the data χ^2/dof increases from around 1.1 to around 1.6, which we consider still fairly reasonable. Most of this χ^2 comes from two outliers that were also inconsistent with the UFD and the rest of the data and, in contrast, the last data point which was an UFD outlier overlaps with the CFD within uncertainties.

The CFD parameters of this wave were given in Table 7 and they are all consistent with their UFD counterparts, except B_2, which lies roughly 2.5 deviations away.

In any case, the effect of this wave is always very small and is even smaller for the CFD.

$D^{1/2}$ partial wave

Given the fact that the $f_2^{3/2}$ wave is so small, the $f_D \equiv f_2^{1/2} + f_2^{3/2}/2$ data and curves shown in Fig. 14 illustrate in practice the $f_2^{1/2}$ changes from CFD to UFD. The modulus of this wave barely changes around the $K_2^*(1430)$ peak region. However, there is a visible deviation in the modulus far from the resonance and in the phase right after the peak. This should not be surprising since the data far from the resonance are not very reliable or consistent with each other. All in all, the χ^2/dof increases from 1.2 to roughly 3. Most of this deviation comes from the last three points above 1.6 GeV of the modulus measured by Aston et al. [6] as well as a few points which are outliers both for the UFD and CFD and quite distant from the other data. In general, it seems like the modulus clearly prefers the solution by Estabrooks et al. [5] over the one by Aston et al. [6], particularly at higher energies.

The CFD parameters of this wave have already been listed in Table 8 and they all change by about 2 deviations. Once more, finding somewhat larger changes in this wave should not be surprising given the poor quality and/or consistency of data outside the resonance peak, as shown in Fig. 14.

5.2.4. CFD F-wave

For this wave, seen in Fig. 15, there are only data above 1.5 GeV, and very few for the phase, all of them dominated by the $K_3^*(1780)$. Both the UFD and CFD yield a fairly good description of the resonance although the χ^2/dof increases from around 1 to 1.5. The CFD parameters are given in Table 9 and their change is sizeable, often beyond 2 standard deviations, although due to correlations the CFD and UFD overlap within uncertainties, as shown in Fig. 15.

5.3. $\pi\pi \to K\bar{K}$ CFD

After discussing $\pi K \to \pi K$, we turn our attention to $\pi\pi \to K\bar{K}$ partial waves to show how they changed from the UFD to the CFD set. Remember these are used only up to 2 GeV. Beyond that, we use Regge parameterizations.

5.3.1. CFD I = 0 S-wave

Let us recall that here we had two sets of incompatible data for the modulus and their corresponding UFD_B and UFD_C, which differ substantially below 1.47 GeV. They both shared the same UFD fit for the phase. Their respective CFD were already shown in Fig. 16.

It can be noticed that in Region II, i.e. above 1.47 GeV, the new CFD_B and CFD_C are once again perfectly compatible within uncertainties both with one another and with the UFD. The same can be said about the phase, although now in the whole energy region.

However, there are sizable changes in the modulus of both UFDs to their respective CFDs in "Region I", i.e. below 1.47. Actually, in both cases, the CFD modulus becomes smaller than its UFD counterpart below 1.25 GeV and larger between 1.3 and 1.47 GeV. This leads to a more pronounced local minimum around 1.2 GeV and a maximum around 1.35 GeV
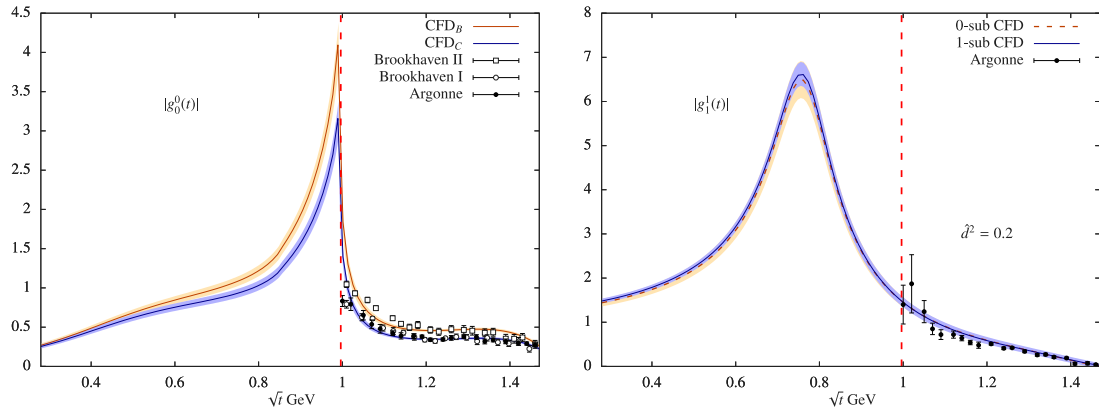
Fig. 35. Dispersive results for the modulus of the $g_0^0(t)$ and $g_1^1(t)$ partial waves using CFD as input. Left: The existence of two acceptable $g_0^0(t)$ CFD descriptions above $K\bar{K}$ threshold leads to two different solutions in the unphysical region. Right: Notice that the non subtracted and the once-subtracted dispersion relations for $g_1^1(t)$ are perfectly compatible even well below the physical region. We have calculated as an illustration the average $\hat{d}$ distance between the two dispersion relations, divided by the relative uncertainty. The vertical dashed line signals the $K\bar{K}$ threshold.

than in their respective UFDs. This double structure is flatter for the CFD_C. All in all the χ^2/dof increases from roughly 1 up to 1.4 for CFD_C, and up to 2 for the CFD_B. Overall the CFD seems more stable compared to our previous determination in [42] due to our constraining simultaneously $\pi K \to \pi K$ and $\pi\pi \to K\bar{K}$.

The parameters of both CFD fits for the phase were already given in Table 10. Note that although we only had one UFD phase, we now have two phases CFD_B and CFD_C. This is because each one is constrained together with their respective moduli, which are different. Nevertheless, the two CFD_B and CFD_C phases are almost identical and therefore indistinguishable in Fig. 16, both overlapping with the UFD. Consequently, their parameters only differ slightly and are always compatible well within uncertainties, both among themselves and with the UFD.

The parameters for the CFD_B and CFD_C moduli are given in Tables 11 and 12. In this case, the D_i parameters controlling the "Region I" clearly differ from their UFD counterparts, whereas the F_i are perfectly compatible with their respective UFD values.

Concerning the dispersive solutions, which we showed in the physical region in Fig. 32 for the UFD_C (Top center) and CFD_C (Top Right), the decrease in the modulus below 1.25 that we have just commented on makes the CFD consistent with the dispersive result. This is the main reason for the improvement in $\hat{d}^2$. Something similar happens for the CFD_B. However, as we have repeatedly noted, we cannot accommodate well the 20 MeV near threshold, which we think is due to our dealing with an isospin symmetric model. Nevertheless, apart from that region, our CFD result is very robust. As it happened in our previous work [42], there is no clear-cut preference for the CFD_B or CFD_C description in terms of the χ^2 and d^2. Fortunately, we have already shown that using one or the other as input for our other dispersion relations is irrelevant. In order to illustrate the results of these other dispersion relations, in this work we have chosen the UFD_C and CFD_C.

With $\pi\pi \to K\bar{K}$ and $\pi K \to \pi K$ data and dispersion relations alone we cannot exclude any of the two incompatible data sets. As it happened in [42], the "dip" solution of the elasticity, favored by the $\pi\pi \to \pi\pi$ dispersive analysis in [48], is consistent with the CFD_B assuming just the two coupled states $\pi\pi$ and $K\bar{K}$, whereas the CFD_C would need a non-negligible contribution from other states like, possibly, 4π. Nonetheless, as pointed out by one of the authors of [9] in [246] there could be some normalization ambiguity affecting the CFD_B solution. Indeed, the CFD_B deviates somewhat more from its UFD_B than the CFD_C from its UFD_C. In any case, as we concluded in [42], we have found that both data sets can be reasonably well described with consistent CFD parameterizations and none of them should be discarded a priori.

The CFD results in the unphysical region are shown in the left panel of Fig. 35, both for the CFD_B and CFD_C. Of course, there are no data in this region, but they can be compared to their UFD counterparts that we showed in the left panel of Fig. 33. Neither the CFD_C nor the CFD_B reveal significant changes.

Finally, let us recall that the phase of the tensor wave of the Brookhaven collaboration [236] is just a model that violates Watson's theorem near $K\bar{K}$ threshold and does not include an $f_2(1810)$, listed in the RPP, as we have done for that wave. Their phase is therefore different from ours, as shown in the right panel of Fig. 18. Unfortunately, this wave was used to extract the data on the $I = 0$ S-wave. We have discarded this phase near threshold in our fits, which satisfy then Watson's theorem, but one might wonder what would happen if we used our UFD tensor wave to extract the $I = 0$ S-wave phase instead of the Brookhaven model. Thus, we have also considered in Appendix C an alternative g_0^0 UFD and CFD. Fortunately, they only differ significantly from the UFD and CFD presented here in the phase, but not the modulus, and only above 1.6 GeV, i.e. outside the applicability range of our g_0^0 dispersive analysis, and in a region whose contribution is insignificant for other dispersion relations.

5.3.2. CFD I = 1 P-wave

As can be seen in Fig. 17, in the physical region, $g_1^1(s)$ barely changes from UFD to CFD. The only small changes, still consistent within uncertainties, occur in the modulus near the $K\bar{K}$ threshold and in the phase and modulus above 1.5 or 1.6 GeV, where scattering data cease to exist. As a consequence, the CFD parameters, already listed in Table 13, barely change with respect to their UFD values or vary within uncertainties. The only exceptions are γ_1, with a different sign and three standard deviations away from its UFD counterpart and $\Gamma_{\rho'}$, two sigmas away. This is not surprising since the $\rho''(1700)$ and $\rho'(1450)$ parameters are not very robust.

The consistency of this wave either with its unsubtracted or subtracted hyperbolic dispersion relation is remarkable, as already seen in the right panels of Fig. 31. Note in the left panels that the relative size of the contributions to these two dispersion relations is rather different, which makes us even more confident in the correct determination of this wave in the physical region.

Moreover, this new CFD parameterization also solves the inconsistency in the *unphysical* region that we showed in the right panel of Fig. 33. Recall that *using the same* UFD input, we obtained two incompatible predictions for the modulus of g_1^1 below $K\bar{K}$. Notice that there are no data in that region, however, it yields an important contribution to other dispersion relations. However, when we look at the CFD modulus, displayed in the right panel of Fig. 35, we see that there is an impressive agreement between the unsubtracted and subtracted results.

We, therefore, consider that this wave is very robust from the $\pi\pi$ threshold up the 1.47 GeV, i.e. *both in the unphysical and physical regions*. This is very important because this unphysical region is a relevant contribution to some dispersion relations, in particular for the $\pi K \rightarrow \pi K$ scalar waves and the precise determination of the $\kappa/K_0^*(700)$ pole that we will provide in Section 6.

5.3.3. CFD I = 0 D-wave

The CFD g_2^0 wave is almost identical to the UFD, as seen in Fig. 18. Actually, for the modulus, it may seem that there is only one curve with its uncertainty, but this is because it almost perfectly overlaps with the UFD. For the CFD phase, the central values deviate a little bit above 1.5 GeV, but always inside the uncertainty band, in a region where there are no data at all on the phase. Let us also remark that the CFD we found here is also similar to the one we obtained in [42].

Given this little variation, it is not a surprise that the CFD parameters, listed in Table 14, change so little with respect to their UFD values. Many parameters do not change at all, some in the last digit, and most within one standard deviation. Only two of them lie above 2 standard deviations away.

Let us also recall that our solution does not suffer from the violation of Watson's theorem in the model used by [8] for the phase. In addition, we have also included an $f_2(1810)$ resonance, to describe the small bump in the modulus in that region whose shape is clearly visible in the phase, which therefore deviates from the Brookhaven-I model above 1.5 GeV. Since Brookhaven-I used this tensor wave to extract the scalar–isoscalar wave, the use of our solution would have lead to different g_0^0 data. This alternative solution is studied in Appendix C. Fortunately, using it does not change our results in the region of applicability of our dispersive analysis.

5.4. High energy region. CFD regge parameterizations

Finally, our CFD Regge parameterization also does not change much. This can be seen in Fig. 25. All UFD central curves lie within the uncertainties of their CFD counterparts. The only exception is the reggeized ρ resonance contribution to $\pi K \rightarrow \pi K$ scattering (bottom left panel), whose contribution clearly lies below the UFD curve. We already found this decrease when imposing only FDRs to $\pi K \rightarrow \pi K$ [41]. Actually, it is responsible for a substantial reduction in the $\hat{d}_{F-}^2$ FDR. It is not very surprising that this contribution, governed by the factorization constant $g_{K/\pi}$, suffers a sizable change, since as already commented when we introduced it, there is little information on it, and its extraction from factorization is somewhat more complicated than for other resonances, see [143].

The Regge parameters for the CFD are listed in Tables 15 and 16. Recall that those parameters that can be fixed using reactions other than πK or $\pi\pi \rightarrow K\bar{K}$ scattering are kept fixed for both UFD and CFD and are given in Table 15. In contrast, those parameters involving strangeness have been allowed to vary in the fits and are given in Table 16. Note that those related to the reggeized-K^* exchange barely change from UFD to CFD. In contrast, the factorization constant $g_{K/\pi}$ decreases by slightly more than two standard deviations, consistently with the observed decrease in the reggeized-ρ contribution commented above. The Pomeron and f_2 factorization constants, $f_{K/\pi}$ and r, also change, but they compensate each other and the effect of this change is small as shown in the top left panel of Fig. 25.

6. Strange resonances and the $\kappa/K_0^*(700)$

6.1. State of the art

Despite the fact that Quantum Chromodynamics (QCD) was formulated almost half a century ago the existence and/or precise properties of some of its lowest-lying states is still under debate, in particular in the strangeness sector. A reliable determination of these strange resonances is crucial for both their own classification in multiplets, as well as for our understanding of intermediate-energy QCD interactions and the low-energy chiral perturbation theory regime. In addition,

these strange resonances appear as a result of πK scattering or re-scattering, and contribute as final states to many of the hadronic processes with net strangeness. Hence, the shape of heavier decays, or their Dalitz plot, depends upon the precise determination of these low-energy interactions. In particular, this is the case of the many hadronic decays of the heavy B and D mesons, whose description nowadays relies on resonance-exchange models. Nonetheless, many of the modern experimental efforts are being directed towards these heavier processes, in particular CP violation or new physics searches. Thus a precise knowledge of these strange resonances is mandatory for model-independent studies of heavier sectors.

Besides their interest as ingredients to describe other processes, the properties and nature of many of these light resonances have been controversial for decades. This is the case of the famous $\kappa/K_0^*(700)$ resonance, which "still needs confirmation" according to the RPP [233]. The confirmation of the existence of this resonance is crucial for completing the lightest scalar nonet of mesons and, given its clear similarities with the $\sigma/f_0(500)$ resonance, it would rule out the $\sigma/f_0(500)$ glueball interpretation, already quite disfavored in the literature (see [13] for a review). Additionally, there are six other strange resonances that dominate $\pi K \to \pi K$ scattering amplitudes below roughly 1.8 GeV. These are: the scalar $K_0^*(1430)$, the vectors $K^*(892)$, $K^*(1410)$ and $K^*(1680)$, the tensor $K_2^*(1430)$ and the $\ell = 3$ resonance $K_3^*(1780)$. Most experimental studies on these resonances are based either on πK scattering experiments studying reactions like $KN \to \pi KN'$ [5,6,117,247–254] or πK rescattering from heavy-meson decays [52,123,255,256]. We have gathered in Fig. 36 the pole determinations of the $K_0^*(1430)$, $K^*(1410)$, $K_2^*(1430)$ and $K_3^*(1780)$, as compiled in the Review of Particle Physics [95]. The large spread of values for each resonance and the existence of multiple incompatible determinations are evident. The main problem is that almost all of those values suffer from systematic deviations and crude model extractions. Their biggest source of systematic uncertainty is that these resonance poles have not been extracted from a sound analytic continuation of the T-matrix to the complex $s_p = M - i\Gamma/2$ plane, but, for the most cases, their listed parameters come out from some sort of Breit–Wigner parameterization. This is not a model-independent definition of a resonance, but a narrow-width approximation for isolated resonances and it has been applied to these strange resonances even though they are not particularly narrow, overlap often with other nearby resonances, or lie close to relevant thresholds. Moreover, even the definition of the Breit–Wigner mass and width has a sizable dependence on the particular choice of Breit–Wigner parameterization, as well as on the background present in the process that is being fitted. In the following sections we will describe and summarize how analytic techniques can improve our amplitude analyses and produce robust and yet simple ways of determining resonance parameters.

Regarding lattice QCD calculations on the strangeness sector, the first dynamical QCD determinations of resonances have only been published in the recent past. There exist several analyses regarding the prominent $K^*(892)$ resonance using $N_f = 2 + 1$ staggered quarks [267] and $N_f = 2$ Wilson quarks [70,268,269]. The $K^*(892)$ is a rather narrow resonance and the use of a naive Breit–Wigner shape may be justified given the available precision, making its extraction from lattice QCD easier. Nonetheless, a precise determination of the parameters of this resonance is crucial from a lattice QCD perspective, as it allows to compare different approaches and to extrapolate these results to physical pion masses, where this channel is very well determined.

More challenging is the analysis and determination of the $\kappa/K_0^*(700)$ resonance, for which a very elaborated use of the Lüscher formalism is required [75,270–286]. Recent lattice QCD analyses, including $N_f = 2 + 1$ Wilson quarks [71,72, 100,287] have been able to extract both the S and P-waves at various quark masses. We already illustrated their phase shifts in the introduction in Fig. 3. For nonphysically heavy pions [100,287], the $\kappa/K_0^*(700)$ was found as a virtual bound state, compatible with unitarized NLO ChPT predictions [102,288]. Nevertheless, it seems that once the pion mass starts approaching the physical value the extraction of the $\kappa/K_0^*(700)$ pole by analytic continuations becomes more unreliable. However, at higher pion masses the $\kappa/K_0^*(700)$ resonance appears robustly and stably as a result of fitting the partial wave. Other exploratory studies of the $\kappa/K_0^*(700)$ and $K^*(892)$ resonances obtained from lattice QCD can be found in [91,268,289–292]. Heavier strange resonances become a great challenge for lattice QCD at close to physical pion masses, as they can in principle couple to several multi-body hadron channels. However, some of these aforementioned works have been able to determine their parameters at higher pion masses.

6.2. Analytic techniques for inelastic resonances

Let us first discuss the inelastic strange resonances. As pointed out throughout the previous sections, a dispersion relation is the most rigorous tool for performing the analytic continuation of a given amplitude. Nevertheless, we do not know a simple set of partial-wave dispersion relations that could be applied up to arbitrarily high energies. We saw in Section 3 that πK partial-wave dispersion relations are only applicable up to roughly the beginning of the inelastic region [164,176]. More complicated dispersion relations which improve the convergence region exist for $\pi\pi$ scattering [293–298], although they have never been applied to $\pi\pi$ experimental data. No equivalent set of equations has been derived so far for πK scattering.

Moreover, even if we do have a dispersive representation of a partial wave in a given area, it is formulated in the first Riemann sheet, whereas resonance poles lie in the second or other Riemann sheets. In Section 1.3, and only for the elastic case, we provided a simple formula, Eq. (19), to access this second Riemann sheet and to obtain the pole position using Eqs. (20) and (21). However, in the inelastic case, since more channels are open, giving access to more sheets, there is no straightforward relation between the first and the contiguous or second sheet. Only within certain approximations, there
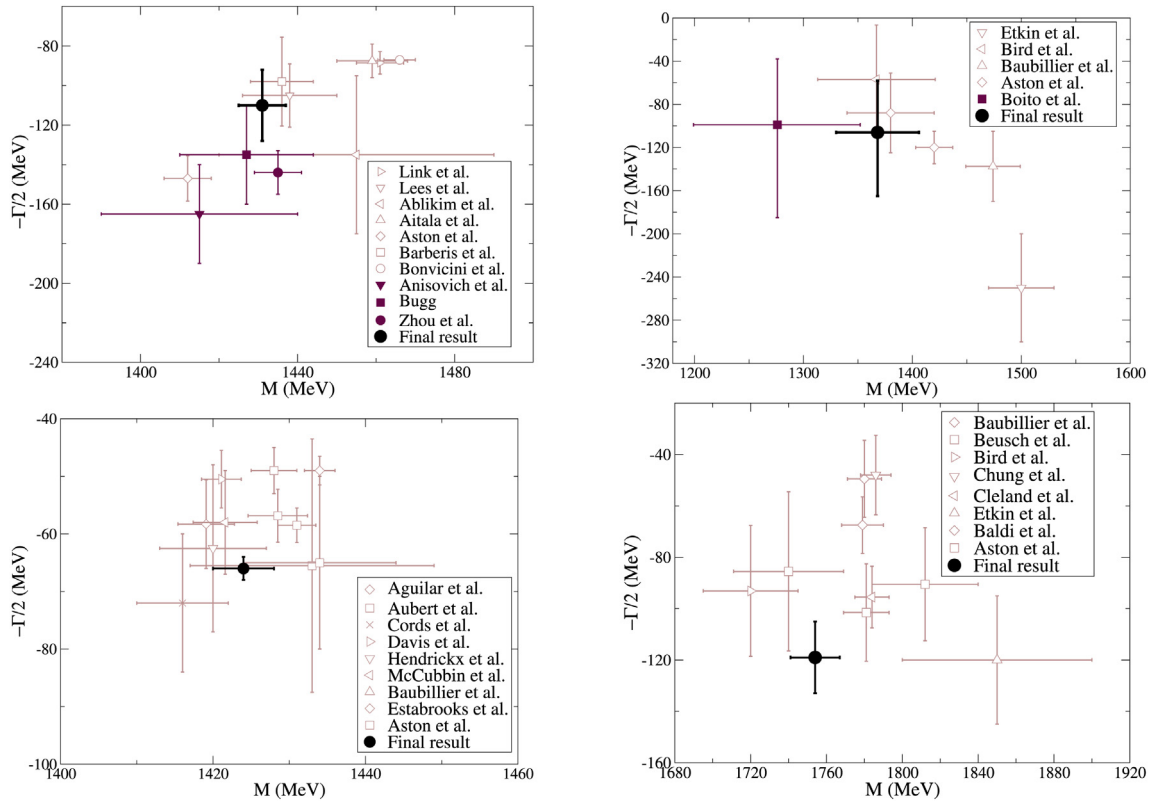
Fig. 36. Determination of the $K_0^*(1430)$ (top-left), $K^*(1410)$ (top-right), $K_2^*(1430)$ (bottom-left) and $K_3^*(1780)$ (bottom-right) poles obtained using the Padé sequence method ("Final Result" [99]). Other values correspond to those listed in the RPP compilation as main results [233], Zhou et al. [257], D.Bugg [258], Anisovich et al. [259], Bonvicini et al. [123], Barberis et al. [260], Aitala et al. [52], Ablikim et al. [255], Lees et al. [256], Link et al. [133], Boito et al. [261], Baubillier et al. [262], Bird et al. [263], Etkin et al. [264], Estabrooks et al. [5], Mccubbin et al. [250], Hendrickx et al. [251], Davis et al. [247], Cords et al. [249], Aubert et al. [265], Aguilar et al. [248], Baldi et al. [252], Cleland et al. [254], Chung et al. [253], Beusch et al. [266].
Source: Figures taken from [99].

are simple equations to write the amplitude in different sheets, but they not only require the knowledge of the amplitude in the first, but also the amplitudes to the other accessible channels. This is relatively simple to implement in coupled-channel models restricted to two-body scattering in just a few different channels, particularly if all the complications of left and circular cuts can be neglected, which is a fair approximation in the inelastic regime (but not in the elastic one). Nevertheless, remember that we aim to avoid model dependencies.

For the reasons just explained, there is a growing interest in exploiting other analytic techniques to extract resonance poles, which could eliminate or produce smaller systematic uncertainties than those of simple model-based extractions. We list here a few of the most successful approaches: The conformal mapping expansion [226,227,299], which includes the dynamical cuts into a conformal mapping variable, thus producing, as a result, a simple fit that could partially mimic some of the analytic requirements. These mappings have been used in our UFD and CFD fits as explained in Section 4.1. Other successful techniques are the Laurent [300,301] and the Laurent–Pietarinen [302–306] methods mostly applied to baryon resonances, which disentangle the resonance pole (Laurent expansion), from a conformal map (Pietarinen expansion) over the partial waves. Two other methods have been used to extract low-energy mesonic resonances. The first one makes use of the Schlessinger continued-fraction method [307] and has been successfully implemented in several different problems [308–310]. Finally, there is the method of sequences of Padé approximants [99,311–313], which will be the central topic of this subsection. They are all different approaches to determine resonance poles without assuming any model relating their coupling to their width parameters. Thus they are much less model-dependent and robust than the usual Breit–Wigner approach used so far in most determinations, very often not even meeting the Breit–Wigner applicability conditions.

All these analytic methods require the knowledge of the scattering amplitude, employing data or a previously fitted parameterization. However, as explained in detail in the introductory sections, determining the experimental data on meson–meson experiments is a complicated task, plagued with systematic uncertainties. As a result, fitting a model to the original data samples may not be robust enough for some of these resonances, on top of which none of these models implement analyticity, crossing, and unitarity at the same time so that the original fits would be partially lacking first-principle constraints. Most often they only consider the scattering of two-body states.

A satisfactory solution follows from applying these analyticity techniques over a parameterization previously constrained to satisfy dispersion relations, as the CFDs obtained either for $\pi\pi$ [48] or πK [41] scattering. This approach was successfully carried out in [99,312,313], respectively. Thus, right below, we summarize the Padé-sequence method and results [99] when applied to πK.

The Padé approximant of order $[N/M]$ of a function $F(s)$ is defined as a rational function that satisfies

$$P_M^N(s, s_0) = \frac{Q_N(s, s_0)}{R_M(s, s_0)} \simeq F(s) + O\left((s - s_0)^{M+N+1}\right), \tag{120}$$

where $Q_N(s, s_0)$ and $R_M(s, s_0)$ are polynomials in s of Nth and M^{th} degree, respectively, and the expansion is centered around a given point s_0.

According to the Montessus de Ballore theorem [314] this sequence of Padé approximants can be used to reach the next continuous Riemann sheet of an amplitude, which is where resonance poles exist [99,311–313]. Notice again that these Padés do not assume any model relationship between the pole position and residue, so that there is way less model dependence when extracting resonances with this method.

For simplicity, in this section we focus on the extraction of isolated resonances, although more resonances can be included in a straightforward way [99]. For isolated poles, the denominator $R_M(s, s_0)$ should be of first degree, and thus the Padé approximant is defined as:

$$P_1^N(s, s_0) = \sum_{k=0}^{N-1} a_k(s - s_0)^k + \frac{a_N(s - s_0)^N}{1 - \frac{a_{N+1}}{a_N}(s - s_0)}. \tag{121}$$

If one expands the amplitude as a Taylor expansion in the real axis around s_0 then the constants $a_n = \frac{1}{n!}F^{(n)}(s_0)$ are given by the nth derivative of the amplitude. Therefore the pole and residue read

$$s_p^N = s_0 + \frac{a_N}{a_{N+1}}, \quad Z^N = -\frac{(a_N)^{N+2}}{(a_{N+1})^{N+1}}. \tag{122}$$

Note that, customarily, the coupling of a resonance to an amplitude is defined as follows:

$$|g|^2 = \frac{16\pi(2\ell + 1)|Z|}{[2q(s_p)]^{2\ell}}, \tag{123}$$

where $q(s)$ is the center-of-mass momentum of the scattering system and ℓ the angular momentum of the partial wave.

If the resonance is not isolated, i.e., there are several overlapping resonances or nearby thresholds, extra poles can be introduced into the Padé by increasing the degree of $R_M(s, s_0)$. These new poles will take account of the other resonances or they will mimic the other analytic structures present in the amplitude. In principle, nearby thresholds are associated with cuts in the complex plane, which can be approximated up to the desired accuracy by including a sufficiently large number of extra poles.

The methodology implemented in [99] to extract strange resonances from the CFD fit in [41] can be summarized as follows:

- We define the variation in the pole position when changing our calculation from N^{th} to $(N + 1)^{th}$ degree. Thus, for each N, starting from $N = 1$, we define $\Delta\sqrt{s_p^N}_{sys} \equiv \left|\sqrt{s_p^N} - \sqrt{s_p^{N-1}}\right|$, which is calculated for a grid of s_0 in a big region surrounding the resonance. We consider our best s_0 as the one which minimizes these uncertainties, thus improving the convergence of the series.
- The statistical uncertainty is thus added employing a Montecarlo re-sampling over the fits.
- We truncate the Padé sequence at a given N when $\Delta\sqrt{s_p^N}_{sys}$ is considerably smaller than the statistical uncertainty.

This procedure makes use of the smallest possible number of derivatives, which usually offers better stability and smaller deviations for the statistical uncertainties. Unfortunately, different parameterizations compatible within uncertainties with the CFD could yield somewhat different derivatives. This might be the only source of some relatively mild model or parameterization dependence, which we will consider as an additional systematic error. Thus, in order to estimate this systematic uncertainty, we extract the resonance pole implementing the whole Padé sequence method but using different functional forms fitted to describe the CFD within uncertainties. We consider this approach to produce a robust, precise determination of resonance parameters and their uncertainties but avoiding or at least reducing considerably any model dependence.

Our recent results applying this Padé sequence method are shown in Fig. 36 for the poles of strange resonances appearing in the πK inelastic region below 1.8 GeV. They can be compared to the values listed in the RPP [233]. This includes the scalar $K_0^*(1430)$, the vector $K^*(1410)$, the tensor $K_2^*(1430)$ and the $\ell = 3$ resonance $K_3^*(1780)$. The $K^*(892)$ and $\kappa/K_0^*(700)$ have also been extracted as shown in Table 21. However, these two are not discussed here as they will be discussed in more detail in the next section, since elastic resonances can be calculated directly from partial-wave dispersion relations. From Fig. 36 it can be noticed that, even with the attached systematic uncertainty, our analytic

Table 21
Poles obtained from the Padé sequence method [99] using as input the CFD results obtained in [41]. The uncertainty for $\sqrt{s_p}$ and $|g|$ include statistical and theoretical (systematic) errors.

	$\sqrt{s_p}$ (MeV)	$|g|$
$\kappa/K_0^*(700)$	$(670 \pm 18) - i(295 \pm 28)$	(4.47 ± 0.40) GeV
$K_0^*(1430)$	$(1431 \pm 6) - i(110 \pm 19)$	(3.82 ± 0.74) GeV
$K^*(892)$	$(892 \pm 1) - i(29 \pm 1)$	(6.1 ± 0.1)
$K^*(1410)$	$(1368 \pm 38) - i(106^{+48}_{-59})$	$(1.89^{+1.77}_{-1.34})$
$K_2^*(1430)$	$(1424 \pm 4) - i(66 \pm 2)$	(3.23 ± 0.22) GeV^{-1}
$K_3^*(1780)$	$(1754 \pm 13) - i(119 \pm 0.14)$	(1.28 ± 0.14) GeV^{-2}

determinations, which do not assume a specific model parameterization, are competitive in precision with the other existing values.

We want to remark that the region occupied by different determinations of each resonance pole in Fig. 36 is much larger than the RPP estimated average. One of the reasons is that only the values with solid symbols are T-matrix poles and used to obtain such an estimate. The rest are just Breit–Wigner parameters, which as discussed above are not a model-independent definition of a resonance, but just a narrow-width approximation valid for isolated resonances. Let us remark that most of these extractions rely on some, but not always the same, Breit–Wigner-like parameterization since it is often modified with further crude model assumptions. In particular, often these parameterizations include barrier factors, or fits with summations of Breit–Wigner forms which do not fulfill unitarity, etc... thus producing big systematic spreads. Notice also how the determination of the width for all these resonances is generally in worse shape than their mass (note that the mass and width scale is different). This is not surprising since the apparent width can become easily process-dependent when not extracted from a rigorous analytic continuation to the pole. Our analytic techniques avoid all these caveats and therefore yield a robust determination of the parameters, whose accuracy is competitive too, if not better than, present estimates.

Finally, this formalism can be adapted in a straightforward way to study other inelastic channels involving meson–meson scattering processes. In a possible future application, we are planning to apply the method to the $f_0(1370)$, $f_0(1500)$ and $f_0(1710)$ resonance poles using as input the dispersively constrained parameterizations of $\pi\pi \to \pi\pi$ [98] and the CFD of $\pi\pi \to K\bar{K}$ that we have just provided here in Section 5.

6.3. Dispersive determination of the $\kappa/K_0^*(700)$ resonance from data

"The weight of the evidence should be proportioned to the strangeness of the facts"

Principle of Laplace, as restated by T. Flournoy in "India to the Planet Mars" (1900),

when commenting Laplace's "Essai philosophique sur la probabilité" (1825).

"We are beginning to think that κ should be classified along with flying saucers, the Loch Ness Monster, and the Abominable Snowman".

A.H.Rosenfeld et al. "Data on Particles and Resonant States" review (1967) [315].

As explained above the situation regarding the $\kappa/K_0^*(700)$ resonance has been debated for several decades, partially because of how unstable its determination is. First, there are several different extractions relying on relatively simple models [16,19,20,23–26,29,31–37,40,316–320]. Of course, as repeatedly explained, the use of conflicting data sets, which do not fulfill first principle's requirements, together with the large model dependencies produce a huge spread of results as shown in Fig. 37. This is once again the situation explained in the previous section, and in Fig. 36, where simple models can produce huge systematic spreads.

Furthermore, the $\kappa/K_0^*(700)$ pole is one of the widest resonances and therefore its pole lies deep in the complex plane. Consequently, as illustrated in the top panel of Fig. 20, the region of its nominal mass is as close to the pole as it is to the πK threshold, the Adler zero, or even the left and circular cuts. Hence a precise and reliable extraction cannot be fully understood without a model-independent way of performing the necessary analytic continuation into the complex plane (for recent reviews we refer to Ref. [13,218]), making sure that all the required analytic structures are accounted for. Of course, those models that include some of these basic features, as well as unitarity – which is essential for a resonant behavior – and some reasonable input from data, generically produce a pole that is not too far from its actual position. Note that it is important to check that the pole lies within the applicability region of the partial-wave expansion in the complex plane (see Appendix D). At any rate, models cannot be used for a precise description of this resonance.
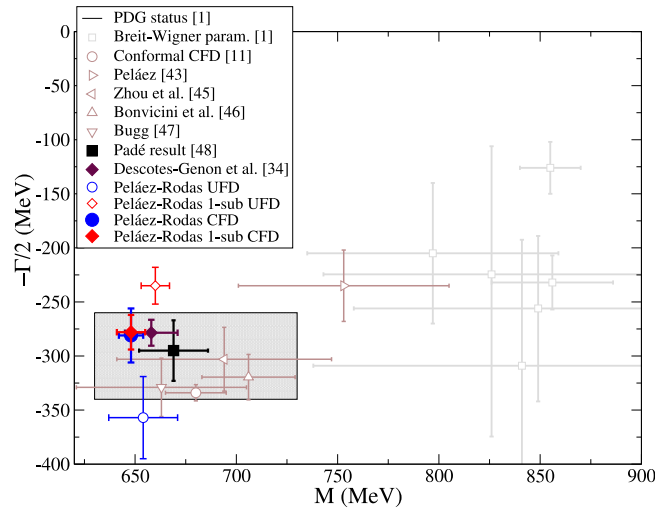
Fig. 37. Determinations of the $\kappa/K_0^*(700)$ pole in the complex plane as illustrated in [47]. Of course, the numbering of the references in [47] is not the same as in here, which we provide next. In particular, Breit–Wigner parameterizations are taken from the RPP compilation [233] (called PDG in [47]), which also includes: Descotes-Genon et al. [97], Bonvicini et al. [123], Bugg [321], Peláez [34], Zhou et al. [257] and the "Padé Result" [99]. The conformal CFD is the simple analytic extrapolation of our parameterization in [41]. The "PDG status" shaded rectangle covers the mass and width estimate in the RPP. Our dispersive extractions of the $\kappa/K_0^*(700)$ pole are also included, using as input for the PWHDR either the UFD or CFD parameterizations. Red and blue points use for the F^- amplitude a once-subtracted or an unsubtracted dispersion relation, respectively. Notice that even when using dispersive approaches the extraction is not fully stable, and the UFD values are inconsistent with one another and deviated by around $2\,\sigma$ from the CFD ones. Only once Roy–Steiner equations are imposed as a constraint for the CFD parameterizations, both pole determinations fall on top of each other, thus producing a negligible systematic uncertainty, as explained in the text.
Source: Figure taken from [47].

All pole positions listed in Fig. 37 are taken from the RPP [233], although there are many other values, like those quoted just above. Most of these determinations (light gray) are simply Breit–Wigner parameters obtained as a result of several fits to different processes. However, not only this is not a model-independent definition of a resonance pole, but it is actually a wrong approximation. Recall that the Breit–Wigner formula is devised for narrow resonances well isolated from other analytic features. From Fig. 20, it is evident that it is not suitable for a resonance so deep in the complex plane, so close to a threshold and other singularities, and so close to the Adler zero imposed by chiral symmetry. The spread of the results in Fig. 37 using a Breit–Wigner formalism speaks for itself about this inadequacy. The rest of the results shown in the figure for the $\kappa/K_0^*(700)$ resonance include at least some basic features arising from QCD [99,123,257,258,321,321–324]. Some others resort to the unitarization of ChPT either by using the N/D or Inverse Amplitude Method (IAM) [23,25,26,34,102] (For recent reviews of ChPT unitarization see [13,218,221,222]). Generically, these approximate the left-hand cut contributions at a given order in ChPT, and make use of dispersion relations to unitarize the ChPT amplitude of a given order. An alternative way of implementing dispersion relations over ChPT in this channel is the one of the Beijing group [208,257], which produces a rather stable result for the pole position. Finally a very sound determination comes from the dispersive study of the Paris group [97]. Here the authors make use of a solution to FTPWDR in [43] obtained without using data in that energy region for the S and P waves. Then they use that solution as input into HPWDR to extract the $\kappa/K_0^*(700)$ resonance. It is also very relevant to remark that in their analysis they showed that the $\kappa/K_0^*(700)$ pole lies within the applicability range of their choice of HPWDR.

On the lattice QCD front, this resonance has also been tackled recently, following developments in the calculation of meson–meson scattering phase shifts, which we illustrated in Fig. 3. Unfortunately, the pole is not a direct observable, but once again it has been extracted using models. Nevertheless, as can be seen in [100,287], at $m_\pi \simeq 400$ MeV the $\kappa/K_0^*(700)$ appears as a virtual bound state, compatible with what we know from unitarized NLO ChPT [102,288]. However, using lighter pion masses between 200 and 400 MeV the pole extraction becomes rather unstable [72], even though the basic features of the partial wave are well described, as seen in Fig. 3. In the aforementioned work the Lüscher formalism [325] was extensively used to produce many different energy levels for each pion mass, which produces a very constrained result on the real axis. The authors of this study, when referring to lighter m_π, stated on the scalar wave that "Even with precise information about the amplitude for real energies, the analytic continuation required to reach any pole is sufficiently large that a unique result is not found" [72]. This supports our idea that a more elaborated, dispersive analysis is needed at lower m_π to extract accurate information when performing analytic continuations. This same behavior can be seen for the $\sigma/f_0(500)$, where for heavier m_π the extraction is pretty stable [289], but becomes rather unstable for pion masses near the physical one [74,288,326].

It is not so clear how large the effect of the Adler zero is when the pion mass is really heavy, and these resonances appear as bound or virtual bound states. Nonetheless, the main problem when dealing with lighter extractions is that
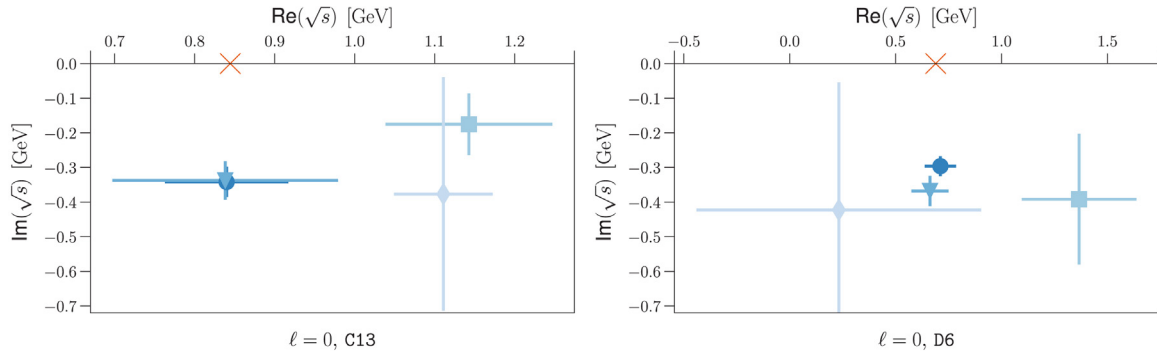
Fig. 38. $\kappa/K_0^*(700)$ poles from lattice calculations [101] with $m_\pi \simeq 317$ MeV (left) and $m_\pi \simeq 176$ MeV (right). Note how the parameterizations including the Adler zero (darker markers) have a smaller spread when the pion mass is lighter, and they produce little systematic spread between themselves.
Source: Figure taken from [101].

the subthreshold features and left-hand cuts start playing a non-negligible role in the extraction. Thus one needs to include as much information as possible to get a reliable determination of the resonance pole position. There exists a very recent lattice QCD determination of the $\kappa/K_0^*(700)$ resonance at close-to-physical pion mass [101]. We have included their figure as Fig. 38 to illustrate our previous explanation. In the left panel, the heavier pion-mass results ($m_\pi \simeq 317$ MeV) are depicted, whereas the lighter pion-mass results are shown on the right panel ($m_\pi \simeq 176$ MeV). Of the four different parameterizations used by the authors, the darker ones are compatible among themselves, and their uncertainties shrink when the pion mass decreases. These two include the Adler zero at LO in ChPT, which produces a significant improvement when extracting the resonance, as the lighter m_π, the closer to the resonance lies the Adler zero. The other two parameterizations are built with K-matrix and effective range formalisms. This picture may illustrate just how challenging the extraction of broad resonances is, and why incorporating first principle features from QCD into our amplitude analyses is paramount to the robust determination of the QCD spectra. Lattice QCD collaborations will be able to access close-to-physical pion mass in the near future and thus, to extract their resonance poles, an approach based on constraining the amplitudes and the data, like ours, seems to be a must.

Nevertheless, despite all this growing support for its existence and properties, the $\kappa/K_0^*(700)$ still carries the "Needs Confirmation" label in the RPP [95]. Thus, following the quotation at the beginning of this subsection, we have very recently proportioned further weight of evidence in support of the existence and precise parameter determination of this strangeness carrying resonance.

Let us first remember that in Eqs. (53)–(55) we have provided several partial-wave projected fixed$-t$ and hyperbolic dispersion relations (FTPWDR and HPWDR, respectively) to constrain the partial waves. In principle, one could think about using FTPWDR rather than HPWDR, because their dependence on $\pi\pi \to K\bar{K}$ is much smaller. However by comparing their respective applicability domains in Fig. D.49 versus Fig. D.51 we see that, even though their applicability on the real axis is rather similar and overlaps widely with the region of the $\kappa/K_0^*(700)$ nominal mass, the domain of validity in the complex plane of the FTPWDR is much smaller and, unfortunately, it cannot reach the position of the $\kappa/K_0^*(700)$ pole. This is why the Paris group, as so do we, have to resort to HPWDR. Note that the choice of the a parameter defining our hyperbolae is paramount. As explained in Section 3 and Appendix D, we could think of changing a to increase the applicability region of the HDR on the real axis, as we have actually done for $\pi\pi \to K\bar{K}$. However, this would narrow down the applicability region in the complex plane, as depicted in Fig. D.51, leaving out the $\kappa/K_0^*(700)$ pole. Thus a compromise between the best a on the real axis and the complex plane must be found, which we consider satisfactory for $a = -10 m_\pi^2$. Of course, right outside their applicability domains, we do not expect an abrupt disruption, but just a smoothly increasing disagreement between both sides of the dispersion relations, as the discrepancies are produced by the πK box diagrams shown in Fig. D.47. Nevertheless, the rigorous determination of the pole with precision demands that we remain inside the applicability domain.

Thus, in [47] we have used our data parametrizations inside the HPWDR and we have found that there is indeed a pole in the expected region in the scalar channel with isospin 1/2. The values of the pole position and the modulus of the coupling are shown in Table 22, compared with other existing determinations in Fig. 37.

Note that we have calculated the poles using both the HPWDR obtained with one or no subtractions for the antisymmetric F^- amplitude (red and blue symbols in Fig. 37). In addition, we have used as input both the UFD (hollow symbols) and CFD (solid symbols).

The first striking feature when we observe our dispersive results in that figure is that the results using the UFD as input with one or no subtractions are incompatible with each other. Actually, the two poles, which should be the same, differ by around 3–4 σ even when they are obtained from the same input. This outcome comes from the fact that, as already seen in Section 5.1 and shown in Fig. 34, the UFD is inconsistent with the dispersive representation. This result

Table 22
Comparison between various poles and residues of the $\kappa/K_0^*(700)$ resonance. The last two lines are our dispersive outputs using the CFD as input. We consider the last line as our best result. Here we also provide the phase (in radians) of the coupling.
Source: Table taken from [47].

	$\sqrt{s_{pole}}$ (MeV)	$|g|$ (GeV)	ϕ_g (rad)
$K_0^*(700)$ [97]	$(658 \pm 13) - i(279 \pm 12)$	–	–
$K_0^*(700)$ [99]	$(670 \pm 18) - i(295 \pm 28)$	4.4 ± 0.4	–
$K_0^*(700)$ 0-sub	$(648 \pm 6) - i(283 \pm 26)$	3.80 ± 0.17	-1.50 ± 0.05
$K_0^*(700)$ 1-sub	$\mathbf{(648 \pm 7) - i(280 \pm 16)}$	$\mathbf{3.81 \pm 0.09}$	$\mathbf{-1.49 \pm 0.07}$

is very important because it illustrates how *even using the same input in the real axis* the extrapolation to the complex plane can be rather unstable depending on the method used unless one makes sure that the input satisfies a whole set of dispersion relations. Moreover, if this happens even using dispersion relations to make the analytic continuation, one can imagine that using any model the instability could be even larger.

In contrast, when we use the CFD, the poles move away from their UFD values by around 2 deviations and the results from the unsubtracted and once-subtracted HPWDR agree perfectly well, as seen in the last two lines of Table 22. Actually, they agree so well that they are hard to distinguish in Fig. 37.

Although both CFD determinations agree remarkably well, we have highlighted in Table 22 the one obtained using the subtracted antisymmetric amplitude F^- because we have found that it is the most stable under variations of the partial waves and modifications of the a parameter. This is not surprising considering that the unsubtracted F^- is dominated mostly by the $\pi\pi \to K\bar{K}$ $g_1^1(t)$ partial wave, in particular by its pseudo threshold region, as shown in Figs. 29 and 35. We thus consider that the result coming from the once subtracted case is more robust, and favor it as our final result.

In the second line of Table 22 we have also provided the value of the $\kappa/K_0^*(700)$ pole that we obtained by applying the method of Padé sequences reviewed in the previous section. It can be seen that, although it is much less precise, it perfectly overlaps within uncertainties with our dispersive determinations, thus validating the method. In addition, in the first line of the same table we supply the previous dispersive result of the Paris Group [97], with which we agree well within uncertainties. We want to emphasize once again that they did not use data on the S and P waves in the elastic region, but solutions of the FTPWDR equations with input from higher energy data and other partial waves. In contrast, ours is obtained from a data fit using the data in that region. They are therefore independent determinations with different input and rather different extractions. For instance, this shows that the fact that their P-wave prediction in [97] does not describe data, as seen in Fig. 23, does not affect dramatically the $\kappa/K_0^*(700)$ determination.

In conclusion, we are confident that this is the kind of confirmation required to settle the existence of this state. Moreover, the pole parameters and couplings are now known with great precision, about an order of magnitude less than currently evaluated in the RPP.

Finally, following the same methods, but applied to the *P*-partial wave, it is also possible to determine the pole and residue of the vector $K^*(892)$ resonance. Actually, as we saw in the third row of Fig. 34, the CFD agreement for the three $f_1^{1/2}(s)$ dispersion relations is remarkable. Note that, since this resonance is much narrower, its associated pole lies very near the real axis and all three partial-wave dispersion relations (four, taking into account the two different subtractions for F^-) can be used for its determination. The difference between using one or another is in the 1 MeV range. We have thus averaged them to find the pole that was already advanced in [47]:

$$\sqrt{s_{K^*(892)}} = (890 \pm 2) - i(25.6 \pm 1.2)\,\text{MeV},$$

and its dimensionless residue has modulus $|g| = (5.69 \pm 0.12)$ and phase $\phi_g = -(0.076 \pm 0.008)$ (in radians).

6.4. On the nature of the $\kappa/K_0^*(700)$

There is growing evidence for the existence of hadrons whose composition falls beyond the ordinary quark–antiquark classification of mesons or the three-quark classification of baryons. Most modern investigations of the dynamical models that form exotic resonances focus on individual angular momenta. This provides a framework to extract the properties of a given resonance at complex-energy values. However, in this section we will briefly summarize our efforts in combining dispersion relations and the analytic properties of amplitudes for complex angular momenta. This helps us to connect resonances of different spins under their Regge trajectories in the squared mass vs. spin, $(s = M^2, J)$, plane (see [103] for a textbook introduction to Regge Theory). A well-known feature of ordinary hadrons is that they can be classified into real and linear Regge trajectories with an almost universal slope of around 0.9 GeV^{-2}. In the case of mesons, it can be naively interpreted in terms of the tension of the rotating flux tube between the quark and antiquark. As a result, strong deviations from this behavior suggest a different microscopic nature.

We are particularly interested in the investigation of the internal structure of the $\kappa/K_0^*(700)$ resonance, debated for many decades. Many different models have determined its structure to be different than that of $q\bar{q}$ mesons. In particular, many past works show some predominant meson–meson (also called molecular) or tetraquark nature for this state [16,25,26,29,31,34,317,318,320,327–330]. Moreover, many of these works find striking similarities between the

$\kappa/K_0^*(700)$ and $\sigma/f_0(500)$ resonances, pointing to a similar internal composition. This last property would rule out the idea of the $\sigma/f_0(500)$ being a glueball, as the $\kappa/K_0^*(700)$, due to its strangeness, cannot be one.

As explained above, Regge Theory emerges as an application of analytic constraints in the complex angular momentum plane. Even though no such thing as an analytic formula for hadronic states exists, we know $q\bar{q}$ meson states should be classified unambiguously by a straight Regge trajectory, with a universal slope. However, both $\kappa/K_0^*(700)$ and $\sigma/f_0(500)$ resonances are at odds with this classification [331,332], which illustrates that it is not possible to accommodate them into Regge families of resonances, or find suitable "Regge partners". Moreover, we shall review below how from dispersion theory it can be shown that the $\kappa/K_0^*(700)$ Regge trajectory does not follow the ordinary behavior and has non-ordinary Regge parameters. Its trajectory is not dominated by its real part, which is not linear, and its slope is 5 times smaller than the universal one for ordinary hadrons. On top of that, the behavior of this trajectory at low energies is similar to that of the $\sigma/f_0(500)$, as will be seen in Fig. 40. This is yet another piece of evidence supporting the idea that the $\kappa/K_0^*(700)$ and $\sigma/f_0(500)$ resonances are non-ordinary hadrons.

In the following, we will briefly summarize the elastic dispersive formalism that allows us to calculate the Regge trajectory of a resonance just from its pole parameters. There are no fits to other resonances involved. More details can be found for mesons in the following Refs. [104–106,237,333–336] or in Refs. [337–339] for baryons. This formalism will be applied here to the $K^*(892)$, $K_0^*(1430)$, and $\kappa/K_0^*(700)$ resonances. The $K_0^*(1430)$ is not completely elastic, but the formalism is still applicable since it predominantly decays to πK with a branching ratio of around $(93 \pm 10)\%$. The other two are purely elastic. The first two are considered ordinary $q\bar{q}$ mesons, and their trajectories come out as such. In contrast, the $\kappa/K_0^*(700)$ is believed to be a non-ordinary resonance and, as we will see next, this is supported by the fact that its trajectory does not follow the expected $q\bar{q}$ behavior.

We first assume that the partial wave can be approximated by the nearest resonance that dominates the line shape as

$$t_l(s) = \frac{\beta(s)}{l - \alpha(s)} + f_{background}(l, s), \tag{124}$$

where $\alpha(s)$ is the Regge trajectory and $\beta(s)$ the residue of the resonance pole. Then, from elastic unitarity

$$\operatorname{Im}\alpha(s) = \sigma_{\pi K}(s)\beta(s), \tag{125}$$

where $\sigma_{\pi K}(s)$ is the two-particle phase space, already defined in Eq. (2). Finally by making use now of the Schwarz reflection symmetry one gets $\alpha^*(s) = \alpha(s^*)$ and $\beta^*(s) = \beta(s^*)$. Note that $\beta(s)$ is real in the real axis above threshold.

Since we are dealing with meson–meson scattering, we already saw in Fig. 20 that partial waves have three main analytic structures in the first Riemann sheet. First and foremost, the right-hand cut is created by s-channel unitarity. Second, the left-hand cut is produced by crossed channel interactions, and lastly, the circular-cut is produced when the two mesons have unequal masses. However, it can be proven [237] that the Regge trajectory $\alpha(s)$ and the residue $\beta(s)$ are only related to the right-hand cut, starting at the first two-particle threshold. It is, therefore, possible to write the customary dispersion relation for the Regge trajectory as

$$\operatorname{Re}\alpha(s) = \alpha(0) + \frac{s}{\pi} \int_{s_{th}}^{\infty} \frac{\operatorname{Im}\alpha(s')}{s'(s' - s)} ds', \tag{126}$$

where we have included one subtraction to ensure convergence, and we have factorized out explicitly the intercept of the trajectory. More subtractions can be included straightforwardly, as can be seen in [105]. It is now clear from these two equations above that obtaining a closed dispersive description for both $\alpha(s)$ and $\beta(s)$ demands solving a system of coupled integral equations. In the case of the $\beta(s)$ function, one first defines the reduced residue as $\gamma(s) = \beta(s)\hat{s}^{-\alpha(s)}\Gamma(\alpha(s)+3/2)$, with $\hat{s} = 4p^2/s_0$. In order to have the right dimensions, we have introduced a scale s_0, conveniently set to $s_0 = 1\text{GeV}^2$ without losing generality. This reduced residue is an analytic function except for a cut on the real axis above threshold, where its phase is known and hence can be obtained from a Muskhelishvili–Omnès function, in a relatively similar approach to the one we followed in Section 3.6. For more details on the derivation, we refer the reader to Refs. [104–106].

The final closed system of equations, for the πK case, reads

$$\operatorname{Re}\alpha(s) = \alpha_0 + \alpha's + \frac{s}{\pi}PV\int_{(m_K+m_\pi)^2}^{\infty} ds' \frac{\operatorname{Im}\alpha(s')}{s'(s' - s)}, \tag{127}$$

$$\operatorname{Im}\alpha(s) = \frac{\sigma_{\pi K}(s)b_0\hat{s}^{\alpha_0+\alpha's}}{|\Gamma(\alpha(s)+\frac{3}{2})|}\exp\left(-\alpha's[1 - \log(\alpha's_0)] + \frac{s}{\pi}PV\int_{(m_K+m_\pi)^2}^{\infty} ds' \frac{\operatorname{Im}\alpha(s')\log\frac{\hat{s}}{\hat{s}'} + \arg\Gamma\left(\alpha(s')+\frac{3}{2}\right)}{s'(s' - s)}\right), \tag{128}$$

$$\beta(s) = \frac{b_0\hat{s}^{\alpha_0+\alpha's}}{\Gamma(\alpha(s)+\frac{3}{2})}\exp\left(-\alpha's[1 - \log(\alpha's_0)] + \frac{s}{\pi}\int_{(m_K+m_\pi)^2}^{\infty} ds' \frac{\operatorname{Im}\alpha(s')\log\frac{\hat{s}}{\hat{s}'} + \arg\Gamma\left(\alpha(s')+\frac{3}{2}\right)}{s'(s' - s)}\right), \tag{129}$$

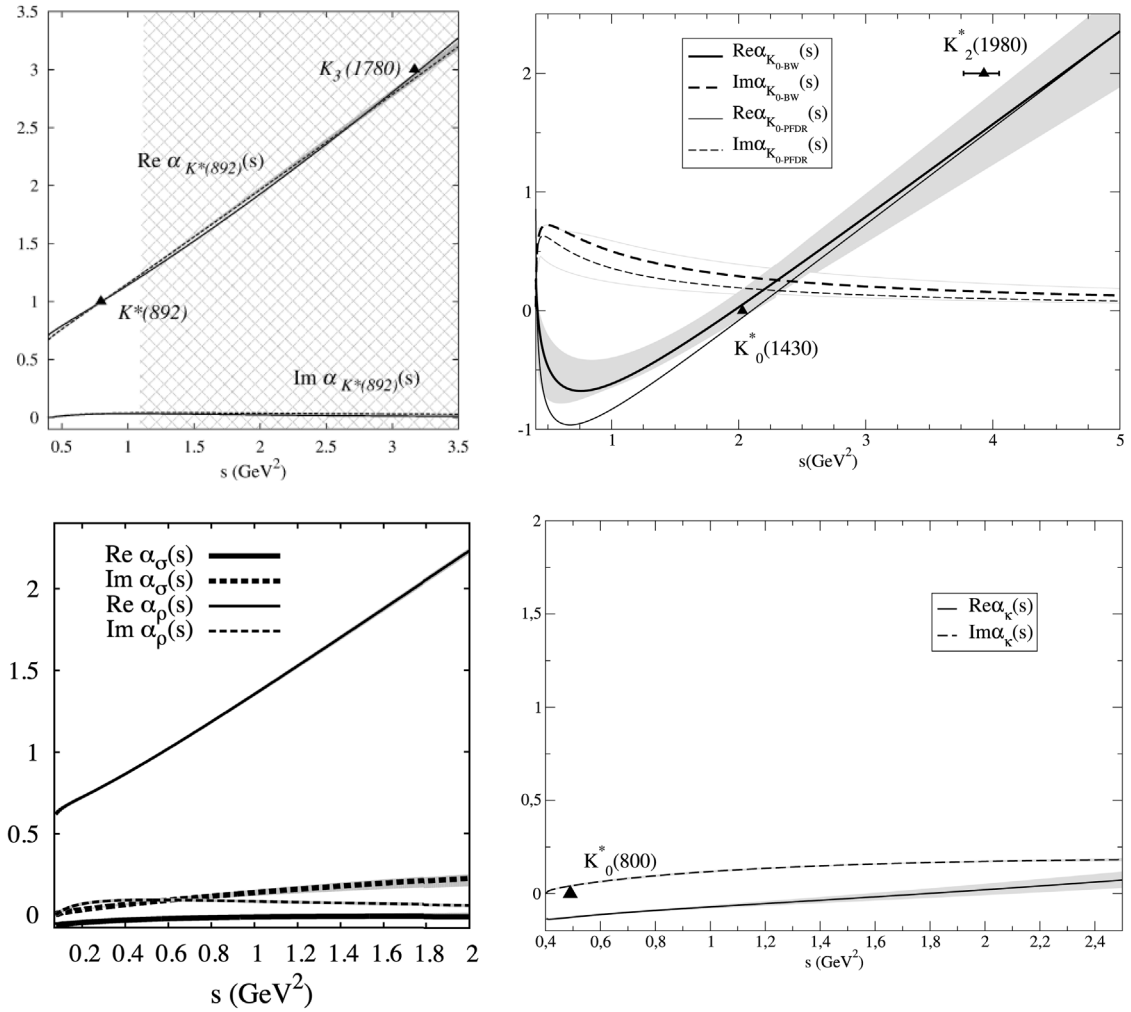where PV denotes the principal value.

Fig. 39. Ordinary vs. non-ordinary Regge trajectories obtained from a dispersive representation with only their lightest pole as input. Let us recall that for ordinary Regge trajectories the imaginary part is negligible and the real part should be a rising straight line. Notice the ordinary linear Regge trajectories of the $K^*(892)$ (Top left), $K_0^*(1430)$ (Top right, we provide two extractions, either from its Breit–Wigner shape or with Padé sequences from data constrained with FDRs) and $\rho(770)$ (Bottom left). In contrast, the $\sigma/f_0(500)$ (Also bottom left) and $\kappa/K_0^*(700)$ (Bottom right) have non-ordinary trajectories.
Source: Figures are taken from [104–106], when the $K_0^*(700)$ was still called $K_0^*(800)$.

As can be easily seen this coupled system of equations depends on three free parameters, which are determined once we impose that the partial wave of Eq. (124) should contain a pole at a given position with a given residue. In particular, in [106], we used the pole positions extracted in [99] employing the Padé sequence method, just explained in Section 6.2 above, as the inputs for the $\kappa/K_0^*(700)$ and $K_0^*(1430)$ resonances. One minor technical remark is in order: for the scalar wave, we also imposed on the integral equations the existence of an Adler zero at the LO ChPT position.

The real and imaginary parts of the resulting trajectories are shown in Fig. 39, compared to similar calculations for other resonances [104,105]. All their resulting parameters are listed in Table 23. The method successfully yields the required Regge parameters and at the same time, the resulting amplitude approximates reasonably well the energy region surrounding each resonance (see the details in [104–106]), consistently with being the dominant contribution there. Notice that the purpose is not to reproduce the partial waves within uncertainties in the whole elastic region, as that could only be achieved by introducing backgrounds that are neglected here.

Let us now briefly discuss these results. The solutions for the $\rho(770)$, $K^*(892)$ and $K_0^*(1430)$ yield ordinary, straight Regge trajectories, at least near and beyond the resonance under consideration, whose slopes are consistent with the universal one. Moreover, when checking higher spin partners, these fall within these trajectories or very close to them, even though the parameters of the "straight line" were not fitted, but obtained from the dispersive representation using only the pole parameters of the lighter particle. On top of that, the real part of the trajectory dominates over the imaginary part above the resonance mass. In contrast, the $\kappa/K_0^*(700)$ and $\sigma/f_0(500)$ trajectories do not fit this universal pattern.

Table 23
Dispersively calculated Regge trajectories [104–106].

	α_0	α' GeV^{-2}	b_0
$\rho(770)$	0.52 ± 0.02	0.902 ± 0.004	
$K_0^*(1430)$	$-1.28^{+0.01}_{-0.17}$	$0.81^{+0.01}_{-0.04}$	$2.5^{+1.1}_{-0.4}$
$K^*(892)$	0.32 ± 0.01	0.83 ± 0.01	0.48 ± 0.03
$\sigma/f_0(500)$	$-0.090^{+0.004}_{-0.012}$	$0.002^{+0.050}_{-0.001}$	
$\kappa/K_0^*(700)$	-0.27 ± 0.03	0.11 ± 0.09	$0.45^{+0.11}_{-0.08}$
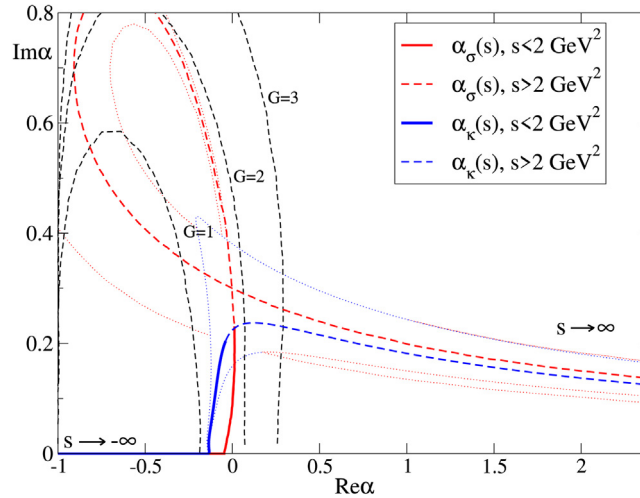
Fig. 40. Trajectories of the $\sigma/f_0(500)$ (red line and area covering uncertainties) and $\kappa/K_0^*(700)$ (blue line and area covering uncertainties) in the (Re α, Im α) plane as functions of s. The lines are continuous and thick for $s < 2\,\mathrm{GeV}^2$, which is where, at most, the method could be justified. Above that energy, we just show the extrapolation of the results. We also show, for comparison, three black dashed lines, labeled with different values of G, which correspond to the trajectories of the corresponding Yukawa potentials $V(r) = Ga\exp(-r/a)/r$ [341,342,344,345] with a's given in the text. This is a colored version of our figure in [106].

These trajectories are highly nonlinear, and the slopes are many times smaller than the ordinary ones. This indicates that the scale of the dynamics that govern the binding of these resonances is larger than typical quark–antiquark dynamics. Furthermore, the imaginary part of the trajectory is larger than its real part, which is the opposite of what is expected for ordinary mesons. This indicates a strong non-ordinary behavior for these two states.

Finally, we also show in Fig. 40 the behavior of both the $\sigma/f_0(500)$ and $\kappa/K_0^*(700)$ Regge trajectories in the (Re α, Im α) plane. Let us remark that the low-energy part of these trajectories resembles those of non-relativistic Yukawa potentials [340–342]. In particular below 2 GeV both trajectories can be approximated by a given potential $V(r) = Ga\exp(-r/a)/r$, which they match from $s = -\infty$ to the two-particle thresholds. At the two-particle thresholds, the imaginary part becomes greater than zero, with a very step rising, which once again can be described by the Yukawa potentials. Up to $s = 2\,\mathrm{GeV}^2$ the $\sigma/f_0(500)$ trajectory is almost equal to that of a $G = 2$ Yukawa potential, while the line with $G = 1.4$ is quite similar to the $\kappa/K_0^*(700)$ trajectory. We can thus estimate the effective ranges of the closest Yukawa potential in the $\sigma/f_0(500)$ case, namely [104] $a_{\pi\pi} = 0.5\,\mathrm{GeV}^{-1} \simeq 0.1\,\mathrm{fm}$, as well as in the $\kappa/K_0^*(700)$ case: $a_{\pi K} = 0.36\,\mathrm{GeV}^{-1} \simeq 0.07\,\mathrm{fm}$. As explained in [106], the ratio between them is numerically very near the inverse of the ratio between the reduced masses of the respective scattering systems. Thus, it seems that the pion and kaon masses set the scale for the binding dynamics and therefore support again a possible "molecular" nature. Let us nevertheless remark that the effective range of the Yukawa potentials needed to mimic these trajectories at low energies is rather small for a meson [106], of the same order of the scalar radius found in [343] for the $\sigma/f_0(500)$.

Altogether, our results support a predominantly non-ordinary microscopic nature for the $\kappa/K_0^*(700)$, whose behavior is very similar to that of the $\sigma/f_0(500)$. These results may suggest that their properties are predominantly controlled by meson–meson dynamics.

7. Other applications

7.1. $\pi K \to \pi K$ threshold and subthreshold parameters from sum rules

As we have already explained in the introduction, the values of the threshold parameters, defined in Eqs. (13) and (14), are of interest for our understanding of low-energy hadron physics, since, in principle, this is the most suitable regime

Table 24

Previous determinations of πK scalar scattering lengths from various approaches. Note that lattice results tend to yield lower values than dispersive results for both scattering lengths

Reference	$m_\pi a_0^{1/2}$	$m_\pi a_0^{3/2}$	Description
Büttiker et al. (2004) [43]	0.224 ± 0.022	-0.0448 ± 0.0077	Dispersive Roy–Steiner
Peláez-Rodas (2016) [41]	0.220 ± 0.010	$-0.0540^{+0.010}_{-0.014}$	Fit constrained with FDR
Bijnens–Ecker (2014) [86]	0.142	-0.071	ChPT LO
Bijnens–Ecker (2014) [86]	$0.173(0.169)$	$-0.064(-0.066)$	ChPT NLO fit 14 (free fit)
Bijnens–Ecker (2014) [86]	$0.224(0.226)$	$-0.048(-0.047)$	ChPT NNLO fit 14 (free fit)
Miao et al. (2004) [87]	–	-0.056 ± 0.023	lattice, improved Wilson quenched
NPLQCD (2006) [88]	$0.1725 \pm 0.0017^{+0.0023}_{-0.0156}$	$-0.0574 \pm 0.016^{+0.0024}_{-0.0058}$	lattice. Domain-wall valence
Flynn–Nieves (2007) [89]	0.175 ± 0.017	–	lattice+Omnès Dispersion Relation
Fu (2012) [91]	0.1819 ± 0.0035	-0.0512 ± 0.0018	lattice, staggered, moving wall source
PACS-CS (2014) [92]	0.182 ± 0.053	-0.060 ± 0.006	lattice, improved Wilson
ETM (2018) [93]	–	-0.059 ± 0.002	lattice, twisted mass.

for low-energy effective field theory. Namely, with the $\pi K \to \pi K$ threshold parameters, we are testing SU(3) Chiral Perturbation Theory (ChPT) and its convergence when the strange quark is taken into account since its mass is not as small as those of non-strange quarks. We emphasize again that we are working in the isospin conserving approximation and for studies of isospin violation in $\pi K \to \pi K$ we refer to [160–163]

The problem to extract these threshold parameters is that the kinematic suppression makes it very hard to obtain precise data, or even data at all, close to threshold. For instance, see all the data plots in Section 2.1 for $\pi K \to \pi K$ partial waves and note that the lowest energy data are at least 100 MeV above threshold, and even those points are rather isolated and usually with large uncertainties. Therefore, extracting threshold parameters directly from scattering data depends strongly on the precise parameterization or model used for the extrapolation down to threshold. It is advisable to avoid such a strong model dependence. As we will see below, some determinations from πK atom lifetimes provide information on scattering lengths, although their uncertainties are rather large.

Sum rules are obtained from dispersion relations evaluated at particular points or limits and this makes their prediction much more robust than direct extractions using a parameterization of the data. The reason lies in the integral nature of the sum rule, which makes rather irrelevant the details of a particular parameterization around threshold, thus suppressing very strongly, if not completely, any model or parameterization dependence. In addition, an integral determination typically yields a much smaller uncertainty. Therefore, generically, sum rules provide the most accurate and robust method to determine threshold parameters.

Moreover, sum rules for threshold parameters provide additional consistency tests for data parameterizations. In this section we will first discuss the scalar scattering lengths, since they have attracted quite some attention recently, discussing also the Adler zeros in these waves. Next, we will present values for both scattering lengths and slopes for all waves up to angular momentum 2 and finally discuss the subthreshold parameters.

7.1.1. Scalar scattering lengths

At present, there is a great deal of interest in the values of the S-wave scattering lengths from ChPT, dispersion theory, and lattice gauge theory communities, since some tension exists between the determinations using these different techniques. This was illustrated in Fig. 4 in the introduction, where we can see in the $(a_0^{1/2}, a_0^{3/2})$ plane that, for both scattering lengths, lattice QCD results (in red) tend to produce lower values than dispersive results (in brown and green). The tension is somewhat more evident for the $a_0^{1/2}$ channel, which, as we have seen, is probably the most controversial one and includes the $\kappa/K_0^*(700)$ meson. Concerning ChPT, the LO receives sizable NLO corrections that take the values closer to lattice results, but in order to reach the dispersive results the NNLO corrections should be even bigger, casting doubts about the good convergence of $SU(3)$ ChPT. Actually, in the extensive ChPT review in [86] it is shown that the πK scattering lengths have the worst convergence of all the observables under consideration. The precise values of all these calculations are shown in Table 24.

Experimentally the best determination, avoiding model dependencies, is the combination

$$a_0^- = \frac{1}{3}(a_0^{1/2} - a_0^{3/2}) = 0.11^{+0.09}_{-0.04} m_\pi^{-1} \quad \text{(DIRAC)}, \tag{130}$$

obtained in 2017 by the DIRAC Collaboration [94] by studying the lifetime of πK atoms at CERN. The relation between the decay width of these atoms and the scattering lengths including isospin violation and QED corrections can be found in [346,347]. The observation of these atoms and their decay lifetime is a remarkable experimental achievement, but the uncertainty of the result, which is represented by a beige band in Fig. 4, labeled DIRAC 17, is not enough to discern between present lattice QCD or dispersive results.

So far, the best dispersive determinations come from the 2004 Roy–Steiner analysis of [43] (Brown ellipse in Fig. 4) or our 2016 fit to data constrained with forward dispersion relations [41] (Green result labeled "FDR-CFD-old" in Fig. 4). Note, however, that their uncertainties are rather large and, as explained several times, that the authors of [43] *solve* the

Roy–Steiner equations without using data in the $\pi K \to \pi K$ elastic region. Also, our result in [41] does not have separate dispersive constraints for each partial wave, but for the whole isospin amplitudes. Actually we only had a sum rule for a_0^-; namely, Eq. (132) below. In what follows we will provide new independent values obtained from sum rules coming from Roy–Steiner equations for each partial wave. Let us emphasize that no convergent sum rule for a_0^+ can be obtained using the dispersion relations provided in this work. Therefore, whenever we quote the dispersive a_0^I value in the isospin basis, its component orthogonal to a_0^- comes directly from the CFD parameterization described in Sections 4.1 and 5.2.

In addition, we will provide different sum rules for the most controversial threshold parameters. In later subsections, we will use them to obtain precise values of the scattering lengths and slopes. Having different sum rules for the same observables, and therefore weighting differently the input, will also provide strong consistency tests of our data parameterizations.

At this point, a technical remark is in order. Threshold parameters correspond to $s = m_+^2$, but setting s directly to this value, which coincides with the lower integration limit, would not allow calculating the principal value needed for real s in the dispersion relations. One should then exert caution to define these sum rules, as the $s \to m_+^2$ limit has to be taken after the dispersion relation has been evaluated with its principal value. For example, a sum rule for the a_0^- scattering length can be obtained from the F^- FDR, (39), as:

$$a_0^- = \frac{m_\pi m_K}{2\pi^2 m_+} \lim_{s \to m_+^2} PV \int_{m_+^2}^\infty \frac{\text{Im } F^-(s')}{(s' - m_-^2)(s' - s)} ds'. \tag{131}$$

Fortunately, the imaginary part of the amplitude $\text{Im } F^-(s') \propto \sqrt{s - m_+^2}$ suppresses the singularity at threshold, and hence the principal value can be removed when taking the limit, to yield

$$a_0^- = \frac{m_\pi m_K}{2\pi^2 m_+} \int_{m_+^2}^\infty \frac{\text{Im } F^-(s')}{(s' - m_-^2)(s' - m_+^2)} ds'. \tag{132}$$

Thus, in this case, the combined appearance of the $s \to m_+^2$ limit and the principal value allows us to get rid of both in the final expression.

However, obtaining a simple algebraic expression for the S-wave b_ℓ^I parameters requires a slightly more elaborated, but rather standard, manipulation [48,180,183] to deal with the divergent contribution arising from the $\text{Im } f_0^I(s)/(s' - s)$ behavior close to threshold. Namely, since this divergence is proportional to $(a_0^I)^2/(s' - m_+^2)^{3/2}$ we can add to our dispersive expression this factor multiplied by

$$PV \int_{m_+^2}^\infty \frac{ds'}{(s' - s)\sqrt{s' - m_+^2}} = 0. \tag{133}$$

When this is done the cancellation of the divergence is directly seen inside the integral, which allows us to get rid of the principal value and the limit outside. The price to pay is the appearance of a new term in the integrand.

In particular, under these manipulations, we can write sum rules for scattering lengths and slopes coming from F^+ [41][3] as follows:

$$SR_1 \equiv b_0^{1/2} + 3a_1^{1/2} + \frac{a_0^{1/2} m_+}{2m_\pi m_K} \tag{134}$$

$$= \frac{m_+}{8\pi^2 m_\pi m_K} \int_{m_+^2}^\infty ds' \left[\frac{\text{Im } F^+(s') + 2\text{Im } F^-(s')}{(s' - m_+^2)^2} - 8m_+ \pi \sqrt{m_\pi m_K} \frac{(a_0^{1/2})^2}{(s' - m_+^2)^{3/2}} - \frac{\text{Im } F^+(s') - 2\text{Im } F^-(s')}{(s' + m_+^2 - 2\Sigma_{\pi K})^2} \right],$$

and

$$SR_2 \equiv b_0^{3/2} + 3a_1^{3/2} + \frac{a_0^{3/2} m_+}{2m_\pi m_K} \tag{135}$$

$$= \frac{m_+}{8\pi^2 m_\pi m_K} \int_{m_+^2}^\infty ds' \left[\frac{\text{Im } F^+(s') - \text{Im } F^-(s')}{(s' - m_+^2)^2} - 8m_+ \pi \sqrt{m_\pi m_K} \frac{(a_0^{3/2})^2}{(s' - m_+^2)^{3/2}} - \frac{\text{Im } F^+(s') + \text{Im } F^-(s')}{(s' + m_+^2 - 2\Sigma_{\pi K})^2} \right].$$

Note that in [41], as long as we only considered FDRs, which are not projected in partial waves, we took these sum rules as additional constraints for our partial-wave fits. Since here we are also considering partial-wave dispersion relations, these are no longer needed as constraints and we will see they are still well satisfied.

If we used FTPWDR we would obtain for a_0^- the same sum rule already obtained from FDR in Eq. (132). However, using the HDR at $t = 0$ and $b = \Delta^2 + a^2 - 2\Delta a$ the dispersion relation for F^-/G^1 can be related to a_0^-, leading to the following

---

[3] We fixed an errata with respect to our published expression in [41].

Table 25

S-wave scattering lengths (m_π units).

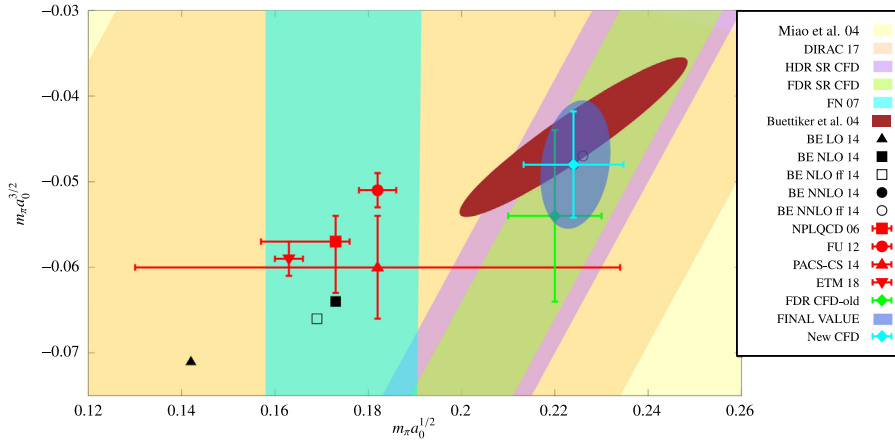|	Ref. [43]	UFD	CFD
$a_0^{1/2}$	0.224 ± 0.022	0.241 ± 0.012	**0.224 ± 0.010**
$a_0^{3/2}$	-0.0448 ± 0.0077	-0.067 ± 0.012	**-0.048 ± 0.006**

Fig. 41. Comparison between various sum rules and determinations coming from different Roy–Steiner equations, compared with both lattice QCD predictions and ChPT calculations. The references in the legend are as in Fig. 4, except that we are now providing as a cyan diamond our new result obtained directly from our dispersively constrained fit to data (CFD), listed in boldface in Table 25, as well as our best or "Final value", shown as a blue ellipse and listed in Table 29. The latter is obtained by combining the dispersive sum rules explained in Section 7.1. Note that the two axes are plotted with different scales to maximize the visibility of the region of interest.

sum rule [43,348]:

$$\frac{8\pi m_+ a_0^-}{m_+^2 - m_-^2} = \frac{1}{2\pi} \int_{4m_\pi^2}^{\infty} \frac{dt'}{t'} \text{Im} \frac{G^1(t', s_b')}{\sqrt{(t' - 4m_\pi^2)(t' - 4m_K^2)}} + \frac{1}{\pi} \int_{m_+^2}^{\infty} ds' \frac{\text{Im } F^-(s', t_b')}{\lambda_{s'}}. \tag{136}$$

This sum rule is dominated by the $\pi\pi \to K\bar{K}$ amplitude and thus, for all means and purposes, it is independent from the value obtained with Eq. (132). In practice, we will calculate this sum rule with $a = -10.9 m_\pi^2$, which maximizes the Roy–Steiner applicability in the $\pi\pi \to K\bar{K}$ channel. Note that we only obtain a sum rule for a_0^- from the HDR without subtractions for F^-, since a_0^- is input in our subtracted F^- HDR case.

At this point, we can use the UFD and CFD parameterizations to determine the $\pi K \to \pi K$ threshold parameters, which can be done either directly from the parameterizations, or from the sum rules, which, being obtained from an integral would suppress the $\pi K \to \pi K$ parameterization dependence. Thus, in Table 25 we have collected the scattering lengths obtained directly from the UFD and CFD parameterizations. Of course, we think the constrained results are better because they are consistent with dispersion relations. We can see that there is a change from UFD to CFD, by roughly 1.5 standard deviations, which brings our CFD results very close to those of the dispersive calculation of the Bonn–Paris group [43]. We are thus providing an independent dispersive confirmation of those older dispersive results, this time using data together with the dispersive constraints, whereas in [43] they were obtained from Roy–Steiner solutions.

We are showing our results obtained directly from our CFD parameterization as a cyan diamond and cross in Fig. 41, which overlaps nicely with the brown ellipse from [43]. Note that it also overlaps with our old result [41], where we only used FDRs as constraints. The use of those FDRs together with the Roy–Steiner equations in this review has moved the central value within the old error bars, and has reduced considerably our uncertainties. Note that the errors in Table 25, plotted as a cross in Fig. 41, are given as uncorrelated since they come from the direct CFD parameterization, where we treat all input parameters as uncorrelated and thus each partial wave as independent. This is a conservative error estimate, but we will discuss below the correlation between scattering lengths once we use the a_0^- numerical values from sum rules.

The nice consistency of the CFD versus the inconsistency of the UFD is illustrated in Table 26. There we see an almost perfect agreement between the a_0^- obtained directly from the CFD parameterization, and the sum rules in Eqs. (132) and (136) using CFD as input. In contrast, for the UFD, the inconsistencies reach the three standard-deviation level.

Therefore, sum rules not only provide stringent constraints but sometimes also the most reliable and precise results for threshold parameters, suppressing model dependencies too. Thus, once we have shown that these two sum-rule determinations with CFD input are consistent, they provide a very stringent and robust result for a_0^- which we have

Table 26

Comparison of the value a_0^- obtained directly from the parameterization versus the value obtained from different sum rules, coming from forward dispersion relations (FDR) Eq. (132) or from hyperbolic dispersion relations (HDR), Eq. (136).

	UFD	CFD
$3m_\pi a_{0, direct}^-$	0.309 ± 0.016	0.273 ± 0.012
$3m_\pi a_{0, FDR}^-$	0.290 ± 0.010	0.275 ± 0.010
$3m_\pi a_{0, HDR}^-$	0.253 ± 0.015	0.274 ± 0.016

Table 27

Comparison between the sum rules of Eqs. (134) and (135) calculated using the UFD or CFD parameterizations as input, versus the values obtained directly from each parameterization.

	UFD	CFD
SR_1	0.187 ± 0.006	$\mathbf{0.182 \pm 0.006}$
Direct_{SR_1}	0.163 ± 0.010	0.176 ± 0.013
SR_2	-0.042 ± 0.004	$\mathbf{-0.039 \pm 0.003}$
Direct_{SR_2}	-0.052 ± 0.005	-0.037 ± 0.006

included in Fig. 41 as light green and purple bands. Let us recall that they are rather independent since the sum rule from FDR, i.e. Eq. (132) (the "FDR SR CFD" green band), is dominated by the scalar $\pi K \to \pi K$ scattering wave, whereas the sum rule from HDR, i.e Eq. (136) (the "HDR SR CFD" purple band) is dominated by the $\pi\pi \to K\bar{K}$ scattering contribution. Incidentally, had we used as input the UFD parameterization, which is not consistent with dispersion relations, these two bands would not even overlap.

A relatively similar pattern is observed in Table 27, where we compare the results of the sum rules SR_1 and SR_2 in Eqs. (134) and (135) using as input either the UFD or CFD parameterizations with their respective values obtained directly from the fits. Once again the CFD results are wonderfully consistent, whereas the UFD shows some tension at the 2 standard deviation level.

So far we have not discussed partial-wave dispersion relations to obtain sum rules, but they can also be expanded around threshold to obtain further integral expressions for threshold parameters. At first, it may seem we have three more sum rules since we can expand the partial-wave fixed-t dispersion relations (FTPWDR) as well as the unsubtracted and once-subtracted partial-wave hyperbolic dispersion relations (HPWDR). However, for the scalar scattering lengths, the HPWDR sum rule with one subtraction coincides with the direct CFD calculation, whereas the unsubtracted HPWDR is almost identical to (136), the only difference is that $a = 0$ for the latter. Finally, the FTPWDR sum rule is identical to (132).

Hence, in practice we just have two independent a_0^- sum rules, i.e., Eqs. (132) and (136). We can now use them to get our final and more reliable values of the scalar scattering lengths in the isospin basis, which are more robust than those in Table 25, obtained directly form the CFD. Of course, for the orthogonal combination $a_0^{1/2} + a_0^{3/2}$ (or for a_0^+ when needed), which does not have a sum rule, we still take the direct CFD parameterization. Thus, the numerical values for the scalar scattering lengths in the isospin basis are listed in Table 28. The first two columns are obtained by using values from each one of our a_0^- sum-rules: FDR Eq. (132) and HDR Eq. (136). Nevertheless, given that the two a_0^- sum rules have rather different inputs, we have calculated their weighted average and statistical error, to which we have added a systematic uncertainty.[4] This constitutes our "Final Value", provided in the third column, for which we quote correlated uncertainties in the isospin basis, whose correlation matrix is provided in the next column. The reason is that, contrary to CFD direct values in Table 25, the calculation for our Final Values is not done from independent partial waves in the isospin basis. Instead, we use the weighted average of sum rules for a_0^-. These correlated uncertainties are represented by an ellipse in Fig. 41. It can be seen that, after rounding up numbers, the central Final Values are almost identical to the CFD result, and the uncertainties are very similar. It is also nicely compatible with previous dispersive or ChPT determinations, provided in the last two columns of Table 28. Note that our estimated uncertainty is somewhat smaller than in [43], in particular, due to the small uncertainty from the FDR sum rule.

In summary, our calculations of the scalar πK scattering lengths show that simple unconstrained fits to data (UFD) yield inconsistent values between the "direct" input and the sum rule output and even between different sum rules. This is amended with the constrained fits to data (CFD), which show a remarkable consistency. In this review, we have thus updated our CFD values for the scattering lengths and we have also provided robust and model-independent results from sum rules for a_0^-, which lead to our "Final Values" in the isospin basis. Both the CFD and "Final Values" are remarkably

---

[4] Calculated as the sum in quadrature of their separation from the mean, divided by two.

Table 28

Determination of the πK scalar scattering lengths using the sum rule for a_0^- with our CFD as input. Let us remind that the combination orthogonal to a_0^- comes directly from the CFD parameterization and not from a sum rule. This is why we provide the correlation matrix in the isospin basis.

	This work sum rules with CFD input			Correlation matrix		Sum rules [43] Fixed-t	NNLO ChPT [85] and [86]*
	FDR	HDR	Final value				
$m_\pi a_0^{1/2}$	0.226 ± 0.010	0.225 ± 0.012	**0.225 ± 0.008**	$\begin{pmatrix} 1 & 0.04 \\ 0.04 & 1 \end{pmatrix}$		0.224 ± 0.022	0.224^*
$m_\pi a_0^{3/2} \quad \times 10$	-0.489 ± 0.052	-0.485 ± 0.066	**-0.480 ± 0.067**			-0.448 ± 0.077	-0.471^*

compatible among themselves and with previous dispersive determinations [43], including our own in [41], although our uncertainties are now much smaller than then. In addition, the consistency between our different sum rules, which are dominated by very different input, provides very robust and parameterization-independent constraints. We can therefore conclude that the two standard deviation tension between dispersive analyses and the bulk of lattice results still remains.

In this subsection, we concentrated on the particular case of scalar scattering lengths. Let us now consider other partial waves and higher orders in the threshold expansion.

7.1.2. Sum rules for other threshold parameters of partial waves up to $\ell = 2$

We provide in this subsection the sum rules for the $\ell = 1, 2$ scattering lengths a_ℓ^I as well as the $\ell = 0, 1, 2$ slopes b_ℓ^I. These are calculated from the low-momentum expansion around threshold of the partial-wave dispersion relations obtained either from "fixed-t" dispersion relations (FTPWDR) Eq. (53) or from hyperbolic dispersion relations in Eqs. (54) and (55) (HPWDR). For this, we first expand their respective kernels (given in Appendix E) in a q^2 power series that we match to the expansion in Eq. (14). We have truncated the expansion at second order on each wave and up to $\ell = 2$ included. Not only do they provide tests for our amplitudes, but also, since all of them have been previously calculated either from sum rules [43] or within ChPT [85], we will be able to compare with those predictions.

The analytic expressions are rather long and we will only provide here the most relevant ones, namely the P-wave scattering lengths and the S-wave slopes for the $+$ and $-$ amplitude isospin combinations. Analytic expressions become unmanageable as the order of the power of q^2 grows, but can be obtained following the method we just described. We will nevertheless provide numerical values for all scattering lengths and slopes up to $\ell = 2$ at the end of the subsection.

Let us then provide first the sum rules for the a_1^I scattering lengths, which we organize according to the type of dispersion relation they come from:

- Scattering length sum rules from FTPWDR for $\ell = 1$:

$$a_1^+ = \frac{1}{\pi} \int_{m_+^2}^{\infty} ds' \left(\frac{-2}{3(s' - m_-^2)^2} \operatorname{Im} f_0^+(s') + \frac{2s'^2 + 4m_+^2(s' - m_-^2) - 2m_+^4}{(s' - m_-^2)^2(s' - m_+^2)^2} \operatorname{Im} f_1^+(s') \right.$$
$$\left. + \frac{-10}{3(s' - m_-^2)^2} \operatorname{Im} f_2^+(s') \right) + \frac{1}{\pi} \int_{4m_\pi^2}^{\infty} dt' \frac{2}{3\sqrt{3}t'^2} \operatorname{Im} g_0^0(t') + \frac{5\lambda(t')}{24\sqrt{3}t'^2} \operatorname{Im} g_2^0(t') + d_{a_1^+},$$

$$a_1^- = \frac{1}{\pi} \int_{m_+^2}^{\infty} ds' \left(\frac{2}{3(s' - m_-^2)^2} \operatorname{Im} f_0^-(s') + \frac{s'^2 - 2s'm_-^2 + m_+^4}{(s' - m_-^2)^2(s' - m_+^2)^2} \operatorname{Im} f_1^-(s') \right.$$
$$\left. + \frac{s'^2 - 2s'(3m_-^2 - 2m_+^2) + m_+^4}{3(s' - m_-^2)^2(s' - m_+^2)^2} \operatorname{Im} f_2^-(s') \right) + d_{a_1^-}, \tag{137}$$

where $d_{a_1^+}$, $d_{a_1^-}$ stand for the contributions from higher partial waves, which are numerically very small but were included in our numerical calculations.

- Scattering length sum rules from HPWDR for $\ell = 1$:

$$a_1^+ = \frac{1}{\pi} \int_{m_+^2}^{\infty} ds' \left(\frac{-2}{3(s' - m_-^2)^2} \operatorname{Im} f_0^+(s') + \frac{2m_+^4(s' - a) - 2s'(2am_-^2 - 3as' + s'^2) + 4m_+^2 s'(m_-^2 - s')}{(a - s')(s' - m_-^2)^2(s' - m_+^2)^2} \operatorname{Im} f_1^+(s') \right.$$
$$\left. + \frac{10 \left(\frac{6as'(-am_-^2 + m_+^2(m_-^2 - a) + 2as' - s'^2)}{(a - s')^2(s' - m_+^2)^2} - 1 \right)}{3(s' - m_-^2)^2} \operatorname{Im} f_2^+(s') \right)$$
$$+ \frac{1}{\pi} \int_{4m_\pi^2}^{\infty} dt' \left(\frac{2}{3\sqrt{3}t'^2} \operatorname{Im} g_0^0(t') + \frac{5(\lambda(t') + 6at')}{24\sqrt{3}t'^2} \operatorname{Im} g_2^0(t') \right) + d_{a_1^+},$$

$$a_1^- = \frac{1}{\pi} \int_{m_+^2}^{\infty} ds' \left(\frac{2}{3(s' - m_-^2)^2} \operatorname{Im} f_0^-(s') + \frac{2m_+^4(a - s') + 2s'(s'(a + s') - 2am_-^2) + 4m_+^2 s'(m_-^2 - s')}{(a - s')(s' - m_-^2)^2(s' - m_+^2)^2} \operatorname{Im} f_1^-(s') \right.$$

$$+ \frac{10}{3(a-s')^2(s'-m_-^2)^2(s'-m_+^2)^2} \operatorname{Im} f_2^-(s') \times$$

$$\left(m_+^4 \left(a^2 - 2as' - 5s'^2 \right) - 2m_+^2 s' \left(-2a^2 - 3m_-^2 \left(a + s' \right) + as' + s'^2 \right) + s' \left(s' \left(a^2 + 4as' + s'^2 \right) - 6am_-^2 \left(a + s' \right) \right) \right) \right)$$

$$+ \frac{1}{\pi} \int_{4m_\pi^2}^\infty dt' \frac{t' + 4m_\pi m_K}{2\sqrt{2} t'^2} \operatorname{Im} g_1^1(t') + d_{a_1^-},$$

$$a_{1,sub}^- = \frac{1}{\pi} \int_{m_+^2}^\infty ds' \left(\frac{2(m_- - m_+)(m_- + m_+)}{3(s'-m_-^2)^2(s'-m_+^2)} \operatorname{Im} f_0^-(s') - \frac{2(m_- - m_+)(m_- + m_+)(m_+^2 + s')}{(s'-m_-^2)^2(s'-m_+^2)^2} \operatorname{Im} f_1^-(s') \right.$$

$$\left. - \frac{10(m_- - m_+)(m_- + m_+)(m_+^2(a-s') + s'(5a+s'))}{3(a-s')(s'-m_-^2)^2(s'-m_+^2)^2} \operatorname{Im} f_2^-(s') \right) + \frac{1}{\pi} \int_{4m_\pi^2}^\infty dt' \frac{\sqrt{2} m_\pi m_K}{t'^2} \operatorname{Im} g_1^1(t') + d_{a_{1,sub}^+},$$

(138)

where the last one is obtained from an HDR with one subtraction for F^-. Once again the d_i terms are due to higher partial waves and they are very small, although we computed them in our calculations. Note that a is one of the parameters that define the hyperbolae, which we have chosen as $a = -10m_\pi^2$ to impose the HDR in our CFD parameterization.

Let us now provide the analytic expressions for the sum rules of the $b_0^\pm$ parameters. Remember that, to perform the double limit between the principal value and $s \to m_+^2$, the singular part of the integrands must be removed, as explained above.

- Scattering slopes sum rules from FTPWDR for $\ell = 0$:

$$b_0^+ = \frac{1}{\pi} \int_{m_+^2}^\infty ds' \left(\frac{2s'^2 + 4m_+^2(s' - m_-^2) - 2m_+^4}{(s'-m_-^2)^2(s'-m_+^2)^2} \operatorname{Im} f_0^+(s') - \frac{m_+^2}{m_\pi m_K} \frac{(a_0^+)^2}{(s'-m_+^2)^{3/2}} \right.$$

$$\left. + \frac{-6}{(s'-m_-^2)^2} \operatorname{Im} f_1^+(s') + \frac{10(s'^2 + 2m_+^2(s' - m_-^2) - m_+^4)}{(s'-m_-^2)^2(s'-m_+^2)^2} \operatorname{Im} f_2^+(s') \right)$$

$$+ \frac{1}{\pi} \int_{4m_\pi^2}^\infty dt' \left(\frac{-2}{\sqrt{3} t'^2} \operatorname{Im} g_0^0(t') + \frac{5\lambda(t')}{8\sqrt{3} t'^2} \operatorname{Im} g_2^0(t') \right) + d_{b_0^+},$$

$$b_0^- = \frac{1}{\pi} \int_{m_+^2}^\infty ds' \left(\left(\frac{\Sigma}{m_\pi m_K(s'-m_-^2)} + \frac{m_+^2}{m_\pi m_K(s'-m_-^2)} \right) \operatorname{Im} f_0^-(s') - \frac{m_+^2}{m_\pi m_K} \frac{(a_0^-)^2}{(s'-m_+^2)^{3/2}} \right.$$

$$+ \frac{(3/2 m_+^4 + 3m_-^4 + 3/2 m_+^2 m_-^2 - 6s'(\Sigma + m_\pi m_K))}{m_\pi m_K(s'-m_+^2)(s'-m_-^2)^2} \operatorname{Im} f_1^-(s')$$

$$\left. + \frac{m_+^2(5/2 m_+^4 + 5m_-^4 + 5/2 m_+^2 m_-^2) + 20s'(m_+^4 + 2/3 m_-^4 - 2/3 m_+^2 m_-^2) + 10s'^2(\Sigma + m_\pi m_K)}{m_\pi m_K(s'-m_+^2)(s'-m_-^2)^2} \operatorname{Im} f_2^-(s') \right) + d_{b_0^-},$$

(139)

- Scattering slopes sum rules from HPWDR for $\ell = 0$:

$$b_0^+ = \frac{1}{\pi} \int_{m_+^2}^\infty ds' \left(\frac{2s'^2 + 4m_+^2(s' - m_-^2) - 2m_+^4}{(s'-m_-^2)^2(s'-m_+^2)^2} \operatorname{Im} f_0^+(s') - \frac{m_+^2}{m_\pi m_K} \frac{(a_0^+)^2}{(s'-m_+^2)^{3/2}} \right.$$

$$- \frac{6 \left(\frac{2a(s'-m_-^2)}{(a-s')(s'-m_+^2)} + 1 \right)}{(s'-m_-^2)^2} \operatorname{Im} f_1^+(s')$$

$$- \frac{10}{(a-s')^2(s'-m_-^2)^2(s'-m_+^2)^2} \operatorname{Im} f_2^+(s') \times$$

$$\left(2m_+^2 \left(m_-^2 \left(a^2 + as' + s'^2 \right) - s' \left(4a^2 - 2as' + s'^2 \right) \right) - s' \left(a^2 \left(6m_-^2 - 11s' \right) + 4as'^2 + s'^3 \right) + m_+^4 \left(a - s' \right)^2 \right) \right)$$

$$\left. + \frac{1}{\pi} \int_{4m_\pi^2}^\infty dt' \left(\frac{-2}{\sqrt{3} t'^2} \operatorname{Im} g_0^0(t') + \frac{5(\lambda(t') + 6at')}{8\sqrt{3} t'^2} \operatorname{Im} g_2^0(t') \right) + d_{b_0^+},$$

$$b_0^- = \frac{1}{\pi} \int_{m_+^2}^\infty ds' \left(-\frac{2 \left(m_+^4 \left(m_-^2 - 2s' \right) + m_+^2 \left(-6m_-^2 s' + 2m_-^4 + 3s'^2 \right) + m_-^2 s'^2 + m_+^6 \right)}{(m_- - m_+)(m_- + m_+)(s'-m_-^2)^2(s'-m_+^2)^2} \operatorname{Im} f_0^-(s') \right.$$

$$
-\frac{6\left(m_-^2 s'\left(a+s'\right)+m_+^4\left(s'-a\right)+m_+^2\left(3s'\left(a+s'\right)-m_-^2\left(a+5s'\right)\right)-2am_-^4\right)}{\left(m_--m_+\right)\left(m_-+m_+\right)\left(a-s'\right)\left(s'-m_-^2\right)^2\left(s'-m_+^2\right)}\operatorname{Im}f_1^-(s')
$$

$$
-\frac{10}{\left(m_--m_+\right)\left(m_-+m_+\right)\left(a-s'\right)^2\left(s'-m_-^2\right)^2\left(s'-m_+^2\right)^2}\operatorname{Im}f_2^-(s')\times
$$

$$
\left(m_+^6\left(a^2-2as'-5s'^2\right)+m_+^4\left(m_-^2\left(a^2+16as'+13s'^2\right)-2s'\left(4a^2+7as'+s'^2\right)\right)\right.
$$

$$
+m_+^2\left(-6m_-^2 s'\left(-a^2+2as'+s'^2\right)+3s'^2\left(a^2+4as'+s'^2\right)+2m_-^4\left(a-s'\right)\left(a+2s'\right)\right)
$$

$$
\left.+m_-^2 s'\left(s'\left(a^2+4as'+s'^2\right)-6am_-^2\left(a+s'\right)\right)\right)
$$

$$
+\frac{1}{\pi}\int_{4m_\pi^2}^\infty dt'\frac{3(t'((m_\pi+m_K)^2-m_\pi m_K)-4(m_\pi m_K)^2)}{2\sqrt{2}m_\pi m_K t'^2}\operatorname{Im}g_1^1(t')+d_{b_0^-},
$$

$$
b_{0,sub}^- = \frac{1}{\pi}\int_{m_+^2}^\infty ds'\left(-\frac{2\left(m_--m_+\right)\left(m_-+m_+\right)\left(m_+^2+s'\right)}{\left(s'-m_-^2\right)^2\left(s'-m_+^2\right)^2}\operatorname{Im}f_0^-(s')+\frac{6\left(m_--m_+\right)\left(m_-+m_+\right)}{\left(s'-m_-^2\right)^2\left(s'-m_+^2\right)}\operatorname{Im}f_1^-(s')\right.
$$

$$
\left.-\frac{10\left(m_+^2-m_-^2\right)\left(a\left(5s'-m_+^2\right)+s'\left(m_+^2+s'\right)\right)}{\left(a-s'\right)\left(s'-m_-^2\right)^2\left(s'-m_+^2\right)^2}\operatorname{Im}f_2^-(s')\right)
$$

$$
-\frac{1}{\pi}\int_{4m_\pi^2}^\infty dt'\frac{3\sqrt{2}m_\pi m_K}{t'^2}\operatorname{Im}g_1^1(t')+d_{b_{0,sub}^-}, \tag{140}
$$

where the last one is obtained from an HDR with one subtraction for F^-. Recall that we have set $a=-10m_\pi^2$. As before, the d_i terms are due to higher partial waves, which we computed in our calculations, although they are numerically very small.

Now, our CFD satisfies the dispersive representation and we have already seen that it yields consistent results for the scalar scattering-length sum rules, whereas the UFD does not necessarily do so. Thus, we provide in Table 29 the evaluation of all previous sum rules, as well as the scattering lengths for the D-waves and the slopes for the P and D-waves – for which we have not provided analytic expressions – using as input our CFD parameterizations obtained in Section 5. The first five columns are the results of this work. The first three correspond to sum-rule results from FTPWDR and from HPWDR with one or no subtractions for F^-. The fourth column contains what we consider our "Final Value" for each parameter, which we have obtained assuming that each one of the three sum-rule values, $x_i\pm\delta x_i$, $i=1\ldots3$, for a given observable x is an independent quantity. This is, of course, an approximation, although we have already shown how different the size of the contributions from different input are for each kind of dispersion relation. We have then used as weights their inverse squared uncertainties $\omega_i=1/(\delta x_i)^2$ to define:

$$
\bar{x}\pm\delta\bar{x}\equiv\left(\sum_{i=1}^3\omega_i x_i\right)\Big/\left(\sum_{i=1}^3\omega_i\right)\pm\left(\sum_{i=1}^3\omega_i\right)^{-1/2},\quad \Delta\bar{x}\equiv\delta\bar{x}+d_S x, \tag{141}
$$

where $\bar{x}\pm\delta\bar{x}$ are the weighted average and the statistical uncertainty (see the RPP Introduction section [95]). However, as we have repeatedly emphasized a substantial part of our uncertainties has a systematic nature. Thus, to stay in the conservative side, we have also added linearly a systematic uncertainty $d_S x$, defined as half the difference between the maximum and minimum central values of the individual sum rules for that observable. Therefore what we are showing in the "Final Value" column in Table 29 is $\bar{x}\pm\Delta\bar{x}$.

In the table we also list for comparison the "direct" calculations from the CFD parameterization, as well as, in the column before the last, the results of the sum rules obtained from "fixed-t" dispersion relations by the Bonn–Paris group [43]. Finally, in the last column, we provide the NNLO SU(3) ChPT values from [85], except for the scalar threshold parameters for which we use the "main numbers" in the review [86], in which the values of the scalar scattering lengths from [43] were included in the fit and therefore they are very consistent with the previous column.

Note that we have imposed Roy–Steiner equations only for our CFD S and P-waves. These are the ones for which we expect the best agreement, first between the different values of the sum rules and also with the direct CFD result. Actually, in the previous subsection we have already seen that the agreement is remarkable for the scalar scattering lengths. For the scalar slopes, there is a few-percent deviation which translates into a two-sigma level average deviation. We consider this quite acceptable because one has to keep in mind that there are no precise data or simply no data at all for these waves until roughly 100 MeV above threshold. Note that, as shown in Table 30, the largest contribution for each of the scalar sum rules is a different one. Therefore, the fact that all our sum rules are fairly compatible among themselves is highly non-trivial. In addition, we are quite consistent with the dispersive results of [43], except for the slope $b_0^{1/2}$, which is lower than ours, but not too far from the direct CFD value, although the NNLO ChPT estimate seems to prefer our sum-rule values.

Concerning the vector threshold parameters for the $I=1/2$ wave, we find a remarkable agreement between our direct CFD results and all our sum rules, partly due to the larger uncertainty of the CFD. Both the scattering length and slope sum-rule results of [43], are significantly lower than all our sum rules, particularly the slope. This is most likely because

Table 29

Determination of the πK threshold parameters using our CFD as input for the sum rules listed throughout this section calculated from the partial-wave dispersion relations FTPWDR, HPWDR, or HPWDR$_{sub}$. The latter refers to the HPWDR sum rules obtained when one subtraction is used in the F^- HDR. We also provide for comparison the direct values of the CFD parameterizations as well as previous results using sum rules from Roy–Steiner equations obtained from fixed-t dispersion relations by the Bonn–Paris Group [43]. The last column lists NNLO ChPT results from [85] except for the scalar scattering lengths for which we used the update in the main fit of [86]. Recall that we are only imposing the S and P Roy–Steiner equations, so that our CFD D waves are not devised to describe the threshold region precisely, but just the region where they are not completely negligible far from threshold. The same happens for the $I = 3/2$, $\ell = 1$ wave. We consider our sum rule results to be more reliable than the direct CFD values, particularly for the three last waves, for which no scattering data exist below 1 GeV. Our "Final Value" for each threshold parameter, obtained by combining the three sum-rule results as explained in the text, is listed in boldface in the central column.

	This work sum rules with CFD input				This work direct CFD	Sum rules [43] Fixed-t	NNLO ChPT [85] and [86]*
	FTPWDR	HPWDR	HPWDR$_{sub}$	Final value			
$m_\pi^3 b_0^{1/2} \times 10$	1.05 ± 0.04	1.05 ± 0.07	1.15 ± 0.04	$\mathbf{1.09 \pm 0.07}$	0.95 ± 0.04	0.85 ± 0.04	1.278
$m_\pi^3 b_0^{3/2} \times 10$	-0.43 ± 0.02	-0.41 ± 0.03	-0.45 ± 0.02	$\mathbf{-0.43 \pm 0.03}$	-0.36 ± 0.04	-0.37 ± 0.03	-0.326
$m_\pi^3 a_1^{1/2} \times 10$	0.228 ± 0.010	0.218 ± 0.008	0.222 ± 0.006	$\mathbf{0.222 \pm 0.009}$	0.20 ± 0.04	0.19 ± 0.01	0.152
$m_\pi^5 b_1^{1/2} \times 10^2$	0.58 ± 0.03	0.59 ± 0.03	0.60 ± 0.03	$\mathbf{0.59 \pm 0.02}$	0.5 ± 0.2	0.18 ± 0.02	0.032
$m_\pi^3 a_1^{3/2} \times 10^2$	0.15 ± 0.05	0.19 ± 0.05	0.17 ± 0.04	$\mathbf{0.17 \pm 0.05}$	0.15 ± 0.11	0.065 ± 0.044	0.293
$m_\pi^5 b_1^{3/2} \times 10^3$	-0.94 ± 0.09	-0.97 ± 0.08	-1.03 ± 0.07	$\mathbf{-0.99 \pm 0.09}$	-1.04 ± 0.8	-0.92 ± 0.17	0.544
$m_\pi^5 a_2^{1/2} \times 10^3$	0.60 ± 0.13	0.54 ± 0.03	0.55 ± 0.02	$\mathbf{0.55 \pm 0.05}$	0.53 ± 0.05	0.47 ± 0.03	0.142
$m_\pi^7 b_2^{1/2} \times 10^4$	-0.89 ± 0.10	-0.96 ± 0.09	-0.95 ± 0.09	$\mathbf{-0.94 \pm 0.09}$	0.20 ± 0.02	-1.4 ± 0.3	-1.98
$m_\pi^5 a_2^{3/2} \times 10^4$	-0.05 ± 0.60	-0.12 ± 0.16	-0.19 ± 0.15	$\mathbf{-0.15 \pm 0.18}$	-0.09 ± 0.03	-0.11 ± 0.27	-0.45
$m_\pi^7 b_2^{3/2} \times 10^4$	-1.12 ± 0.10	-1.14 ± 0.09	-1.14 ± 0.09	$\mathbf{-1.13 \pm 0.06}$	-0.03 ± 0.01	-0.96 ± 0.26	0.61

Table 30

Largest single contribution to each one of the sum rules listed in Table 29. Notice that for higher angular momentum the FTPWDR are dominated by asymptotic physics. Thus we have included a systematic uncertainty associated with the different Regge models as described in the text. Recall that for the scalar scattering lengths a_0^I HPWDR$_{sub}$ is the same as the direct CFD calculation as it includes subtractions for both isospins.

	Largest contribution to the sum rules											
	$a_0^{1/2}$	$b_0^{1/2}$	$a_0^{3/2}$	$b_0^{3/2}$	$a_1^{1/2}$	$b_1^{1/2}$	$a_1^{3/2}$	$b_1^{3/2}$	$a_2^{1/2}$	$b_2^{1/2}$	$a_2^{3/2}$	$b_2^{3/2}$
FTPWDR	$f_0^{1/2}(s)$	$f_0^{1/2}(s)$	a_0^+	$f_1^{1/2}(s)$	$f_1^{1/2}(s)$	$f_1^{1/2}(s)$	$g_0^0(s)$	$g_0^0(s)$	Regge$_{\pi K}$	$g_0^0(s)$	Regge$_{\pi K}$	$g_0^0(s)$
HPWDR	$g_1^1(s)$	$g_1^1(s)$	$g_1^1(s)$	$g_1^1(s)$	$g_1^1(s)$	$f_1^{1/2}(s)$	$f_1^{1/2}(s)$	$g_0^0(s)$	$g_1^1(s)$	$g_0^0(s)$	$g_0^0(s)$	$g_0^0(s)$
HPWDR$_{sub}$	$a_0^{1/2}$	a_0^-	$a_0^{3/2}$	a_0^-	$f_1^{1/2}(s)$	$f_1^{1/2}(s)$	a_0^-	$g_0^0(s)$	$g_1^1(s)$	$g_0^0(s)$	$g_0^0(s)$	$g_0^0(s)$

their description of the $K^*(892)$ resonance yields a larger mass than observed in πK scattering. Nonetheless, they are fairly compatible with our direct CFD value, once again due to the large uncertainty of the latter.

When discussing the $I = 3/2$, $\ell = 1$ wave, we have to keep in mind that it is so small that it is usually neglected in the literature and it has no data below 1 GeV, very far from threshold (see Fig. 10). For this reason, we did not expect our direct CFD result to be very reliable. However, the fact that the sum rules for this wave are dominated by other waves allows us to obtain very accurate values for its threshold parameters. Remarkably, all three sum rules are perfectly consistent among themselves at the one-sigma level, even when their uncertainties are much smaller than that of the CFD direct result, which is nevertheless very consistent with them. The sum-rule results of [43] are perfectly compatible with our direct CFD calculation and consistent at roughly the 2-sigma level with our sum rules.

The D-waves are the first for which we do not impose their own Roy–Steiner equations. They are modified from UFD to CFD indirectly because they enter as input in the Roy–Steiner equations of the S and P-waves, and also in the forward dispersion relations. Remember we have chosen existing Breit–Wigner-like parameterizations to describe the data around the resonance and that there are no data below roughly 1 GeV, where they are almost negligible. Hence, the direct parameterizations carry little, if any, information about threshold dynamics. Thus, in principle, our CFD results are not expected to be very reliable there. The situation may be even worse for the $I = 3/2$ case because it is almost negligible everywhere (see Fig. 13). As a matter of fact, we were only interested in the bulk of their contribution to dispersion relations above 1 GeV. Surprisingly, the scattering lengths from sum rules are perfectly consistent with each other for both the $I = 1/2$ and $I = 3/2$ partial waves, and even with their CFD parameterization as well as with the results in [245]. The slopes of the D-wave CFD are meaningless, but our sum rules are fairly consistent among themselves and with [245]. Note that we confirm the negative sign for $b_2^{3/2}$, at odds with the positive NNLO ChPT estimate. Of course, the direct CFD slope-parameters for the D-waves are less reliable than those obtained from sum rules, as there is a lack of data, we chose very simple parameterizations and we have not imposed partial-wave dispersion relations on these waves.

As a technical remark, let us note that, as shown in Table 30, while the asymptotic region for $\ell = 2$ is almost negligible for sum rules obtained from HPWDR, it dominates the FTPWDR sum rules for D-wave scattering lengths, and also plays a significant role for the slopes. Unfortunately, these contributions present a sizable, although not dominant, dependence on second or even third-order derivatives on the t-variable of the Regge model. As explained in Section 4.3 we use

Table 31
Adler zero positions $\sqrt{s_A}$ (GeV), for the $I = 1/2$ and $I = 3/2$ S-waves from dispersion relations using as input either the UFD or CFD parameterizations. Recall that the LO ChPT result is $\simeq 0.486$ GeV for $I = 1/2$ and $\simeq 0.516$ GeV for $I = 3/2$.

	UFD $I = 1/2$	CFD $I = 1/2$	UFD $I = 3/2$	CFD $I = 3/2$
$\sqrt{s_{A_{FTPWDR}}}$	$0.477^{+0.0010}_{-0.007}$	$0.466^{+0.006}_{-0.005}$	$0.530^{+0.013}_{-0.016}$	$0.549^{+0.008}_{-0.0010}$
$\sqrt{s_{A_{HPWDR}}}$	$0.473^{+0.011}_{-0.009}$	$0.466^{+0.007}_{-0.005}$	$0.537^{+0.016}_{-0.019}$	$0.551^{+0.009}_{-0.0010}$
$\sqrt{s_{A_{HPWDR_{sub}}}}$	$0.481^{+0.008}_{-0.008}$	$0.470^{+0.010}_{-0.005}$	$0.532^{+0.013}_{-0.016}$	$0.552^{+0.008}_{-0.010}$

two different asymptotic models: On the one hand, the one for the πK channel [143], which comes from the $\pi\pi$ Regge model through factorization, and, on the other hand, the Veneziano model [144] for $\pi\pi \to K\bar{K}$. As shown in Section 4.3 these two models produce fairly consistent descriptions of the close-to-forward region on the s variable. As a result, it is irrelevant whether we use one or the other inside our S and P-waves dispersion relations. But, unfortunately, their second or third derivatives with respect to t are incompatible and this is precisely a relevant contribution to the D-wave sum rules (Fig. 26 illustrates that this incompatibility already occurs for the first and second derivatives). Thus, for our D-wave sum rules, we provide in Table 29 the average of the two models with a combined uncertainty coming from the statistical error and a systematic error estimated as the difference between the two.

All in all, we therefore consider that our CFD and its uncertainty estimates for the S and P waves give a very consistent description of the threshold parameters. The D waves, which are needed as input and were devised to reproduce data above 1 GeV and particularly their dominant resonance region, still provide a decent description at threshold of the scattering lengths, but not the slopes, although we can obtain reliable values for them from our sum rules.

To summarize, our most reliable and accurate "Final Values" for threshold parameters are those coming from sum-rule determinations and are listed in Tables 28 and 29. This is one of the main novelties in this report and one of the main applications of our constrained parameterizations.

7.1.3. Adler zeros and subthreshold parameters

There are certain subthreshold quantities of interest. First of all, Adler zeros, which are zeros of scalar partial waves that appear due to the spontaneous chiral symmetry breaking pattern of QCD. In particular, Goldstone bosons should couple derivatively among themselves and therefore their scattering amplitude should have a zero at $s = 0$. However, pions and kaons are not pure Goldstone bosons and have a small mass (not so small for kaons). At low energies and sufficiently far and below threshold the amplitude basically behaves as a polynomial so we still expect a zero not exactly at $s = 0$ but displaced by a magnitude of $O(M_P^2)$ where M_P is the mass of the pseudoscalar meson. These zeros are a dynamical feature of chiral symmetry, which are not seen in other waves where there are always zeros right at threshold due to the $q^{2\ell}$ behavior. These zeros were first found by S.L. Adler [158] using current algebra, which is equivalent to LO ChPT. We have already used their LO ChPT values inside our low-energy $S^{1/2}$ and $S^{3/2}$ parameterizations in Eqs. (73) and (75). These are $\sqrt{s_{A,LO}} = \sqrt{\Sigma_{\pi K}} \simeq 0.516$ GeV for $I = 3/2$ and $\simeq 0.486$ GeV for isospin 1/2, as obtained from Eq. (76). Their position in the complex s plane has been represented in Fig. 20.

Of course, their LO value does not have to be the true position, we just use it as a reasonable value to define our parameterization. But we have calculated their actual values by looking for zeros of partial-wave dispersion relations in the real axis below threshold, using either the UFD or the CFD parameterizations as input. The results are listed in Table 31. There we see that the three kinds of dispersion relations yield very consistent values, which makes our result very robust. The UFD results are closer to the LO ChPT result. However, the CFD values are somewhat different from those of UFD and roughly 3-sigmas away from the LO calculation, which could be clear evidence that NLO ChPT corrections are needed at this level of precision.

As a technical remark, one may wonder if we could change our value of the Adler zero in our parameterizations to this CFD result. However, we should recall that our parameterizations are only chosen to describe data in the physical region. We have indeed adopted a particular analytic form to be able to imitate some basic features (like Adler zeros, or some resonant given shape), but our parametrizations are not model-independent, just a reasonable fit to data to be used as input for the dispersion relations. We do not need them to be accurate outside the physical region. That is what dispersion integrals are for. In addition, we chose our low-energy partial wave parameterizations as truncated conformal expansions avoiding the circular-cut and the Adler zero is very close to that cut, or even inside as the the $I = 1/2$ dispersive CFD case. It makes no sense to try to be accurate with the truncated conformal expansion at the border or outside its applicability limit. Thus, the robust results are the dispersive ones and, as it happened with the $\kappa/K_0^*(700)$ pole, the UFD and CFD parameterizations can only be expected to provide a fair but model-dependent approximation of features in the complex plane outside the physical real axis.

Other interesting quantities are the coefficients of the so-called subthreshold expansion, obtained around the $t \to 0$ and $\nu \to 0$ limit. In the πK scattering case this means $s = u = \Sigma_{\pi K}$. The ChPT calculations are expected to converge better in this region because there is no threshold singularity. Fortunately, our set of dispersion relations can be continued below the physical region, so that we can make use of these sets to determine the amplitudes and their derivatives with

Table 32

Determinations of the coefficients of the πK subthreshold expansion from various approaches. Although we use 3 different dispersive families, for C_{00}^+ and C_{01}^+ the HDR is exactly the same as the fixed-t one. Note that the "+" cases do not have two different HDR values because their HDR is always once-subtracted.

	This work sum rules with CFD input			Sum rules Büttiker et al. [43]	NNLO ChPT Bijnens et al. [85]	Sum rules Lang et al. [349]
	Fixed-t	HDR	HDR$_{sub}$			
C_{00}^+	1.52 ± 0.56	like fixed-t		2.01 ± 1.10	0.278	-0.52 ± 2.03
C_{10}^+	0.96 ± 0.11	1.04 ± 0.11		0.87 ± 0.08	0.898	0.55 ± 0.07
C_{01}^+	2.34 ± 0.05	like fixed-t		2.07 ± 0.10	3.8	2.06 ± 0.22
C_{11}^+	-0.047 ± 0.006	-0.050 ± 0.006		-0.066 ± 0.010	-0.10	-0.04 ± 0.02
C_{00}^-	9.11 ± 0.35	9.54 ± 0.38	9.04 ± 0.39	8.92 ± 0.38	8.99	7.31 ± 0.90
C_{10}^-	0.45 ± 0.05	0.38 ± 0.02	0.39 ± 0.02	0.31 ± 0.01	0.088	0.21 ± 0.04
C_{01}^-	0.68 ± 0.02	0.66 ± 0.02	0.68 ± 0.02	0.62 ± 0.06	0.71	0.51 ± 0.10
F_{CD}^+	3.55 ± 0.64	3.71 ± 0.64		3.90 ± 1.50	2.11	

high accuracy. We adopt the standard definition:

$$F^+(s,t) = \sum_{ij} C_{ij}^+ \left(\frac{t}{m_{\pi^+}^2}\right)^i \left(\frac{\nu}{4m_{\pi}+m_K}\right)^{2j}, \quad F^-(s,t) = \frac{\nu}{4m_{\pi}+m_K} \sum_{ij} C_{ij}^- \left(\frac{t}{m_{\pi^+}^2}\right)^i \left(\frac{\nu}{4m_{\pi}+m_K}\right)^{2j}, \quad (142)$$

where the parameters C_{ij} are dimensionless and $\nu = s - u$. We have obtained their algebraic expressions by expanding the Kernels in Appendix E in terms of t, ν. These expansions are then introduced in Eqs. (53)–(55) to obtain the corresponding sum rules. However, these are lengthy expressions and we will just list the numerical results in Table 32. Note we provide values using our CFD parameterization as input for our three kinds of dispersion relations (without projecting on partial waves) obtained either from Fixed-t or HDR (either with no or one subtraction for F^-). We also provide the symmetric amplitude evaluated at the Cheng–Dashen point $\nu = 0$, $t = 2m_\pi^2$, which is of interest for the next subsection. Previous calculations obtained within dispersive and ChPT approaches are also listed for comparison.

Note that our sum-rule determinations are very consistent among themselves, all of them within one standard deviation of the others. Our results, although equal in sign and relatively similar in size to those obtained in [43] are sometimes significantly different in terms of standard deviations. Note also that our results have in most cases somewhat smaller uncertainties.

7.2. πK σ-term

Another interesting application of our results is in the calculation of the so-called πK σ-term. This requires an extrapolation of the $\pi K \to \pi K$ amplitude to an unphysical point, which can be achieved in a robust and model-independent way thanks to our dispersive formalism.

The relevance of σ-terms is due to their relation to $\langle H | m_q q\bar{q} | H \rangle$, which tests the QCD mass terms inside a hadron H. The σ-term is nothing but the scalar form factor of the H hadron evaluated at zero momentum transfer, which intuitively yields a contribution to the hadron mass and also sets the normalization of the scalar form factor itself. Unfortunately, no single scalar hadronic probe is accessible experimentally at low-energies, and therefore it has to be obtained indirectly through the scattering of two hadrons, one of which is the hadron of interest, which appears also in the final state. The simplest possibility is, therefore, the scattering process $\Phi(q)H(p) \to \Phi(q')H(p')$, where Φ is a pseudo-Nambu–Goldstone Boson i.e. π, K, η, most frequently, a pion. Note that in the t-channel of this process it is possible to exchange two Goldtone bosons to form a scalar current that would therefore couple to the HH system. The use of Goldstone bosons leads to a low-energy theorem [350,351], to be introduced below, that relates the scattering amplitude to the scalar form factor.

The archetypal example is the πN σ-term, because it probes the role of quark masses in the total mass of the nucleon (see [352] for an up-to-date pedagogical and historical introduction). This is actually the system for which the low-energy theorem was first introduced in [350], although it was later corrected in [351]. There are many phenomenological determinations [189–191,353–355] and effective-field-theory-based calculations [188,192–194,354,356–358]. Generically, modern phenomenological data-driven determinations cluster around a value of $\simeq 60$ MeV. However, there is some tension with modern lattice-QCD calculations [359–363], which favor a value closer to $\simeq 40$ MeV.[5] For our purposes, the most interesting study is the dispersive analysis of πN scattering in [188,192] since the authors used as their framework a system of hyperbolic dispersion relations similar to the ones described in this work, hence allowing for robust extractions of the πK σ-term for different low energy inputs [192–194].

Since our dispersive formalism is very similar, it is straightforward to apply it to calculate the πK σ-term [365,366], setting $H = K$. Let us first define the scalar form-factor of the kaon, $\Gamma_K(t)$, as:

$$\Gamma_K(t) = \left\langle K^0\left(p'\right) | \hat{m}(\bar{u}u + \bar{d}d) | K^0(p) \right\rangle, \quad \hat{m} = \frac{1}{2}(m_u + m_d), \quad t = (p'-p)^2, \quad (143)$$

---

[5] While this manuscript was under referee's revision, a new Lattice-QCD determination was published [364], which value is compatible with the dispersive determinations.

Then, the πK σ-term is defined as:

$$\sigma_{\pi K} \equiv \frac{\Gamma_K(0)}{2m_\pi}. \tag{144}$$

Now, as commented above, the scalar form factor is not directly measurable but, thanks to chiral symmetry, is related to the πK symmetric amplitude through the following low-energy theorem, in which a "soft-pion" is probing the kaon [351]:

$$F_\pi^2 F^+(t, \nu) = \Gamma_K(t) + q'^\mu q^\nu r_{\mu\nu}, \tag{145}$$

where F_π is the pion decay constant and $q'^\mu q^\nu r_{\mu\nu}$ is the so-called remainder, which is not determined by chiral symmetry, although it must have the same analytic structure than the scattering amplitude. This remainder is suppressed by evaluating the expression at the Cheng–Dashen point [350], $t = 2m_\pi^2$, $\nu = (s - u) = 0$, where:

$$F_\pi^2 F_{CD}^+ = \Gamma_K\left(2m_\pi^2\right) + \Delta_{\pi K}^{CD}. \tag{146}$$

For brevity F_{CD}^+, $\Delta_{\pi K}^{CD}$ stand, respectively, for the scattering amplitude and remainder evaluated at the Cheng–Dashen point. The final step to obtain $\sigma_{\pi K}$ is to evaluate the difference

$$\Delta_\sigma = \Gamma_K\left(2m_\pi^2\right) - \Gamma_K(0). \tag{147}$$

All in all, we can recast $\sigma_{\pi K}$ as follows:

$$2m_\pi \sigma_{\pi K} = F_\pi^2 F_{CD}^+ - \Delta_\sigma - \Delta_{\pi K}^{CD}. \tag{148}$$

Of course, the very $\sigma_{\pi K}$ and all these quantities can be evaluated using ChPT [85,366]. However, in the spirit of this report, we aim at a data-driven determination. Remember that we expect the remainder to be small at the Cheng–Dashen point. We also expect Δ_σ to be relatively small since it is the difference between not too distant values of t (and the scalar form factor only has the right cut starting at twice that distance). These expectations have been explicitly checked within NLO ChPT [366]. Therefore the dominant term should be the one containing F_{CD}^+, which is the part that we have indeed calculated from data using our CFD as input for the sum rule.

Actually, in the previous section, we presented our evaluation of two subthreshold sum-rules for F_{CD}^+: one obtained from fixed-t dispersion relations and another one from HDR (note that for the symmetric case we always have one-subtraction). The numerical results are displayed in the final row of Table 32 and they come out perfectly compatible with one another and with similar uncertainties. In this case, we do not combine the two results as we did for the threshold parameters in Eq. (141), because now the two values are strongly correlated by their subtraction constant. Hence, we have just taken their average, and for the uncertainty we have added half of their difference to their statistical error, which is the same for both. On the whole:

$$F_{CD}^+ = 3.6 \pm 0.7, \tag{149}$$

which is the main result of this section. In particular, this number is compatible with the estimate obtained by the Bonn–Paris group [43], although our result is slightly lower and our uncertainties are twice smaller. In contrast, it is in a $\sim 2\sigma$ tension with the value estimated from NNLO ChPT in [85] (no errors), which is already about 50% larger than the range of values from 1.2 to 1.4 estimated to NLO in [366]. Note that with our F_{CD}^+ value, the relative sizes of the remainder and Δ_σ terms become even smaller.

As a future prospect, in order to extract completely the $\sigma_{\pi K}$-term from data in a robust and precise way, one would need [365]:

- A data-driven determination of F_{CD}^+, like the one we have just obtained here from a dispersive sum rule using our CFD as input.
- A determination of the remainder $\Delta_{\pi K}^{CD}$. Remember this has been made small on purpose, by choosing the Cheng–Dashen point. The best calculation is that of [366], based on NLO ChPT, that yields:

$$\Delta_{\pi K}^{CD} = [0.013...0.021]\, m_\pi^2.$$

Thus, the remainder estimate[6] is about two orders of magnitude less than our value $F_\pi^2 F_{CD}^+ = (1.6 \pm 0.64) m_\pi^2$. This is a consistency check that the use of the Cheng–Dashen point truly suppresses the remainder. In that work, it has also been shown that, even though corrections can appear on each separated term, they cancel in the difference. This should keep on happening even for higher-order corrections, so we think that the theoretical estimation of the smallness of this difference might be fairly reliable, even when we have seen that one of the terms in the difference is much larger than its NLO value.

---

[6] We thank B. Kubis for explaining to us that, although in [366] other ranges were obtained when using $F^2 = F_K^2$ or $F_\pi F_K$, which might be legitimate from the point of view of the chiral expansion, being a soft *pion* SU(2) theorem the "correct" choice is $F^2 = F_\pi^2$.

- Calculate the Δ_σ difference dispersively. Remember this only concerns the scalar form factor evaluated at two different momentum transfers below threshold, where no further analytic structures exist and the dependence should be smooth. We think it could also be obtained from data by using the coupled-channel MO formalism for the $\pi\pi \to K\bar{K}$ scalar form factor developed in [367]. Maybe it could even be possible to update some of the input used there with our CFD.

Unfortunately, we have not been able to find any lattice calculations of the kaon sigma term. There are calculations of the kaon mass dependence on quark masses (see for instance the review [368] and references therein) and in principle an extraction of this sigma term seems feasible. However, such a calculation is far beyond our scope and capabilities, since one has to deal with the usual lattice technicalities of finite volume effects, continuum extrapolation, physical mass extrapolation, different actions, scale setting, etc... (see [369] and references therein for a review on light hadron masses from lattice). There are indirect extractions of the sigma term, or more precisely the scalar form factor of the kaon from lattice data, but using ChPT or a resummed version of it (see [370–372]. These result in an estimate of $\Gamma_K(0)$ in the range 0.4 to 0.6. We nevertheless hope that our result, and the persistent tension with ChPT calculations, or at least the apparent need for large ChPT corrections, can raise interest in the lattice community to calculate this number.

In summary, using our CFD as input for two sum rules for the F^+ symmetric amplitude, we have been able to provide a robust and precise determination, from a dispersive analysis of data, of the dominant contribution to the kaon σ-term. As it happened with other quantities of interest, our value is consistent with previous dispersive results, although our smaller uncertainties reveal, once more, some tension with the perturbative calculations within $SU(3)$ ChPT.

7.3. $\pi\pi \to K\bar{K}$ And $(g-2)_\mu$

Another topic of interest, where dispersion relations provide a solid framework to work with, is the hadronic contribution to the $(g-2)_\mu$. Explaining in detail the different approaches towards the $(g-2)_\mu$ determination is out of our scope and we refer the reader to the recent review on Ref. [373]. Nevertheless, we comment very briefly on the motivation for its study. The anomalous magnetic moment of the muon can be determined both theoretically, either data-driven or from lattice QCD, and experimentally (see for instance [374–376]). Of all the Standard Model contributions to $(g-2)_\mu$ both the QED and electroweak contributions have been obtained from perturbation theory to a high degree of accuracy. Nowadays the largest factor to the final uncertainty comes from hadronic contributions, which have to be calculated in a non-perturbative way. These are classified according to their diagram topology into the so-called Hadron Vacuum Polarization (*HVP*) and Hadronic Light by Light (*HLbL*) terms. In the past these contributions were determined using various models, hence producing large systematic uncertainties. However, in the last few years, considerable improvements have been made to this topic, led by dispersive formalisms applied to existing data analyses including mesonic final states. A theoretical study group, the *Muon $g-2$ Theory Initiative* [373] was recently formed, to lead the analyses as well as weighting and averaging the theoretical evaluations regarding the various $(g-2)_\mu$ contributions. Their recent final result [373] reads

$$a_\mu^{\text{SM}} = 116591810(43) \times 10^{-11}. \tag{150}$$

The experimental determination made almost 20 years ago by the E821 collaboration at Brookhaven [374,375] had at the time of the publication smaller uncertainties than both the *HVP* and *HLbL* theoretical predictions. At present, two major experiments are underway to refine the experimental uncertainties with more data and higher statistics. The first one is the Fermilab Muon $g-2$ collaboration (FNAL) [377], the second one is the proposed g-2/EDM experiment J-PARC initiative, which will perform a new experimental design [378]. Both of them expect to reduce the $(g-2)_\mu$ error by a factor of 4. During the referee revision of this manuscript, the FNAL collaboration released its first result [379], which still has not achieved the precision goal. It is in excellent agreement with the previous E821 measurement and, when both are combined, yield the present experimental average

$$a_\mu^{exp} = 116592061(41) \times 10^{-11} \quad (0.35\text{ppm}). \tag{151}$$

This theoretical determination lies below the experimental value by $4.2\,\sigma$. Nonetheless, a recent lattice QCD determination of the leading-order hadronic vacuum polarization [380], with similar precision to dispersive studies, yields a larger value than those previous theoretical determinations. This result, together with the rest of the dominant contributions would eliminate the discrepancy with data.

Further studies will be needed to make the dispersive, lattice, and experimental numbers agree or to confirm the discrepancy.

7.3.1. Hadronic-vacuum polarization

As explained above, both the *HVP* and *HLbL* contribute to similar order to the muonic $(g-2)_\mu$ term. Thus a precise and robust calculation of these quantities is paramount to extract the most rigorous value and compare properly between the various approaches involved in the determination of this observable.

The hadronic vacuum polarization can be best extracted from $e^+e^- \to$ hadrons. The biggest contribution, by far, comes from the $\pi\pi$ channel, due to its low threshold. Recent dispersive analyses have been applied to this $e^+e^- \to \pi^+\pi^-$
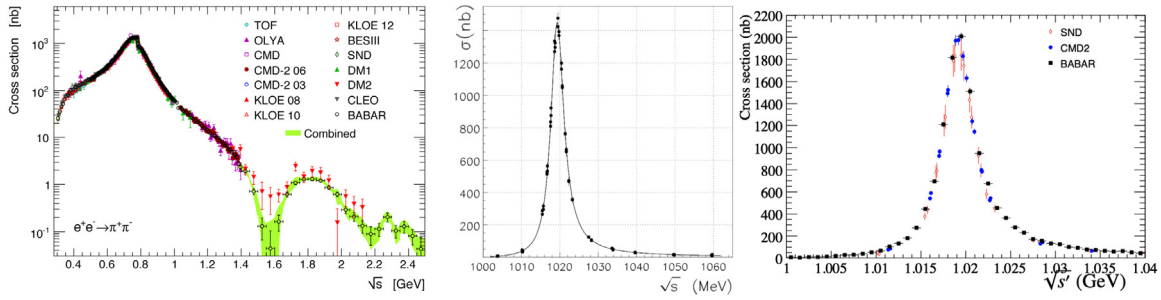
Fig. 42. Cross sections of the reactions $e^+e^- \to \pi^+\pi^-$ (left panel), $e^+e^- \to K_S K_L$ (center panel) and $e^+e^- \to K^+K^-$ (right panel). Notice how the main contribution to the *HVP*, which is the region around the $\rho - \omega$ resonances mixing, is purely elastic.
Source: Figures taken from [381] (left), [382] (center) and [383] (right).

channel [199], which includes modern high statistic data samples. This work is a dispersive implementation based on the well-known Roy equations [44], and is an update over a previous solution on $\pi\pi$ scattering [182], with a slight modification of the *P*-wave. After taking into account the various subtleties required to analyze the new experimental data, the most robust determination of the two-pion contribution to the Hadronic-vacuum polarization reads

$$a_\mu^{\pi\pi}\big|_{\leq 1\text{GeV}} = 495.0(1.5)(2.1) \times 10^{-10}. \tag{152}$$

One may wonder if including the $K\bar{K}$ inelasticity could potentially modify this result, however as seen in Table VI of Ref. [373] the contribution saturates very close to the $\rho - \omega$ peaks, which are shown in Fig. 42 (left panel). If one takes into account that the $K\bar{K}$ threshold of a *P*-wave does not produce any noticeable cusp effect then the result quoted above should not vary appreciably. However the uncertainties are dominated by statistics, and as seen above they are pretty low, so including a larger region and the inelasticity could produce in principle a non-negligible effect.

The second and third biggest contributions to the *HVP* of the muon are $\pi^+\pi^-\pi^0$ and $K^+K^-/K_S K_L$ (center and right panels of Fig. 42) respectively. These are already one order of magnitude smaller both in the magnitude and uncertainty than the $\pi\pi$ contribution. Of the two, the latter is dominated by the $\phi(1020)$ resonance decay into two kaons, which cannot be determined from our dispersive approach. The next low energy contribution would be the 4π channel, which is of the same order as the 3π and KK channels. Finally, only a few higher-energy channels add relatively small contributions compared to the dominant $\pi\pi$ final state.

7.3.2. HLbL

One of the largest sources of uncertainty to the calculation of the $(g-2)_\mu$ is the *HLbL* scattering. Unfortunately, this contribution cannot be calculated perturbatively, and thus must be determined from data analyses or lattice QCD, as it is done for the *HVP*.

However, the *HLbL* contribution is much more challenging in structure, as it is created by four-point functions. As can be seen in Fig. 1 of [384], at low energies the mesonic contribution is dominated by several resonances, in particular the $f_0(980)$ and $a_0(980)$, as well as by charged pion and kaon loops and the pion/kaon box. For a recent and detailed review, we refer the reader again to Ref. [373].

Modern approaches consist of implementing dispersive formulations to relate the off-shell contributions to the $(g-2)_\mu$ with on-shell, measurable quantities. Then, each of these contributions has a physical unambiguous definition. These projects aim to determine with high accuracy separated contributions to the $(g-2)_\mu$, and elucidate the experimental uncertainties required to improve the knowledge on the anomalous magnetic moment.

One of the first dispersive formalisms is explained in detail in Ref. [385], where they define a dispersion relation for the Pauli form factor. Albeit successful in reproducing the pion-pole contribution of a *VMD* model to the $(g-2)_\mu$, no explicit formulas have been derived so far for generic contributions.

The other main approach [386,387] consists of describing in a dispersive way the polarization tensor for off-shell photon–photon scattering, for which the analytic structures of all the components must be first derived. The contribution to the anomalous magnetic moment of the muon can thus be determined from projections over this four-point function. This would be the equivalent of the dispersive description of the *HVP*. However, the fact that we are now dealing with four-point functions makes the task highly complicated.

Several works have been recently published making use of this formalism to determine different pion contributions to the $(g-2)_\mu$ like the pion pole [388,389], two pion contributions [390,391] or the pion box [392]. These are considered to be part of the dominant *HLbL* contributions to the $(g-2)_\mu$.

Extensions to the kaon box seem to be straightforward [373]. However, as seen from Dyson–Schwinger equations, the kaon-box contribution is very suppressed compared to the leading pion one [393], once again due to the larger kaon mass. Nevertheless, as explained in section 4.6.1. of Ref. [373] two-kaon contributions could produce larger effects. This channel
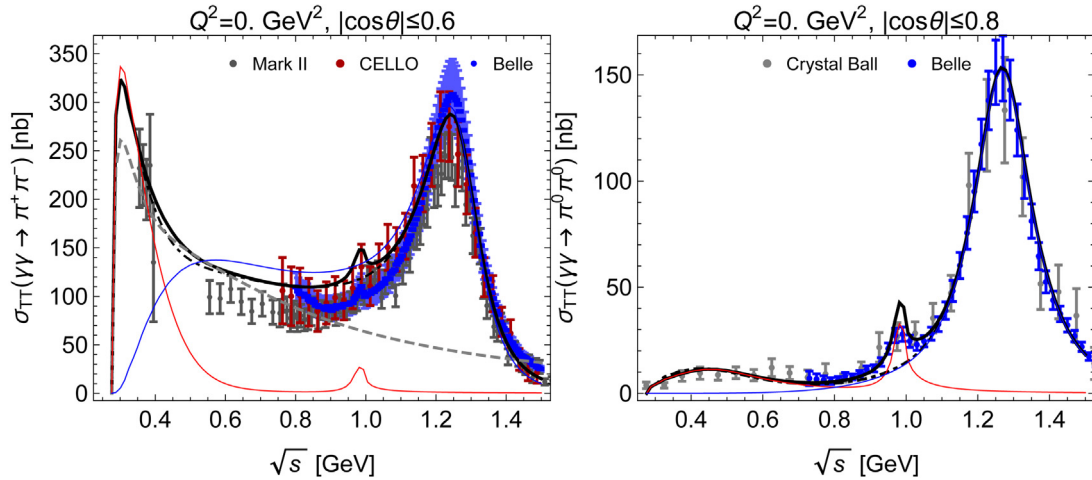
Fig. 43. Cross-sections of the reactions $\gamma\gamma \to \pi^+\pi^-$ (left panel) and $\gamma\gamma \to \pi^0\pi^0$ (right panel). Notice the enhancement at around 1 GeV as a result of including the $K\bar{K}$ channel, which gives rise to the $f_0(980)$ resonance contribution, depicted as the continuous red line in both figures. *Source:* The figure is taken from [203].

not only produces some contribution to the rescattering effects inside the pion/kaon loops but also gives rise to a better constraint over the $f_0(980)$, $a_0(980)$ and $f_2(1270)$, $f_2'(1525)$ resonances contributing to the $(g-2)_\mu$.

Finally, several recent dispersive analyses have been published studying the one or doubly virtual photon scattering into hadrons $\gamma^{(*)}\gamma^* \to \pi\pi(K\bar{K})$ [203,204,210,212,213], most of them including both $\pi\pi$ and $K\bar{K}$ final states, and their contributions to the anomalous magnetic moment of the muon. In some of these works, a previous dispersive determination carried out by our group [42] was already implemented, as shown in Fig. 43, which entails the relevance of this reaction for the precise extraction of the $(g-2)_\mu$. For more details on the topic, we refer the reader to Ref. [394]. We hope that our final dispersive results presented in this report will help these groups to obtain a more reliable determination of the *HLbL* contribution to the $(g-2)_\mu$ following their various approaches.

Note: While this manuscript was under referee's revision, an analysis of the $f_0(980)$ contribution to *HLbL* was completed [395]. It studies $\gamma\gamma \to \pi\pi(K\bar{K})$ with a Muskhelishvili–Omnès method, whose functions are taken from an N/D analysis [396] that fits the $\pi\pi \to \pi\pi$ Madrid–Krakow dispersive analysis [48] and the $\pi\pi \to K\bar{K}$ analysis presented here. The result, well below 10^{-11}, is fairly similar to previous narrow widths estimates, although it illustrates how to go beyond this simple approximation and include rescattering effects using as an ingredient our dispersive results.

8. Summary & conclusions

Let us come to an end by summarizing the main items we have reviewed and our main new results. For the sake of clarity and brevity, we omit in this summary any citation since we have provided aplenty in the main text.

Studies of $\pi K \to \pi K$ and $\pi\pi \to K\bar{K}$ scattering have been the subject of considerable interest since they were first measured around four decades ago. These interactions are not only relevant by themselves, but also because they appear in the final states of numerous hadronic processes. In addition, they are key to hadron spectroscopy, providing one of the main sources of information on the existence and properties of strange resonances — and therefore on the classification of mesons in symmetry multiplets as well as their inner structure. Moreover, in their low-energy regime, these interactions constitute a test-ground for Chiral Perturbation Theory (ChPT) as well as the most recent lattice QCD developments.

Unfortunately, for many decades, the study of $\pi K \to \pi K$ and $\pi\pi \to K\bar{K}$ scattering data has been hindered by the conflict within and between different data sets and affected by large model dependencies. Moreover, we have reviewed here how these data are also in severe conflict with several dispersion relations. However, the wealth of data on hadronic processes collected over the last years, the unprecedented statistics obtained in present and planned experiments, together with the recent theoretical advances in lattice QCD and ChPT, call for a consistent, precise, model-independent, and easy to implement description of $\pi K \to \pi K$ and $\pi\pi \to K\bar{K}$ amplitudes.

In this review, we have shown how this demand can be met by constraining the data description with dispersion relations. As a matter of fact, the two problems commented above can be overcome with the use of dispersion theory, which is a direct consequence of the strong analyticity constraints derived from causality and relativistic crossing symmetry.

Hence, the main result of this review is:

- a dispersively constrained and precise, but still rather simple, simultaneous description of $\pi K \to \pi K$ and $\pi\pi \to K\bar{K}$ scattering data and its uncertainties, which is consistent with an ample sample of dispersion relations. This is what we have called the "Constrained Fit to Data" (CFD) parameterization set.

We have then illustrated several applications of using this CFD as input to obtain other results of interest:

- a rigorous dispersive determination of the existence and parameters of the controversial $\kappa/K_0^*(700)$ scalar meson,
- model-independent determinations of other strange resonances below 2 GeV, reducing their model dependencies employing analytic techniques,
- precise and model-independent values of the threshold and subthreshold parameters, using sum rules derived from different dispersive representations.

In addition, we have reviewed other dispersive applications that use or may profit from some of the previous results, namely, the dispersive study of the non-ordinary $\kappa/K_0^*(700)$ Regge trajectory, the πK sigma term, as well as the contribution of $\pi\pi \to K\bar{K}$ to some hadronic corrections in the calculation of $(g-2)_\mu$.

Hence, after stating our motivation and goals in Section 1, we have reviewed in Section 2 the existing data, explaining the conflicts both within some given data sets and between different experiments.

In Section 3 we have presented first a brief pedagogical introduction to dispersion relations, reviewing also seminal works and the state of the art for $\pi K \to \pi K$ and $\pi\pi \to K\bar{K}$ dispersive approaches. Next, we have derived the different kinds of dispersion relations of relevance for our purposes, although the detailed and lengthy expressions of their integral kernels are provided in Appendix E. The reason to use several types of relations is twofold. On the one hand, they have different applicability regions, both in the real axis and on the complex plane. On the other hand, even for the same observables, they may have different inputs or they may weigh them in non-equivalent ways. The discussion of the applicability ranges, which we have shown how to maximize, is probably the most technical one and has been relegated to the long and thorough Appendix D. In particular, we use forward dispersion relations (FDR) because, apart from their simplicity, they only involve πK amplitudes, and constrain them up to 1.6 GeV. However, in order to study πK partial waves individually, we need to project them out of either fixed-t (FTPWDR) or hyperbolic dispersion relations (HPWDR). Both of them are limited to ∼1 GeV for real values of the energy. The FTPWDRs depend little on $\pi\pi \to K\bar{K}$, but cannot reach the $\kappa/K_0^*(700)$ pole in the complex plane, whereas the HPWDRs reach this pole region, but have sizable contributions from this crossed channel. At this point, it is therefore relevant to consider also FTPWDR and HPWDR for the crossed channel $\pi\pi \to K\bar{K}$, which, as a technical difficulty, need input from the pseudo-physical regime below the $K\bar{K}$ threshold, where no data exist and the amplitude has to be treated with the so-called Muskhelishvili–Omnès method, explained in Section 3.6.

Thus, after the various dispersive representations have been introduced, we have presented in Section 4 a set of Unconstrained Fits to Data (UFD), paying particular attention to the evaluation of systematic uncertainties. For this we have used very simple parameterizations, but flexible enough to accommodate later the dispersive constraints. Our aim with these simple choices is that they should be easy to implement in future studies, either of phenomenological or experimental nature. However, at the end of Section 4, we have reviewed how, this UFD, which is a very nice looking fit to data, was shown in some of our previous works to be inconsistent with FDR for $\pi K \to \pi K$ and HPWDR for $\pi\pi \to K\bar{K}$. Moreover, we have shown here that the UFD also fails to satisfy the $\pi K \to \pi K$ FTPWDR and reach the largest inconsistencies for the $\pi K \to \pi K$ HPWDR. It is therefore evident that simple fits to data, including fits using particular models, are not adequate to produce a precise and reliable description of $\pi K \to \pi K$ and $\pi\pi \to K\bar{K}$.

Consequently, in Section 5, we have presented our main result: the Constrained Fit to Data (CFD). We have explicitly shown that it satisfies our collection of dispersion relations while still describing fairly well the data. Of course, some deviations from the best possible fit to experiment occur, but these are in general relatively mild and are needed to ensure the fulfillment of the dispersive representations. It is also worth noticing that this is the first time that both the $\pi K \to \pi K$ and $\pi\pi \to K\bar{K}$ channels are constrained simultaneously, which completes our previous dispersive analyses.

Once the CFD is available, we use it in Section 6 to study the strange resonances that appear in $\pi K \to \pi K$ scattering. First, it is used as input to build sequences of Padé approximants out of successive derivatives of the amplitude. This is relevant because dispersion relations are formulated in the first Riemann sheet, whereas the poles associated with resonances lie on the contiguous one. Remarkably, these Padé series are shown to converge to the analytic continuation of the amplitude to the next continuous Riemann sheet. The advantage of the method is that the existence of poles and their parameters can thus be determined by avoiding model-dependent assumptions. The only caveats are the sources of uncertainty, which, apart from those of the CFD, come from the numerical calculation of higher derivatives and the truncation of the series. Nevertheless, the results are very robust and competitive with model-based determinations.

In the elastic region it is even possible to get rid of those additional caveats and uncertainties since there is a direct relation between the first and second sheets and resonances can be studied with a fully model-independent and precise dispersive formalism. Actually, in Section 6 we have reviewed our recent work where, using our dispersive analysis of data, we confirmed the existence of the $\kappa/K_0^*(700)$ that the Review of Particle Physics is asking for. In addition, we supply a high precision determination of its parameters, which come in fair agreement with a previous dispersive determination using the FTPWDR prediction inside HPWDR by the Paris group. We concluded this section with a dispersive determination of the $\kappa/K_0^*(700)$ Regge trajectory, which strongly supports its non-ordinary nature.

We started Section 7 using the CFD as input for a precise and model-independent determination of πK threshold and subthreshold parameters. We provide the expressions of these sum-rules, derived from dispersive integrals. Threshold and subthreshold parameters are of relevance to test Chiral Perturbation Theory or to determine its low-energy constants. In this context, the most significant result is a new dispersive and precise determination of the scalar $\pi K \to \pi K$ scattering

lengths. Our values are consistent with the dispersive solution of the Paris group, although our result is obtained from dispersively constrained data fits rather than a solution to dispersion relations. Therefore, the tension between dispersive values and existing lattice results lingers on.

Finally, also in Section 7 we address other possible applications of the dispersive constraints, which require further input besides our scattering parameterization. This is the case of the σ-term determination, as well as the $\pi\pi \rightarrow K\bar{K}$ possible contribution to the $(g-2)_\mu$.

In conclusion, dispersion relations are a very powerful tool for hadron physics. In this report we have not only reviewed but also provided new results concerning their application to $\pi K \rightarrow \pi K$ and $\pi\pi \rightarrow K\bar{K}$ scattering data up to $\sim$1.6 and $\sim$1.5 GeV, respectively. Our main new outcome is a consistent and precise constrained description of these data in terms of simple parameterizations easy to implement for further studies. We have shown here how the use of this approach allows us to determine the existence and/or properties of strange resonances, to provide precise determinations of low-energy observables, as well as several other applications. We hope these results can be of use for further studies both for the phenomenology and experimental communities working on hadron physics.

Declaration of competing interest

Acknowledgments

Appendix A. Conformal expansion for elastic waves

Let us briefly describe here the kind of parameterizations that we have been using for our fits in the elastic region, commenting on the features that make them particularly well suited for that case. Similar conformal expansions have been used for a long time in hadron physics [397–403] and have been recently revived for the particular cases of $\pi\pi$ scattering in [51,226,299] or πK scattering in [101,227]. The specific parameterization described here was introduced by us in [41].

As explained in Section 4.1, thanks to the elastic unitarity condition in Eq. (17), elastic partial-wave amplitudes in the complex s-plane can be recast as

$$f_\ell(s) = \frac{q^{2\ell}}{\Phi_\ell(s) - iq^{2\ell}\sigma(s)}. \tag{A.1}$$

Note we have introduced the *effective range function* $\Phi_\ell(s)$ which *in the elastic region in the real axis*, satisfies:

$$\Phi_\ell(s) = \frac{2q^{2\ell+1}}{\sqrt{s}} \cot\delta_\ell(s). \tag{A.2}$$

Consequently, $\Phi_\ell(s)$ is real in the real axis between πK threshold and the first inelastic threshold. Hence, $\Phi_\ell(s)$ does not have an elastic cut, but still has left-hand, circular, and inelastic cuts, as shown in Fig. A.44. Since $\Phi_\ell(s)$ has no singularities from πK threshold to the next inelastic threshold s_0, we can expand $\Phi_\ell(s)$ in powers of momentum q. This is the so-called "Effective range expansion", whose radius of convergence is small because the circular cut lies rather close to $q = 0$, i.e., $s = m_+^2$.

There is however a better way to use the largest possible domain of analyticity, which is to perform an expansion in powers of a conformal variable that maps the whole complex plane into the unit circle. For πK scattering, due to the circular-cut, it is convenient to introduce first another change of variable

$$y(s) = \left(\frac{s - \Delta_{K\pi}}{s + \Delta_{K\pi}}\right)^2, \tag{A.3}$$

which maps the circular cut into the left real axis. As a result, $\Phi_\ell(y(s))$ only has a right-hand "inelastic" cut and a left-hand cut, as shown in Fig. A.44.b. It is now that we define the conformal variable

$$w(y) = \frac{\sqrt{y} - \alpha\sqrt{y_0 - y}}{\sqrt{y} + \alpha\sqrt{y_0 - y}}, \quad y_0 = y(s_0), \tag{A.4}$$
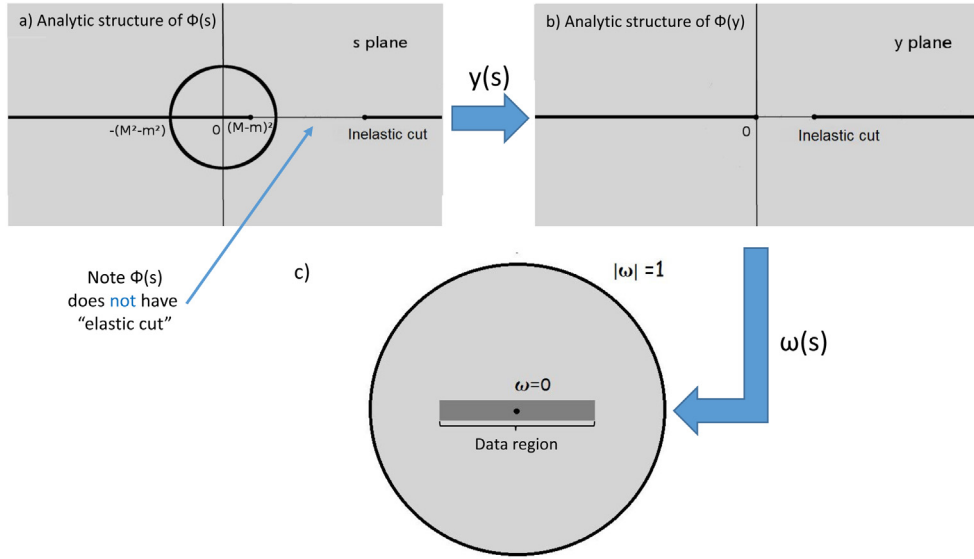
Fig. A.44. Analytic structure in different variables of the πK effective range function $\Phi_\ell(s)$: (a) $\Phi_\ell(s)$ in the s-plane has the same structure as $f(s)$ (see top panel of Fig. 20), except for the absence of the elastic cut. (b) In the $y(s)$-plane the circular-cut disappears. (c) The conformal variable $\omega(y)$ maps the whole analyticity domain of $\Phi_\ell(y)$ inside the unit circle, whereas the cut singularities are confined to $|\omega| = 1$. Note that ω will be defined so that the data region is roughly centered around $\omega = 0$ and not too close to the border.

to map the cut y-plane into the unit circle in the ω-plane. This leads to the structure seen in Fig. A.44. The s_0 constant, with units of energy squared, will set the maximum energy where this conformal series is real and applicable in the real axis. In principle, we could use the *truncated* expression beyond that point, but then, it does no longer have the desired analytic properties, and actually $\cot \delta_\ell$ may become a complex number. In practice, we could use this fact to accommodate some inelasticity contributions, in a purely phenomenological way.

Except for the tiny $P^{3/2}$ and $D^{3/2}$-waves, the parameter α is chosen so that the center of the conformal expansion $\omega = 0$ corresponds to the intermediate point between the πK threshold and the energy of the last data point to be fitted with the conformal formula. In this way, we ensure that the fitted data lies well inside the $\omega = 1$ circle, far from the border and roughly centered around $\omega = 0$, as shown in Fig. A.44. Actually, for the $S^{1/2}$ and $P^{1/2}$ waves, the data fitted with the elastic formalism lie at $|\omega| < 0.45$. In contrast, for the $S^{3/2}$-wave the data lie at $|\omega| < 0.6$. The $P^{3/2}$ and $D^{3/2}$-waves are an exception, because their data starts at 1 GeV, far from the πK threshold. Thus we have chosen their α parameters so that the center of the conformal expansion corresponds to the intermediate point where their data exist. With this choice, the data fitted with this conformal expansion lie at $|\omega| < 0.6$.

It is important to realize that, after these two changes of variable, the singularities now lie at the boundary $|\omega| = 1$. Thus, the effective range function has an analytic expansion $\Phi_\ell(s) = \sum_n B_n w(s)^n$ convergent in the whole $|\omega| < 1$ circle. Therefore, in terms of s, the domain of analyticity of the conformal mapping extends to the whole complex plane outside the circular cut, with a left-hand cut from $(M - m)^2$ to $-\infty$ and a right-hand cut above the first inelastic threshold. This is the power of conformal mappings.

Finally, as explained in the main text, it is customary to abuse the notation and write:

$$\cot \delta_\ell(s) = \frac{\sqrt{s}}{2q^{2\ell+1}} \Phi_\ell(s) \tag{A.5}$$

as a function in the complex s plane. With this definition, in the elastic region of the real axis, we can write

$$\cot \delta_\ell(s) = \frac{\sqrt{s}}{2q^{2\ell+1}} \Phi_\ell(s) = \frac{\sqrt{s}}{2q^{2\ell+1}} \sum_n B_n w(s)^n. \tag{A.6}$$

This is still not the general form we presented in Eq. (68) in Section 4.1, that we repeat here

$$\cot \delta_\ell(s) = \frac{\sqrt{s}}{2q^{2\ell+1}} F(s) \sum_n B_n \omega(s)^n. \tag{A.7}$$

So far we have seen the $F(s) = 1$ case. But, let us recall that, due to chiral symmetry, scalar partial waves have a so-called Adler zero below threshold, which is easily implemented in the partial waves by writing a pole factor in front of the $\Phi_\ell(s)$

Table B.33

$P^{1/2}$-wave alternative solution parameters. The first four parameters correspond to the elastic parameterization Eq. (86), whereas the rest of the parameters correspond to the inelastic formula Eq. (88).

Parameters	UFD	CFD
B_0	1.144 ± 0.048	1.137 ± 0.048
B_1	0.90 ± 0.60	0.45 ± 0.60
B_2	1.72 ± 1.01	0.78 ± 1.01
m_r	0.8955 ± 0.0018 GeV	0.8947 ± 0.0018 GeV
a_1	-2.17 ± 0.18 GeV^{-2}	-1.66 ± 0.18 GeV^{-2}
a_2	-2.10 ± 0.28 GeV^{-2}	-1.74 ± 0.28 GeV^{-2}
a_3	-1.33 ± 0.09 GeV^{-4}	-1.36 ± 0.09 GeV^{-4}
$\sqrt{s_{r1}}$	0.896 GeV (fixed)	0.896 GeV (fixed)
$\sqrt{s_{r2}}$	1.343 ± 0.013 GeV	1.344 ± 0.013 GeV
$\sqrt{s_{r3}}$	1.647 ± 0.005 GeV	1.655 ± 0.005 GeV
e_1	1 (fixed)	1 (fixed)
e_2	0.048 ± 0.008	0.067 ± 0.008
e_3	0.307 ± 0.016	0.320 ± 0.016
G_1	0.029 ± 0.005 GeV	0.046 ± 0.005 GeV
G_2	0.218 ± 0.042 GeV	0.210 ± 0.042 GeV
G_3	0.303 ± 0.018 GeV	0.290 ± 0.018 GeV

expansion, as follows:

$$\Phi_\ell(s) = \frac{1}{s - s_{Adler}} \sum_n B_n w(s)^n. \tag{A.8}$$

In other words, choosing $F(s) = 1/(s - s_{Adler})$ above. In addition, when there is a narrow well-established resonance and the phase crosses $\pi/2$ at m_r it is also convenient to extract a factor out of the conformal expansion as:

$$\Phi_\ell(s) = (s - m_r^2) \sum_n B_n w(s)^n, \tag{A.9}$$

to accelerate the convergence of the fit. This is nothing but choosing $F(s) = (s - m_r^2)$ above.

These are the expressions, truncated to the minimum number of terms needed to get an acceptable χ^2/dof, that we have used for our parameterizations of πK scattering in the elastic region. However, note that the expression above also provides an analytic extension of Φ_ℓ to the complex plane, which, by means of Eq. (65), yields a fairly good approximation to the partial wave f_ℓ, as long as one is not too far from the elastic region. Actually, we have seen that we find poles for the $\kappa/K_0^*(700)$ and $K^*(892)$ resonances using our conformal parameterizations and, in particular, the CFD conformal parameterization yields reasonable values for both poles and residues. But, of course, these values are model-dependent, since their extraction relies on a particular parameterization. To obtain model-independent results for resonances, one has to rely on dispersion relations, as we do in this report.

Appendix B. Alternative P-wave and form factors

As explained in Section 2, there are P-wave measurements from other processes than scattering. In particular, Ref. [134] details how it could be possible to determine the elastic phase shift of the P-wave around the resonance region from the results of the FOCUS collaboration [133]. The main motivation is twofold. First, there exists some tension between the $K^*(892)$ parameters coming from production experiments and those coming from heavier decays as listed in the RPP [233], particularly for the width of the resonance. Second, should the width be smaller, it would affect our dispersive results, and it could also lead to different results for those works which use the πK vector form factor in their analyses [136–141,228,261]. On top of all the above, our P-wave UFD does not agree very well with the final CFD result, which is surprising considering how small the data uncertainties are. It seems that there might be a non-trivial systematic deviation within the original experimental data, which could help explain this tension [141].

For all these reasons we will implement an alternative fit for the P-wave elastic phase shifts, based on the "pseudo-data" produced by V. Bernard in [141] (Fig. 2 therein) as a result of re-sampling the P-wave fit by the FOCUS collaboration [133]. The rest of the partial waves will remain untouched and are given in Section 4. Once we obtain an Unconstrained Fit to these new Data (UFD) we then procure an alternative Constrained Fit to Data (CFD), following the approach detailed in Section 4.4. We list in Table B.33 the alternative UFD and CFD parameters for this P-wave.

Including this "pseudo-data" into the fits is a bit problematic, as it has been produced from a smooth parameterization. This results in strong, unknown correlations between different bins, both for the central values and uncertainties. As a consequence, no flawless fit to this partial wave can be attained. For simplicity, we have decided to use an ordinary χ^2 function, for which we have produced many $\mathcal{O}(10^3)$ fits to different re-samplings over the "pseudo-data". Hence, instead of using the Minuit [404] crude estimate of the uncertainties, we have calculated the variance of its parameters over the
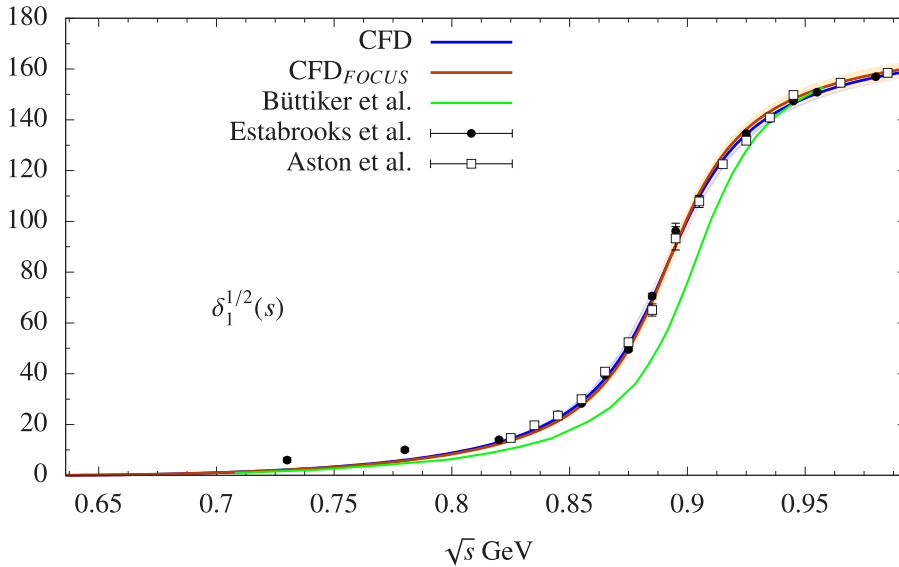
Fig. B.45. Comparison between the original CFD fit (blue) to the *P*-wave from production data [5,6], and the alternative CFD (orange) obtained by using the FOCUS collaboration [133] data.

many re-samplings. On top of that, we have taken some of these re-samples as data samples so that we can define several χ^2 over this partial wave, which are combined into an averaged χ^2 afterward. This way we obtain a stable and normalized definition of a pseudo-χ^2-like function for this partial wave and thus all partial waves and dispersion relations can now be imposed following our approach. An alternative description could be obtained using bootstrapping techniques, but this would demand a bigger set of fits to the Montecarlo re-sampling of the initial parameterization and we should deal with the values of each bin rather than the parameters themselves. This is incompatible with our simplistic approach, where we focus on one fit with simple parameter uncertainties, and thus it will not be used.

First, notice that the alternative and original inelastic parameters of Tables 6 and B.33 are very similar. This result is not surprising as we are using the same data input on this inelastic region. The main difference now is that the alternative UFD describes a narrower $K^*(892)$ resonance, which contributes a bit less to the dispersive inputs.

Additionally, the alternative CFD result is quite compatible with the original fit as seen in Fig. B.45, with a small deviation associated with the different width of the $K^*(892)$. Moreover, both CFD results bend towards one another, producing a much similar pole position for the $K^*(892)$ than the UFD fits. On top of that, the result of the rest of the partial waves is barely any different from before.

Taking into account that we do not have access to measured data here, and the null improvement altogether we cannot say we favor this alternative solution over the original scattering data. However, we have decided to include its parameters here, in case data from heavier decays were extracted in the future. Once additional data were measured for this partial wave, they could be compared to this alternative solution to see if the new information favors this alternative fit over the older data.

Finally, should one use this fit instead of the original one, the CFD dispersive resonance pole for the $K^*(892)$ would read

$$\sqrt{s_p} = (891 \pm 2) - i(23.9 \pm 3.0)\,\text{MeV}, \quad |g| = (5.49 \pm 0.19), \quad \phi_g = -(0.065 \pm 0.011), \qquad \text{CFD FOCUS}$$

$$\sqrt{s_p} = (890 \pm 2) - i(25.6 \pm 1.2)\,\text{MeV}, \quad |g| = (5.69 \pm 0.12), \quad \phi_g = -(0.076 \pm 0.008), \qquad \text{CFD Original} \quad \text{(B.1)}$$

where we have taken the average between the fixed-t and the two HDR dispersive values. Notice that the mass is almost equal to the original CFD, although the width has moved by around 1.3 σ from the original value.

Besides the little changes to the alternative *P*-wave, the rest of the partial waves barely change, if they change at all. The $\kappa/K_0^*(700)$ resonance extracted from this analysis is perfectly compatible with our original value, and the new *S*-wave scattering lengths obtained using this *P*-wave are almost identical to the CFD ones, as listed in Table B.34. Notice we have called this new solution CFD$_{\text{FOCUS}}$ for practical purposes.

In summary, let us recall once again that the idea of implementing an alternative *P*-wave comes from the fact that the production data [5,6] could potentially suffer from a faulty extraction in the region around the $K^*(892)$ mass. Alternatively, in this section, we have provided a dispersive study of a fit compatible with that of the FOCUS collaboration [133], which is consistent with new analyses performed in the recent past for form factors, as well as heavier decays and Dalitz plots extractions.

Table B.34
S-wave scattering lengths (m_π units).

	CFD$_{FOCUS}$	CFD	Ref. [43]
$a_0^{1/2}$	**0.220 ± 0.011**	**0.224 ± 0.011**	0.224 ± 0.022
$a_0^{3/2}$	**−0.049 ± 0.007**	**−0.048 ± 0.006**	−0.0448 ± 0.0077

Table C.35
Parameters of the alternative ϕ_0^0.

Parameter	UFD	CFD$_B$	CFD$_C$
B_1	23.5 ± 1.3	22.1 ± 1.3	23.5 ± 1.3
B_2	29.0 ± 1.3	27.6 ± 1.3	29.1 ± 1.3
B_3	0.01 ± 1.60	1.7 ± 1.6	0.6 ± 1.6
C_1	12.0890 fixed	10.0142 fixed	9.0032fixed
C_2	13.6 ± 2.6	11.1 ± 2.6	10.9 ± 2.6
C_3	−12.9 ± 2.3	−16.0 ± 5.2	−16.0 ± 5.2
C_4	−13.1 ± 2.2	−14.3 ± 2.2	−13.9 ± 2.2
C_5	4.0 ± 2.4	4.5 ± 2.4	4.6 ± 2.4

Table C.36
Parameters of the UFD$_B$ and CFD$_B$ fits to $|g_0^0|$.

Parameter	UFD$_B$	CFD$_B$
D_0	0.588 ± 0.010	0.590 ± 0.010
D_1	−0.380 ± 0.013	−0.339 ± 0.013
D_2	0.12 ± 0.01	0.13 ± 0.01
D_3	−0.09 ± 0.01	−0.12 ± 0.01
F_1	−0.04329 fixed	−0.04195 fixed
F_2	−0.008 ± 0.009	−0.008 ± 0.009
F_3	−0.028 ± 0.007	−0.034 ± 0.007
F_4	0.026 ± 0.007	0.038 ± 0.007

Table C.37
Parameters of the UFD$_C$ and CFD$_C$ fits to $|g_0^0|$.

Parameter	UFD$_C$	CFD$_C$
D_0	0.462 ± 0.008	0.447 ± 0.008
D_1	−0.267 ± 0.013	−0.237 ± 0.013
D_2	0.11 ± 0.01	0.10 ± 0.01
D_3	−0.078 ± 0.009	−0.087 ± 0.009
F_1	−0.04153 fixed	−0.03658 fixed
F_2	−0.010 ± 0.008	−0.016 ± 0.008
F_3	−0.023 ± 0.007	−0.023 ± 0.007
F_4	0.021 ± 0.006	0.027 ± 0.006

Appendix C. Alternative g_0^0 wave

As explained in Sections 4.2, 5.3 and in [42] the Brookhaven experiment [236] used only two resonances, $f_2(1270)$ and $f_2'(1525)$, to describe their data on the $g_2^0(t)$ partial wave. However, we have included a third resonance $f_2(1810)$ following several experiments that claimed its existence and because we have found that it helps obtain a better data fit. Of course, since their g_2^0 wave was used to extract their g_0^0 data, if one now assumes that the $f_2(1810)$ resonance exists, this should produce non-negligible deviations in the data on the scalar–isoscalar phase above roughly 1.6 GeV. On top of that, the parameterization used by the Brookhaven collaboration violates Watson's theorem at lower energies. This is evident if one notices that they obtain a different value for their $g_2^0(t)$ phase right above the $K\bar{K}$ threshold from the $\pi\pi$ phase they should match right below (see Fig. 18). Hence, the first few data bins by [236], shown in Fig. 16, should also be corrected.

We list in Table C.35 the parameters of the "Alternative CFD" $g_0^0(t)$ solution shown in Fig. C.46, obtained by extracting the $g_0^0(t)$ phase from [236] using our own $g_2^0(t)$ wave, rather than the faulty one used by the experimental collaboration. One could wonder if this modification would produce a significant effect in the dispersive results of the $g_0^0(t)$, and thus propagate it to the rest of the partial waves through the dispersion relations. Fortunately, the affected region lies above 1.6 GeV, which is already highly suppressed as input to the $g_0^0(t)$ dispersion relation itself, and its modulus is small there, yielding a negligible effect when changing the parameters between the fit to the original data (Table 10) and the alternative one. Let us recall here that our dispersion relations can be applied only up to 1.47 GeV, and thus they cannot constrain the region where this new $g_0^0(t)$ deviates substantially from the original one. Moreover, no other dispersion relation is modified by this new solution.
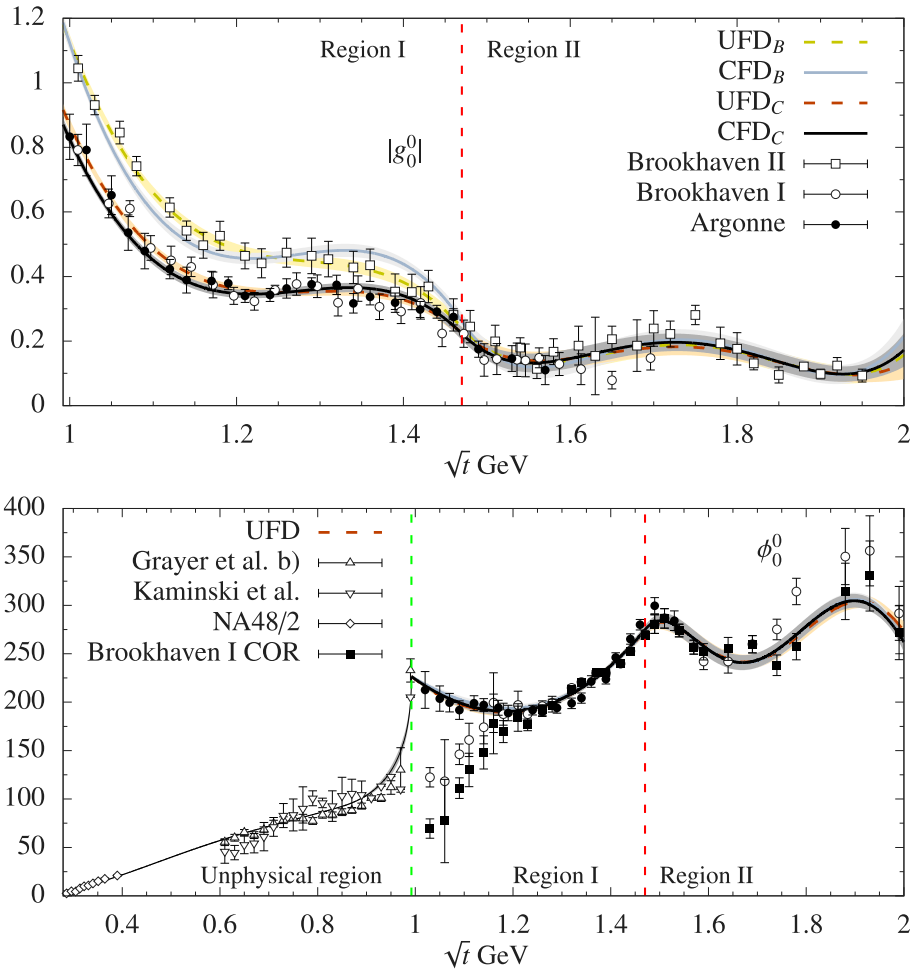
Fig. C.46. Alternative $\pi\pi \to K\bar{K}$ scattering data on the scalar–isoscalar partial wave g_0^0, coming from [7] (Argonne), [8] (Brookhaven-I) and [9] (Brookhaven-II). As explained in the main text, below $K\bar{K}$ threshold, due to Watson's Theorem and the fact that no multi-pion states are observed, the $\pi\pi \to K\bar{K}$ phase shift is precisely that of $\pi\pi \to \pi\pi$ scattering. Thus, in that region, we provide a representative sample of such data coming from scattering experiments which is the data we plot in that region [145] (Grayer et al. solution b), [146,147] (Kaminski et al.), or the very precise $K_{\ell 4}$ decays from [148] (NA48/2).

Notice, as shown in Fig. C.46 that the solutions of the "Alternative CFD" $g_0^0(t)$ and the original one shown in Fig. 16 are very similar for the modulus. This is also reflected in the parameters listed in Tables C.36 and C.37, which are almost equal to those fitting the original data, shown in Tables 10 and 11. Of course, there is a difference between the phases above 1.6 GeV, which could be relevant if one is trying to describe this process up to higher energies.

All in all, we consider this alternative solution as slightly favored over the one in the text, although there we have preferred to stick to the data quoted in the original experimental works, without introducing these further complications. There are several experimental pieces of evidence for the $f_2(1810)$ resonance, which could in principle decay copiously to this channel, and including it clearly improves our fit to the data as explained in [42]. However, using one solution or the other does not modify in any way our dispersive results nor does it introduce any noticeable systematic effect. We have checked that the scattering lengths and the $\kappa/K_0^*(700)$ resonance remain perfectly compatible with the original $g_0^0(t)$ values.

Appendix D. Applicability regions for dispersion relations

In this appendix, we will describe how to calculate the applicability domain of different dispersion relations and how to maximize it, either in the real axis or to make it reach the complex plane in the $\kappa/K_0^*(700)$ region. For Hyperbolic Dispersion Relations (HDR) this translates into specific choices of the a parameter defining the hyperbolae. Our approach will be similar to that in [188,201] and we will study the applicability range both for the s-channel $\pi K \to \pi K$ and for the t-channel $\pi\pi \to K\bar{K}$.
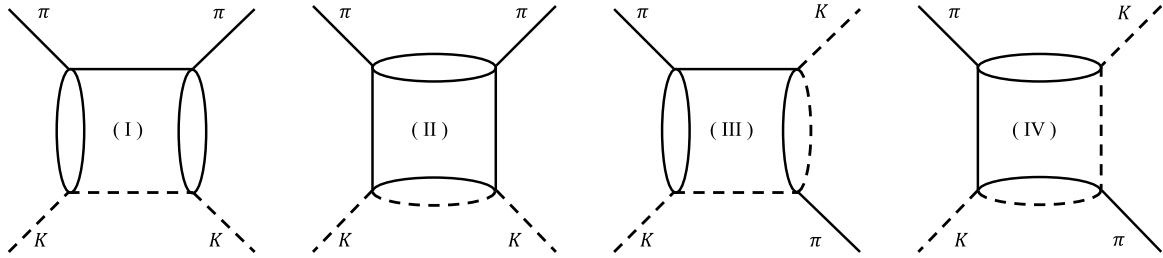
Fig. D.47. Unitarity box diagrams that are used to calculate the double spectral regions of πK scattering. Contrary to Feynman diagrams, unitarity or Cutkosky diagrams have all internal lines on-shell. Continuous lines denote pions while dashed lines denote kaons.

To this end, we will first calculate the double spectral regions, where the imaginary part of the amplitude becomes also imaginary and therefore the Mandelstam analyticity hypothesis does not hold (see [405] for a textbook introduction). This is necessary for the partial-wave projections of the dispersion relations themselves and thus apply directly to the "external" or "unprimed" s, t, u variables. Second, we have to ensure the convergence of the partial-wave expansion of the imaginary parts inside the dispersive integral, which means that it is to be used only inside the (large) Lehmann ellipse [406–408]. This constraint affects directly the "internal" or "primed" variables s', t', u' as well as z'_s, $\lambda_{s'}$, etc.

D.1. Double spectral regions and Lehmann ellipses

Our analysis follows the general scheme of [97,188,201,245,409,409]. Namely, we assume that the $F(s, t, u)$ matrix elements, considered as functions of two independent complex variables, obey Mandelstam (or maximal) analyticity [155]. This means that the amplitude has only those singularities that are required by bound states (poles in the real axis below threshold) or unitarity (cuts) in each of the s, t, and u channels. Let us very briefly explain the mathematical consequences of this assumption, although for a detailed and pedagogical introduction we refer the reader to [405].

In the two-body scattering of pions and kaons there are no bound states, at least not at the physical pion mass, so that $F(s, t)$, for a given t, can be written as a dispersion relation over the right and left kinematic cuts in the s variable. These cuts are the consequence of intermediate particles becoming real. For instance if real particles can be produced in the s-channel for a given energy s then we find a singularity in the form of a discontinuity $D_s(s, t) = [F(s+i\epsilon, t) - F(s-i\epsilon, t)]/2i$, whose value is constrained by s-channel unitarity. Note that, due to Schwarz reflection, i.e. $F(s^*, t) = F^*(s, t)$, in the real s axis $D_s(s, t)$ is nothing but the imaginary part of F, and therefore real. However, if we now continue D_s in the complex t variable, D_s might turn complex. We can then write a dispersion relation in the t variable, not for the amplitude F, but for D_s over the regions where it has a discontinuity due to a kinematic cut in the t channel. Such a discontinuity of D_s in the t variable is called the double spectral function $\rho_{st} = [D_s(s, t+i\epsilon) - D_s(s, t-i\epsilon)]/2i$ and is once again constrained by t channel unitarity. Similarly, we can define ρ_{su} and ρ_{tu}. Therefore, Mandelstam analyticity implies that πK and $\pi\pi \to K\bar{K}$ scattering amplitudes can be written as a sum of double integrals over the regions where the spectral functions ρ_{st}, ρ_{su} and ρ_{tu} have support. These areas are called double spectral regions. Intuitively, the lowest kinematic discontinuities are found when the lowest possible number of particles can become on-shell on each diagram. Since the minimum number of legs in pion and kaon interaction vertices is four, the "unitarity" or Cutkosky box diagrams that we show in Fig. D.47 will give us the double spectral regions. Since these regions contain the singularities of F in the Mandelstam plane, they have to be avoided when writing dispersion relations and limit the applicability of the dispersive approach. Let us then calculate the boundaries of the double spectral regions, using the unitarity box diagrams in Fig. D.47.

The equations that describe the boundary of the support of the spectral function ρ_{st} are:

$$b_I(s, t) : (t - 16m_\pi^2)\lambda_s - 64m_\pi^4 s = 0, \tag{D.1}$$
$$b_{II}(s, t) : (t - 4m_\pi^2)(s - (m_K + 3m_\pi)^2) - 32m_\pi^3 m_+ = 0,$$

where the subscripts I and II indicate what diagram yields each constraint. For the s-channel they apply at $s > m_+^2$ and $s > (m_K + 3m_\pi)^2$, respectively. By means of $s \leftrightarrow u$ crossing, similar equations are obtained for ρ_{ut}. The equations that describe the boundary of the support of ρ_{us} are

$$b_{III}(s, t) : (s - m_-^2)(t + s - m_+^2)\left(\left((3m_\pi - m_K)m_+ + s\right)^2 + t(s - m_+^2)\right) = 0, \tag{D.2}$$
$$b_{IV}(s, t) : (s - m_-^2)(t + s - m_+^2)\left((m_K^2 + 2m_K m_\pi + 5m_\pi^2 - s)^2 + t(s - (m_K + 3m_\pi)^2)\right) = 0.$$

For the s-channel they apply at $s > m_+^2$, $u > (m_K + 3m_\pi)^2$ and $s > (m_K + 3m_\pi)^2$, $u > m_+^2$, respectively.

The support of these double spectral regions can be seen in Fig. D.48 as black areas in the (s, u) plane. Note the $s \leftrightarrow u$ symmetry of the plot. In order to write a dispersion relation, these areas must be avoided. This is one kind of constraint on the applicability of dispersion relations.
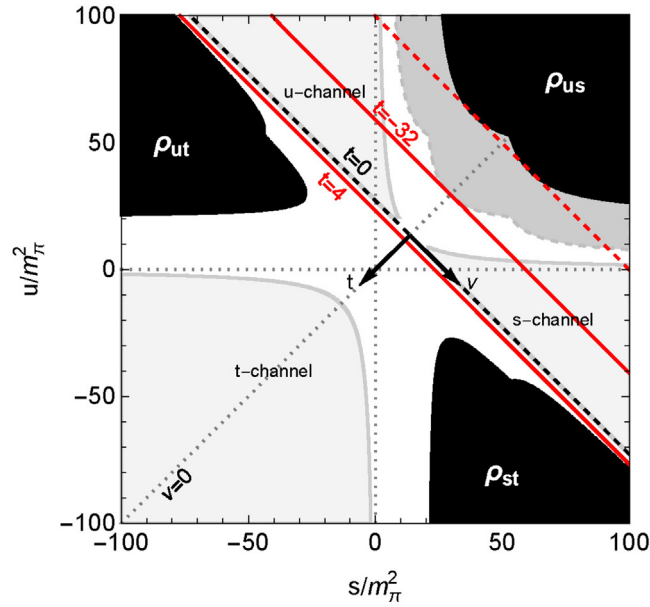
Fig. D.48. Mandelstam (s, u) plane for the πK scattering amplitude. Note we use units of m_π^2. The physical regions for $\pi K \to \pi K$ scattering (s and u-channels) as well as that for $\pi\pi \to K\bar{K}$ (t-channel) are shown as light gray areas. The double spectral regions ρ_{st}, ρ_{ut} and ρ_{us} are represented by black areas. The arrows, starting at $(t, v) = (0, 0)$ show the directions of increasing t and $v = s - u$. Also shown are several parallel lines of constant t. The dark gray area is the region excluded by the s-channel Lehmann ellipse.

In addition, there is another constraint because partial-wave expansions of Im $F(s, t)$ in terms of Legendre polynomials $P_\ell(z)$ converge in the complex z plane within the so-called Lehmann ellipse [406–408]

$$\frac{(\text{Re } z)^2}{A^2} + \frac{(\text{Im } z)^2}{B^2} = 1, \tag{D.3}$$

of foci $z = \pm 1$. Here $A^2 - B^2 = 1$, i.e., the A semi-axis along the real axis is larger than that along the imaginary direction, B. The size of this ellipse of convergence is given by the real $z^{max} = A$ where it first touches a singularity of Im $F(s, t)$, i.e., reaches the double spectral region.

In this report, we have to consider four Lehmann ellipses. The reason is that we have been discussing both $\pi K \to \pi K$ and $\pi\pi \to K\bar{K}$ scattering, which correspond to the s-channel and t-channel of the same amplitude $F(s, t, u)$, respectively. Therefore, we are interested in both the s-channel partial-wave expansion, using the z_s variable, and the t-channel partial waves in terms of the z_t variable. Note that these are "external" variables, in the sense that they are not integrated inside dispersion relations. However, we also use each one of these s-channel and t-channel partial-wave expansions with respect to the $z_{s'}$ and $z_{t'}$ "internal" variables, respectively. All these Lehmann ellipses give rise to different constraints on the applicability of the dispersion relations.

Let us now see how all these constraints limit the applicability region of different kinds of dispersion relations.

D.2. Constraints on fixed-t dispersion relations

Fixed-t dispersion relations are very effective in the study of both equal mass and different mass particles. In Fig. D.48 we have plotted several straight lines corresponding to fixed values of t. The first relevant observation is that for forward scattering $t = 0$, the double spectral regions are avoided for all s. Therefore the forward dispersion relations for πK scattering that we have used in Section 3.3 are well-defined for any value of s. However, it is also obvious that this is an exceptional case. Actually, it can be noticed that the most restrictive boundary for fixed positive t is that of ρ_{st} (or, by symmetry, ρ_{ut}). Thus, if we define $T(s)$ as the solutions of the boundary conditions, by solving Eqs. (D.1) we find:

$$T_{st}(s) = 16m_\pi^2 + \frac{64m_\pi^4 s}{\lambda_s}, \quad \forall s \leq s_0, \tag{D.4}$$

$$T_{st}(s) = 4m_\pi^2 + \frac{32m_\pi^3 m_+}{s - (m_K + 3m_\pi)^2}, \quad \forall s \geq s_0, \tag{D.5}$$

where

$$s_0 = m_K^2 + 4m_K m_\pi + 5m_\pi^2 + 2m_\pi \sqrt{5m_K^2 + 12m_K m_\pi + 8m_\pi^2}. \tag{D.6}$$

Using Eq. (D.5), we find that $t = 4m_\pi^2$ is the first fixed-t line that touches the double spectral regions, for t positive. We have plotted it as a continuous red line in Fig. D.48, asymptotically tangent to ρ_{st} and ρ_{ut} for $\nu = \infty$ and $\nu = -\infty$, respectively. For negative t, if we use Eq. (D.4), we find that the ρ_{us} region is touched by the fixed-$t = -16m_\pi m_+ \simeq -72.75m_\pi^2$ line, which is shown as a dotted red line tangent to two points of ρ_{us}. Recall that for fixed-t dispersion relations we are integrating Im $F(s', t)$ over some polynomial of s', for all values of s'. Thus, if we want Im $F(s', t)$ to be real for all values of s' we find a first constraint:

$$-16m_\pi m_+ < t < 4m_\pi^2, \tag{D.7}$$

required to avoid the double spectral regions.

Let us now remark for completeness that fixed-s or fixed-u dispersion relations are of little use in the physical regions. This is clearly seen in Fig. D.48 for πK scattering, since for the s-channel the highest fixed-u straight line touches the ρ_{ut} double spectral region almost at the s channel threshold, and would therefore be practically useless. It is actually below threshold once we explain in the next section that we should also avoid the dark gray region. The situation is similar for the u-channel and fixed-s. For $\pi\pi \to K\bar{K}$ it is not straightforward from the figure, but the applicability region of fixed-s or fixed-u dispersion relations is very limited, well below the $K\bar{K}$ threshold, as shown for $\pi\pi \to N\bar{N}$ in [45]. Moreover, from the figure it is also clear that forward dispersion relations for $\pi\pi \to K\bar{K}$, i.e. $\nu = 0$, are of no use since that straight line passes right through the ρ_{us} double spectral region. Thus, in practice, fixed-variable dispersion relations for the πK amplitude are only useful for fixed-t.

However, Eq. (D.7) is not the only constraint. There are others, even more stringent, due to the fact that we have to build Im $F(s', t)$ through the partial-wave expansion in $z_{s'} = 1 - 2s't/\lambda_{s'}$. The first value where the corresponding Lehmann ellipse touches the double spectral region is $A_{s'} \equiv z_{s'}^{max} \equiv 1 + 2s'T_{st}(s')/\lambda_{s'}$, which we have seen that for fixed-t lines occurs at $t = 4m_\pi^2$. Once we have obtained the positive end of the ellipse, the negative end is just $-z_{s'}^{max}$. Thus the convergence of the internal partial wave series demands $-z_{s'}^{max} \le z_{s'} \le z_{s'}^{max}$, which translates into the following restriction for t

$$-\frac{\lambda_{s'}}{s'} - T_{st}(s') \le t \le T_{st}(s'). \tag{D.8}$$

The upper applicability bound is given directly by the double-spectral region $T_{st}(s')$ and we have already seen in Fig. D.48 that for fixed-t straight lines it lies at $4m_\pi^2$. However the lower bound in Eq. (D.8) depends also on $\lambda_{s'}/s'$ and is given by the dark gray dashed curve that encloses the dark gray region in Fig. D.48, which thus has to be avoided for our fixed-t dispersion relations. This implies $t > -32m_\pi^2$. All in all, the applicability of fixed-t dispersion relations is limited to:

$$-32m_\pi^2 < t < 4m_\pi^2. \tag{D.9}$$

Both the fixed-$t = -32m_\pi^2$ and $t = 4m_\pi^2$ straight lines are plotted as a red continuous lines in Fig. D.48. It is only between these two lines that fixed-t dispersion relations are well defined.

So far we have not projected the outcome of the dispersion relation in partial waves. What we have seen up to now would be valid to constrain $F(s, t)$. However, we want to constrain partial waves using Roy–Steiner equations to rewrite unphysical cuts in terms of the physical ones within the dispersion relation, as explained in the main text. This representation has its own constraints on its applicability that we review next.

D.3. Complex applicability domain of partial-wave relations from fixed-t dispersion relations

Here we follow closely the excellent account in [97]. Hence, if we want to obtain partial-wave dispersion relations using the Roy–Steiner representation from fixed-t dispersion relations (FTPWDR), we have to project the amplitude obtained from the latter, as follows:

$$f_\ell(s) = \frac{1}{32\pi N} \int_{-1}^{1} dz_s \, P_\ell(z_s) F(s, t(z_s)) = \frac{s}{16\pi N \lambda_s} \int_{-\lambda_s/s}^{0} dt \, P_\ell(z_s(t)) F(s, t), \tag{D.10}$$

where $N = 1, 2$ for non-identical and identical particles, respectively, and $F(s, t(z_s))$ will be obtained from fixed-t dispersion relations. Note that now we are interested in the applicability domain within the complex plane of the *external* variable s. From the definition of the s-channel cosine of the scattering angle, $z_s = 1 + 2st/\lambda_s$, which is integrated over real values in (D.10), we see that if s is complex then t is integrated along a complex segment. Hence, in the integrand of the fixed-t dispersion relation we now need Im $F(s', t)$ for real values of s' but complex values of t.

Let us then rewrite the $z_{s'}$ Lehmann–Martin ellipse [406–408] in terms of the t variable. The t ellipse has now foci at real $t = -\lambda_{s'}/s'$ and $t = 0$ and the new semi-axes are $\tilde{A} = \lambda_{s'}A/2s'$ and $\tilde{A}^2 - \tilde{B}^2 = (\lambda_{s'}/2s')^2$. Its eccentricity is $\epsilon = \sqrt{1 - \tilde{B}^2/\tilde{A}^2} = 1/A$.

It is now convenient to rewrite the equation of the ellipse in polar coordinates $(T(\theta), \theta)$ with respect to the second foci $t = 0$ at the origin of the plane. Namely

$$T(s', \theta) = \frac{\tilde{A}(1 - \epsilon^2)}{1 + \epsilon \cos \theta} = \frac{T_{st}(s')(\lambda_{s'} + s'T_{st}(s'))}{\lambda_{s'} \cos^2 \frac{\theta}{2} + s'T_{st}(s')}. \tag{D.11}$$
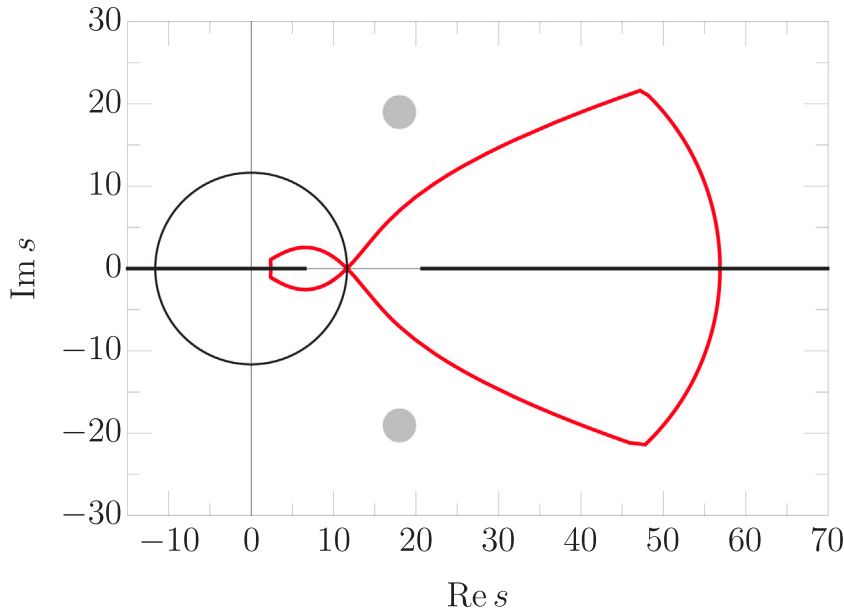
Fig. D.49. The domain of validity for the Roy–Steiner representation of partial waves obtained from fixed-t dispersion relations (FTPWDR) for $\pi K \to \pi K$ scattering, in m_π units. The shadowed areas represent the region where the $\kappa/K_0^*(700)$ pole lies in the second Riemann sheet.

This equation defines the maximum allowed value for the modulus of t for a given value of the integration variable s'. Beware, however, that t lies inside the applicability region only if it falls inside all the ellipses for all possible s' over which we integrate. Therefore, the boundary of the applicability region is given by

$$T(\theta) = \min_{s_{th} \leq s'} T(s', \theta). \tag{D.12}$$

Finally, the allowed values for s in the complex plane are those for which $|t| \leq T(\theta)$. But $t = T(\theta)\exp(i\theta) = \lambda_s(z_s - 1)/2s$, with $0 \leq z_s - 1 \leq 1$ real, so that the largest modulus of t for a given value of s is $t = -\lambda_s/s$. Therefore the boundary in the s complex plane is given by

$$\lambda_s + sT(\theta)\exp(i\theta) = 0, \tag{D.13}$$

which corresponds to the red line shown in Fig. D.49. Within that line, we can safely apply FTPWDR. Note that in the real axis this means that we can use FTPWDR relations up to $s \sim 57m_\pi^2$, or $\sqrt{s_{max}} \simeq 1.05$ GeV. Unfortunately, this region does not reach the position of the $\kappa/K_0^*(700)$ pole and is the main reason to use partial-wave dispersion relations obtained from hyperbolic dispersion relations (HPWDR), whose applicability region we study next.

D.4. Constraints on hyperbolic dispersion relations

Relatively similar constraints appear if, instead of fixed-t dispersion relations we choose other ways of fixing one variable. Actually, Steiner and Hite [164] showed, for πN scattering, that hyperbolae of the form $(s - a)(u - a) = b$ are the most convenient curves to avoid the double spectral regions passing through both direct and crossed channels, without introducing further cuts and provide reasonably simple integration kernels after the partial-wave projection. The applicability of the $a = 0$ case for πK scattering was studied in [97]. In [42] the general case with $a \neq 0$ was analyzed, paying particular attention to maximizing the πK and $\pi\pi \to K\bar{K}$ applicability regions in the real axis, in order to constraint data fits. In this appendix we will review the general case, but now it is also very relevant that, with an appropriate choice of a, the $\kappa/K_0^*(700)$ pole should lie within the πK applicability domain, while still having a rather large applicability region in the real axis.

In contrast to the fixed-t case, we use hyperbolic dispersion relations (HDR) both for the s-channel and t-channel, i.e. both for πK and $\pi\pi \to K\bar{K}$ scattering. Let us emphasize again that we have to consider the projection in terms of "external" variables of $F(s, t)$ into partial waves for the two channels, according to Eq. (11) and (12), respectively. In addition, the applicability of both projections will have to be studied concerning "internal" integration variables, since in practice Im $F(s', t')$ is built from the sum of partial waves.

Thus, on the one hand, for a fixed value of a, the family of hyperbolas $(s-a)(u-a) = b$ has to avoid all double spectral regions for all values of b needed to perform the partial-wave projection. On the other hand, for a fixed a, we have to calculate the restrictions on b to remain within the corresponding Lehmann ellipse.

Let us then explain in detail how to calculate these applicability domains.

D.4.1. Lehmann ellipses for the partial-wave expansion in internal variables

In contrast to the fixed-t case, now t' also changes in Im $F(s', t')$ simultaneously with the integration variable s'. Thus, for a given a, neither s' nor t' are fixed, but instead, they determine the value of the parameter

$$b(s', t', a) = (s' - a)(2\Sigma - s' - t' - a), \tag{D.14}$$

that characterizes the hyperbola in the Mandelstam plane. Thus, the applicability constraints will be given in terms of this parameter.

- *Internal s-channel partial-wave expansion*

  This case is very similar to the fixed-t analysis of πK scattering. Thus, the internal partial-wave expansion for the s-channel converges for angles $z_{s'}(s', t') = 1 + 2s't'/\lambda_{s'}$ inside the Lehmann ellipse [406–408]

$$\frac{(\mathrm{Re}\, z_{s'})^2}{A_s^2} + \frac{(\mathrm{Im}\, z_{s'})^2}{B_s^2} = 1, \tag{D.15}$$

  with foci at $z_{s'} = \pm 1$. The maximum value of $z_{s'}$, which defines the large semi-axis, touches the double spectral region at $t' = T_{st}(s')$, namely

$$A_s \equiv z_{s'}^{max} = 1 + \frac{2s' T_{st}(s')}{\lambda_{s'}}, \quad \forall s' \geq m_+^2. \tag{D.16}$$

  The minimum real value of the ellipse is therefore $z_{s'}^{min} = -z_{s'}^{max}$ and thus $z_{s'}$ is constrained to lie within

$$-z_{s'}^{max} \leq z_{s'} \leq z_{s'}^{max}, \quad \forall s' \geq m_+^2, \tag{D.17}$$

  which translates into the following restriction on t'

$$-\frac{\lambda_{s'}}{s'} - T_{st}(s') \leq t' \leq T_{st}(s'), \quad \forall s' \geq m_+^2. \tag{D.18}$$

  Now, using Eq. (D.14) we obtain a set of bounds for b:

$$\begin{aligned} b_s^-(s', a) &\leq b \leq b_s^+(s', a), \quad \forall s' \geq m_+^2 > a \\ b_s^-(s', a) &\equiv (s' - a)(2\Sigma - s' - T_{st}(s') - a), \\ b_s^+(s', a) &\equiv (s' - a)\left(2\Sigma - s' + \frac{\lambda_{s'}}{s'} + T_{st}(s') - a\right). \end{aligned} \tag{D.19}$$

  Thus, the final range of values allowed for b to avoid the double spectral regions in the s-channel contributions to the HDRs is

$$b_s^-(a) \leq b \leq b_s^+(a), \quad \forall s' \geq m_+^2 > a, \tag{D.20}$$

  where

$$b_s^-(a) \equiv \min_{s_{th} \leq s'} b_s^-(s', a), \quad b_s^+(a) \equiv \max_{s_{th} \leq s'} b_s^+(s', a). \tag{D.21}$$

  Note that it is required that $a < m_+^2$, independently of b.

- *Internal t-channel partial-wave expansion*

  For the t-channel the partial-wave expansion in the angle $z_{t'}(s', t')$, also converges within a Lehmann ellipse

$$\frac{(\mathrm{Re}\, z_{t'})^2}{A_t^2} + \frac{(\mathrm{Im}\, z_{t'})^2}{B_t^2} = 1, \tag{D.22}$$

  of foci $z_{t'} = \pm 1$ and $A_t^2 - B_t^2 = 1$. However, now we cannot follow a similar argument as for the s-channel because the angle in the t' channel is

$$z_{t'}^2 = \frac{\nu'}{4q_\pi(t')q_K(t')}, \quad \nu' = s' - u', \tag{D.23}$$

  which becomes pure imaginary in the pseudo-physical region $t_\pi \leq t \leq t_K$ and one cannot write an ordering relation as in Eq. (D.17). Nevertheless, we are interested in the bounds for b and these can be recast in terms of $z_{t'}^2$, since, along the hyperbolae

$$\nu'^2 = (t' - 2\Sigma + 2a)^2 - 4b(s', t', a), \tag{D.24}$$

  so that

$$z_{t'}^2 = \frac{(t' - 2\Sigma + 2a)^2 - 4b(s', t', a)}{16q_\pi(t')^2 q_K(t')^2}, \tag{D.25}$$

where all squares are real, although not necessarily positive. We can then obtain an ellipse for $z_{t'}^2$ by simply squaring the ellipse for $z_{t'}$ in Eq. (D.22) above. Namely:

$$\frac{(\text{Re } z_{t'}^2 - \frac{1}{2})^2}{\hat{A}_t^2} + \frac{(\text{Im } z_{t'}^2)^2}{\hat{B}_t^2} = 1, \tag{D.26}$$

where $\hat{A}_t = (A_t^2 + B_t^2)/2 = A_t^2 - 1/2$ and $\hat{B}_t = A_t B_t = A_t \sqrt{A_t^2 - 1}$ are the new semi-axes of the ellipse. The new center lies at $(1/2, 0)$ and the new foci are located at $1/2 \pm \sqrt{\hat{A}_t^2 - \hat{B}_t^2} = 1/2 \pm 1/2$. Therefore, for real $z_{t'}^2$, the condition to remain within the ellipse $1/2 - \hat{A}_t^2 \leq z_{t'}^2 \leq 1/2 + \hat{A}_t^2$ can be recast as

$$1 - A_t^2 \leq z_{t'}^2 \leq A_t^2. \tag{D.27}$$

We still have to determine A_t. Once again, the most restrictive bound comes from ρ_{st}. Given the $s \leftrightarrow u$ symmetry of the t channel, visible in Fig. D.48, and the proportionality between $z_{t'}$ and ν', it is convenient to rewrite the double spectral boundaries in (D.1) in terms of t, ν to obtain, respectively

$$\nu_{st}(t) = \frac{1}{t - 16m_\pi^2}\left[(t - 8m_\pi^2)^2 + 4m_\pi \sqrt{t}\sqrt{(t - 16m_\pi^2)m_K^2 + 16m_\pi^4}\right], \tag{D.28}$$

$$\nu_{st}(t) = \frac{16m_\pi^3 m_K + 12m_\pi m_+ t + t^2}{t - 4m_\pi^2}, \tag{D.29}$$

where in the s-channel they apply for all $t \geq 4t_\pi$ and $t \geq t_\pi$, respectively. Denoting the first value of ν that touches the boundary by

$$N_{st}(t) \equiv \min \nu_{st}(t), \tag{D.30}$$

we obtain the maximum value of the angle and therefore the semiaxis as

$$z_{t'}^{\max}(t') = \frac{N_{st}(t')}{4q_\pi(t')q_K(t')} \equiv A_t \quad \forall t' \geq t_K. \tag{D.31}$$

Now, using Eq. (D.27) together with (D.30), we obtain the restriction for ν'

$$16[q_\pi(t')q_K(t')]^2 - N_{st}(t')^2 \leq \nu'^2 \leq N_{st}(t')^2, \quad \forall t' \geq t_K. \tag{D.32}$$

Finally, the restriction for b is obtained just by translating ν'^2 into b

$$b_t^-(t', a) \leq b \leq b_t^+(t', a), \quad \forall t' \geq t_\pi > a, \tag{D.33}$$

with

$$b_t^-(t', a) = \frac{(t' - 2\Sigma + 2a)^2 - N_{st}(t')^2}{4},$$

$$b_t^+(t', a) = \frac{(t' - 2\Sigma + 2a)^2 - 16[q_\pi(t')q_K(t')]^2 + N_{st}(t')^2}{4}. \tag{D.34}$$

Once again, since we are integrating in the internal variable t', the total bounds are defined as

$$b_t^-(a) = \max_{t' > t_\pi} b_t^-(t', a),$$

$$b_t^+(a) = \min_{t' > t_\pi} b_t^+(t', a), \tag{D.35}$$

and the allowed values of b for a fixed a that do not touch any boundary while expanding in partial waves the t-channel contributions inside the HDR are

$$b_t^-(a) \leq b \leq b_t^+(a), \quad \forall t' \geq t_\pi \geq a. \tag{D.36}$$

Note that now we are requiring $t_\pi > a$, independently of b.

D.4.2. Lehmann ellipses for the partial-wave projection on external variables

In the previous subsection we have studied the constraints due to the fact that the imaginary parts of the amplitude *inside* dispersion relations are integrated from threshold to infinity either on the internal variable s' or t'. In practice, these imaginary parts of the amplitude are obtained from their partial-wave expansions, which only converge within their respective Lehmann ellipses. Besides, the whole amplitude should not touch the double spectral representation.

We are now interested in hyperbolic dispersion relations projected into partial waves (HPWDR), in order to compare with the existing data and to continue them to the complex plane in search for poles associated with resonances. We will see next that, in contrast to the FTPWDR, the HPWDR apply to both the s-channel and t-channel partial waves. Hence, we will now be integrating HDRs, either with respect to the external s-channel $\cos z_s$ or the t-channel $\cos z_t$, between -1 and 1. In addition, we should require that these partial-wave expansions in external angles should also converge.

- **s-channel partial-wave projection**

We have already seen that the ρ_{st} constraints are the strongest ones. We have also shown that the values of b must lie within the intervals in Eqs. (D.20) and (D.36), for all $s' \geq m_+^2$ and $t' \geq t_\pi$. For brevity, we write the two intervals together using the two labels separated by a comma as $b \in [b_{s,t}^-(a), b_{s,t}^+(a)]$. Now, the external s, t must also fall in the hyperbolae and thus we have to make sure that $b(s, t, a) = (s - a)(2\Sigma - s - t - a)$ lies within those intervals. Since the integration range $-1 \leq z_s \leq 1$ translates into

$$-\frac{\lambda_s}{s} \leq t \leq 0, \tag{D.37}$$

then, given a fixed a, the parameter $b(s, t)$ due to the s-channel projection will vary between

$$b^{min}(s, a) \leq b \leq b^{max}(s, a), \quad s \geq m_+^2 > a, \tag{D.38}$$
$$b^{min}(s, a) = (s - a)(2\Sigma - s - a),$$
$$b^{max}(s, a) = (s - a)\left(2\Sigma - s + \frac{\lambda_s}{s} - a\right) = (s - a)\left(\frac{\Delta^2}{s} - a\right).$$

Therefore, the interval $[b^{min}(s, a), b^{max}(s, a)]$ has to be fully included in the $[b_{s,t}^-(a), b_{s,t}^+(a)]$ intervals. For a given a, we define $s^{max}(a)$ as the largest value of s for which this occurs, which is calculated as follows: First, let us define $s_{s,t}^-(a)$ and $s_{s,t}^+(a)$ as the values of s such that:

$$b_{s,t}^-(a) = b^{min}(s_{s,t}^-(a), a), \quad b_{s,t}^+(a) = b^{max}(s_{s,t}^+(a), a). \tag{D.39}$$

In view of the definition of $b_{s,t}^{min}$ and $b_{s,t}^{max}$ in Eq. (D.38), these are quadratic equations with two solutions each:

$$s_{s,t}^{-(\pm)} = \Sigma \pm \sqrt{(\Sigma - a)^2 - b_{s,t}^-(a)}, \tag{D.40}$$
$$s_{s,t}^{+(\pm)} = \frac{1}{2a}\left[[\Delta^2 + a^2 - b_{s,t}^+(a)]^2 \pm \sqrt{[\Delta^2 + a^2 - b_{s,t}^+(a)]^2 - 4a^2\Delta^2}\right]. \tag{D.41}$$

Let us consider a given $a < 0$, which ensures $a < m_+^2$ (similar arguments follow if $0 < a < m_+^2$, but are of less relevance to have large applicability regions). Then, the applicability of the HPWDR is reduced to those s belonging to the intervals $[s_{s,t}^{-(-)}(a), s_{s,t}^{-(+)}(a)] \cap [s_{s,t}^{+(+)}(a), s_{s,t}^{+(-)}(a)]$. Now, since we want to compare with data we need to choose a so that some physical region $m_+^2 \leq s \leq s_{max}(a)$ lies inside those intervals. The calculation of that s_{max} is done numerically and for $a < 0$ it is $s_{max} = min\{s_{s,t}^{-(+)}(a), s_{s,t}^{+(-)}(a)\}$.

For instance, if we choose a to maximize the domain of applicability of the s-channel projection, the strongest restriction comes from the t-channel Lehmann ellipse and we should use

$$a = -13.9\, m_\pi^2, \quad s_{max} \simeq 50m_\pi^2 \simeq 0.98\,\text{GeV}^2, \quad \sqrt{s_{max}} \simeq 0.989\,\text{GeV},$$
$$b_t^-(a) \simeq -592\, m_\pi^4, \quad b_t^+(a) \simeq 1070\, m_\pi^4. \tag{D.42}$$

In the left panel of Fig. D.50 we show a representative sample of these hyperbolae, showing in blue the intersection with the s-channel physical region. The boundary cases correspond to the thicker lines.

However, in Appendix D.5, we will see that this choice is not so good for our purposes, because the applicability domain in the complex plane does not reach the $\kappa/K_0^*(700)$ pole and its uncertainties.

In contrast, the authors of [97] choose $a = 0$, so that $s^{max} \simeq 45m_\pi^2$, i.e. $\sqrt{s^{max}} \simeq 0.934\,\text{GeV}$, but they showed that the $\kappa/K_0^*(700)$ pole lies within their applicability region, as we will also show in Appendix D.5.

Finally, in this review, we will mostly use

$$a = -10\, m_\pi^2, \quad s_{max} \simeq 49m_\pi^2 \simeq 0.954\,\text{GeV}^2, \quad \sqrt{s_{max}} \simeq 0.976\,\text{GeV},$$
$$b_t^-(a) \simeq -690m_\pi^4, \quad b_t^+(a) \simeq 997\, m_\pi^4, \tag{D.43}$$

which ensures that the applicability domain covers the $\kappa/K_0^*(700)$ pole region, but still reaches rather high in the real axis, since we only lose 13 MeV of applicability compared to the $a = -13.9m_\pi^2$ case. Our choice will be explained in detail in Appendix D.5.

- **t-channel partial-wave projection**

The relation between b and the cosine of the scattering angle z_t is now quadratic and is then better to carry out the analysis in terms of z_t^2. Thus, to perform the t-channel projection we need to consider the whole interval

$$0 \leq \frac{\nu^2}{16q_\pi^2 q_K^2} = \frac{(t - 2\Sigma + 2a)^2 - 4b}{16q_\pi^2 q_K^2} = \frac{(t - 2\Sigma + 2a)^2 - 4b}{(t - t_\pi)(t - t_K)} \leq 1. \tag{D.44}$$

For a given a, it can be translated into an interval of applicability for b, by defining:

$$b^{min}(t, a) = \frac{1}{4}(t - 2\Sigma + 2a)^2 \geq 0, \quad b^{max}(t, a) = a(t - 2\Sigma) + a^2 + \Delta^2. \tag{D.45}$$
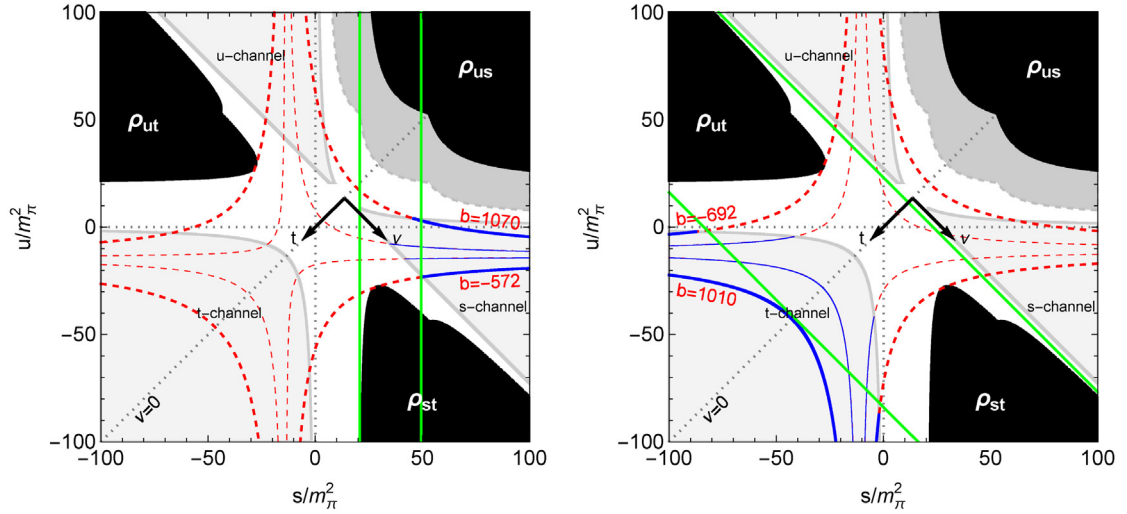
Fig. D.50. We plot in the Mandelstam (s, u) plane explained in Fig. D.48, a representative sample of the $(s-a)(u-a) = b$ hyperbolae used to obtain HPWDR, in m_π units. They are represented as dashed red lines when they lie outside the corresponding physical region and as continuous blue lines when they lie inside. The thicker ones correspond to the limiting b values. On the left panel, we show those that maximize the applicability region in the real axis for the πK analysis (s-channel), with $a = -13.9 m_\pi^2$. Green straight lines mark the minimum and maximum values of s valid for these dispersion relations. Let us recall that we do not use exactly this value of a when we want to reach the $\kappa/K_0^*(700)$ region in the complex plane. For this, it is better to use $a = -10 m_\pi^2$ which has only a slightly lower reach, as explained in the main text. On the right panel we show the hyperbolae used for $\pi\pi \to K\bar{K}$ (s-channel), with $a = -10.9 m_\pi^2$. Green straight lines mark the minimum and maximum values of t valid for these dispersion relations.

Paying attention to the signs of $t - t_\pi$ and $t - t_K$, then b must lie within:

$$b^{min}(t, a) \leq b \leq b^{max}(t, a), \quad \forall t_\pi \leq t \leq t_K, \tag{D.46}$$

$$b^{max}(t, a) \leq b \leq b^{min}(t, a), \quad \forall t > t_K \quad (\text{or } t < t_\pi). \tag{D.47}$$

Thus, we need these ranges above to be fully contained in the $[b_{s,t}^-(a), b_{s,t}^+(a)]$ that we obtained from the internal variable constraints in Eqs. (D.20) and (D.36). In particular, in order to maximize the domain of applicability in the real t axis by choosing a we search for the value $t = t_{max}$ where both the maximum and minimum values of b coincide with $b_{s,t}^-(a)$ and $b_{s,t}^+(a)$. Using Eq. (D.44) and taking into account that the projection is made between $z_t^2 = 0$ and $z_t^2 = 1$ this means

$$z_t^2(t_{max}, b_{s,t}^-(a)) = 1,$$
$$z_t^2(t_{max}, b_{s,t}^+(a)) = 0. \tag{D.48}$$

Once again, the restriction from the t-channel is stronger than that from the s-channel, and we find that the applicability range is maximized with the following choice:

$$a = -10.9 m_\pi^2, \quad -0.286 \, \text{GeV}^2 \, (\sim 15 m_\pi^2) \leq t \leq 2.19 \, \text{GeV}^2 \, (\sim 112 m_\pi^2),$$
$$b_t^-(a) = -672 \, m_\pi^4, \quad b_t^+(a) = 1010 \, m_\pi^4. \tag{D.49}$$

Note that this means that the applicability domain in the physical region extends from $K\bar{K}$ threshold $\sqrt{t_K} \simeq 0.992 \, \text{GeV}$ up to $\sqrt{t} \simeq \sqrt{2.19} \, \text{GeV} \simeq 1.47 \, \text{GeV}$, which is the interval we used in the Roy–Steiner dispersive analysis of $\pi\pi \to \bar{K}K$ data [42]. In the right panel of Fig. D.50 we show a representative sample of this family of hyperbolae, whose intersection with the s-channel physical region we have highlighted in blue. The boundary cases correspond to the thicker lines.

In contrast, for the choice $a = 0$, as in [43], $\sqrt{t_{max}} \sim 1.3 \, \text{GeV}$[7]. It is then clear that the optimization of a is more relevant in $\pi\pi \to K\bar{K}$ than in $\pi K \to \pi K$ since an optimal choice of a enlarges the applicability interval to study $\pi\pi \to K\bar{K}$ data by an additional 67% in terms of t for its physical region.

---

[7] In [43] the authors wrote $t_{max} = 70 m_\pi^2$, or $\sqrt{t_{max}} \simeq 1.17 \, \text{GeV}$, but in [97] they corrected their double spectral boundary equations. When using the correct ones the actual value is $\sim 1.3 \, \text{GeV}$.

D.5. Complex applicability domain of s-channel partial-wave hyperbolic dispersion relations

In the main text we have reviewed the model-independent and precise extraction of the pole parameters associated to strange resonances that are produced in the elastic regime of πK scattering, i.e. the scalar $\kappa/K_0^*(700)$ and $K^*(892)$ vector resonance. This can be done because in the elastic regime there is a zero in the first Riemann sheet for each pole in the second and they are easily related through Eqs. (19), (20) and (21). In Appendix D.3 we just saw that the FTPWDR does not reach the region of interest for the $\kappa/K_0^*(700)$. We, therefore, need to study the applicability domains of HPWDR in the complex s plane, which can differ substantially from one another, depending on the choice of a. Actually, the domain for the $a = 0$ case for πK scattering was already shown in [97]. Here we will give the details for the general case $a \neq 0$, for which we will follow the account given in [188] for πN scattering, in order to determine the semi-axes of the Lehmann ellipses, which can be done from real values of s, t.

Thus, we are now interested in complex values of the external variable s of the partial waves $f_\ell(s)$. These are obtained as an integration over $0 \leq z_s = 1 + 2st/\lambda_s \leq 1$, which means that t is integrated over a complex segment between 0 and λ_s/s. Therefore, in the dispersive integrals from s-channel contributions we will now need Im $F(s', t')$ for real $m_+^2 \leq s'$ but complex t'. This is relatively similar to the fixed-t case, although now s' and t' are related through the hyperbolae $(s - a)(u - a) = b$. Consequently, the b parameter will also be complex.

In addition, in contrast with the case of fixed-t dispersion relations, for HDR we also have s-channel contributions where we have to study the convergence of Im $F(t', s')$ with $t_\pi \leq t'$ real and s' related to t' through the hyperbolae equation.

Let us then start with the derivation of the range of validity over the s-channel Lehmann–Martin ellipse, which is again defined throughout the ellipse with foci at $t = -\lambda_{s'}/s'$ and $t = 0$. However, since s and t are now related by a hyperbolae, it is better to recast our conditions in terms of the parameter $b = (s - a)(2\Sigma - s - t - a)$. With this change of variable, the partial-wave projection in Eq. (D.10) is recast as:

$$f_\ell(s) = \frac{-s}{16\pi N(s-a)\lambda_s} \int_{(s-a)(\Delta^2/s-a)}^{(s-a)(2\Sigma-s-a)} db\, P_\ell(z_s(t(s,b,a))) F\left(s, 2\Sigma - s - a - \frac{b}{s-a}\right). \tag{D.50}$$

Thus we have to consider an ellipse on b with foci at $b_s = (s' - a)(2\Sigma - s' - a)$ and $b_s = (s' - a)(2\Sigma - s' + \lambda_{s'}/s' - a)$. The calculation is now more complicated since this ellipse does not have any fixed foci. Nonetheless, we have seen in Eqs. (D.38) above how the maximum and minimum of b can be calculated. Then, denoting the ellipse boundary by $(B_s(s', \theta), \theta)$, calculated in polar coordinates from the origin of coordinates, B falls inside all possible ellipses if

$$B_s(\theta) = \min_{s_{th} \leq s' \leq \infty} B_s(s', \theta). \tag{D.51}$$

Next, we have to consider the t-channel Lehmann–Martin ellipse. As discussed above, the relation between b and z_t is quadratic, so it is better to write the ellipse in terms of z_t^2. Also, for the $\pi\pi \to K\bar{K}$ contributions it is better to use the t, ν variables. We already did this in Eqs. (D.26) to (D.34), where we found the extremes of the b_t ellipse. Once again we rewrite that ellipse in polar coordinates $(B_t(t', \theta), \theta)$. However, since t' is integrated from $\pi\pi$ threshold, we have to consider only the values of b inside all possible ellipses as t' varies. All things considered, the final applicability bound on b due to the s-channel contributions is given by

$$B_t(\theta) = \min_{4m_\pi^2 \leq t' \leq \infty} B(t', \theta). \tag{D.52}$$

Finally, the s variable will remain inside the boundary anytime the b values needed for the s-channel partial wave projection are inside their limits. We use again the partial wave projection formula of Eq. (D.10), and perform the corresponding change of variables from t to b. At the end of the day, we get that the boundary of applicability in the complex s plane is given by these two equations

$$(2\Sigma - s - a)(s - a) + B_{s,t}(\theta)\exp(i\theta) = 0. \tag{D.53}$$

The regions of applicability corresponding to both ellipses are shown in Fig. D.51, where we have used $a = -10m_\pi^2$ to maximize the applicability in the real axis while the $\kappa/K_0^*(700)$ pole and its uncertainties still lie within the boundaries. There it can be noticed that the boundary due to the s-channel contribution (Green line, using B_t in the equation above) is more restrictive than that due to the s-channel (Red line, using B_s in the equation above). The blue line represents the s-channel boundary of the $a = 0$ case, used in [97], where they first showed that with HPWDR it was possible to reach the $\kappa/K_0^*(700)$ pole, although the applicability domain in the real axis is somewhat smaller.

Appendix E. Integral kernels

In Section 3, we detailed the derivation of several Roy–Steiner-like equations, which, after projecting into partial waves, provide us with the necessary tools to perform a rigorous and model-independent coupled study of both $\pi\pi \to K\bar{K}$ and $\pi K \to \pi K$ scattering. The integral kernels corresponding to the t-channel dispersion relations for F^+ and F^-, with one and no subtractions, respectively, were already given in [42]. Here we will compile not only those but the whole system
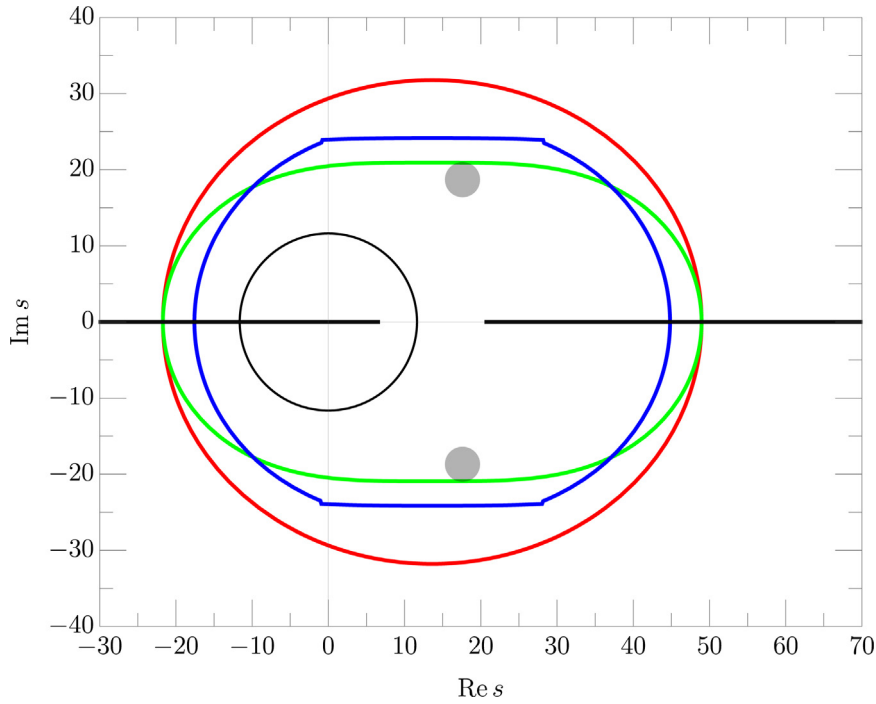
Fig. D.51. The domain of validity in the complex s-plane of partial-wave hyperbolic dispersion relations for $\pi K \to \pi K$ scattering, in m_π units. The red curve depicts the allowed region due to the s-channel contributions, whereas the green line encloses the very same region for the t-channel contributions, both calculated for $a = -10m_\pi^2$. The blue line represents the applicability area for $a = 0$, as used in [97]. The shadow areas represent the region where the $\kappa/K_0^*(700)$ pole lies at. Although the applicability region can be extended in the real axis by choosing $a = -13.9m_\pi^2$, then the $\kappa/K_0^*(700)$ pole would lie outside the applicability domain. This is why $a = -10m_\pi^2$ was used in [47] to obtain its parameters. The black lines represent the physical, left and circular cuts characteristic of πK scattering partial waves.

of integrands we have used in this review. Namely, we present kernels for fixed-t and hyperbolic dispersion relations in the s- and t-channels.

Let us recall that the hyperbolae we use for our dispersion relations are defined through the equation $(s-a)(u-a) = b$, as well as some previous useful definitions:

$$z_s = 1 + \frac{2st}{\lambda_s}, \quad \lambda_s = (s - m_+^2)(s - m_-^2) = s^2 - 2s\Sigma + \Delta^2 = 4s\, q_{K\pi}^2(s).$$

In addition, to simplify our equations, we will now define

$$x(t, s') = \frac{4q_K(t)q_\pi(t)}{2s' + t - 2\Sigma}, \quad A(t, s') = \operatorname{artanh}\left(x(t, s')\right),$$

$$B(s, s') = \frac{s}{\lambda_s}\left[\log\left(s' + s - 2\Sigma\right) - \log\left(s' - \frac{\Delta^2}{s}\right)\right],$$

$$C(s, s') = 1 - \frac{2s(s' + s - 2\Sigma)}{\lambda_s}. \tag{E.1}$$

Beware that $C(s, s') \neq C(s', s)$ and that both expressions will appear below.

Let us recall that the s variable corresponds to the "output" partial wave, while s' and t' correspond to the "internal" variables of the "input" amplitudes that are integrated. At the same time, in what follows, ℓ and ℓ' stand for the "output" and "input" angular momenta respectively.

E.1. Fixed-t kernels

In this subsection we provide the explicit expressions for the $L_{\ell\ell'}^l(s, s')$ and $L_{\ell\ell'}^\pm(s, t')$ kernels needed in the partial-wave dispersion relations in Eq. (53), only up to vector waves, as no tensor wave dispersion relation is implemented in this work. Nevertheless, tensor waves are used as input for the dispersion relations of the other waves. Then, the dominant s-channel kernels we need read

$$L_{0,0}^+(s, s') = \frac{s^2}{s'^2(s' - s)} - \frac{2\Sigma s' - 2\Delta^2}{s'\lambda_{s'}} + \frac{\Delta^2 + s's + 2\Sigma s}{s'^2 s} + B(s, s'),$$

$$L_{0,1}^{+}(s, s') = 3\frac{(s'^3 + s'^2 s - s's^2 + s\Delta^2)}{s'^2\lambda_{s'}} + 3C(s', s)B(s, s'),$$

$$L_{1,0}^{+}(s, s') = -\frac{2s}{\lambda_s} + C(s, s')B(s, s'),$$

$$L_{1,1}^{+}(s, s') = \frac{s\lambda_s}{\lambda_{s'}s'(s' - s)} + \frac{\lambda_s}{s'\lambda_{s'}} + \frac{6s(\Delta^2 - s'(2s + s' - 2\Sigma))}{\lambda_{s'}\lambda_s} + 3\,C(s', s)C(s, s')B(s, s'),$$

$$L_{0,0}^{-}(s, s') = \frac{1}{s' - s} - B(s, s'),$$

$$L_{0,1}^{-}(s, s') = 3\left[\frac{1}{s' - s} - \frac{2s'}{\lambda_{s'}} - \frac{s'\lambda_s}{(s' - s)s\lambda_{s'}} - C(s', s)B(s, s')\right],$$

$$L_{1,0}^{-}(s, s') = -C(s, s')B(s, s') - 2\frac{s}{\lambda_s},$$

$$L_{1,1}^{-}(s, s') = \frac{s'\lambda_s}{(s' - s)s\lambda_{s'}} - 3C(s', s)\left(C(s, s')B(s, s') + 2\frac{sC(s', s)}{\lambda_s}\right). \tag{E.2}$$

In addition, the t-channel contribution kernels are way simpler

$$L_{0,2\ell}^{0}(s, t') = \frac{2(2\ell) + 1}{\sqrt{3}}(q_\pi(t')q_K(t'))^{2\ell}\frac{s}{\lambda_s}\left[\log\left(1 + \frac{\lambda_s}{st'}\right) - \frac{\lambda_s}{st'}\right],$$

$$L_{1,2\ell}^{0}(s, t') = \frac{2(2\ell) + 1}{\sqrt{3}}(q_\pi(t')q_K(t'))^{2\ell}\frac{s}{\lambda_s}\left[\left(1 + \frac{2st'}{\lambda_s}\right)\log\left(1 + \frac{\lambda_s}{st'}\right) - 2\right]. \tag{E.3}$$

E.2. Hyperbolic kernels

E.2.1. t-channel projection

In this subsection we provide the explicit expressions for the $G_{\ell\ell'}^{I}(t, t')$, $G_{\ell\ell'}^{\pm}(t, s')$, $\hat{G}_{\ell\ell'}^{I}(t, t')$ and $\hat{G}_{\ell\ell'}^{\pm}(t, s')$ kernels, with $\ell \le 2$, needed in the partial-wave dispersion relations in Eqs. (56) and (57). Note that, in the input, partial waves with $\ell' > 2$ will be safely neglected, except for the $\ell' = 4$ partial wave used for the g_2^0 equation, which nevertheless gives a very small contribution.

We start by listing the kernels appearing in the $g_1^1(t)$ dispersion relation. As in the main text of [42], for the antisymmetric case, those with a hat correspond to one-subtraction and those without to the unsubtracted case

$$G_{1,3}^{1}(t, t') = \hat{G}_{1,3}^{1}(t, t') = \frac{7}{48}(t' + t - 4\Sigma + 10a), \tag{E.4}$$

$$G_{1,0}^{-}(t, s') = 4\sqrt{2}\left[\frac{(2s' - 2\Sigma + t)A(t, s') - 4q_K(t)q_\pi(t)}{16(q_K(t)q_\pi(t))^3}\right],$$

$$G_{1,1}^{-}(t, s') = 12\sqrt{2}\left[P_1(z_{s'})\frac{(2s' - 2\Sigma + t)A(t, s') - 4q_K(t)q_\pi(t)}{16(q_K(t)q_\pi(t))^3} - \frac{2s'}{3(s' - a)\lambda_{s'}}\right],$$

$$G_{1,2}^{-}(t, s') = 20\sqrt{2}\left[P_2(z_{s'})\frac{(2s' - 2\Sigma + t)A(t, s') - 4q_K(t)q_\pi(t)}{16(q_K(t)q_\pi(t))^3} - \frac{2s'z_s'}{(s' - a)\lambda_{s'}}\right.$$
$$\left. + \frac{s'^2(2s' + t - 2\Sigma)^2}{2(s' - a)^2\lambda_{s'}^2} - \frac{24s'^2(q_K(t)q_\pi(t))^2}{5(s' - a)^2\lambda_s'^2}\right],$$

$$\hat{G}_{1,0}^{-}(t, s') = 4\sqrt{2}\left[(s' - \Sigma + t/2)\frac{A(t, s') - 4q_K(t)q_\pi(t)}{16(q_K(t)q_\pi(t))^3} - \frac{1}{3\lambda_{s'}}\right],$$

$$\hat{G}_{1,1}^{-}(t, s') = 12\sqrt{2}\left[(s' - \Sigma + t/2)P_1(z_{s'})\frac{A(t, s') - 4q_K(t)q_\pi(t)}{16(q_K(t)q_\pi(t))^3} - \frac{1}{3\lambda_{s'}}\right],$$

$$\hat{G}_{1,2}^{-}(t, s') = 20\sqrt{2}\left[(s' - \Sigma + t/2)P_2(z_{s'})\frac{A(t, s') - 4q_K(t)q_\pi(t)}{16(q_K(t)q_\pi(t))^3} - \frac{1}{3\lambda_{s'}} - \frac{2s'^2t}{\lambda_{s'}^2(s' - a)}\right],$$

where $P_l(z_{s'})$ are the Legendre polynomials. For the symmetric case, we find

$$G_{2,4}^{0}(t, t') = \frac{3}{8}(t + t' - 4\Sigma + 7a), \tag{E.5}$$

$$G_{2,0}^{+}(t, s') = \frac{\sqrt{3}(2s' + t - 2\Sigma)^2}{32q_K(t)^5 q_\pi(t)^5}\left[(3 - x(t, s')^2)A(t, s') - 3x(t, s')\right],$$

$$G_{2,1}^{+}(t, s') = \frac{3\sqrt{3}(2s' + t - 2\Sigma)^2}{32q_K(t)^5 q_\pi(t)^5}P_1(z_{s'})\left[(3 - x(t, s')^2)A(t, s') - 3x(t, s')\right],$$

$$G_{2,2}^+(t,s') = 5\sqrt{3}\left[\frac{(2s'+t-2\Sigma)^2}{32q_K(t)^5 q_\pi(t)^5}P_2(z_{s'})\Big((3-x(t,s')^2)A(t,s')-3x(t,s')\Big)\frac{16s'^2 t}{5(s'-a)^2\lambda_{s'}^2}\right].$$

Finally, for the $g_0^0(t)$ dispersion relation the kernels we need are

$$G_{0,2}^0(t,t') = \frac{5}{16}(t+t'-4\Sigma+6a),$$

$$G_{0,0}^+(t,s') = \sqrt{3}\left[\frac{A(t,s')}{q_K(t)q_\pi(t)}+\frac{2(\Sigma-s')}{\lambda_{s'}}\right],$$

$$G_{0,1}^+(t,s') = 3\sqrt{3}\left[\frac{A(t,s')}{q_K(t)q_\pi(t)}P_1(z_{s'})-\frac{(2s'+2t-2\Sigma)}{\lambda_{s'}}-\frac{2at}{(s'-a)\lambda_{s'}}\right],$$

$$G_{0,2}^+(t,s') = 5\sqrt{3}\left[\frac{A(t,s')}{q_K(t)q_\pi(t)}P_2(z_{s'})-\frac{2s-2\Sigma}{\lambda_{s'}}-\frac{6st(\Delta^2+s'(3s'+2t-4\Sigma))}{(s'-a)\lambda_{s'}^2}\right.$$
$$\left.+\frac{3s'^2 t(2s'+t-2\Sigma)^2}{2(s'-a)^2\lambda_{s'}^2}-\frac{8s'^2 t(q_K(t)q_\pi(t))^2}{(s'-a)^2\lambda_{s'}^2}\right]. \tag{E.6}$$

E.2.2. s-channel projection

Finally, we provide the $K_{\ell,\ell'}^\pm(s,s')$, $\hat{K}_{\ell,\ell'}^\pm(s,s')$, $K_{\ell,\ell'}^I(s,t')$ and $\hat{K}_{\ell,\ell'}^I(s,t')$ kernels needed for the dispersive integrals in Eqs. (54) and (55). Let us recall that in this case we neglect $\ell \geq 2$, since their contribution to the partial waves of interest is very small. The conventions regarding the variables and angular momenta are the ones explained above. The s-channel kernels of the unsubtracted antisymmetric amplitude thus read

$$K_{0,0}^+(s,s') = \frac{2((s'+\Sigma)\Delta^2-2s'\Sigma)}{s'^2\lambda_{s'}}-\frac{s'^2+2s'(\Sigma-s)-2s\Sigma}{s'^2(s'-s)}+B(s,s'), \tag{E.7}$$

$$K_{0,0}^-(s,s') = \frac{1}{s'-s}-B(s,s'),$$

$$K_{0,1}^+(s,s') = 3\left[\frac{s(s'+2\Sigma)-\Delta^2}{\lambda_{s'}s}-\frac{s'\lambda_s}{(a-s')\lambda_{s'}s}+C(s',s)B(s,s')\right],$$

$$K_{0,1}^-(s,s') = -3\left[\frac{(s's+\Delta^2)}{\lambda_{s'}s}-\frac{s'(3s^2-2\Sigma s+\Delta^2)}{(a-s')\lambda_{s'}s}+C(s',s)B(s,s')\right],$$

$$K_{1,0}^+(s,s') = -K_{1,0}^-(s,s') = C(s,s')B(s,s')+2\frac{s}{\lambda_s},$$

$$K_{1,1}^+(s,s') = 3C(s',s)\left[C(s,s')B(s,s')+2\frac{s}{\lambda_s}\right]+\frac{s'(a-s)\lambda_s}{(s'-s)s(a-s')\lambda_{s'}},$$

$$K_{1,1}^-(s,s') = -3C(s',s)\left[C(s,s')B(s,s')+2\frac{s}{\lambda_s}\right]+\frac{s'(a-s)\lambda_s}{(s'-s)s(a-s')\lambda_{s'}}, \tag{E.8}$$

whereas the once-subtracted kernels for the antisymmetric case read

$$\hat{K}_{0,0}^-(s,s') = \frac{1}{s'-s}-B(s,s')+\frac{\lambda_s}{2s\lambda_{s'}}-2\frac{(s-\Sigma)}{\lambda_{s'}},$$

$$\hat{K}_{0,1}^-(s,s') = 3\left[\frac{1}{s'-s}-2\frac{(s'+s-\Sigma)}{\lambda_{s'}}-\frac{\lambda_s(s'+s)}{2(s'-s)s\lambda_{s'}}-C(s',s)B(s,s')\right],$$

$$\hat{K}_{1,0}^-(s,s') = -C(s,s')B(s,s')-\frac{2s}{\lambda_s}-\frac{\lambda_s}{6s\lambda_{s'}},$$

$$\hat{K}_{1,1}^-(s,s') = -3C(s',s)\left[C(s,s')B(s,s')+\frac{2s}{\lambda_s}\right]+\frac{(s'+s)\lambda_s}{2s(s'-s)\lambda_{s'}}. \tag{E.9}$$

Next, we provide the kernels for the t-channel contribution, which read

$$K_{0,0}^0(s,t') = \frac{1}{\sqrt{3}}\frac{s}{\lambda_s}\left[\log\left(1+\frac{\lambda_s}{st'}\right)-\frac{\lambda_s}{st'}\right],$$

$$K_{0,2}^0(s,t') = \frac{5}{\sqrt{3}}[q_\pi(t')q_K(t')]^2\frac{s}{\lambda_s}\left[\log\left(1+\frac{\lambda_s}{st'}\right)-\frac{\lambda_s}{st'}\right]+\frac{\sqrt{3}\lambda_s(s-a)}{16st'},$$

$$K_{1,0}^0(s,t') = \frac{1}{\sqrt{3}}\frac{s}{\lambda_s}\left[P_1(z_s)\log\left(1+\frac{\lambda_s}{st'}\right)-2\right],$$
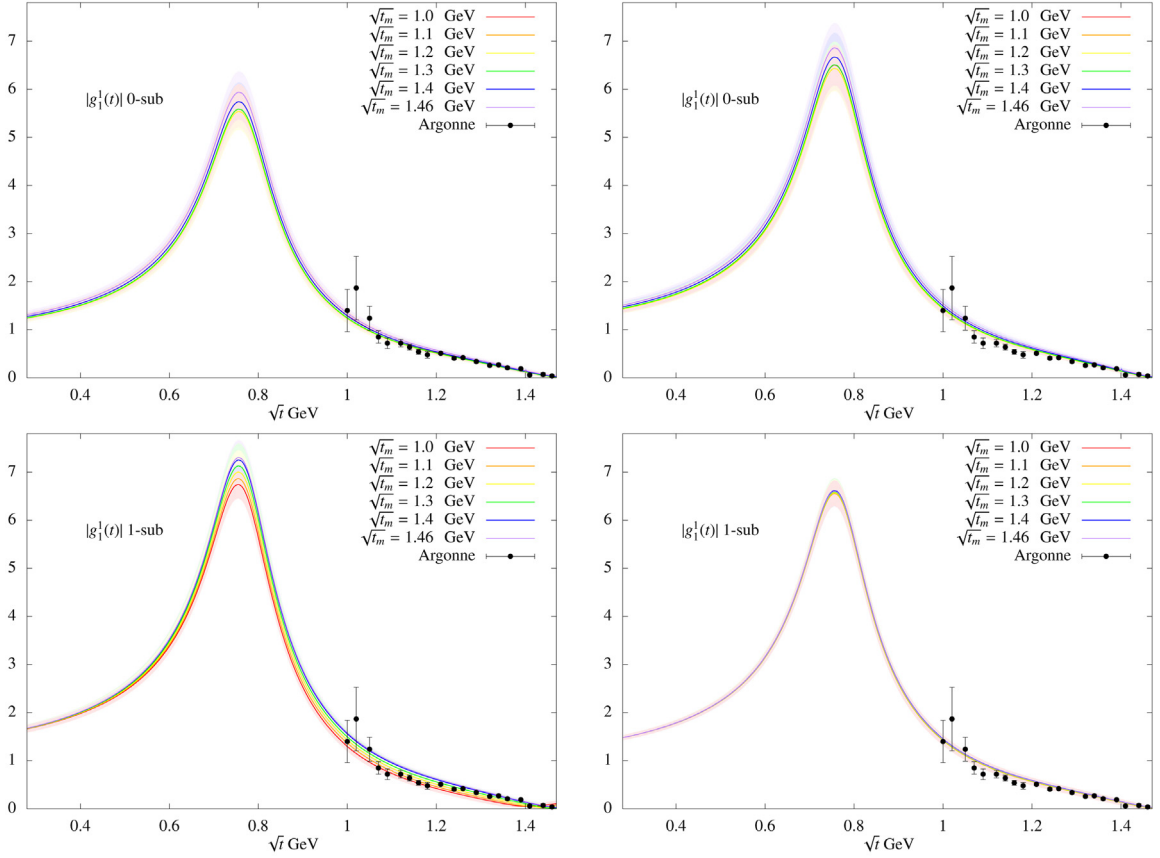
Fig. F.52. Comparison of the unsubtracted (top) or once-subtracted (bottom) HPWDR output, when using different matching points t_m for $g_1^1(t)$. Notice the much better agreement between outputs with different choices of matching points when using as input the CFD (right) rather than the UFD (left), particularly for the subtracted case.

$$K_{1,2}^0(s, t') = \frac{5}{\sqrt{3}} \frac{s}{\lambda_s} [q_\pi(t') q_K(t')]^2 P_1(z_s) \left[\log\left(1 + \frac{\lambda_s}{st'}\right) - 2 \right] + \frac{5\lambda_s(s-a)}{16\sqrt{3}st'},$$

$$K_{0,1}^1(s, t') = \frac{3}{4\sqrt{2}} \frac{s(t' + 2s - 2\Sigma)}{\lambda_s} \left[\log\left(1 + \frac{\lambda_s}{st'}\right) - \frac{\lambda_s}{s(t' + 2s - 2\Sigma)} \right],$$

$$K_{1,1}^1(s, t') = \frac{3}{4\sqrt{2}} \frac{s(t' + 2s - 2\Sigma)}{\lambda_s} \left[P_1(z_s) \log\left(1 + \frac{\lambda_s}{st'}\right) - 2 \right],$$

$$\hat{K}_{0,1}^1(s, t') = \frac{3}{4\sqrt{2}} \frac{s(t' + 2s - 2\Sigma)}{\lambda_s} \left[\log\left(1 + \frac{\lambda_s}{st'}\right) - \frac{2\lambda_s}{t's} + \frac{\lambda_s^2}{t's^2(t' + 2s - 2\Sigma)} \right],$$

$$\hat{K}_{1,1}^1(s, t') = \frac{3}{4\sqrt{2}} \frac{s(t' + 2s - 2\Sigma)}{\lambda_s} \left[P_1(z_s) \log\left(1 + \frac{\lambda_s}{st'}\right) - 2 \right] - \frac{\lambda_s}{8\sqrt{2}t's}, \tag{E.10}$$

where once again we have used a hat for the once-subtracted kernels of the F^- amplitude.

All these kernels produce smooth integrable inputs in the physical region, they are suppressed at higher energies and match the kinematic behavior of every partial wave. They also produce the left and circular-cut structures required by partial-wave projection.

Appendix F. Muskhelishvili–Omnès Matching conditions

In Sections 3 and 4.4 we detailed our choice of the matching point t_m for the different $\pi\pi \to K\bar{K}$ partial waves. We decided to modify slightly our previous value in [42] from $\sqrt{t_m} = 1.2$ GeV to $\sqrt{t_m} = 1$ GeV for the $g_1^1(t)$ partial wave for practical convenience, and used $\sqrt{t_m} = 1.2$ GeV for the other two partial waves studied here, i.e. $g_0^0(t)$ and $g_2^0(t)$.

One may wonder if varying this t_m substantially modifies the dispersive constraint for the crossed-channel partial waves, as it imposes a mathematical matching condition between the dispersion relations of Section 3.6 right below t_m
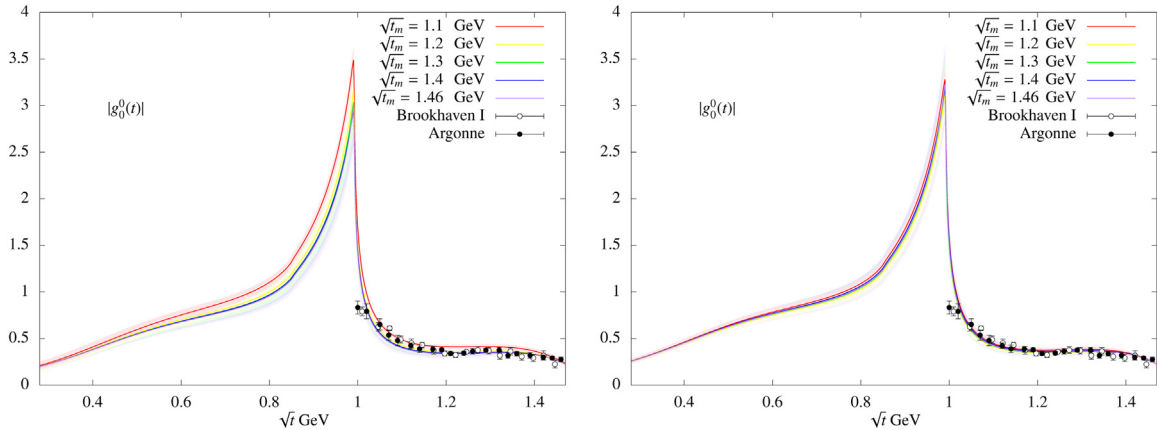
Fig. F.53. Comparison of the HPWDR output, when using different matching points t_m for $g_0^0(t)$. Notice the much better agreement between the outputs with different choices of matching points when using the CFD (right) instead of the UFD (left) as input.

and the fitted partial waves right above. Of course, if the CFD fits were perfect, this matching condition would not produce any noticeable effect, and thus the dispersive partial wave would always be compatible within uncertainties regardless of the matching point.

Of the three partial waves, only g_1^1 and g_0^0 contribute substantially to the πK system and g_2^0 can be considered "decoupled" from the rest. In the following, we will focus on the former two.

Regarding $g_1^1(t)$, different choices of t_m within a rather large region produce perfectly compatible results for its CFD dispersive output, both in the unsubtracted and once-subtracted cases, as shown in Fig. F.52. This is an improvement upon the UFD case, which nevertheless also yields quite similar results with different choices of t_m within that range. However, the higher the matching point t_m, the larger the dispersive uncertainty band. This is the main reason why we have chosen t_m as small as possible, namely, $t_m = 1$ GeV^2, taking advantage of the fact that the cusp and isospin breaking effects around $K\bar{K}$ threshold are negligible in this wave.

The situation concerning $g_0^0(t)$ is more complicated, mostly because using $\sqrt{t_m} \leq 1.1$ GeV produces significant deviations from data and thus matching points close to $K\bar{K}$ threshold should be avoided. As detailed in Sections 4.4 and 5.3 this could be explained by isospin breaking effects, which, among other things imply the existence of a double threshold, one for K^+K^- and another one for $K^0\bar{K}^0$. These effects are enhanced in this wave due to the nearby $f_0(980)$ resonance and cannot be well reproduced by our dispersive formalism, which is isospin-symmetric. Nevertheless, as seen in Fig. F.53, if one chooses t_m above this energy, different matching points again produce dispersive results fairly compatible within uncertainties in the physical region. Moreover, there is a clear improvement in the pseudo-physical region when using the CFD as input instead of the UFD. In terms of the $\hat{d}^2$ function defined in Section 4.4, and excluding the region within 20 MeV of the $K\bar{K}$ threshold, the CFD $\hat{d}^2$ vary between less than 1 and 1.4 σ, which we consider perfectly acceptable for our purposes. On top of that, the contribution of this partial wave to the rest of the coupled system is already small, so that varying this matching condition produces negligible effects, well within our original statistical uncertainties.

References

[1] Y. Cho, et al., Study of $K^-\pi^-$ scattering using the reaction $K^-d \rightarrow K^-\pi^-pp_s$, Phys. Lett. 32B (1970) 409–412, http://dx.doi.org/10.1016/0370-2693(70)90510-1.

[2] A.M. Bakker, et al., A determination of the I=3/2 $K\pi$ elastic-scattering cross section from the reaction $K^-n \rightarrow pK^-\pi^-$ at 3 GeV/c, Nuclear Phys. B24 (1970) 211–220, http://dx.doi.org/10.1016/0550-3213(70)90064-7.

[3] D. Linglin, et al., $K^-\pi^-$ Elastic scattering cross-section measured in 14.3 Gev/c K^-p interactions, Nuclear Phys. B57 (1973) 64–76, http://dx.doi.org/10.1016/0550-3213(73)90333-7.

[4] B. Jongejans, R.A. van Meurs, A.G. Tenner, H. Voorthuis, P.M. Heinen, W.J. Metzger, H.G.J.M. Tiecke, R.T. Van de Walle, Study of the $I = 3/2$ $K^-\pi^-$ elastic scattering from the reaction $K^-p \rightarrow K^-\pi^-p\pi^+$ at 4.25-GeV/c incident K^- momentum, Nuclear Phys. B67 (1973) 381–394, http://dx.doi.org/10.1016/0550-3213(73)90203-4.

[5] P. Estabrooks, R.K. Carnegie, A.D. Martin, W.M. Dunwoodie, T.A. Lasinski, D.W.G.S. Leith, Study of $K\pi$ scattering using the reactions $K^{\pm}p \rightarrow K^{\pm}\pi^+n$ and $K^{\pm}p \rightarrow K^{\pm}\pi^-\Delta^{++}$ at 13 GeV/c, Nuclear Phys. B133 (1978) 490–524, http://dx.doi.org/10.1016/0550-3213(78)90238-9.

[6] D. Aston, et al., A study of $K^-\pi^+$ scattering in the reaction $K^-p \rightarrow K^-\pi^+n$ at 11 GeV/c, Nuclear Phys. B296 (1988) 493–526, http://dx.doi.org/10.1016/0550-3213(88)90028-4.

[7] D.H. Cohen, D.S. Ayres, R. Diebold, S.L. Kramer, A.J. Pawlicki, A.B. Wicklund, Amplitude analysis of the K^-K^+ system produced in the reactions $\pi^-p \rightarrow K^-K^+n$ and $\pi^+n \rightarrow K^-K^+p$ at 6 GeV/c, Phys. Rev. D22 (1980) 2595, http://dx.doi.org/10.1103/PhysRevD.22.2595.

[8] A. Etkin, et al., Amplitude analysis of the $K_S^0K_S^0$ system produced in the reaction $\pi^-p \rightarrow K_S^0K_S^0n$ at 23-GeV/c, Phys. Rev. D25 (1982) 1786, http://dx.doi.org/10.1103/PhysRevD.25.1786.

[9] R.S. Longacre, et al., A measurement of $\pi^-p \rightarrow K_S^0 K_S^0 n$ at 22-GeV/c and a systematic study of the 2^{++} meson spectrum, Phys. Lett. B177 (1986) 223–227, http://dx.doi.org/10.1016/0370-2693(86)91061-0.

[10] A. Gomez Nicola, J. Peláez, Meson-meson scattering within one loop chiral perturbation theory and its unitarization, Phys. Rev. D 65 (2002) 054009, http://dx.doi.org/10.1103/PhysRevD.65.054009, arXiv:hep-ph/0109056.

[11] B. Ananthanarayan, G. Colangelo, J. Gasser, H. Leutwyler, Roy equation analysis of $\pi\pi$ scattering, Phys. Rep. 353 (2001) 207–279, http://dx.doi.org/10.1016/S0370-1573(01)00009-6, arXiv:hep-ph/0005297.

[12] G. Colangelo, J. Gasser, H. Leutwyler, $\pi\pi$ Scattering, Nuclear Phys. B603 (2001) 125–179, http://dx.doi.org/10.1016/S0550-3213(01)00147-X, arXiv:hep-ph/0103088.

[13] J.R. Peláez, From controversy to precision on the σ meson: a review on the status of the non-ordinary $f_0(500)$ resonance, Phys. Rep. 658 (2016) 1, http://dx.doi.org/10.1016/j.physrep.2016.09.001, arXiv:1510.00653.

[14] M. Hoferichter, J. Ruiz de Elvira, B. Kubis, U.-G. Meißner, Roy–Steiner-equation analysis of pion–nucleon scattering, Phys. Rep. 625 (2016) 1–88, http://dx.doi.org/10.1016/j.physrep.2016.02.002, arXiv:1510.06039.

[15] C.B. Lang, The πK scattering and related processes, Fortschr. Phys. 26 (1978) 509, http://dx.doi.org/10.1002/prop.19780261002.

[16] E. van Beveren, T. Rijken, K. Metzger, C. Dullemond, G. Rupp, J. Ribeiro, A low lying scalar meson nonet in a unitarized meson model, Z. Phys. C 30 (1986) 615–620, http://dx.doi.org/10.1007/BF01571811, arXiv:0710.4067.

[17] K.L. Au, D. Morgan, M.R. Pennington, Meson dynamics beyond the quark model: A study of final state interactions, Phys. Rev. D35 (1987) 1633, http://dx.doi.org/10.1103/PhysRevD.35.1633.

[18] R. Kaminski, L. Lesniak, J.P. Maillet, Relativistic effects in the scalar meson dynamics, Phys. Rev. D50 (1994) 3145–3157, http://dx.doi.org/10.1103/PhysRevD.50.3145, arXiv:hep-ph/9403264.

[19] D.V. Bugg, B.S. Zou, A.V. Sarantsev, New results on $\pi\pi$ phase shifts between 600-MeV and 1900-MeV, Nuclear Phys. B471 (1996) 59–89, http://dx.doi.org/10.1016/0550-3213(96)00166-6.

[20] S. Ishida, M. Ishida, T. Ishida, K. Takamatsu, T. Tsuru, Analysis of $K\pi$ scattering phase shift and existence of $\kappa(900)$ particle, Progr. Theoret. Phys. 98 (1997) 621–629, http://dx.doi.org/10.1143/PTP.98.621, arXiv:hep-ph/9705437.

[21] R. Kaminski, L. Lesniak, B. Loiseau, Three channel model of meson-meson scattering and scalar meson spectroscopy, Phys. Lett. B413 (1997) 130–136, http://dx.doi.org/10.1016/S0370-2693(97)01090-3, arXiv:hep-ph/9707377.

[22] B. Bajc, S. Fajfer, R. Oakes, T. Pham, Resonant and nonresonant $D^+ \rightarrow K^-\pi^+$ semileptonic decays, Phys. Rev. D 58 (1998) 054009, http://dx.doi.org/10.1103/PhysRevD.58.054009, arXiv:hep-ph/9710422.

[23] J.A. Oller, E. Oset, J.R. Peláez, Nonperturbative approach to effective chiral Lagrangians and meson interactions, Phys. Rev. Lett. 80 (1998) 3452–3455, http://dx.doi.org/10.1103/PhysRevLett.80.3452, arXiv:hep-ph/9803242.

[24] J.A. Oller, E. Oset, Chiral symmetry amplitudes in the s wave isoscalar and isovector channels and the σ, $f_0(980)$, $a_0(980)$ scalar mesons, Nuclear Phys. A620 (1997) 438–456, http://dx.doi.org/10.1016/S0375-9474(99)00427-3, arXiv:hep-ph/9702314, http://dx.doi.org/10.1016/S0375-9474(97)00160-7; Nucl. Phys. A 652 (1999) 407, Erratum.

[25] J.A. Oller, E. Oset, J.R. Peláez, Meson-meson interaction in a nonperturbative chiral approach, Phys. Rev. D59 (1999) 074001, http://dx.doi.org/10.1103/PhysRevD.59.074001, arXiv:hep-ph/9804209, http://dx.doi.org/10.1103/PhysRevD.60.099906, http://dx.doi.org/10.1103/PhysRevD.75.099903; Phys. Rev. D 75 (2007) 099903, Erratum.

[26] J.A. Oller, E. Oset, N/D Description of two meson amplitudes and chiral symmetry, in: Hadron Spectroscopy. Proceedings, Workshop, Frascati, Italy, March 8-12, 1999, Phys. Rev. D60 (1999) 074023, http://dx.doi.org/10.1103/PhysRevD.60.074023, arXiv:hep-ph/9809337.

[27] F. Guerrero, J.A. Oller, $K\bar{K}$ Scattering amplitude to one loop in chiral perturbation theory, its unitarization and pion form-factors, Nuclear Phys. B 537 (1999) 459–476, http://dx.doi.org/10.1016/S0550-3213(98)00663-4, arXiv:hep-ph/9805334; Nucl. Phys. B 602 (2001) 641–643, Erratum.

[28] P. Minkowski, W. Ochs, Identification of the glueballs and the scalar meson nonet of lowest mass, Eur. Phys. J. C9 (1999) 283–312, http://dx.doi.org/10.1007/s100529900044, arXiv:hep-ph/9811518, http://dx.doi.org/10.1007/s100520050533.

[29] D. Black, A.H. Fariborz, F. Sannino, J. Schechter, Evidence for a scalar $\kappa(900)$ resonance in πK scattering, Phys. Rev. D58 (1998) 054012, http://dx.doi.org/10.1103/PhysRevD.58.054012, arXiv:hep-ph/9804273.

[30] M.P. Locher, V.E. Markushin, H.Q. Zheng, Structure of $f_0(980)$ from a coupled channel analysis of S-wave $\pi\pi$ scattering, Eur. Phys. J. C4 (1998) 317–326, http://dx.doi.org/10.1007/s100529800766, arXiv:hep-ph/9705230, http://dx.doi.org/10.1007/s100520050210.

[31] F.E. Close, N.A. Tornqvist, Scalar mesons above and below 1-GeV, J. Phys. G 28 (2002) R249–R267, http://dx.doi.org/10.1088/0954-3899/28/10/201, arXiv:hep-ph/0204205.

[32] N. Kelkar, M. Nowakowski, K. Khemchandani, Collision times in $\pi\pi$ and π^-K scattering and spectroscopy of meson resonances, Nuclear Phys. A 724 (2003) 357–374, http://dx.doi.org/10.1016/S0375-9474(03)01555-0, arXiv:hep-ph/0307184.

[33] L. Maiani, F. Piccinini, A. Polosa, V. Riquer, A new look at scalar mesons, Phys. Rev. Lett. 93 (2004) 212002, http://dx.doi.org/10.1103/PhysRevLett.93.212002, arXiv:hep-ph/0407017.

[34] J.R. Peláez, Light scalars as tetraquarks or two-meson states from large N_c and unitarized chiral perturbation theory, Modern Phys. Lett. A19 (2004) 2879–2894, http://dx.doi.org/10.1142/S0217732304016160, arXiv:hep-ph/0411107.

[35] C. Amsler, N. Tornqvist, Mesons beyond the naive quark model, Phys. Rep. 389 (2004) 61–117, http://dx.doi.org/10.1016/j.physrep.2003.09.003.

[36] E. van Beveren, J.E. Costa, F. Kleefeld, G. Rupp, From the kappa via the $D_0^{*0}(2317)$ to the χ_0^0: Connecting light and heavy scalar mesons, Phys. Rev. D 74 (2006) 037501, http://dx.doi.org/10.1103/PhysRevD.74.037501, arXiv:hep-ph/0509351.

[37] R.L. Jaffe, Ordinary and extraordinary hadrons, in: Proceedings, 4th International Workshop on QCD - Theory and Experiment (QCD@Work 2007), AIP Conf. Proc. 964 (2007) 1–13, http://dx.doi.org/10.1063/1.2823850, arXiv:hep-ph/0701038; Prog. Theor. Phys. Suppl. 168 (2007) 127.

[38] M. Albaladejo, J. Oller, Identification of a scalar glueball, Phys. Rev. Lett. 101 (2008) 252002, http://dx.doi.org/10.1103/PhysRevLett.101.252002, arXiv:0801.4929.

[39] P. Guo, R. Mitchell, M. Shepherd, A.P. Szczepaniak, Amplitudes for the analysis of the decay $J/\psi \rightarrow K^+K^-\pi^0$, Phys. Rev. D 85 (2012) 056003, http://dx.doi.org/10.1103/PhysRevD.85.056003, arXiv:1112.3284.

[40] A.H. Fariborz, E. Pourjafarabadi, S. Zarepour, S.M. Zebarjad, Chiral nonet mixing in πk scattering, Phys. Rev. D 92 (2015) 113002, http://dx.doi.org/10.1103/PhysRevD.92.113002, arXiv:1511.01623.

[41] J. Peláez, A. Rodas, Pion-kaon scattering amplitude constrained with forward dispersion relations up to 1.6 GeV, Phys. Rev. D 93 (7) (2016) 074025, http://dx.doi.org/10.1103/PhysRevD.93.074025, arXiv:1602.08404.

[42] J. Peláez, A. Rodas, $\pi\pi \rightarrow K\bar{K}$ Scattering up to 1.47 GeV with hyperbolic dispersion relations, Eur. Phys. J. C 78 (11) (2018) 897, http://dx.doi.org/10.1140/epjc/s10052-018-6296-9, arXiv:1807.04543.

[43] P. Büttiker, S. Descotes-Genon, B. Moussallam, A new analysis of πK scattering from Roy and Steiner type equations, Eur. Phys. J. C33 (2004) 409–432, http://dx.doi.org/10.1140/epjc/s2004-01591-1, arXiv:hep-ph/0310283.

[44] S.M. Roy, Exact integral equation for pion pion scattering involving only physical region partial waves, Phys. Lett. 36B (1971) 353–356, http://dx.doi.org/10.1016/0370-2693(71)90724-6.

[45] F. Steiner, On the convergence of finite energy sum rules in non-forward directions, Phys. Lett. 32B (1970) 294–296, http://dx.doi.org/10.1016/0370-2693(70)90531-9.

[46] F. Steiner, Partial wave crossing relations for meson–baryon scattering, Fortschr. Phys. 19 (1971) 115–159, http://dx.doi.org/10.1002/prop.19710190302.

[47] J. Peláez, A. Rodas, Determination of the lightest strange resonance $K_0^*(700)$ or κ, from a dispersive data analysis, Phys. Rev. Lett. 124 (17) (2020) 172001, http://dx.doi.org/10.1103/PhysRevLett.124.172001, arXiv:2001.08153.

[48] R. García-Martín, R. Kamiński, J.R. Peláez, J. Ruiz de Elvira, F.J. Ynduráin, The pion-pion scattering amplitude. IV: Improved analysis with once subtracted Roy-like equations up to 1100 MeV, Phys. Rev. D83 (2011) 074004, http://dx.doi.org/10.1103/PhysRevD.83.074004, arXiv:1102.2183.

[49] R. Kaminski, J.R. Peláez, F.J. Ynduráin, The pion-pion scattering amplitude. III. Improving the analysis with forward dispersion relations and roy equations, Phys. Rev. D77 (2008) 054015, http://dx.doi.org/10.1103/PhysRevD.77.054015, arXiv:0710.1150.

[50] R. Kaminski, J.R. Peláez, F.J. Ynduráin, The pion-pion scattering amplitude. II. Improved analysis above $\bar{K}K$ threshold, Phys. Rev. D74 (2006) 014001, http://dx.doi.org/10.1103/PhysRevD.74.014001, arXiv:hep-ph/0603170; Phys. Rev. D 74 (2006) 079903, Erratum.

[51] J.R. Peláez, F.J. Ynduráin, The pion-pion scattering amplitude, Phys. Rev. D71 (2005) 074016, http://dx.doi.org/10.1103/PhysRevD.71.074016, arXiv:hep-ph/0411334.

[52] E. Aitala, et al., E791 Collaboration, Dalitz plot aanalysis of the decay $D^+ \to K^-\pi^+\pi^+$ and the study of the $K\pi$ scalar amplitudes, Phys. Rev. Lett. 89 (2002) 121801, http://dx.doi.org/10.1103/PhysRevLett.89.121801, arXiv:hep-ex/0204018.

[53] E.M. Aitala, et al., E791 Collaboration, Model independent measurement of S-wave $K^-\pi^+$ systems using $D^+ \to K\pi\pi$ decays from Fermilab E791, Phys. Rev. D73 (2006) 032004, http://dx.doi.org/10.1103/PhysRevD.73.032004, arXiv:hep-ex/0507099; Phys. Rev. D 74 (2006) 059901, Erratum.

[54] J.M. Link, et al., FOCUS Collaboration, The $K^-\pi^+$ S-wave from the $D^+ \to K^-\pi^+\pi^+$ decay, Phys. Lett. B681 (2009) 14–21, http://dx.doi.org/10.1016/j.physletb.2009.09.057, arXiv:0905.4846.

[55] B. Aubert, et al., BaBar Collaboration, Improved measurement of the CKM angle γ in $B^\mp \to D^{(*)}K^{(*)\mp}$ decays with a dalitz plot analysis of D decays to $K_S^0\pi^+\pi^-$ and $K_S^0K^+K^-$, Phys. Rev. D 78 (2008) 034023, http://dx.doi.org/10.1103/PhysRevD.78.034023, arXiv:0804.2089.

[56] A. Poluektov, et al., Belle Collaboration, Evidence for direct CP violation in the decay $B \to D^*K$, $D \to K_S\pi^+\pi^-$ and measurement of the CKM phase ϕ_3, Phys. Rev. D 81 (2010) 112002, http://dx.doi.org/10.1103/PhysRevD.81.112002, arXiv:1003.3360.

[57] R. Aaij, et al., LHCb Collaboration, Measurement of CP violation and constraints on the CKM angle γ in $B^\pm \to DK^\pm$ with $D \to K_S^0\pi^+\pi^-$ decays, Nuclear Phys. B 888 (2014) 169–193, http://dx.doi.org/10.1016/j.nuclphysb.2014.09.015, arXiv:1407.6211.

[58] R. Aaij, et al., LHCb Collaboration, A study of CP violation in $B^\pm \to DK^\pm$ and $B^\pm \to D\pi^\pm$ decays with $D \to K_S^0K^\pm\pi^\mp$ final states, Phys. Lett. B 733 (2014) 36–45, http://dx.doi.org/10.1016/j.physletb.2014.03.051, arXiv:1402.2982.

[59] B. Aubert, et al., BaBar Collaboration, Dalitz-plot analysis of the decays $B^\pm \to K^\pm\pi^\mp\pi^\pm$, in: R. Brenner, C. de los Heros, J. Rathsman (Eds.), Phys. Rev. D 72 (2005) 072003, http://dx.doi.org/10.1103/PhysRevD.72.072003, arXiv:hep-ex/0507004; Phys. Rev. D 74 (2006) 099903, Erratum.

[60] R. Aaij, et al., LHCb Collaboration, Model-independent search for CP violation in $D^0 \to K^-K^+\pi^-\pi^+$ and $D^0 \to \pi^-\pi^+\pi^+\pi^-$ decays, Phys. Lett. B 726 (2013) 623–633, http://dx.doi.org/10.1016/j.physletb.2013.09.011, arXiv:1308.3189.

[61] R. Aaij, et al., LHCb Collaboration, First measurement of the CP-violating phase $\phi_s^{d\bar{d}}$ in $B_s^0 \to (K^+\pi^-)(K^-\pi^+)$ decays, J. High Energy Phys. 03 (2018) 140, http://dx.doi.org/10.1007/JHEP03(2018)140, arXiv:1712.08683.

[62] R. Aaij, et al., LHCb Collaboration, Search for CP violation through an amplitude analysis of $D^0 \to K^+K^-\pi^+\pi^-$ decays, J. High Energy Phys. 02 (2019) 126, http://dx.doi.org/10.1007/JHEP02(2019)126, arXiv:1811.08304.

[63] R. Aaij, et al., LHCb Collaboration, Measurement of CP violation in the phase space of $B^\pm \to K^\pm\pi^+\pi^-$ and $B^\pm \to K^\pm K^+K^-$ decays, Phys. Rev. Lett. 111 (2013) 101801, http://dx.doi.org/10.1103/PhysRevLett.111.101801, arXiv:1306.1246.

[64] R. Aaij, et al., LHCb Collaboration, Measurements of CP violation in the three-body phase space of charmless $B^\pm$ decays, Phys. Rev. D90 (11) (2014) 112004, http://dx.doi.org/10.1103/PhysRevD.90.112004, arXiv:1408.5373.

[65] I. Bediaga, T. Frederico, O. Lourenço, CP Violation and CPT invariance in $B^\pm$ decays with final state interactions, Phys. Rev. D89 (9) (2014) 094013, http://dx.doi.org/10.1103/PhysRevD.89.094013, arXiv:1307.8164.

[66] J.H. Alvarenga Nogueira, I. Bediaga, A.B.R. Cavalcante, T. Frederico, O. Lourenço, CP Violation: Dalitz interference, CPT, and final state interactions, Phys. Rev. D92 (5) (2015) 054010, http://dx.doi.org/10.1103/PhysRevD.92.054010, arXiv:1506.08332.

[67] I. Bediaga, C. Göbel, Direct CP violation in beauty and charm hadron decays, Prog. Part. Nucl. Phys. 114 (2020) 103808, http://dx.doi.org/10.1016/j.ppnp.2020.103808, arXiv:2009.07037.

[68] S. Adhikari, et al., GlueX Collaboration, Strange hadron spectroscopy with a secondary K_L beam at glueX, 2017, arXiv:1707.05284.

[69] M. Amaryan, et al., KLF Collaboration, Strange hadron spectroscopy with secondary K_L bbeam in hall D, 2020, arXiv:2008.08215.

[70] S. Prelovsek, L. Leskovec, C. Lang, D. Mohler, $K\pi$ Scattering and the K^* decay width from lattice QCD, Phys. Rev. D 88 (5) (2013) 054508, http://dx.doi.org/10.1103/PhysRevD.88.054508, arXiv:1307.0736.

[71] D.J. Wilson, J.J. Dudek, R.G. Edwards, C.E. Thomas, Resonances in coupled πK, ηK scattering from lattice QCD, Phys. Rev. D 91 (5) (2015) 054008, http://dx.doi.org/10.1103/PhysRevD.91.054008, arXiv:1411.2004.

[72] D.J. Wilson, R.A. Briceno, J.J. Dudek, R.G. Edwards, C.E. Thomas, The quark-mass dependence of elastic πK scattering from QCD, Phys. Rev. Lett. 123 (4) (2019) 042002, http://dx.doi.org/10.1103/PhysRevLett.123.042002, arXiv:1904.03188.

[73] D.J. Wilson, R.A. Briceno, J.J. Dudek, R.G. Edwards, C.E. Thomas, Coupled $\pi\pi$, $K\bar{K}$ scattering in P-wave and the ρ resonance from lattice QCD, Phys. Rev. D92 (9) (2015) 094502, http://dx.doi.org/10.1103/PhysRevD.92.094502, arXiv:1507.02599.

[74] R.A. Briceño, J.J. Dudek, R.G. Edwards, D.J. Wilson, Isoscalar $\pi\pi$, $K\bar{K}$, $\eta\eta$ scattering and the σ, f_0, f_2 mesons from QCD, Phys. Rev. D97 (5) (2018) 054513, http://dx.doi.org/10.1103/PhysRevD.97.054513, arXiv:1708.06667.

[75] R.A. Briceño, J.J. Dudek, R.D. Young, Scattering processes and resonances from lattice QCD, Rev. Modern Phys. 90 (2) (2018) 025001, http://dx.doi.org/10.1103/RevModPhys.90.025001, arXiv:1706.06223.

[76] Y. Nambu, Axial vector current conservation in weak interactions, Phys. Rev. Lett. 4 (1960) 380–382, http://dx.doi.org/10.1103/PhysRevLett.4.380, [107(1960)].

[77] Y. Nambu, Quasiparticles and gauge invariance in the theory of superconductivity, in: J. Taylor (Ed.), Phys. Rev. 117 (1960) 648–663, http://dx.doi.org/10.1103/PhysRev.117.648.

[78] J. Goldstone, Field theories with superconductor solutions, Nuovo Cim. 19 (1961) 154–164, http://dx.doi.org/10.1007/BF02812722.

[79] J. Goldstone, A. Salam, S. Weinberg, Broken symmetries, Phys. Rev. 127 (1962) 965–970, http://dx.doi.org/10.1103/PhysRev.127.965.

[80] J. Donoghue, E. Golowich, B.R. Holstein, Dynamics of the Standard Model, Vol. 2, CUP, 2014, http://dx.doi.org/10.1017/CBO9780511524370, URL https://www.cambridge.org/core/books/dynamics-of-the-standard-model/639475F2E0F99E2334D01BD648D2F993.

[81] A. Dobado, A. Gomez-Nicola, A.L. Maroto, J. Peláez, Effective lagrangians for the standard model, in: Theoretical and Mathematical Physics, Springer Verlag, 1997, URL https://books.google.es/books?id=6dTvAAAAMAAJ&dq=editions:ISBN3642638899&hl=es.

[82] S. Scherer, M.R. Schindler, A Primer for Chiral Perturbation Theory, Vol. 830, Springer Verlag, 2012, http://dx.doi.org/10.1007/978-3-642-19254-8.

[83] J. Gasser, H. Leutwyler, Chiral perturbation theory to one loop, Ann. Physics 158 (1984) 142, http://dx.doi.org/10.1016/0003-4916(84)90242-2.

[84] J. Gasser, H. Leutwyler, Chiral perturbation theory: Expansions in the mass of the strange quark, Nuclear Phys. B 250 (1985) 465–516, http://dx.doi.org/10.1016/0550-3213(85)90492-4.

[85] J. Bijnens, P. Dhonte, P. Talavera, πK Scattering in three flavor ChPT, J. High Energy Phys. 05 (2004) 036, http://dx.doi.org/10.1088/1126-6708/2004/05/036, arXiv:hep-ph/0404150.

[86] J. Bijnens, G. Ecker, Mesonic low-energy constants, Ann. Rev. Nucl. Part. Sci. 64 (2014) 149–174, http://dx.doi.org/10.1146/annurev-nucl-102313-025528, arXiv:1405.6488.

[87] C. Miao, X.-i. Du, G.-w. Meng, C. Liu, Lattice study on kaon pion scattering length in the I=3/2 channel, Phys. Lett. B595 (2004) 400–407, http://dx.doi.org/10.1016/j.physletb.2004.05.073, arXiv:hep-lat/0403028.

[88] S.R. Beane, P.F. Bedaque, T.C. Luu, K. Orginos, E. Pallante, A. Parreno, M.J. Savage, πK Scattering in full QCD with domain-wall valence quarks, Phys. Rev. D74 (2006) 114503, http://dx.doi.org/10.1103/PhysRevD.74.114503, arXiv:hep-lat/0607036.

[89] J.M. Flynn, J. Nieves, Elastic s-wave $B\pi$, $D\pi$, DK and $K\pi$ scattering from lattice calculations of scalar form-factors in semileptonic decays, Phys. Rev. D75 (2007) 074024, http://dx.doi.org/10.1103/PhysRevD.75.074024, arXiv:hep-ph/0703047.

[90] J. Nagata, S. Muroya, A. Nakamura, Lattice study of $K\pi$ scattering in $I = 3/2$ and 1/2, Phys. Rev. C 80 (2009) 045203, http://dx.doi.org/10.1103/PhysRevC.84.019904, arXiv:0812.1753;   Phys. Rev. C 84 (2011) 019904, Erratum.

[91] Z. Fu, Lattice study on πK scattering with moving wall source, Phys. Rev. D85 (2012) 074501, http://dx.doi.org/10.1103/PhysRevD.85.074501, arXiv:1110.1422.

[92] K. Sasaki, N. Ishizuka, M. Oka, T. Yamazaki, PACS-CS Collaboration, Scattering lengths for two pseudoscalar meson systems, Phys. Rev. D89 (5) (2014) 054502, http://dx.doi.org/10.1103/PhysRevD.89.054502, arXiv:1311.7226.

[93] C. Helmes, C. Jost, B. Knippschild, B. Kostrzewa, L. Liu, F. Pittler, C. Urbach, M. Werner, ETM Collaboration, Hadron-hadron interactions from $N_f = 2 + 1 + 1$ lattice QCD: $I = 3/2$ πK scattering length, Phys. Rev. D98 (11) (2018) 114511, http://dx.doi.org/10.1103/PhysRevD.98.114511, arXiv:1809.08886.

[94] B. Adeva, et al., DIRAC Collaboration, First πK atom lifetime and πK scattering length measurements, Phys. Lett. B 735 (2014) 288–294, http://dx.doi.org/10.1016/j.physletb.2014.06.043, arXiv:1403.0845.

[95] P. Zyla, et al., Particle Data Group Collaboration, Review of particle physics, Prog. Theor. Exp. Phys. 2020 (8) (2020) 083C01, http://dx.doi.org/10.1093/ptep/ptaa104.

[96] W. Ochs, The status of glueballs, J. Phys. G40 (2013) 043001, http://dx.doi.org/10.1088/0954-3899/40/4/043001, arXiv:1301.5183.

[97] S. Descotes-Genon, B. Moussallam, The $K_0^*(800)$ scalar resonance from Roy-Steiner representations of πK scattering, Eur. Phys. J. C48 (2006) 553, http://dx.doi.org/10.1140/epjc/s10052-006-0036-2, arXiv:hep-ph/0607133.

[98] J.R. Peláez, A. Rodas, J. Ruiz de Elvira, Dispersive analysis of the $\kappa/K_0^*(700)$ meson and other light strange resonances, in: Proceedings, International Workshop on E+E- Collisions from Phi To Psi (PhiPsi19): Novosibirsk, Russian Federation, EPJ Web Conf. 212 (2019) 03003, http://dx.doi.org/10.1051/epjconf/201921203003.

[99] J.R. Peláez, A. Rodas, J. Ruiz de Elvira, Strange resonance poles from $K\pi$ scattering below 1.8 GeV, Eur. Phys. J. C77 (2) (2017) 91, http://dx.doi.org/10.1140/epjc/s10052-017-4668-1, arXiv:1612.07966.

[100] J.J. Dudek, R.G. Edwards, C.E. Thomas, D.J. Wilson, Hadron Spectrum Collaboration, Resonances in coupled $\pi K - \eta K$ scattering from quantum chromodynamics, Phys. Rev. Lett. 113 (18) (2014) 182001, http://dx.doi.org/10.1103/PhysRevLett.113.182001, arXiv:1406.4158.

[101] G. Rendon, L. Leskovec, S. Meinel, J. Negele, S. Paul, M. Petschlies, A. Pochinsky, G. Silvi, S. Syritsyn, $I = 1/2$ S-Wave and P-wave $K\pi$ scattering and the κ and K^* resonances from lattice QCD, 2020, arXiv:2006.14035.

[102] J. Nebreda, J.R. Peláez., Strange and non-strange quark mass dependence of elastic light resonances from SU(3) unitarized chiral perturbation theory to one loop, Phys. Rev. D81 (2010) 054035, http://dx.doi.org/10.1103/PhysRevD.81.054035, arXiv:1001.5237.

[103] P.D.B. Collins, Regge theory and particle physics, Phys. Rep. 1 (1971) 103–234, http://dx.doi.org/10.1016/0370-1573(71)90007-X.

[104] J.T. Londergan, J. Nebreda, J.R. Peláez, A. Szczepaniak, Identification of non-ordinary mesons from the dispersive connection between their poles and their Regge trajectories: The $f_0(500)$ resonance, Phys. Lett. B729 (2014) 9–14, http://dx.doi.org/10.1016/j.physletb.2013.12.061, arXiv:1311.7552.

[105] J.A. Carrasco, J. Nebreda, J.R. Peláez, A.P. Szczepaniak, Dispersive calculation of complex Regge trajectories for the lightest f_2 resonances and the $K^*(892)$, Phys. Lett. B749 (2015) 399–406, http://dx.doi.org/10.1016/j.physletb.2015.08.019, arXiv:1504.03248.

[106] J.R. Peláez, A. Rodas, The non-ordinary Regge behavior of the $K_0^*(800)$ or κ -meson versus the ordinary $K_0^*(1430)$, Eur. Phys. J. C77 (6) (2017) 431, http://dx.doi.org/10.1140/epjc/s10052-017-4994-3, arXiv:1703.07661.

[107] W.R. Frazer, J.R. Fulco, Partial-wave dispersion relations for the process $\pi\pi \to N\bar{N}$, Phys. Rev. 117 (1960) 1603–1609, http://dx.doi.org/10.1103/PhysRev.117.1603.

[108] C. Goebel, Determination of the $\pi^-\pi$ interaction strength from $\pi^- N$ scattering, Phys. Rev. Lett. 1 (1958) 337–339, http://dx.doi.org/10.1103/PhysRevLett.1.337.

[109] G.F. Chew, F.E. Low, Unstable particles as targets in scattering experiments, Phys. Rev. 113 (1959) 1640–1648, http://dx.doi.org/10.1103/PhysRev.113.1640.

[110] H. Bingham, et al., A new analysis of $K\pi$ scattering as observed in $K^+p \to K^+\pi^0\Delta^{++}$ from 3-GeV/c to 13-GeV/c, Nuclear Phys. B 41 (1972) 1–34, http://dx.doi.org/10.1016/0550-3213(72)90419-1.

[111] S. Baker, et al., A study of $K^+\pi^-$ elastic scattering in the reaction $K^+n \to K^+\pi^-p$ between 2.0-GeV/c and 3.0-GeV/c, in: G. Cohen-Tannoudji (Ed.), Nuclear Phys. B 99 (1975) 211, http://dx.doi.org/10.1016/0550-3213(75)90002-4.

[112] P. Estabrooks, A.D. Martin, Amplitudes and production mechanisms for $K^*(890)$ resonance production at 4-GeV/c, Nuclear Phys. B102 (1976) 537–548, http://dx.doi.org/10.1016/0550-3213(76)90436-3.

[113] P. Estabrooks, et al., Amplitudes and exchange mechanisms for $K^*(890)$ and $K^*(1420)$ production, Phys. Lett. 60B (1976) 473–477, http://dx.doi.org/10.1016/0370-2693(76)90710-3.

[114] P. Estabrooks, et al., A study of $K^*(890)$ and $K^*(1420)$ production mechanisms in $K^+p \to K^+\pi^-\Delta^{++}$ at 13-GeV/c, Nuclear Phys. B106 (1976) 61–76, http://dx.doi.org/10.1016/0550-3213(76)90369-2.

[115] B.R. Martin, D. Morgan, G. Shaw, Pion Pion Interactions in Particle Physics, Academic Press, London, 1976, p. 460.

[116] J. Nys, V. Mathieu, C. Fernández-Ramírez, A. Jackura, M. Mikhasenko, A. Pilloni, N. Sherrill, J. Ryckebusch, A.P. Szczepaniak, G. Fox, JPAC Collaboration, Features of $\pi\Delta$ photoproduction at high energies, Phys. Lett. B779 (2018) 77–81, http://dx.doi.org/10.1016/j.physletb.2018.01.075, arXiv:1710.09394.

[117] R. Mercer, et al., $K\pi$ Scattering phase shifts determined from the reactions $K^+p \to K^+\pi^-\Delta^{++}$ and $K^+p \to K^0\pi^0\Delta^{++}$, Nuclear Phys. B32 (1971) 381–414, http://dx.doi.org/10.1016/0550-3213(71)90483-4.

[118] K.M. Watson, The effect of final state interactions on reaction cross-sections, Phys. Rev. 88 (1952) 1163–1171, http://dx.doi.org/10.1103/PhysRev.88.1163.

[119] O. Dumbrajs, R. Koch, H. Pilkuhn, G.c. Oades, H. Behrens, J.j. De Swart, P. Kroll, Compilation of coupling constants and low-energy parameters. 1982 edition, Nuclear Phys. B216 (1983) 277–335, http://dx.doi.org/10.1016/0550-3213(83)90288-2.

[120] M. Ablikim, et al., BESIII Collaboration, Study of $D^+ \to K^-\pi^+e^+\nu_e$, Phys. Rev. D94 (3) (2016) 032001, http://dx.doi.org/10.1103/PhysRevD.94.032001, arXiv:1512.08627.

[121] P. del Amo Sanchez, et al., BaBar Collaboration, Analysis of the $D^+ \to K^-\pi^+e^+\nu_e$ decay channel, Phys. Rev. D83 (2011) 072001, http://dx.doi.org/10.1103/PhysRevD.83.072001, arXiv:1012.1810.

[122] J.M. Link, et al., FOCUS Collaboration, Dalitz plot analysis of the $D^+ \rightarrow K^-\pi^+\pi^+$ decay in the FOCUS experiment, Phys. Lett. B653 (2007) 1–11, http://dx.doi.org/10.1016/j.physletb.2007.06.070, arXiv:0705.2248.

[123] G. Bonvicini, et al., CLEO Collaboration, Dalitz plot analysis of the $D^+ \rightarrow K^-\pi^+\pi^+$ decay, Phys. Rev. D78 (2008) 052001, http://dx.doi.org/10.1103/PhysRevD.78.052001, arXiv:0802.4214.

[124] J.P. Lees, et al., BaBar Collaboration, Measurement of the I=1/2 $K\pi$ $\mathcal{S}$-wave amplitude from dalitz plot analyses of $\eta_c \rightarrow K\bar{K}\pi$ in two-photon interactions, Phys. Rev. D93 (2016) 012005, http://dx.doi.org/10.1103/PhysRevD.93.012005, arXiv:1511.02310.

[125] P.C. Magalhaes, M.R. Robilotta, K.S.F.F. Guimaraes, T. Frederico, W. de Paula, I. Bediaga, A.C.d. Reis, C.M. Maekawa, G.R.S. Zarnauskas, Towards three-body unitarity in $D^+ \rightarrow K^-\pi^+\pi^+$, Phys. Rev. D84 (2011) 094001, http://dx.doi.org/10.1103/PhysRevD.84.094001, arXiv:1105.5120.

[126] K.S.F.F. Guimarães, O. Lourenço, W. de Paula, T. Frederico, A.C. dos Reis, Final state interaction in $D^+ \rightarrow K^-\pi^+\pi^+$ with $K\pi$ $I = 1/2$ and 3/2 channels, J. High Energy Phys. 08 (2014) 135, http://dx.doi.org/10.1007/JHEP08(2014)135, arXiv:1404.3797.

[127] S.X. Nakamura, Coupled-channel analysis of $D^+ \rightarrow K^-\pi^+\pi^+$ decay, Phys. Rev. D93 (1) (2016) 014005, http://dx.doi.org/10.1103/PhysRevD.93.014005, arXiv:1504.02557.

[128] P.C. Magalhães, M.R. Robilotta, $D^+ \rightarrow K^-\pi^+\pi^+$ - The weak vector current, Phys. Rev. D 92 (9) (2015) 094005, http://dx.doi.org/10.1103/PhysRevD.92.094005, arXiv:1504.06346.

[129] F. Niecknig, B. Kubis, Dispersion-theoretical analysis of the $D^+ \rightarrow K^-\pi^+\pi^+$ dalitz plot, J. High Energy Phys. 10 (2015) 142, http://dx.doi.org/10.1007/JHEP10(2015)142, arXiv:1509.03188.

[130] F. Niecknig, B. Kubis, Consistent dalitz plot analysis of Cabibbo-favored $D^+ \rightarrow \bar{K}\pi\pi^+$ decays, Phys. Lett. B780 (2017) 471–478, http://dx.doi.org/10.1016/j.physletb.2018.03.048, arXiv:1708.00446.

[131] V. Bernard, N. Kaiser, U.G. Meißner, Threshold parameters of πK scattering in QCD, Phys. Rev. D43 (1991) 2757–2760, http://dx.doi.org/10.1103/PhysRevD.43.R2757.

[132] D. Epifanov, et al., Belle Collaboration, Study of $\tau- \rightarrow K_S\pi^-\nu_\tau$ decay at Belle, Phys. Lett. B 654 (2007) 65–73, http://dx.doi.org/10.1016/j.physletb.2007.08.045, arXiv:0706.2231.

[133] J. Link, et al., FOCUS Collaboration, Evidence for new interference phenomena in the decay $D^+ \rightarrow K^-\pi^+\mu^+\nu$, Phys. Lett. B 535 (2002) 43–51, http://dx.doi.org/10.1016/S0370-2693(02)01715-X, arXiv:hep-ex/0203031.

[134] B. Ananthanarayan, K. Shivaraj, Comment on evidence for new interference phenomena in the decay $D^+ \rightarrow K^-\pi^+\mu^+\nu$, Phys. Lett. B 628 (2005) 223–227, http://dx.doi.org/10.1016/j.physletb.2005.09.047, arXiv:hep-ph/0508116.

[135] S. Paramesvaran, BaBar Collaboration, Selected topics in tau physics from babar, in: Meeting of the Division of Particles and Fields of the American Physical Society, DPF 2009, 2009, pp. 1–6, arXiv:0910.2884.

[136] D. Boito, R. Escribano, M. Jamin, $K\pi$ Vector form factor constrained by $\tau \rightarrow K\pi\nu_\tau$ and K_{l3} decays, J. High Energy Phys. 09 (2010) 031, http://dx.doi.org/10.1007/JHEP09(2010)031, arXiv:1007.1858.

[137] V. Bernard, D. Boito, E. Passemar, Dispersive representation of the scalar and vector $K\pi$ form factors for $\tau \rightarrow K\pi\nu_\tau$ and K_{l3} decays, in: G. Lafferty, S. Soldner-Rembold (Eds.), Nucl. Phys. B Proc. Suppl. 218 (2011) 140–145, http://dx.doi.org/10.1016/j.nuclphysbps.2011.06.024, arXiv:1103.4855.

[138] R. Escribano, S. González-Solís, M. Jamin, P. Roig, Combined analysis of the decays $\tau^- \rightarrow K_S\pi^-\nu_\tau$ and $\tau^- \rightarrow K^-\eta\nu_\tau$, J. High Energy Phys. 09 (2014) 042, http://dx.doi.org/10.1007/JHEP09(2014)042, arXiv:1407.6590.

[139] S. Gonzàlez-Solís, A. Miranda, J. Rendón, P. Roig, Exclusive hadronic tau decays as probes of non-SM interactions, Phys. Lett. B 804 (2020) 135371, http://dx.doi.org/10.1016/j.physletb.2020.135371, arXiv:1912.08725.

[140] J. Rendón, P. Roig, G. Toledo Sánchez, Effective-field theory analysis of the $\tau^- \rightarrow (K\pi)^-\nu_\tau$ decays, Phys. Rev. D 99 (9) (2019) 093005, http://dx.doi.org/10.1103/PhysRevD.99.093005, arXiv:1902.08143.

[141] V. Bernard, First determination of $f_+(0)|V_{us}|$ from a combined analysis of $\tau \rightarrow K\pi\nu_\tau$ decay and πK scattering with constraints from $K_{\ell3}$ decays, J. High Energy Phys. 06 (2014) 082, http://dx.doi.org/10.1007/JHEP06(2014)082, arXiv:1311.2569.

[142] S.J. Lindenbaum, R.S. Longacre, Coupled channel analysis of $J^{PC} = 0^{++}$ and 2^{++} isoscalar mesons with masses below 2-GeV, Phys. Lett. B274 (1992) 492–497, http://dx.doi.org/10.1016/0370-2693(92)92022-9.

[143] J.R. Peláez, F.J. Ynduráin, Regge analysis of pion pion (and pion kaon) scattering for energy $s^{1/2} > 1.4$ GeV, Phys. Rev. D69 (2004) 114001, http://dx.doi.org/10.1103/PhysRevD.69.114001, arXiv:hep-ph/0312187.

[144] G. Veneziano, Construction of a crossing-symmetric, Regge behaved amplitude for linearly rising trajectories, Nuovo Cim. A57 (1968) 190–197, http://dx.doi.org/10.1007/BF02824451.

[145] G. Grayer, et al., High statistics study of the reaction $\pi^-p \rightarrow \pi^-\pi^+n$: Apparatus, method of analysis, and general features of results at 17-GeV/c, Nuclear Phys. B75 (1974) 189–245, http://dx.doi.org/10.1016/0550-3213(74)90545-8.

[146] R. Kaminski, L. Lesniak, K. Rybicki, Separation of S-wave pseudoscalar and pseudovector amplitudes in $\pi^-p \uparrow \rightarrow \pi^+\pi^-n$ reaction on polarized target, Z. Phys. C 74 (1997) 79–91, http://dx.doi.org/10.1007/s002880050372, arXiv:hep-ph/9606362.

[147] R. Kaminski, L. Lesniak, K. Rybicki, A joint analysis of the S-wave in the $\pi^+\pi^-$ and $\pi^0\pi^0$ data, Eur. Phys. J. Direct 4 (1) (2002) 4, http://dx.doi.org/10.1007/s1010502c0004, arXiv:hep-ph/0109268.

[148] J.R. Batley, et al., NA48/2 Collaboration, Observation of a cusp-like structure in the $\pi^0\pi^0$ invariant mass distribution from $K^\pm \rightarrow \pi^\pm\pi^0\pi^0$ decay and determination of the $\pi\pi$ scattering lengths, Phys. Lett. B633 (2006) 173–182, http://dx.doi.org/10.1016/j.physletb.2005.11.087, arXiv:hep-ex/0511056.

[149] B. Moussallam, Couplings of light $I = 0$ scalar mesons to simple operators in the complex plane, Eur. Phys. J. C71 (2011) 1814, http://dx.doi.org/10.1140/epjc/s10052-011-1814-z, arXiv:1110.6074.

[150] S.D. Protopopescu, M. Alston-Garnjost, A. Barbaro-Galtieri, S.M. Flatte, J.H. Friedman, T.A. Lasinski, G.R. Lynch, M.S. Rabin, F.T. Solmitz, $\pi\pi$ Partial wave analysis from reactions $\pi^+p \rightarrow \pi^+\pi^-\Delta^{++}$ and $\pi^+p \rightarrow K^+K^-\Delta^{++}$ at 7.1-GeV/c, Phys. Rev. D7 (1973) 1279, http://dx.doi.org/10.1103/PhysRevD.7.1279.

[151] P. Estabrooks, A.D. Martin, $\pi\pi$ Phase shift analysis below the $K\bar{K}$ threshold, Nuclear Phys. B79 (1974) 301–316, http://dx.doi.org/10.1016/0550-3213(74)90488-X.

[152] B. Hyams, et al., $\pi\pi$ Phase shift analysis from 600-MeV to 1900-MeV, Nuclear Phys. B64 (1973) 134–162, http://dx.doi.org/10.1016/0550-3213(73)90618-4.

[153] H. Nussenzveig, Causality and Dispersion Relations, in: Mathematics in science and engineering, Academic Press, 1972, URL https://books.google.com/books?id=OvZ0vgAACAAJ.

[154] R.J. Eden, P.V. Landshoff, D.I. Olive, J.C. Polkinghorne, The Analytic S-Matrix, Cambridge Univ. Press, Cambridge, 1966.

[155] S. Mandelstam, Determination of the pion - nucleon scattering amplitude from dispersion relations and unitarity. General theory, Phys. Rev. 112 (1958) 1344–1360, http://dx.doi.org/10.1103/PhysRev.112.1344.

[156] S. Mandelstam, Dispersion relations in strong-coupling physics, Rep. Progr. Phys. 25 (1) (1962) 99–162, http://dx.doi.org/10.1088/0034-4885/25/1/304.

[157] M. Froissart, Asymptotic behavior and subtractions in the Mandelstam representation, Phys. Rev. 123 (1961) 1053–1057, http://dx.doi.org/10.1103/PhysRev.123.1053.

[158] S.L. Adler, Consistency conditions on the strong interactions implied by a partially conserved axial vector current, Phys. Rev. 137 (1965) B1022–B1033, http://dx.doi.org/10.1103/PhysRev.137.B1022, [140(1964)].

[159] J. Gasser, G. Wanders, One channel Roy equations revisited, Eur. Phys. J. C10 (1999) 159–173, http://dx.doi.org/10.1007/s100529900086, arXiv:hep-ph/9903443.

[160] A. Nehme, P. Talavera, Isospin breaking corrections to low-energy πK scattering, Phys. Rev. D 65 (2002) 054023, http://dx.doi.org/10.1103/PhysRevD.65.054023, arXiv:hep-ph/0107299.

[161] A. Nehme, Isospin breaking in low-energy charged pion and kaon elastic scattering, Eur. Phys. J. C 23 (2002) 707–718, http://dx.doi.org/10.1007/s100520200902, arXiv:hep-ph/0111212.

[162] B. Kubis, U.-G. Meißner, Isospin violation in low-energy charged pion kaon scattering, Phys. Lett. B 529 (2002) 69–76, http://dx.doi.org/10.1016/S0370-2693(02)01192-9, arXiv:hep-ph/0112154.

[163] B. Kubis, U.-G. Meißner, Isospin violation in pion kaon scattering, Nuclear Phys. A 699 (2002) 709–731, http://dx.doi.org/10.1016/S0375-9474(01)01318-5, arXiv:hep-ph/0107199.

[164] G.E. Hite, F. Steiner, New dispersion relations and their application to partial-wave amplitudes, Nuovo Cim. A18 (1973) 237–270, http://dx.doi.org/10.1007/BF02722827.

[165] M.R. Pennington, S.D. Protopopescu, How Roy's equations resolve the up-down ambiguity and reproduce the S^* resonance, Phys. Rev. D7 (1973) 2591–2596, http://dx.doi.org/10.1103/PhysRevD.7.2591.

[166] J.L. Basdevant, J.C. Le Guillou, H. Navelet, Crossing and physical partial-wave amplitudes, Nuovo Cim. A7 (1972) 363–396, http://dx.doi.org/10.1007/BF02832836.

[167] J.L. Basdevant, C.D. Froggatt, J.L. Petersen, $\pi\pi$ Phenomenology below 1100 MeV, Phys. Lett. 41B (1972) 178–182, http://dx.doi.org/10.1016/0370-2693(72)90456-X.

[168] J.L. Basdevant, C.D. Froggatt, J.L. Petersen, Role of crossing and the ρ meson in low energy $\pi\pi$ amplitudes, Phys. Lett. 41B (1972) 173–177, http://dx.doi.org/10.1016/0370-2693(72)90455-8.

[169] J.L. Basdevant, C.D. Froggatt, J.L. Petersen, Construction of phenomenological $\pi\pi$ amplitudes, Nuclear Phys. B72 (1974) 413–453, http://dx.doi.org/10.1016/0550-3213(74)90152-7.

[170] C. Froggatt, J. Petersen, Phase shift analysis of $\pi^+\pi^-$ scattering between 1.0-GeV and 1.8-GeV based on fixed momentum transfer analyticity. 2, Nuclear Phys. B 129 (1977) 89–110, http://dx.doi.org/10.1016/0550-3213(77)90021-9.

[171] F.P. Palou, F.J. Ynduráin, Low-energy $\pi\pi$ scattering parameters, Nuovo Cim. A19 (1974) 245–254, http://dx.doi.org/10.1007/BF02801850.

[172] N. Hedegaard-Jensen, A phenomenological investigation of $\pi\pi \to KK$ partial-wave amplitudes from hyperbolic dispersion relations, Nuclear Phys. B 77 (1974) 173–188, http://dx.doi.org/10.1016/0550-3213(74)90311-3.

[173] N.O. Johannesson, J.L. Petersen, Coupled-channel study of the S-wave $\pi\pi \to K\bar{K}$ interaction, Nuclear Phys. B68 (1974) 397–412, http://dx.doi.org/10.1016/0550-3213(74)90320-4.

[174] F.P. Palou, J.L. Sanchez Gomez, F.J. Ynduráin, Low-energy parameters for scattering of pions and kaons, Z. Phys. A274 (1975) 161–164, http://dx.doi.org/10.1007/BF01408468.

[175] B. Bonnier, N. Johannesson, Upper bound of $I = 0$ exchange in $K\pi$ scattering, Nuclear Phys. B 101 (1975) 72–76, http://dx.doi.org/10.1016/0550-3213(75)90294-1.

[176] N. Johannesson, G. Nilsson, An analysis of low-energy πK scattering, Nuovo Cim. A43 (1978) 376, http://dx.doi.org/10.1007/BF02730436.

[177] N. Johannesson, L. Sollin, A soluble realistic model for low-energy πK scattering, Nuovo Cimento A 43 (1978) 389, http://dx.doi.org/10.1007/BF02730437.

[178] S. Descotes-Genon, N.H. Fuchs, L. Girlanda, J. Stern, Analysis and interpretation of new low-energy $\pi\pi$ scattering data, Eur. Phys. J. C24 (2002) 469–483, http://dx.doi.org/10.1007/s10052-002-0965-3, arXiv:hep-ph/0112088.

[179] R. Kaminski, L. Lesniak, B. Loiseau, Elimination of ambiguities in $\pi\pi$ phase shifts using crossing symmetry, Phys. Lett. B551 (2003) 241–248, http://dx.doi.org/10.1016/S0370-2693(02)03021-6, arXiv:hep-ph/0210334.

[180] R. Kaminski, R. García-Martín, P. Grynkiewicz, J.R. Peláez, F.J. Ynduráin, New dispersion relations in the description of $\pi\pi$ scattering amplitudes, in: Proceedings, 10th International Workshop on Meson Production, Properties and Interaction (MESON 2008): Cracow, Poland, June 6-10, 2008, Internat. J. Modern Phys. A24 (2009) 402–409, http://dx.doi.org/10.1142/S0217751X09043730, arXiv:0809.4766.

[181] R. Kaminski, Dispersion relations with crossing symmetry for $\pi\pi$ D- and F-wave amplitudes, Phys. Rev. D83 (2011) 076008, http://dx.doi.org/10.1103/PhysRevD.83.076008, arXiv:1103.0882.

[182] I. Caprini, G. Colangelo, H. Leutwyler, Regge analysis of the $\pi\pi$ scattering amplitude, Eur. Phys. J. C72 (2012) 1860, http://dx.doi.org/10.1140/epjc/s10052-012-1860-1, arXiv:1111.7160.

[183] J. Nebreda, J.R. Peláez, G. Ríos, Determination of SU(2) chiral perturbation theory low energy constants from a precise description of pion-pion scattering threshold parameters, Phys. Rev. D88 (2013) 054001, http://dx.doi.org/10.1103/PhysRevD.88.054001, arXiv:1205.4129.

[184] P. Byd˜zovský, R. Kamiński, V. Nazari, Dispersive analysis of the S-, P-, D-, and F-wave $\pi\pi$ amplitudes, Phys. Rev. D94 (11) (2016) 116013, http://dx.doi.org/10.1103/PhysRevD.94.116013, arXiv:1611.10070.

[185] M. Albaladejo, N. Sherrill, C. Fernández-Ramírez, A. Jackura, V. Mathieu, M. Mikhasenko, J. Nys, A. Pilloni, A.P. Szczepaniak, Khuri-Treiman equations for $\pi\pi$ scattering, Eur. Phys. J. C78 (7) (2018) 574, http://dx.doi.org/10.1140/epjc/s10052-018-6045-0, arXiv:1803.06027.

[186] I. Caprini, G. Colangelo, H. Leutwyler, Mass and width of the lowest resonance in QCD, Phys. Rev. Lett. 96 (2006) 132001, http://dx.doi.org/10.1103/PhysRevLett.96.132001, arXiv:hep-ph/0512364.

[187] R. García-Martín, R. Kaminski, J.R. Peláez, J. Ruiz de Elvira, Precise determination of the $f_0(600)$ and $f_0(980)$ pole parameters from a dispersive data analysis, Phys. Rev. Lett. 107 (2011) 072001, http://dx.doi.org/10.1103/PhysRevLett.107.072001, arXiv:1107.1635.

[188] C. Ditsche, M. Hoferichter, B. Kubis, U.G. Meißner, Roy-Steiner equations for pion-nucleon scattering, J. High Energy Phys. 06 (2012) 043, http://dx.doi.org/10.1007/JHEP06(2012)043, arXiv:1203.4758.

[189] J. Gasser, H. Leutwyler, M. Locher, M. Sainio, Extracting the pion-nucleon sigma-term from data, Phys. Lett. B 213 (1988) 85–90, http://dx.doi.org/10.1016/0370-2693(88)91052-0.

[190] J. Gasser, H. Leutwyler, M. Sainio, Sigma term update, Phys. Lett. B 253 (1991) 252–259, http://dx.doi.org/10.1016/0370-2693(91)91393-A.

[191] J. Gasser, H. Leutwyler, M. Sainio, Form-factor of the sigma term, Phys. Lett. B 253 (1991) 260–264, http://dx.doi.org/10.1016/0370-2693(91)91394-B.

[192] M. Hoferichter, J. Ruiz de Elvira, B. Kubis, U.-G. Meißner, High-precision determination of the Pion-Nucleon σ term from Roy-Steiner equations, Phys. Rev. Lett. 115 (2015) 092301, http://dx.doi.org/10.1103/PhysRevLett.115.092301, arXiv:1506.04142.

[193] M. Hoferichter, J. Ruiz de Elvira, B. Kubis, U.-G. Meißner, Remarks on the pion–nucleon σ-term, Phys. Lett. B 760 (2016) 74–78, http://dx.doi.org/10.1016/j.physletb.2016.06.038, arXiv:1602.07688.

[194] J. Ruiz de Elvira, M. Hoferichter, B. Kubis, U.-G. Meißner, Extracting the σ-term from low-energy pion-nucleon scattering, J. Phys. G 45 (2) (2018) 024001, http://dx.doi.org/10.1088/1361-6471/aa9422, arXiv:1706.01465.

[195] M. Hoferichter, J. Ruiz de Elvira, B. Kubis, U.-G. Meißner, Matching pion-nucleon Roy-Steiner equations to chiral perturbation theory, Phys. Rev. Lett. 115 (19) (2015) 192301, http://dx.doi.org/10.1103/PhysRevLett.115.192301, arXiv:1507.07552.

[196] D. Siemens, J. Ruiz de Elvira, E. Epelbaum, M. Hoferichter, H. Krebs, B. Kubis, U.G. Meißner, Reconciling threshold and subthreshold expansions for pion–nucleon scattering, Phys. Lett. B 770 (2017) 27–34, http://dx.doi.org/10.1016/j.physletb.2017.04.039, arXiv:1610.08978.

[197] M. Hoferichter, B. Kubis, J. Ruiz de Elvira, H.W. Hammer, U.G. Meißner, On the $\pi\pi$ continuum in the nucleon form factors and the proton radius puzzle, Eur. Phys. J. A 52 (11) (2016) 331, http://dx.doi.org/10.1140/epja/i2016-16331-7, arXiv:1609.06722.

[198] M. Hoferichter, B. Kubis, J. Ruiz de Elvira, P. Stoffer, Nucleon matrix elements of the antisymmetric quark tensor, Phys. Rev. Lett. 122 (12) (2019) 122001, http://dx.doi.org/10.1103/PhysRevLett.122.122001, arXiv:1811.11181;   Phys. Rev. Lett. 124 (2020) 199901, Erratum.

[199] G. Colangelo, M. Hoferichter, P. Stoffer, Two-pion contribution to hadronic vacuum polarization, J. High Energy Phys. 02 (2019) 006, http://dx.doi.org/10.1007/JHEP02(2019)006, arXiv:1810.00007.

[200] R. García-Martín, B. Moussallam, MO Analysis of the high statistics belle results on $\gamma\gamma \to \pi^+\pi^-, \pi^0\pi^0$ with chiral constraints, Eur. Phys. J. C 70 (2010) 155–175, http://dx.doi.org/10.1140/epjc/s10052-010-1471-7, arXiv:1006.5373.

[201] M. Hoferichter, D.R. Phillips, C. Schat, Roy-Steiner equations for $\gamma\gamma \to \pi\pi$, Eur. Phys. J. C71 (2011) 1743, http://dx.doi.org/10.1140/epjc/s10052-011-1743-x, arXiv:1106.4147.

[202] B. Moussallam, Unified dispersive approach to real and virtual photon-photon scattering at low energy, Eur. Phys. J. C73 (2013) 2539, http://dx.doi.org/10.1140/epjc/s10052-013-2539-y, arXiv:1305.3143.

[203] I. Danilkin, M. Vanderhaeghen, Dispersive analysis of the $\gamma\gamma^* \to \pi\pi$ process, Phys. Lett. B 789 (2019) 366–372, http://dx.doi.org/10.1016/j.physletb.2018.12.047, arXiv:1810.03669.

[204] M. Hoferichter, P. Stoffer, Dispersion relations for $\gamma^*\gamma^* \to \pi\pi$: helicity amplitudes, subtractions, and anomalous thresholds, J. High Energy Phys. 07 (2019) 073, http://dx.doi.org/10.1007/JHEP07(2019)073, arXiv:1905.13198.

[205] H. Nielsen, G.C. Oades, A phenomenological investigation of pion-kaon scattering, Nuclear Phys. B55 (1973) 301–321, http://dx.doi.org/10.1016/0550-3213(73)90423-9.

[206] B. Ananthanarayan, P. Büttiker, Comparison of pion kaon scattering in SU(3) chiral perturbation theory and dispersion relations, Eur. Phys. J. C19 (2001) 517–528, http://dx.doi.org/10.1007/s100520100629, arXiv:hep-ph/0012023.

[207] B. Ananthanarayan, P. Büttiker, B. Moussallam, πK Sum rules and the SU(3) chiral expansion, Eur. Phys. J. C22 (2001) 133–148, http://dx.doi.org/10.1007/s100520100766, arXiv:hep-ph/0106230.

[208] H.Q. Zheng, Z.Y. Zhou, G.Y. Qin, Z. Xiao, J.J. Wang, N. Wu, The κ resonance in s-wave πK scatterings, Nuclear Phys. A733 (2004) 235–261, http://dx.doi.org/10.1016/j.nuclphysa.2003.12.021, arXiv:hep-ph/0310293.

[209] M. Albaladejo, J.T. Daub, C. Hanhart, B. Kubis, B. Moussallam, How to employ $\bar{B}_d^0 \to J/\psi\left(\pi\eta, \bar{K}K\right)$ decays to extract information on $\pi\eta$ scattering, J. High Energy Phys. 04 (2017) 010, http://dx.doi.org/10.1007/JHEP04(2017)010, arXiv:1611.03502.

[210] I. Danilkin, O. Deineka, M. Vanderhaeghen, Theoretical analysis of the $\gamma\gamma \to \pi^0\eta$ process, Phys. Rev. D 96 (11) (2017) 114018, http://dx.doi.org/10.1103/PhysRevD.96.114018, arXiv:1709.08595.

[211] S. Ropertz, C. Hanhart, B. Kubis, A new parametrization for the scalar pion form factors, Eur. Phys. J. C78 (12) (2018) 1000, http://dx.doi.org/10.1140/epjc/s10052-018-6416-6, arXiv:1809.06867.

[212] I. Danilkin, O. Deineka, M. Vanderhaeghen, Dispersive analysis of the $\gamma^*\gamma^* \to \pi\pi$ process, Phys. Rev. D 101 (5) (2020) 054008, http://dx.doi.org/10.1103/PhysRevD.101.054008, arXiv:1909.04158.

[213] O. Deineka, I. Danilkin, M. Vanderhaeghen, On the importance of left-hand cuts in the $\gamma\gamma^* \to \pi\pi$ process, Acta Phys. Polon. B 50 (2019) 1901–1910, http://dx.doi.org/10.5506/APhysPolB.50.1901.

[214] A. Dobado, J. Peláez, A global fit of $\pi\pi$ and πK elastic scattering in ChPT with dispersion relations, Phys. Rev. D 47 (1993) 4883–4888, http://dx.doi.org/10.1103/PhysRevD.47.4883, arXiv:hep-ph/9301276.

[215] A. Dobado, J.R. Peláez, The inverse amplitude method in chiral perturbation theory, Phys. Rev. D56 (1997) 3057–3073, http://dx.doi.org/10.1103/PhysRevD.56.3057, arXiv:hep-ph/9604416.

[216] M. Jamin, J.A. Oller, A. Pich, S-Wave $K\pi$ scattering in chiral perturbation theory with resonances, Nuclear Phys. B 587 (2000) 331–362, http://dx.doi.org/10.1016/S0550-3213(00)00479-X, arXiv:hep-ph/0006045.

[217] A. Gomez Nicola, J. Peláez, G. Ríos, The inverse amplitude method and adler zeros, Phys. Rev. D 77 (2008) 056006, http://dx.doi.org/10.1103/PhysRevD.77.056006, arXiv:0712.2763.

[218] D.-L. Yao, L.-Y. Dai, H.-Q. Zheng, Z.-Y. Zhou, A review on partial-wave dynamics with chiral effective field theory and dispersion relation, 2020, arXiv:2009.13495.

[219] J. Nieves, E. Ruiz Arriola, Bethe-salpeter approach for unitarized chiral perturbation theory, Nuclear Phys. A679 (2000) 57–117, http://dx.doi.org/10.1016/S0375-9474(00)00321-3, arXiv:hep-ph/9907469.

[220] G.F. Chew, S. Mandelstam, Theory of low-energy pion pion interactions, Phys. Rev. 119 (1960) 467–477, http://dx.doi.org/10.1103/PhysRev.119.467.

[221] J.A. Oller, A Brief Introduction to Dispersion Relations, in: SpringerBriefs in Physics, vol. 9783030135829, Springer, 2019, http://dx.doi.org/10.1007/978-3-030-13582-9.

[222] J.R. Peláez, A. Rodas, J.R. de Elvira, Precision dispersive approaches versus unitarized chiral perturbation theory for the lightest scalar resonances $\sigma/f_0(500)$ and $\kappa/K_0^*(700)$, Eur. Phys. J. ST 230 (6) (2021) 1539–1574, http://dx.doi.org/10.1140/epjs/s11734-021-00142-9, arXiv:2101.06506.

[223] J.P. Ader, C. Meyers, B. Bonnier, General features of low energy $K\pi$ scattering from physical region method, Phys. Lett. 46B (1973) 403–406, http://dx.doi.org/10.1016/0370-2693(73)90152-4.

[224] R. Omnès, On the solution of certain singular integral equations of quantum field theory, Nuovo Cim. 8 (1958) 316–326, http://dx.doi.org/10.1007/BF02747746.

[225] N. Muskhelishvili, Singular Integral Equations, Springer, Dordrecht, 1953, http://dx.doi.org/10.1007/978-94-009-9994-7.

[226] I. Caprini, Finding the sigma pole by analytic extrapolation of $\pi\pi$ scattering data, Phys. Rev. D77 (2008) 114019, http://dx.doi.org/10.1103/PhysRevD.77.114019, arXiv:0804.3504.

[227] S. Cherry, M. Pennington, There is no $\kappa(900)$, Nuclear Phys. A 688 (2001) 823–841, http://dx.doi.org/10.1016/S0375-9474(00)00587-X, arXiv:hep-ph/0005208.

[228] B. Moussallam, Analyticity constraints on the strangeness changing vector current and applications to $\tau \to K\pi\nu_\tau, \tau \to K\pi\pi\nu_\tau$, Eur. Phys. J. C 53 (2008) 401–412, http://dx.doi.org/10.1140/epjc/s10052-007-0464-7, arXiv:0710.0548.

[229] R. Navarro Perez, J.E. Amaro, E. Ruiz Arriola, Statistical error analysis for phenomenological nucleon-nucleon potentials, Phys. Rev. C89 (6) (2014) 064006, http://dx.doi.org/10.1103/PhysRevC.89.064006, arXiv:1404.0314.

[230] R. Navarro Pérez, E. Ruiz Arriola, J. Ruiz de Elvira, Self-consistent statistical error analysis for $\pi\pi$ scattering, Phys. Rev. D91 (2015) 074014, http://dx.doi.org/10.1103/PhysRevD.91.074014, arXiv:1502.03361.

[231] V. Bernard, N. Kaiser, U.G. Meißner, πK Scattering in chiral perturbation theory to one loop, Nuclear Phys. B 357 (1991) 129–152, http://dx.doi.org/10.1016/0550-3213(91)90461-6.

[232] J. Link, et al., FOCUS Collaboration, Hadronic mass spectrum analysis of $D^+ \to K^-\pi^+\mu^+\nu$ decay and measurement of the $K^*(892)^0$ mass and width, Phys. Lett. B 621 (2005) 72–80, http://dx.doi.org/10.1016/j.physletb.2005.06.062, arXiv:hep-ex/0503043.

[233] P. Zyla, et al., Particle Data Group Collaboration, Review of particle physics, Prog. Theor. Exp. Phys. 2020 (8) (2020) 083C01, http://dx.doi.org/10.1093/ptep/ptaa104.

[234] J.H. Kühn, A. Santamaria, Tau decays to pions, Z. Phys. C 48 (1990) 445–452, http://dx.doi.org/10.1007/BF01572024.

[235] S. Anderson, et al., CLEO Collaboration, Hadronic structure in the decay $\tau^- \to \pi^-\pi^0\nu_\tau$, Phys. Rev. D61 (2000) 112002, http://dx.doi.org/10.1103/PhysRevD.61.112002, arXiv:hep-ex/9910046.

[236] A. Etkin, et al., Evidence for two new 0^{++} mesons and a possible scalar decuplet, Phys. Rev. D25 (1982) 2446, http://dx.doi.org/10.1103/PhysRevD.25.2446.

[237] P.D.B. Collins, An Introduction to Regge Theory and High-Energy Physics, in: Cambridge Monographs on Mathematical Physics, Cambridge Univ. Press, Cambridge, UK, 2009, URL http://www-spires.fnal.gov/spires/find/books/www?cl=QC793.3.R4C695.

[238] S. Donnachie, H.G. Dosch, O. Nachtmann, P. Landshoff, Pomeron physics and QCD, in: Cambridge Monographs on Particle Physics, Nuclear Physics and Cosmology, Cambridge University Press, 2005, URL https://books.google.it/books?id=WpGHPwAACAAJ.

[239] V.N. Gribov, in: Y.L. Dokshitzer, J. Nyiri (Eds.), Strong Interactions of Hadrons At High Energies: Gribov Lectures on Theoretical Physics, Cambridge University Press, 2012, URL http://cambridge.org/catalogue/catalogue.asp?isbn=9780521856096.

[240] C. Lovelace, A novel application of Regge trajectories, Phys. Lett. 28B (1968) 264–268, http://dx.doi.org/10.1016/0370-2693(68)90255-4.

[241] J.A. Shapiro, Narrow-resonance model with Regge behavior for $\pi\pi$ scattering, Phys. Rev. 179 (1969) 1345–1353, http://dx.doi.org/10.1103/PhysRev.179.1345.

[242] K. Kawarabayashi, S. Kitakado, H. Yabuki, Veneziano's model and nonet scheme for 1^- and 2^+ mesons, Phys. Lett. 28B (1969) 432–435, http://dx.doi.org/10.1016/0370-2693(69)90344-X.

[243] N. Achasov, S. Devyanin, G. Shestakov, The $S^* - \delta^0$ mixing as a threshold phenomenon, Phys. Lett. B 88 (1979) 367–371, http://dx.doi.org/10.1016/0370-2693(79)90488-X.

[244] C. Hanhart, B. Kubis, J.R. Peláez, Investigation of $a_0 - f_0$ mixing, Phys. Rev. D 76 (2007) 074028, http://dx.doi.org/10.1103/PhysRevD.76.074028, arXiv:0707.0262.

[245] P. Büttiker, S. Descotes-Genon, B. Moussallam, πK Scattering inputs to ChPT, in: Quantum Chromodynamics. Proceedings, 10th High-Energy International Conference, QCD'03, Montpellier, France, July 2-9, 2003, Nuclear Phys. Proc. Suppl. 133 (2004) 223–226, http://dx.doi.org/10.1016/j.nuclphysbps.2004.04.169, arXiv:hep-ph/0310045, [223(2003)].

[246] D. Morgan, M. Pennington, New data on the $K\bar{K}$ threshold region and the nature of the $f_0(S^*)$, Phys. Rev. D 48 (1993) 1185–1204, http://dx.doi.org/10.1103/PhysRevD.48.1185.

[247] P.J. Davis, S.E. Derenzo, S.M. Flatte, M. Alston-Garnjost, G.R. Lynch, F.T. Solmitz, Unsplit K^*'S, Phys. Rev. Lett. 23 (1969) 1071, http://dx.doi.org/10.1103/PhysRevLett.23.1071.

[248] M. Aguilar-Benitez, R. Eisner, J. Kinson, Properties of the $K^*(890)$ and $K^*(1420)$ in K^-p interactions at 3.9 and 4.6 Gev/c, Phys. Rev. D 4 (1971) 2583–2628, http://dx.doi.org/10.1103/PhysRevD.4.2583.

[249] D. Cords, et al., $K^*(890)$ Production in the charge-exchange reaction $K^+n \to K^+\pi^-p$ at 9 Gev/c, Phys. Rev. D 4 (1971) 1974–1978, http://dx.doi.org/10.1103/PhysRevD.4.1974.

[250] N. McCubbin, L. Lyons, The reaction $K^-p \to K^-\pi^+n$ at 3.6-GeV/c, Nuclear Phys. B 86 (1975) 13–62, http://dx.doi.org/10.1016/0550-3213(75)90073-5.

[251] K. Hendrickx, P. Cornet, F. Grard, V. Henri, R. Windmolders, D. Vignaud, D. Burlaud, S. Tavernier, K^* Production in $K^+n \to K\pi n$ at 8.25-GeV/c, Nuclear Phys. B 112 (1976) 189–212, http://dx.doi.org/10.1016/0550-3213(76)90530-7.

[252] R. Baldi, T. Bohringer, P. Dorsaz, V. Hungerbuhler, M. Kienzle-Focacci, M. Martin, A. Mermoud, C. Nef, P. Siegrist, Observation of the $K^*(1780)$ in the reaction $K^+p \to K_S^0\pi^+p$ at 10-GeV/c, Phys. Lett. B 63 (1976) 344–348, http://dx.doi.org/10.1016/0370-2693(76)90279-3.

[253] S. Chung, et al., Study of $K^*(1780)$ in the reaction $K^-p \to K^-\pi^+n$ at 6-GeV/c, Phys. Rev. Lett. 40 (1978) 355–358, http://dx.doi.org/10.1103/PhysRevLett.40.355.

[254] W. Cleland, et al., Study of the reactions $K^\pm p \to K_S^0\pi^\pm p$ at 30-Gev/c and 50-Gev/c: Description of the apparatus and amplitude analysis of the $K_S^0\pi$ system, Nuclear Phys. B 208 (1982) 189–227, http://dx.doi.org/10.1016/0550-3213(82)90114-6.

[255] M. Ablikim, et al., BES Collaboration, Partial wave analysis of $\chi_{c0} \to \pi^+\pi^-K^+K^-$, Phys. Rev. D 72 (2005) 092002, http://dx.doi.org/10.1103/PhysRevD.72.092002, arXiv:hep-ex/0508050.

[256] J. Lees, et al., BaBar Collaboration, Dalitz plot analysis of $\eta_c \to K^+K^-\eta$ and $\eta_c \to K^+K^-\pi^0$ in two-photon interactions, Phys. Rev. D 89 (11) (2014) 112004, http://dx.doi.org/10.1103/PhysRevD.89.112004, arXiv:1403.7051.

[257] Z. Zhou, H. Zheng, An improved study of the kappa resonance and the non-exotic s wave πK scatterings up to $\sqrt{s} = 2.1$GeV of LASS data, Nuclear Phys. A 775 (2006) 212–223, http://dx.doi.org/10.1016/j.nuclphysa.2006.06.170, arXiv:hep-ph/0603062.

[258] D.V. Bugg, Comments on the σ and κ, Phys. Lett. B572 (2003) 1–7, http://dx.doi.org/10.1016/j.physletb.2004.06.050; Phys. Lett. B 595 (2004) 556, Erratum.

[259] A. Anisovich, A. Sarantsev, K-Matrix analysis of the $K\pi$ S-wave in the mass region 900-MeV - 2100-MeV and nonet classification of scalar $q\bar{q}$ states, Phys. Lett. B 413 (1997) 137–146, http://dx.doi.org/10.1016/S0370-2693(97)01089-7, arXiv:hep-ph/9705401.

[260] D. Barberis, et al., WA102 Collaboration, A study of the centrally produced $K^*(892)\bar{K}^*(892)$ and $\phi\omega$ systems in pp interactions at 450-GeV/c, Phys. Lett. B 436 (1998) 204–210, http://dx.doi.org/10.1016/S0370-2693(98)00962-9, arXiv:hep-ex/9807021.

[261] D.R. Boito, R. Escribano, M. Jamin, $K\pi$ Vector form-factor, dispersive constraints and $\tau \to \nu_\tau K\pi$ decays, Eur. Phys. J. C 59 (2009) 821–829, http://dx.doi.org/10.1140/epjc/s10052-008-0834-9, arXiv:0807.4883.

[262] M. Baubillier, et al., Birmingham-CERN-Glasgow-Michigan State-Paris Collaboration, A partial-wave analysis of the $K\pi\pi$ system produced in the reaction $K^-p \to \bar{K}^0\pi^+\pi^-n$ at 8.25-GeV/c, Nuclear Phys. B 202 (1982) 21–42, http://dx.doi.org/10.1016/0550-3213(82)90219-X.

[263] F.P. Bird, Cherenkov ring imaging and spectroscopy of charged K^*-charged K^* interactions at 11-GeV/c, 1988.

[264] A. Etkin, et al., Measurement and partial-wave analysis of the reaction $K^-p \to K_S^0\pi^+\pi^-n$ at 6-GeV/c, Phys. Rev. D 22 (1980) 42–60, http://dx.doi.org/10.1103/PhysRevD.22.42.

[265] B. Aubert, et al., Babar Collaboration, The $e^+e^- \to K^+K^-\pi^+\pi^-$, $K^+K^-\pi^0\pi^0$ and $K^+K^-K^+K^-$ cross-sections measured with initial-state radiation, Phys. Rev. D76 (2007) 012008, http://dx.doi.org/10.1103/PhysRevD.76.012008, arXiv:0704.0630.

[266] E. Konigs, et al., A partial wave analysis of the $(\bar{K}^0\pi^+\pi^-)$ system produced in $K^-p \to \bar{K}^0\pi^+\pi^-n$ at 10-GeV/c, Phys. Lett. B 74 (1978) 282–286, http://dx.doi.org/10.1016/0370-2693(78)90573-7.

[267] Z. Fu, K. Fu, Lattice QCD study on $K^*(892)$ meson decay width, Phys. Rev. D 86 (2012) 094507, http://dx.doi.org/10.1103/PhysRevD.86.094507, arXiv:1209.0350.

[268] C. Lang, L. Leskovec, D. Mohler, S. Prelovsek, $K\pi$ Scattering for isospin 1/2 and 3/2 in lattice QCD, Phys. Rev. D 86 (2012) 054508, http://dx.doi.org/10.1103/PhysRevD.86.054508, arXiv:1207.3204.

[269] G.S. Bali, S. Collins, A. Cox, G. Donald, M. Göckeler, C. Lang, A. Schäfer, ρ And K^* resonances on the lattice at nearly physical quark masses and $N_f = 2$, Phys. Rev. D 93 (5) (2016) 054509, http://dx.doi.org/10.1103/PhysRevD.93.054509, arXiv:1512.08678.

[270] M. Lüscher, Two particle states on a torus and their relation to the scattering matrix, Nuclear Phys. B354 (1991) 531–578, http://dx.doi.org/10.1016/0550-3213(91)90366-6.

[271] K. Rummukainen, S.A. Gottlieb, Resonance scattering phase shifts on a nonrest frame lattice, Nuclear Phys. B 450 (1995) 397–436, http://dx.doi.org/10.1016/0550-3213(95)00313-H, arXiv:hep-lat/9503028.

[272] P.F. Bedaque, Aharonov-bohm effect and nucleon nucleon phase shifts on the lattice, Phys. Lett. B 593 (2004) 82–88, http://dx.doi.org/10.1016/j.physletb.2004.04.045, arXiv:nucl-th/0402051.

[273] C. Kim, C. Sachrajda, S.R. Sharpe, Finite-volume effects for two-hadron states in moving frames, Nuclear Phys. B 727 (2005) 218–243, http://dx.doi.org/10.1016/j.nuclphysb.2005.08.029, arXiv:hep-lat/0507006.

[274] Z. Fu, Rummukainen-Gottlieb's formula on two-particle system with different mass, Phys. Rev. D 85 (2012) 014506, http://dx.doi.org/10.1103/PhysRevD.85.014506, arXiv:1110.0319.

[275] L. Leskovec, S. Prelovsek, Scattering phase shifts for two particles of different mass and non-zero total momentum in lattice QCD, Phys. Rev. D 85 (2012) 114507, http://dx.doi.org/10.1103/PhysRevD.85.114507, arXiv:1202.2145.

[276] M. Gockeler, R. Horsley, M. Lage, U.-G. Meißner, P. Rakow, A. Rusetsky, G. Schierholz, J. Zanotti, Scattering phases for meson and baryon resonances on general moving-frame lattices, Phys. Rev. D 86 (2012) 094513, http://dx.doi.org/10.1103/PhysRevD.86.094513, arXiv:1206.4141.

[277] S. He, X. Feng, C. Liu, Two particle states and the S-matrix elements in multi-channel scattering, J. High Energy Phys. 07 (2005) 011, http://dx.doi.org/10.1088/1126-6708/2005/07/011, arXiv:hep-lat/0504019.

[278] M. Lage, U.-G. Meißner, A. Rusetsky, A method to measure the antikaon-nucleon scattering length in lattice QCD, Phys. Lett. B 681 (2009) 439–443, http://dx.doi.org/10.1016/j.physletb.2009.10.055, arXiv:0905.0069.

[279] V. Bernard, M. Lage, U.-G. Meißner, A. Rusetsky, Scalar mesons in a finite volume, J. High Energy Phys. 01 (2011) 019, http://dx.doi.org/10.1007/JHEP01(2011)019, arXiv:1010.6018.

[280] M. Döring, U.G. Meißner, E. Oset, A. Rusetsky, Unitarized chiral perturbation theory in a finite volume: scalar meson sector, Eur. Phys. J. A 47 (2011) 139, http://dx.doi.org/10.1140/epja/i2011-11139-7, arXiv:1107.3988.

[281] M. Döring, U.G. Meißner, Finite volume effects in pion-kaon scattering and reconstruction of the $\kappa(800)$ resonance, JHEP 01 (2012) 009, http://dx.doi.org/10.1007/JHEP01(2012)009, arXiv:1111.0616.

[282] D. Agadjanov, U.-G. Meißner, A. Rusetsky, Partial twisting for scalar mesons, J. High Energy Phys. 01 (2014) 103, http://dx.doi.org/10.1007/JHEP01(2014)103, arXiv:1310.7183.

[283] M. Döring, U. Meißner, E. Oset, A. Rusetsky, Scalar mesons moving in a finite volume and the role of partial wave mixing, Eur. Phys. J. A 48 (2012) 114, http://dx.doi.org/10.1140/epja/i2012-12114-6, arXiv:1205.4838.

[284] M.T. Hansen, S.R. Sharpe, Multiple-channel generalization of Lellouch-Luscher formula, Phys. Rev. D 86 (2012) 016007, http://dx.doi.org/10.1103/PhysRevD.86.016007, arXiv:1204.0826.

[285] R.A. Briceno, Z. Davoudi, Moving multichannel systems in a finite volume with application to proton-proton fusion, Phys. Rev. D 88 (9) (2013) 094507, http://dx.doi.org/10.1103/PhysRevD.88.094507, arXiv:1204.1110.

[286] P. Guo, J. Dudek, R. Edwards, A.P. Szczepaniak, Coupled-channel scattering on a torus, Phys. Rev. D88 (1) (2013) 014501, http://dx.doi.org/10.1103/PhysRevD.88.014501, arXiv:1211.0929.

[287] R. Brett, J. Bulava, J. Fallica, A. Hanlon, B. Hörz, C. Morningstar, Determination of s- and p-wave $I = 1/2$ $K\pi$ scattering amplitudes in $N_f = 2+1$ lattice QCD, Nucl. Phys. B 932 (2018) 29–51, http://dx.doi.org/10.1016/j.nuclphysb.2018.05.008, arXiv:1802.03100.

[288] D. Guo, A. Alexandru, R. Molina, M. Mai, M. Döring, Extraction of isoscalar $\pi\pi$ phase-shifts from lattice QCD, Phys. Rev. D 98 (1) (2018) 014507, http://dx.doi.org/10.1103/PhysRevD.98.014507, arXiv:1803.02897.

[289] S. Prelovsek, T. Draper, C.B. Lang, M. Limmer, K.-F. Liu, N. Mathur, D. Mohler, Lattice study of light scalar tetraquarks with $I = 0, 2, 1/2, 3/2$: Are σ and κ tetraquarks? Phys. Rev. D 82 (2010) 094507, http://dx.doi.org/10.1103/PhysRevD.82.094507, arXiv:1005.0948.

[290] Z.-W. Fu, Lattice calculation of κ meson, Chin. Phys. C 36 (2012) 489–497, http://dx.doi.org/10.1088/1674-1137/36/6/003, arXiv:1111.1835.

[291] Z. Fu, The preliminary lattice QCD calculation of κ meson decay width, J. High Energy Phys. 01 (2012) 017, http://dx.doi.org/10.1007/JHEP01(2012)017, arXiv:1110.5975.

[292] C. Alexandrou, J.O. Daldrop, M. Dalla Brida, M. Gravina, L. Scorzato, et al., Lattice investigation of the scalar mesons $a_0(980)$ and κ using four-quark operators, J. High Energy Phys. 1304 (2013) 137, http://dx.doi.org/10.1007/JHEP04(2013)137, arXiv:1212.1418.

[293] G. Auberson, L. Epele, G. Mahoux, F. Simao, Rigorous absolute bounds for pion-pion scattering. 1. Solving a first extremum problem, Nuclear Phys. B 73 (1974) 314–338, http://dx.doi.org/10.1016/0550-3213(74)90022-4.

[294] G. Auberson, L. Epele, G. Mahoux, F. Simao, Rigorous absolute bounds for pion-pion scattering. 2. Solving modified Szego-Meiman problems, Ann. Inst. H. Poincare Phys. Theor. 26 (1977) 107–108, [Erratum: Ann.Inst.H.Poincare Phys.Theor. 22, 317–366 (1975)].

[295] G. Auberson, L. Epele, G. Mahoux, F. Simao, Rigorous absolute bounds for pion-pion scattering. 3. Dispersion relations on algebraic manifolds and computation of bounds, Nuclear Phys. B 94 (1975) 311–336, http://dx.doi.org/10.1016/0550-3213(75)90494-0.

[296] G. Mahoux, S.M. Roy, G. Wanders, Physical pion pion partial-wave equations based on three channel crossing symmetry, Nuclear Phys. B70 (1974) 297–316, http://dx.doi.org/10.1016/0550-3213(74)90480-5.

[297] S. Roy, G. Wanders, Partial-wave equations and analyticity domain of pion-pion scattering amplitudes, Nuclear Phys. B 141 (1978) 220–240, http://dx.doi.org/10.1016/0550-3213(78)90507-2.

[298] S. Roy, G. Wanders, Analyticity of pion-pion partial-wave amplitudes and crossing symmetric dispersion relations, Phys. Lett. B 74 (1978) 347–349, http://dx.doi.org/10.1016/0370-2693(78)90674-3.

[299] F.J. Ynduráin, R. García-Martín, J.R. Peláez, Experimental status of the $\pi\pi$ isoscalar S-wave at low energy: $f_0(600)$ pole and scattering length, Phys. Rev. D76 (2007) 074034, http://dx.doi.org/10.1103/PhysRevD.76.074034, arXiv:hep-ph/0701025.

[300] J.A. Oller, Final state interactions in hadronic D decays, Phys. Rev. D71 (2005) 054030, http://dx.doi.org/10.1103/PhysRevD.71.054030, arXiv:hep-ph/0411105.

[301] Z.-H. Guo, J.A. Oller, Probabilistic interpretation of compositeness relation for resonances, Phys. Rev. D93 (9) (2016) 096001, http://dx.doi.org/10.1103/PhysRevD.93.096001, arXiv:1508.06400.

[302] A. Švarc, M. Hadzimehmedovic, H. Osmanovic, J. Stahov, L. Tiator, R.L. Workman, Introducing the Pietarinen expansion method into the single-channel pole extraction problem, Phys. Rev. C88 (3) (2013) 035206, http://dx.doi.org/10.1103/PhysRevC.88.035206, arXiv:1307.4613.

[303] A. ˇSvarc, M. Hadˇzimehmedović, R. Omerović, H. Osmanović, J. Stahov, Poles of Karlsruhe-Helsinki KH80 and KA84 solutions extracted by using the Laurent-Pietarinen method, Phys. Rev. C89 (4) (2014) 045205, http://dx.doi.org/10.1103/PhysRevC.89.045205, arXiv:1401.1947.

[304] A. ˇSvarc, M. Hadˇzimehmedović, H. Osmanović, J. Stahov, R.L. Workman, Pole structure from energy-dependent and single-energy fits to GWU-SAID πN elastic scattering data, Phys. Rev. C91 (1) (2015) 015207, http://dx.doi.org/10.1103/PhysRevC.91.015207, arXiv:1405.6474.

[305] A. Švarc, M. Hadˇzimehmedović, H. Osmanović, J. Stahov, L. Tiator, R.L. Workman, Pole positions and residues from pion photoproduction using the Laurent-Pietarinen expansion method, Phys. Rev. C89 (6) (2014) 065208, http://dx.doi.org/10.1103/PhysRevC.89.065208, arXiv:1404.1544.

[306] A. ˇSvarc, M. Hadˇzimehmedović, H. Osmanović, J. Stahov, L. Tiator, R.L. Workman, Generalization of the model-independent Laurent–Pietarinen single-channel pole-extraction formalism to multiple channels, Phys. Lett. B 755 (2016) 452–455, http://dx.doi.org/10.1016/j.physletb.2016.02.058, arXiv:1512.07403.

[307] L. Schlessinger, Use of analyticity in the calculation of nonrelativistic scattering amplitudes, Phys. Rev. 167 (1968) 1411–1423, http://dx.doi.org/10.1103/PhysRev.167.1411.

[308] R.-A. Tripolt, I. Haritan, J. Wambach, N. Moiseyev, Threshold energies and poles for hadron physical problems by a model-independent universal algorithm, Phys. Lett. B 774 (2017) 411–416, http://dx.doi.org/10.1016/j.physletb.2017.10.001, arXiv:1610.03252.

[309] R.-A. Tripolt, P. Gubler, M. Ulybyshev, L. Von Smekal, Numerical analytic continuation of euclidean data, Comput. Phys. Comm. 237 (2019) 129–142, http://dx.doi.org/10.1016/j.cpc.2018.11.012, arXiv:1801.10348.

[310] D. Binosi, R.-A. Tripolt, Spectral functions of confined particles, Phys. Lett. B 801 (2020) 135171, http://dx.doi.org/10.1016/j.physletb.2019.135171, arXiv:1904.08172.

[311] P. Masjuan, J.J. Sanz-Cillero, Padé approximants and resonance poles, Eur. Phys. J. C73 (2013) 2594, http://dx.doi.org/10.1140/epjc/s10052-013-2594-4, arXiv:1306.6308.

[312] P. Masjuan, J. Ruiz de Elvira, J.J. Sanz-Cillero, Precise determination of resonance pole parameters through Padé approximants, Phys. Rev. D90 (9) (2014) 097901, http://dx.doi.org/10.1103/PhysRevD.90.097901, arXiv:1410.2397.

[313] I. Caprini, P. Masjuan, J. Ruiz de Elvira, J.J. Sanz-Cillero, Uncertainty estimates of the σ-pole determination by Padé approximants, Phys. Rev. D93 (7) (2016) 076004, http://dx.doi.org/10.1103/PhysRevD.93.076004, arXiv:1602.02062.

[314] R.d. Montessus de Ballore, Sur les fractions continues algébriques, Bull. Soci. Math. France 30 (1902) 28–36, http://dx.doi.org/10.24033/bsmf.653.

[315] A.H. Rosenfeld, A. Barbaro-Galtieri, W.J. Podolsky, L.R. Price, P. Soding, C.G. Wohl, M. Roos, W.J. Willis, Data on particles and resonant states, Rev. Modern Phys. 39 (1967) 1–51, http://dx.doi.org/10.1103/RevModPhys.39.1.

[316] R. Jaffe, K. Johnson, Unconventional states of confined quarks and gluons, Phys. Lett. B60 (1976) 201, http://dx.doi.org/10.1016/0370-2693(76)90423-8.

[317] R.L. Jaffe, Multi-quark hadrons. 1. The phenomenology of $Q^2\bar{Q}^2$ mesons, Phys. Rev. D15 (1977) 267, http://dx.doi.org/10.1103/PhysRevD.15.267.

[318] D. Black, A.H. Fariborz, F. Sannino, J. Schechter, Putative light scalar nonet, Phys. Rev. D59 (1999) 074026, http://dx.doi.org/10.1103/PhysRevD.59.074026, arXiv:hep-ph/9808415.

[319] R. Jaffe, Exotica, Phys. Rep. 409 (2005) 1–45, http://dx.doi.org/10.1016/j.physrep.2004.11.005, arXiv:hep-ph/0409065.

[320] F. Giacosa, Mixing of scalar tetraquark and quarkonia states in a chiral approach, Phys. Rev. D 75 (2007) 054007, http://dx.doi.org/10.1103/PhysRevD.75.054007, arXiv:hep-ph/0611388.

[321] D.V. Bugg, An update on the kappa, Phys. Rev. D81 (2010) 014002, http://dx.doi.org/10.1103/PhysRevD.81.014002, arXiv:0906.3992.

[322] D. Bugg, The kappa in $J/\psi \rightarrow K^+\pi^-K^-\pi^+$, Eur. Phys. J. A 25 (2005) 107–114, http://dx.doi.org/10.1140/epja/i2005-10033-3, arXiv:hep-ex/0510026; Eur. Phys. J. A 26 (2005) 151, Erratum.

[323] D. Bugg, The kappa in E791 data for $D \rightarrow K\pi\pi$, Phys. Lett. B 632 (2006) 471–474, http://dx.doi.org/10.1016/j.physletb.2005.11.019, arXiv:hep-ex/0510019.

[324] D. Bugg, Decays of σ, κ, $a_0(980)$ and $f_0(980)$, Eur. Phys. J. C 47 (2006) 57–64, http://dx.doi.org/10.1140/epjc/s2006-02561-3, arXiv:hep-ph/0603089.

[325] M. Lüscher, Signatures of unstable particles in finite volume, Nuclear Phys. B364 (1991) 237–254, http://dx.doi.org/10.1016/0550-3213(91)90584-K.

[326] R.A. Briceño, J.J. Dudek, R.G. Edwards, D.J. Wilson, Isoscalar $\pi\pi$ scattering and the σ meson resonance from QCD, Phys. Rev. Lett. 118 (2) (2017) 022002, http://dx.doi.org/10.1103/PhysRevLett.118.022002, arXiv:1607.05900.

[327] J.R. Peláez, On the nature of light scalar mesons from their large N_c behavior, Phys. Rev. Lett. 92 (2004) 102001, http://dx.doi.org/10.1103/PhysRevLett.92.102001, arXiv:hep-ph/0309292.

[328] E. van Beveren, D. Bugg, F. Kleefeld, G. Rupp, The nature of σ, κ, $a_0(980)$ and $f_0(980)$, Phys. Lett. B 641 (2006) 265–271, http://dx.doi.org/10.1016/j.physletb.2006.08.051, arXiv:hep-ph/0606022.

[329] T. Wolkanowski, M. Sołtysiak, F. Giacosa, $K_0^*(800)$ As a companion pole of $K_0^*(1430)$, Nuclear Phys. B909 (2016) 418–428, http://dx.doi.org/10.1016/j.nuclphysb.2016.05.025, arXiv:1512.01071.

[330] S. Agaev, K. Azizi, H. Sundu, The nonet of the light scalar tetraquarks: The mesons $a_0(980)$ and $K_0^*(800)$, Phys. Lett. B 789 (2019) 405–412, http://dx.doi.org/10.1016/j.physletb.2018.12.059, arXiv:1804.02519.

[331] A.V. Anisovich, V.V. Anisovich, A.V. Sarantsev, Systematics of q anti-q states in the (n, M^2) and (J, M^2) planes, Phys. Rev. D62 (2000) 051502, http://dx.doi.org/10.1103/PhysRevD.62.051502, arXiv:hep-ph/0003113.

[332] P. Masjuan, E. Ruiz Arriola, W. Broniowski, Systematics of radial and angular-momentum Regge trajectories of light non-strange $q\bar{q}$-states, Phys. Rev. D85 (2012) 094006, http://dx.doi.org/10.1103/PhysRevD.85.094006, arXiv:1203.4782.

[333] G. Epstein, Rising meson trajectories, Phys. Rev. 166 (1968) 1633–1637, http://dx.doi.org/10.1103/PhysRev.166.1633.

[334] S.-Y. Chu, G. Epstein, P. Kaus, R.C. Slansky, F. Zachariasen, Crossing-symmetric rising Regge trajectories, Phys. Rev. 175 (1968) 2098–2105, http://dx.doi.org/10.1103/PhysRev.175.2098.

[335] R. Fiore, L.L. Jenkovszky, V. Magas, F. Paccanoni, A. Papa, Analytic model of Regge trajectories, Eur. Phys. J. A 10 (2001) 217–221, http://dx.doi.org/10.1007/s100500170133, arXiv:hep-ph/0011035.

[336] V.N. Gribov, The Theory of Complex Angular Momenta: Gribov Lectures on Theoretical Physics, in: Cambridge Monographs on Mathematical Physics, Cambridge University Press, 2007, http://dx.doi.org/10.1017/CBO9780511534959, URL http://www.cambridge.org/uk/catalogue/catalogue.asp?isbn=0521307848.

[337] R. Fiore, L.L. Jenkovszky, F. Paccanoni, A. Prokudin, Baryonic Regge trajectories with analyticity constraints, Phys. Rev. D 70 (2004) 054003, http://dx.doi.org/10.1103/PhysRevD.70.054003, arXiv:hep-ph/0404021.

[338] C. Fernández-Ramírez, I.V. Danilkin, V. Mathieu, A.P. Szczepaniak, Understanding the nature of $\Lambda(1405)$ through Regge physics, Phys. Rev. D93 (7) (2016) 074015, http://dx.doi.org/10.1103/PhysRevD.93.074015, arXiv:1512.03136.

[339] J.A. Silva-Castro, C. Fernandez-Ramirez, M. Albaladejo, I.V. Danilkin, A. Jackura, V. Mathieu, J. Nys, A. Pilloni, A.P. Szczepaniak, G. Fox, JPAC Collaboration, Regge phenomenology of the N^* and Δ^* poles, Phys. Rev. D99 (3) (2019) 034003, http://dx.doi.org/10.1103/PhysRevD.99.034003, arXiv:1809.01954.

[340] C. Lovelace, D. Masson, Calculation of Regge poles, in: High-Energy Physics. Proceedings, 11th International Conference, ICHEP'62, Geneva, Switzerland, Jul 4-11, 1962, 1962, pp. 510–512.

[341] A.O. Barut, F. Calogero, Singularities in angular momentum of the scattering amplitude for a class of soluble potentials, Phys. Rev. 128 (3) (1962) 1383, http://dx.doi.org/10.1103/PhysRev.128.1383.

[342] A. Ahmadzadeh, P.G. Burke, C. Tate, Regge trajectories for Yukawa potentials, Phys. Rev. 131 (3) (1963) 1315, http://dx.doi.org/10.1103/PhysRev.131.1315.

[343] M. Albaladejo, J.A. Oller, On the size of the σ meson and its nature, Phys. Rev. D86 (2012) 034003, http://dx.doi.org/10.1103/PhysRevD.86.034003, arXiv:1205.6606.

[344] C. Lovelace, D. Masson, Calculation of Regge poles by continued fractions - I, Il Nuovo Cimento (1955-1965) 26 (3) (1962) 472–484, http://dx.doi.org/10.1007/BF02771819.

[345] P. Burke, C. Tate, A program for calculating Regge trajectories in potential scattering, Comput. Phys. Comm. 1 (1969) 97–105, http://dx.doi.org/10.1016/0010-4655(69)90003-4.

[346] J. Schweizer, Decay widths and energy shifts of $\pi\pi$ and πK atoms, Phys. Lett. B 587 (2004) 33–40, http://dx.doi.org/10.1016/j.physletb.2004.03.007, arXiv:hep-ph/0401048.

[347] J. Schweizer, Spectra and decays of $\pi\pi$ and πK atoms, Eur. Phys. J. C 36 (4) (2004) 483–501, http://dx.doi.org/10.1140/epjc/s2004-01959-1, arXiv:hep-ph/0405034.

[348] A. Karabarbounis, G. Shaw, Low-energy $K\pi$ scattering, J. Phys. G6 (1980) 583, http://dx.doi.org/10.1088/0305-4616/6/5/005.

[349] C.B. Lang, W. Porod, Symmetry breaking and the πK amplitudes in the unphysical region, Phys. Rev. D21 (1980) 1295, http://dx.doi.org/10.1103/PhysRevD.21.1295.

[350] T.P. Cheng, R.F. Dashen, Is $SU(2)xSU(2)$ a better symmetry than $SU(3)$? Phys. Rev. Lett. 26 (1971) 594, http://dx.doi.org/10.1103/PhysRevLett.26.594.

[351] L.S. Brown, W. Pardee, R. Peccei, Adler-weisberger theorem reexamined, Phys. Rev. D 4 (1971) 2801–2810, http://dx.doi.org/10.1103/PhysRevD.4.2801.

[352] J.M. Alarcón, Brief history of the pion–nucleon sigma term, Eur. Phys. J. ST 230 (6) (2021) 1609–1622, http://dx.doi.org/10.1140/epjs/s11734-021-00145-6.

[353] R. Koch, A new determination of the πN sigma term using hyperbolic dispersion relations in the (ν^2, t) plane, Z. Phys. C 15 (1982) 161–168, http://dx.doi.org/10.1007/BF01571999.

[354] N. Fettes, U.-G. Meißner, Pion-nucleon scattering in chiral perturbation theory. 2.: Fourth order calculation, Nuclear Phys. A 676 (2000) 311, http://dx.doi.org/10.1016/S0375-9474(00)00199-8, arXiv:hep-ph/0002162.

[355] M. Pavan, I. Strakovsky, R. Workman, R. Arndt, The pion-nucleon sigma term is definitely large: Results from a G.W.U. analysis of pi nucleon scattering data, in: H. Haberzettl, W. Briscoe (Eds.), PiN Newslett. 16 (2002) 110–115, arXiv:hep-ph/0111066.

[356] J. Alarcón, J. Martin Camalich, J. Oller, The chiral representation of the πN scattering amplitude and the pion-nucleon sigma term, Phys. Rev. D 85 (2012) 051503, http://dx.doi.org/10.1103/PhysRevD.85.051503, arXiv:1110.3797.

[357] J. Alarcón, L. Geng, J. Martin Camalich, J. Oller, The strangeness content of the nucleon from effective field theory and phenomenology, Phys. Lett. B 730 (2014) 342–346, http://dx.doi.org/10.1016/j.physletb.2014.01.065, arXiv:1209.2870.

[358] I. Fernando, J. Alarcón, J. Goity, Baryon masses and σ terms in SU(3) BChPT x 1/N_c, Phys. Lett. B 781 (2018) 719–722, http://dx.doi.org/10.1016/j.physletb.2018.04.054, arXiv:1804.03094.

[359] S. Dürr, et al., Lattice computation of the nucleon scalar quark contents at the physical point, Phys. Rev. Lett. 116 (17) (2016) 172001, http://dx.doi.org/10.1103/PhysRevLett.116.172001, arXiv:1510.08013.

[360] Y.-B. Yang, A. Alexandru, T. Draper, J. Liang, K.-F. Liu, xQCD Collaboration, πN And strangeness sigma terms at the physical point with chiral fermions, Phys. Rev. D 94 (5) (2016) 054503, http://dx.doi.org/10.1103/PhysRevD.94.054503, arXiv:1511.09089.

[361] A. Abdel-Rehim, C. Alexandrou, M. Constantinou, K. Hadjiyiannakou, K. Jansen, C. Kallidonis, G. Koutsou, A. Vaquero Aviles-Casco, ETM Collaboration, Direct evaluation of the quark content of nucleons from lattice QCD at the physical point, Phys. Rev. Lett. 116 (25) (2016) 252001, http://dx.doi.org/10.1103/PhysRevLett.116.252001, arXiv:1601.01624.

[362] G.S. Bali, S. Collins, D. Richtmann, A. Schäfer, W. Söldner, A. Sternbeck, RQCD Collaboration, Direct determinations of the nucleon and pion σ terms at nearly physical quark masses, Phys. Rev. D 93 (9) (2016) 094504, http://dx.doi.org/10.1103/PhysRevD.93.094504, arXiv:1603.00827.

[363] S. Borsanyi, Z. Fodor, C. Hoelbling, L. Lellouch, K.K. Szabo, C. Torrero, L. Varnhorst, Ab-initio calculation of the proton and the neutron's scalar couplings for new physics searches, 2020, arXiv:2007.03319.

[364] R. Gupta, S. Park, M. Hoferichter, E. Mereghetti, B. Yoon, T. Bhattacharya, Pion–nucleon sigma term from lattice QCD, Phys. Rev. Lett. 127 (24) (2021) 242002, http://dx.doi.org/10.1103/PhysRevLett.127.242002, arXiv:2105.12095.

[365] J. Gasser, M.E. Sainio, Sigma term physics, in: Physics and Detectors for DAPHNE. Proceedings, 3rd International Workshop, DAPHNE'99, Frascati, Italy, November 16-19, 1999, Frascati Phys. Ser. 16 (1999) 659–668, arXiv:hep-ph/0002283.

[366] M. Frink, B. Kubis, U.-G. Meißner, Analysis of the pion kaon sigma term and related topics, Eur. Phys. J. C25 (2002) 259–276, http://dx.doi.org/10.1007/s10052-002-0975-1, arXiv:hep-ph/0203193.

[367] M. Hoferichter, C. Ditsche, B. Kubis, U.G. Meißner, Dispersive analysis of the scalar form factor of the nucleon, J. High Energy Phys. 06 (2012) 063, http://dx.doi.org/10.1007/JHEP06(2012)063, arXiv:1204.6251.

[368] A. Bazavov, et al., MILC Collaboration, Nonperturbative QCD simulations with 2+1 flavors of improved staggered quarks, Rev. Modern Phys. 82 (2010) 1349–1417, http://dx.doi.org/10.1103/RevModPhys.82.1349, arXiv:0903.3598.

[369] Z. Fodor, C. Hoelbling, Light hadron masses from lattice QCD, Rev. Modern Phys. 84 (2012) 449, http://dx.doi.org/10.1103/RevModPhys.84.449, arXiv:1203.4789.

[370] J.T. Daub, H.K. Dreiner, C. Hanhart, B. Kubis, U.G. Meißner, Improving the hadron physics of non-standard-model decays: Example bounds on R-parity violation, J. High Energy Phys. 01 (2013) 179, http://dx.doi.org/10.1007/JHEP01(2013)179, arXiv:1212.4408.

[371] V. Bernard, S. Descotes-Genon, G. Toucas, Determining the chiral condensate from the distribution of the winding number beyond topological susceptibility, J. High Energy Phys. 12 (2012) 080, http://dx.doi.org/10.1007/JHEP12(2012)080, arXiv:1209.4367.

[372] J.T. Daub, C. Hanhart, B. Kubis, A model-independent analysis of final-state interactions in $\bar{B}^0_{d/s} \to J/\psi\pi\pi$, J. High Energy Phys. 02 (2016) 009, http://dx.doi.org/10.1007/JHEP02(2016)009, arXiv:1508.06841.

[373] T. Aoyama, et al., The anomalous magnetic moment of the muon in the standard model, Phys. Rep. 887 (2020) 1–166, http://dx.doi.org/10.1016/j.physrep.2020.07.006, arXiv:2006.04822.

[374] G. Bennett, et al., Muon g-2 Collaboration, Measurement of the positive muon anomalous magnetic moment to 0.7 ppm, Phys. Rev. Lett. 89 (2002) 101804, http://dx.doi.org/10.1103/PhysRevLett.89.101804, arXiv:hep-ex/0208001; Phys. Rev. Lett. 89 (2002) 129903, Erratum.

[375] G. Bennett, et al., Muon g-2 Collaboration, Measurement of the negative muon anomalous magnetic moment to 0.7 ppm, Phys. Rev. Lett. 92 (2004) 161802, http://dx.doi.org/10.1103/PhysRevLett.92.161802, arXiv:hep-ex/0401008.

[376] G.W. Bennett, et al., Muon g-2 Collaboration, Final report of the muon E821 anomalous magnetic moment measurement at BNL, Phys. Rev. D 73 (2006) 072003, http://dx.doi.org/10.1103/PhysRevD.73.072003, arXiv:hep-ex/0602035.

[377] J. Grange, et al., Muon g-2 Collaboration, Muon (g-2) technical design report, 2015, arXiv:1501.06858.

[378] N. Saito, J-PARC g-'2/EDM Collaboration, A novel precision measurement of muon g-2 and EDM at J-PARC, in: T. Fukuyama, R.N. Mohapatra (Eds.), AIP Conf. Proc. 1467 (2012) 45–56, http://dx.doi.org/10.1063/1.4742078.

[379] B. Abi, et al., Muon g-2 Collaboration, Measurement of the positive muon anomalous magnetic moment to 0.46 ppm, Phys. Rev. Lett. 126 (14) (2021) 141801, http://dx.doi.org/10.1103/PhysRevLett.126.141801, arXiv:2104.03281.

[380] S. Borsanyi, et al., Leading hadronic contribution to the muon magnetic moment from lattice QCD, Nature 593 (7857) (2021) 51–55, http://dx.doi.org/10.1038/s41586-021-03418-1, arXiv:2002.12347.

[381] M. Davier, A. Hoecker, B. Malaescu, Z. Zhang, A new evaluation of the hadronic vacuum polarisation contributions to the muon anomalous magnetic moment and to $\alpha(m_Z^2)$, Eur. Phys. J. C 80 (3) (2020) 241, http://dx.doi.org/10.1140/epjc/s10052-020-7792-2, arXiv:1908.00921; Eur. Phys. J. C 80 (2020) 410, Erratum.

[382] M. Achasov, et al., Measurements of the parameters of the $\phi(1020)$ resonance through studies of the processes $e^+e^- \to K^+K^-$, $K_S K_L$, and $\pi^+\pi^-\pi^0$, Phys. Rev. D 63 (2001) 072002, http://dx.doi.org/10.1103/PhysRevD.63.072002, arXiv:hep-ex/0009036.

[383] J. Lees, et al., BaBar Collaboration, Precision measurement of the $e^+e^- \to K^+K^-(\gamma)$ cross section with the initial-state radiation method at BABAR, Phys. Rev. D 88 (3) (2013) 032013, http://dx.doi.org/10.1103/PhysRevD.88.032013, arXiv:1306.3600.

[384] A. Nyffeler, Hadronic light-by-light scattering in the muon g − 2, in: A. Denig, C.-F. Redmer (Eds.), EPJ Web Conf. 218 (2019) 01001, http://dx.doi.org/10.1051/epjconf/201921801001, arXiv:1710.09742.

[385] V. Pauk, M. Vanderhaeghen, Anomalous magnetic moment of the muon in a dispersive approach, Phys. Rev. D 90 (11) (2014) 113012, http://dx.doi.org/10.1103/PhysRevD.90.113012, arXiv:1409.0819.

[386] G. Colangelo, M. Hoferichter, M. Procura, P. Stoffer, Dispersive approach to hadronic light-by-light scattering, J. High Energy Phys. 09 (2014) 091, http://dx.doi.org/10.1007/JHEP09(2014)091, arXiv:1402.7081.

[387] G. Colangelo, M. Hoferichter, M. Procura, P. Stoffer, Dispersion relation for hadronic light-by-light scattering: theoretical foundations, J. High Energy Phys. 09 (2015) 074, http://dx.doi.org/10.1007/JHEP09(2015)074, arXiv:1506.01386.

[388] M. Hoferichter, B.-L. Hoid, B. Kubis, S. Leupold, S.P. Schneider, Dispersion relation for hadronic light-by-light scattering: pion pole, J. High Energy Phys. 10 (2018) 141, http://dx.doi.org/10.1007/JHEP10(2018)141, arXiv:1808.04823.

[389] M. Hoferichter, B.-L. Hoid, B. Kubis, S. Leupold, S.P. Schneider, Pion-pole contribution to hadronic light-by-light scattering in the anomalous magnetic moment of the muon, Phys. Rev. Lett. 121 (11) (2018) 112002, http://dx.doi.org/10.1103/PhysRevLett.121.112002, arXiv:1805.01471.

[390] G. Colangelo, M. Hoferichter, B. Kubis, M. Procura, P. Stoffer, Towards a data-driven analysis of hadronic light-by-light scattering, Phys. Lett. B738 (2014) 6–12, http://dx.doi.org/10.1016/j.physletb.2014.09.021, arXiv:1408.2517.

[391] G. Colangelo, M. Hoferichter, M. Procura, P. Stoffer, Dispersion relation for hadronic light-by-light scattering: two-pion contributions, J. High Energy Phys. 04 (2017) 161, http://dx.doi.org/10.1007/JHEP04(2017)161, arXiv:1702.07347.

[392] G. Colangelo, M. Hoferichter, M. Procura, P. Stoffer, Rescattering effects in the hadronic-light-by-light contribution to the anomalous magnetic moment of the muon, Phys. Rev. Lett. 118 (23) (2017) 232001, http://dx.doi.org/10.1103/PhysRevLett.118.232001, arXiv:1701.06554.

[393] G. Eichmann, C.S. Fischer, R. Williams, Kaon-box contribution to the anomalous magnetic moment of the muon, Phys. Rev. D 101 (5) (2020) 054015, http://dx.doi.org/10.1103/PhysRevD.101.054015, arXiv:1910.06795.

[394] I. Danilkin, C.F. Redmer, M. Vanderhaeghen, The hadronic light-by-light contribution to the muon's anomalous magnetic moment, Prog. Part. Nucl. Phys. 107 (2019) 20–68, http://dx.doi.org/10.1016/j.ppnp.2019.05.002, arXiv:1901.10346.

[395] I. Danilkin, M. Hoferichter, P. Stoffer, A dispersive estimate of scalar contributions to hadronic light-by-light scattering, Phys. Lett. B 820 (2021) 136502, http://dx.doi.org/10.1016/j.physletb.2021.136502, arXiv:2105.01666.

[396] I. Danilkin, O. Deineka, M. Vanderhaeghen, Data-driven dispersive analysis of the $\pi\pi$ and πK scattering, Phys. Rev. D 103 (11) (2021) 114023, http://dx.doi.org/10.1103/PhysRevD.103.114023, arXiv:2012.11636.

[397] S. Ciulli, A stable and convergent extrapolation procedure for the scattering amplitude.i, Nuovo Cimento A 61 (1969) 787–816, http://dx.doi.org/10.1007/BF02819619.

[398] S. Ciulli, A stable and convergent extrapolation procedure for the scattering amplitude. 2. Least squares and interpolation in roots of unity, Nuovo Cimento A 62 (1969) 301–318, http://dx.doi.org/10.1007/BF02731811.

[399] R. Cutkosky, B. Deo, Analysis of low-energy K^+p scattering data by a new method, Phys. Rev. D 1 (1970) 2547–2557, http://dx.doi.org/10.1103/PhysRevD.1.2547.

[400] A. Nogova, J. Pisut, Determination of the Δ(1236) pole position, Nuclear Phys. B 61 (1973) 445–454, http://dx.doi.org/10.1016/0550-3213(73)90375-1; Nucl. Phys. B 65 (1973) 544, Erratum.

[401] A. Nogova, J. Pisut, P. Presnajder, A method to determine resonance parameters from partial-wave amplitudes, Nuclear Phys. B 61 (1973) 438–444, http://dx.doi.org/10.1016/0550-3213(73)90374-X.

[402] M. Ciulli, S. Ciulli, A guide to analytic extrapolations. 1. A program for optimal extrapolation to interior points, Comput. Phys. Comm. 18 (1979) 215, http://dx.doi.org/10.1016/0010-4655(79)90115-2.

[403] I. Caprini, M. Ciulli, S. Ciulli, C. Pomponiu, I. Sabba-Stefanescu, M. Sararu, A guide to analytic extrapolations. 2. A problem to be used in finding analytic correlations of data, and for the detecting zeros and poles of the scattering amplitude, Comput. Phys. Comm. 18 (1979) 305–326, http://dx.doi.org/10.1016/0010-4655(79)90001-8.

[404] F. James, M. Roos, Minuit: A system for function minimization and analysis of the parameter errors and correlations, Comput. Phys. Comm. 10 (1975) 343–367, http://dx.doi.org/10.1016/0010-4655(75)90039-9.

[405] A. Martin, T. Spearman, Elementary Particle Theory, North-Holland Pub. Co. 1970, URL https://books.google.com/books?id=sxAzAAAAMAAJ.

[406] H. Lehmann, Analytic properties of scattering amplitudes as functions of momentum transfer, Nuovo Cim. 10 (1958) 579.

[407] A. Martin, Extension of the axiomatic analyticity domain of scattering amplitudes by unitarity. I, Nuovo Cim. A42 (1965) 930–953, http://dx.doi.org/10.1007/BF02720568.

[408] A. Martin, Extension of the axiomatic analyticity domain of scattering amplitudes by unitarity. II, Nuovo Cim. A42 (1966) 1219–1244, http://dx.doi.org/10.1007/BF02719361.

[409] G. Höhler, Numerical Data and Functional Relationships in Science and Technology. Group I: Nuclear and Particle Physics. Vol. 9: Elastic and Charge Exchange Scattering of Elementary Particles. B: Pion-Nucleon Scattering. Pt. 2: Methods and Results of Phenomenology, Springer, Berlin, Germany, 1984, (1983) 601 P. (Landolt-Boernstein. New Series, I/9B2).